T2R2 東京科学大学 リサーチリポジトリ
Science Tokyo Research Repository

論文 / 著書情報
Article / Book Information

題目(和文)	Al-Li-Cu系合金の相分解における微視的組織変化および微量添加元素の効果
Title(English)	Microstructure Evolution and Role of Microalloying Elements in Phase Decomposition of Al-Li-Cu Base Alloys
著者(和文)	廣澤渉一
Author(English)	shoichi hirosawa
出典(和文)	学位:工学博士, 学位授与機関:東京工業大学, 報告番号:甲第3673号, 授与年月日:1998年3月26日, 学位の種別:課程博士, 審査員:
Citation(English)	Degree:Doctor of Engineering, Conferring organization: Tokyo Institute of Technology, Report number:甲第3673号, Conferred date:1998/3/26, Degree Type:Course doctor, Examiner:
学位種別(和文)	博士論文
Type(English)	Doctoral Thesis

Powered by T2R2 (Science Tokyo Research Repository)

Microstructure Evolution and Role of Microalloying Elements in Phase Decomposition of Al-Li-Cu Base Alloys

BY

Shoichi Hirosawa

Doctoral Thesis

Department of Metallurgical Engineering
Tokyo Institute of Technology

1998

Microstructure Evolution and Role of Microalloying Elements in Phase Decomposition of Al-Li-Cu Base Alloys

Contents

Chapter 1 General Introduction

Chapter 4 Microstructure Evolution of Cu Atom Clustering and Kinetics of Low-Temperature Precipitation in Al-Cu Alloys with Microalloying Elements

Chapter 5 Microstructure Evolution of Li Atom Ordering and Kinetics of Low-Temperature Precipitation in Al-Li Alloys with Microalloying Elements

Chapter 6 Microstructure Evolution of Solute Atom Clusters and Kinetics of Low-Temperature Precipitation in Al-Li-Cu Alloys with Microalloying Elements

Chapter 7 Nucleation Mechanism of T_1 Phase Precipitation in Al-Li-Cu Alloys

Chapter 8 Prediction of Effects of Microalloying Elements and Application to Alloy Designing of New Al-Li-Cu Base Alloys

LIST OF PUBLICATIONS FOR THE PRESENT THESIS

ABSTRACT OF THE PRESENT THESIS

Acknowledgments

Chapter 1
General Introduction

1.1 Introduction

"Developing new materials for specific, or as yet unknown, purposes is the lifeblood of industry" — *The Times*. The history of materials development is as old as the history of civilization. From the ancient Egypt, the Stone, Bronze and Iron ages to our own time, the development of new materials has drastically innovated in the latest engineering and technology of those days. In the industrial revolution in the later 18th century, for example, mass production of steel stimulated huge diversity in all fields of industrial engineering. In the period of world wars, the evolution of high-strength aluminum alloys played an important role in the competitive development of military fighter aircrafts. Since the oil crisis in 1973, furthermore, lower-density materials have been extensively required with the intention of direct replacement of conventional materials resulting in both the improved performance and fuel savings of airplane, motor and space vehicles. An aluminum-lithium alloy is a most promising and high-powered candidate in pursuit of such purposes.

1.1.1 Al-Li alloy as a new light material

Lithium is the lightest metallic element found in nature with density of 0.534g/cm^3 at 300K, which is about one-fifths of that of aluminum(i.e. 2.7g/cm^3), and each 1mass% addition to aluminum reduces alloy density by about 3% and also increases modulus by about 5%[1]. The addition of lithium also allows the precipitation hardening of aluminum during phase decomposition occurring in the binary alloys. Figure 1.1[2] shows the equilibrium and metastable phase diagram of the Al-Li system, which is typically of age-hardening type because of a marked decreasing solubility of Li in the α single-phase with decreasing temperature. The transient metastable δ'(Al_3Li) phase is well recognized to be responsible for the age-hardening of Al-Li alloys. The δ' phase is normally formed homogeneously with a spherical shape having a $L1_2$-type ordered structure prior to the equilibrium B32-type δ(AlLi) phase. The atomic arrangements of unit cells of the two phases are illustrated in Fig.1.2. In general, plastic deformation of the Al-Li alloys strengthened by the δ' phase is believed to take place in the following manners. In the under-aged condition, δ' particles are cut by moving pair dislocations; i.e. superlattice dislocation mechanism, whereas in the over-aged condition, dislocations move away leaving Orowan loops at the δ' particles; i.e. by-pass mechanism. Under the peak aging condition;

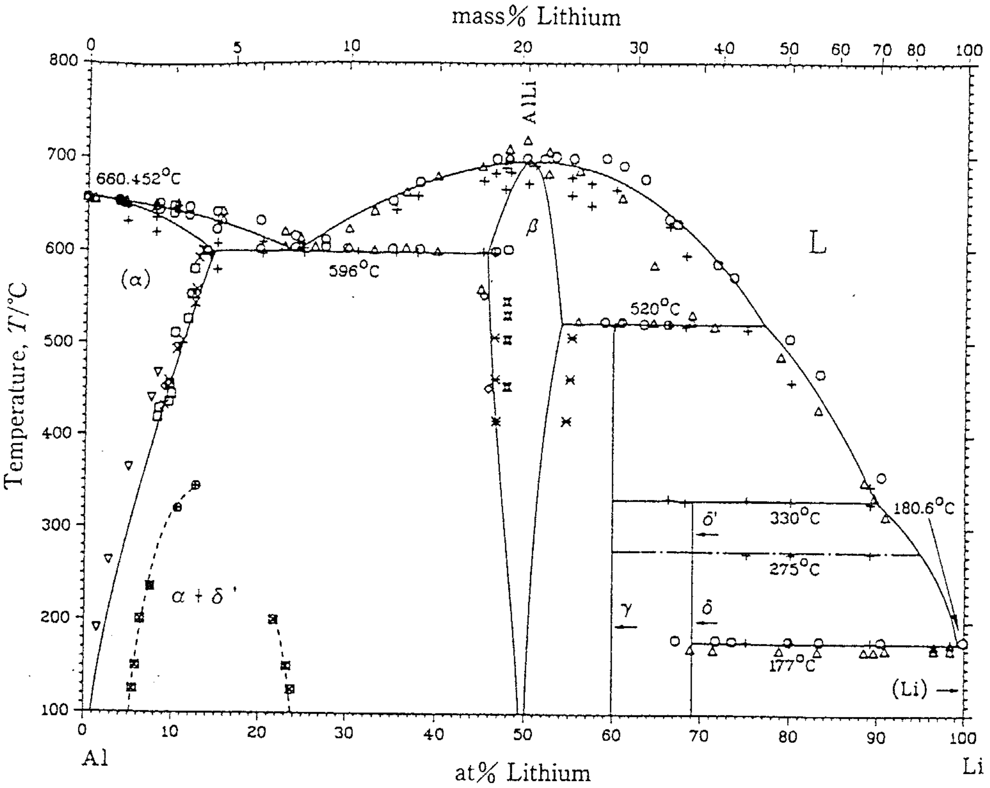

Fig. 1 The Al-Li metastable phase diagram(3).
α : aluminum primary solid solution,
δ' : $L1_2$-type metastable phase of Al_3Li, and
β : B32-type stable phase of AlLi.

Fig.1.1 The equilibrium and metastable phase diagram of Al-Li system[2].

α :aluminum primary solid solution
δ' :$L1_2$-type metastable phase of Al_3Li
β(δ) :B32-type stable phase of AlLi

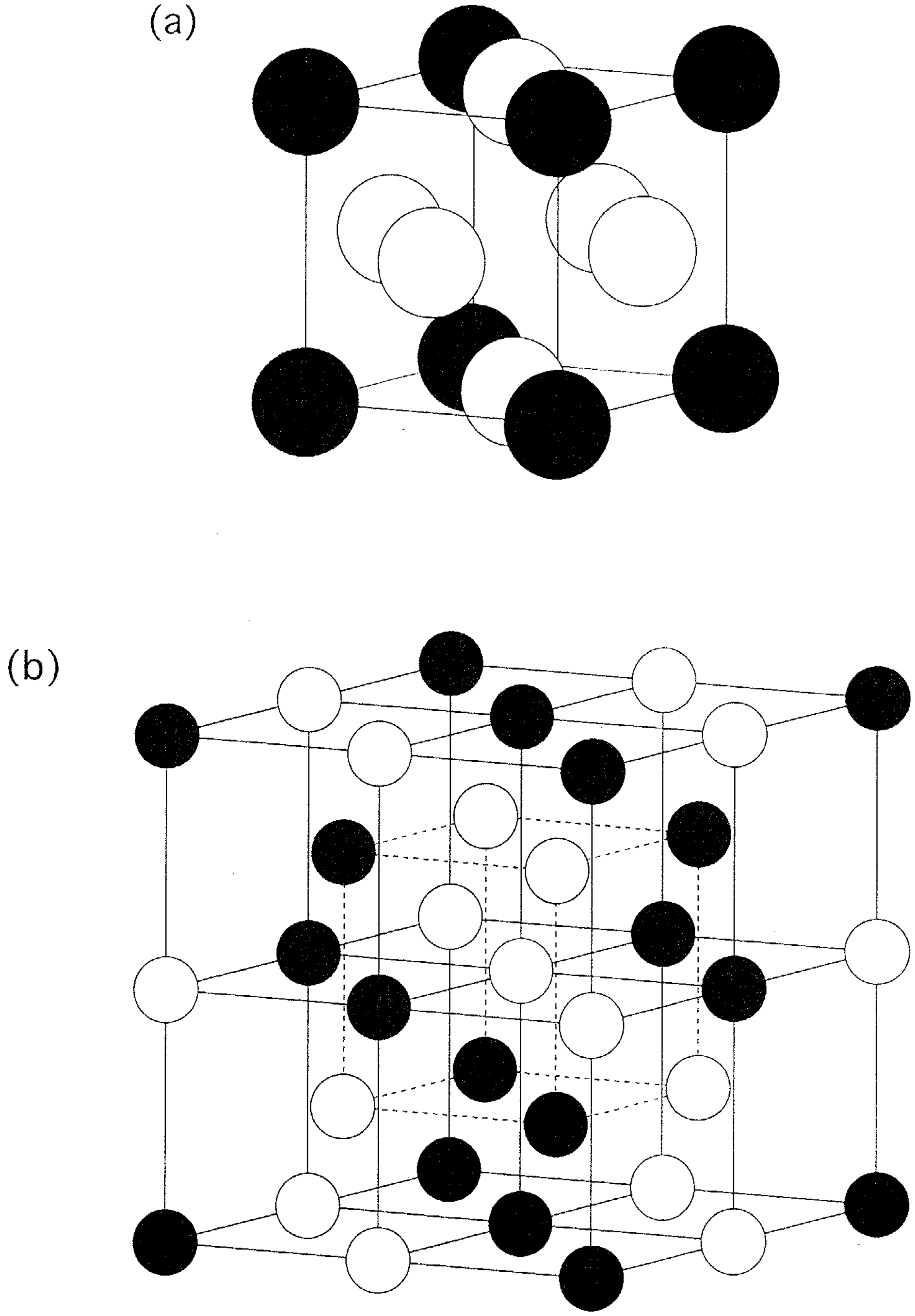

Fig.1.2 Unit cells of crystal structures of two precipitates in Al-Li alloys; (a) metastable δ' (Al_3Li) phase having a $L1_2$-structure and (b) stable δ (AlLi) phase having a B32-structure. The open and solid circles represent Al and Li atoms, respectively.

i.e. T6 temper condition, it is reported that the proof stress to levels of ~350MPa is achieved in an Al-Li binary alloy[3]. In the selection of new light materials for the 21st century, therefore, it is reasonable that Al-Li alloys have been received considerable attention due to their excellent combination of high specific strength and low density.

From a viewpoint of commercial applications, however, the δ' phase is not worth while to be a predominant strengthening phase because mechanical properties of the Al-Li alloys strengthened by the δ' phase are too poor to be utilized as a material for structural components. As described above, under-aged conditions, which are normally applied to commercial Al-Li alloys as an optimum heat treatment condition[4], inevitably cause dislocations to move in pairs on a particular slip plane by cutting δ' particles. This deformation mechanism results in a low ductility and low fracture toughness of Al-Li alloys so that the stress concentration at grain boundaries induced by the dislocation pileup eventually leads to grain boundary failure. The addition of alloying elements is an effective method to improve such poor mechanical properties of Al-Li alloys.

Aside from the industrial importance, the phase decomposition of Al-Li alloys also has drawn much attention among scientists because a somewhat interesting behavior is observed in the supersaturated solid solutions. In general, phase decompositions occurring in quenched alloys can be divided into two categories; i.e. clustering and ordering processes. When Al-Li alloys are quenched from α into $\alpha+\delta$' two-phase region in Fig.1.1, however, a simultaneous reaction of both processes takes place. Khachaturyan *et al.* [5] made a theoretical investigation on the precipitation paths of quenched Al-Li alloys using a mean-field thermodynamic model. Their theoretical analysis predicts that disordered solid solution congruently orders followed by decomposition into two ordered regions with different Li concentrations. The final microstructure consisting of both ordered δ' particles and the disordered matrix, thus, is developed so that the Li-lean region eventually disorders due to the instability of free energies with respect to the composition and/or the degree of order. This theoretical prediction is extensively accepted now because some experimental results[6-8] and computational analysis[9] strongly support the fact that congruent ordering precedes decomposition in the Al-Li system. However, little is known about the detailed effects of third additional elements on the decomposition behavior of Al-Li alloys.

1.1.2 Development of Al-Li-Cu base alloys

Although the Scleron alloy was developed in the early 1920s, most of commercial

Al-Li alloys were registered in the middle 1980s and early 1990s, when airframe manufactures stimulated the development of new light materials, as shown in Table 1.1. As a major additional element to Al-Li alloys, Cu has been utilized to produce new strengthening phases such as GP zone, θ '(Al_2Cu) and T_1(Al_2LiCu) in place of the δ ' phase. Equilibrium and proposed metastable phase diagrams at 473K of the Al-Li-Cu system are illustrated in Figs.1.3 and 1.4[10, 11]. Zr is also added to retard recrystallization resulting in a decreased grain size of the alloys, which is caused by the dispersoid formation of fine β '(Al_3Zr) particles. In a fabrication process, however, such the developed Al-Li alloys; e.g. the 2090(Al-Li-Cu-Zr), 2091, 8090 and 8091(Al-Li-Cu-Mg-Zr) alloys, must be inevitably subjected to the stretch temper by 3-7% prior to artificial aging treatments to promote the homogeneous precipitation of the above strengthening phases (i.e. T8 temper condition). Since such pre-worked temper is quite unpractical especially for the fabrication of large component parts, however, further attempts have been conducted to obtain the same mechanical properties without stretching as those of the T8 temper alloys on the basis of a small addition of various alloying elements. The latest registered 2094, 2095, 2096 and 2195 alloys, which contain small amounts of Mg and Ag, successfully achieve the excellent mechanical strength without stretching of the highest tensile strength over 700MPa[12-14] among all ingot metallurgy(I/M) aluminum alloys. The high strength by the simultaneous addition of Mg and Ag entirely attributes to the transgranular precipitation of the T_1(Al_2LiCu) phase[14-16], which is normally formed at subgrain boundaries in the formerly registered Al-Li-Cu alloys without stretching.

The thin plate-like T_1 phase, which is observed to lie on four {111} planes in the Al matrix, is classified to be of hexagonal structure with a stacking sequence of ABABAB... . This implies that the T_1 phase formation inevitably introduces a high number density of stacking faults in the fcc Al; i.e. ABCABABC..., nevertheless, whose stacking fault energy is so high (e.g. $\sim$0.15J/m^2[17]) that hexagonal closed-packed (hcp) phases can not directly nucleate. Therefore, it becomes necessary to consider the presence of some heterogeneous nucleation sites for the T_1 phase, for example, by taking into account the roles of small additional elements and quenched-in excess vacancies. Although some mechanisms have been proposed so far[18-23], the accelerated T_1 phase precipitation by the combined Mg and Ag addition is still under debate because of the discrepancy between them. One interesting point is why these elements can stimulate the T_1 phase nucleation, nevertheless, whose composition does not contain them at all. From both technological and phenomenological points of view, therefore, it is quite important to elucidate the mechanism

Table 1.1 Chemical compositions of registered Al-Li alloys.

Alloys	Li	Cu	Mg	Ag	Zr	Mn	Cr	Zn	Other	Al	Registered year
Scleron*	0.1	3	—	—	—	0.6	—	12	—	bal.	1924
2020*	1.0	4.5	—	—	—	0.8	—	—	0.15Cd	bal.	1974
2090	1.9-2.6	2.4-3.0	0.25	—	0.08-0.15	0.05	0.05	0.10	—	bal.	1984
2091	1.7-2.3	1.8-2.5	1.1-1.9	—	0.04-0.16	0.10	0.10	0.25	—	bal.	1985
2094	0.7-1.4	4.4-5.2	0.25-0.8	0.25-0.6	0.04-0.18	0.25	—	0.25	—	bal.	1990
2095	0.7-1.5	3.9-4.6	0.25-0.8	0.25-0.6	0.04-0.18	0.25	—	0.25	—	bal.	1990
2195	0.8-1.2	3.7-4.3	0.25-0.8	0.25-0.6	0.08-0.16	0.25	—	0.25	—	bal.	1992
2096	1.3-1.9	2.3-3.0	0.25-0.8	0.25-0.6	0.04-0.18	0.25	—	0.25	—	bal.	1993
2097	1.2-1.8	2.5-3.1	0.35	—	0.08-0.16	0.10-0.6	—	0.35	—	bal.	1993
2197	1.3-1.7	2.5-3.2	0.25	—	0.08-0.15	0.10-0.15	—	0.05	—	bal.	1993
5091	1.2-1.4	—	3.7-4.2	—	—	—	—	—	—	bal.	1992
8090	2.2-2.7	1.0-1.6	0.6-1.3	—	0.04-0.16	0.1	0.1	0.25	—	bal.	1984
8091	2.4-2.8	1.6-2.2	0.50-1.2	—	0.08-0.16	0.1	0.1	0.25	—	bal.	1985
8093	1.9-2.6	1.0-1.6	0.9-1.6	—	0.04-0.14	0.1	0.1	0.25	—	bal.	1990

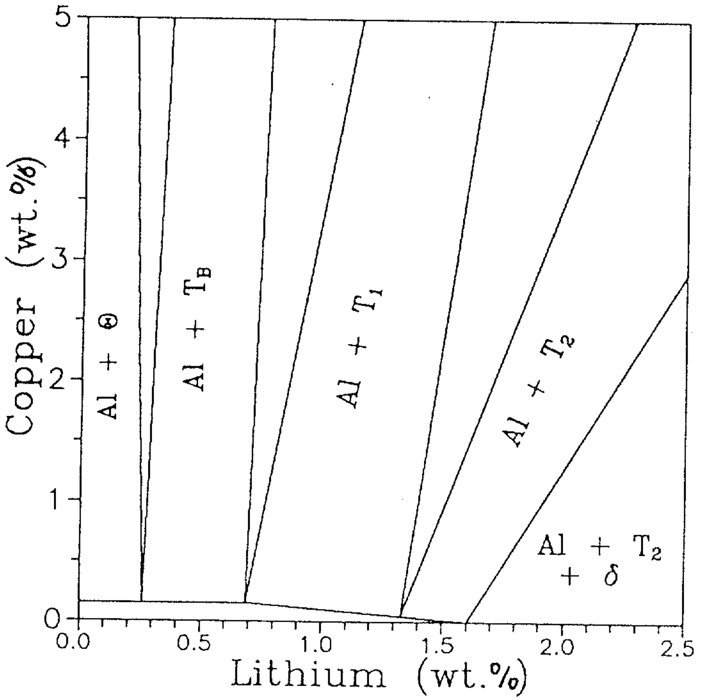

Fig.1.3 Equilibrium Al-Li-Cu phase diagram at 473K[10].

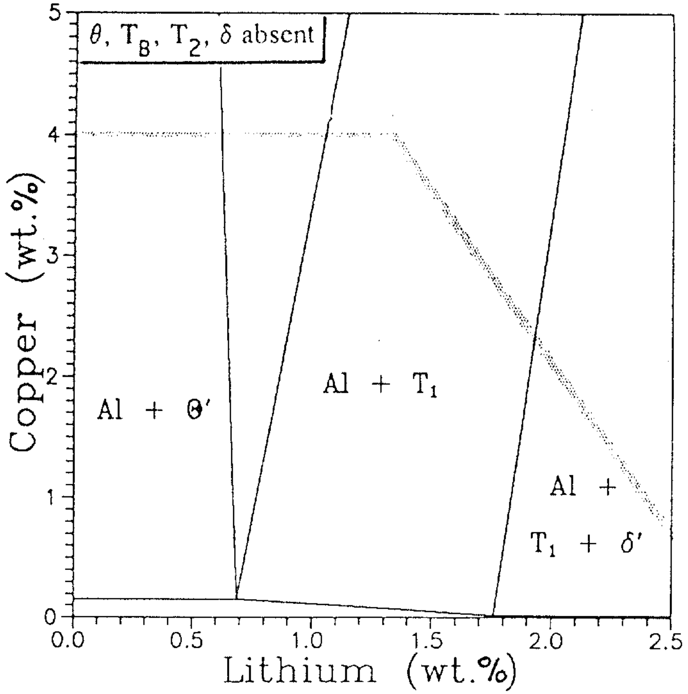

Fig.1.4 Proposed metastable phase diagram at 473K for equilibria of α-Al with θ', T_1 and δ'. Solubility limit at 773K is as gray line in diagram[11].

of the transgranular T_1 phase precipitation occurring in Al-Li-Cu alloys containing small amounts of Mg and Ag.

1.1.3 Effects of microalloying elements

Small additions of some alloying elements are of prime importance to improve mechanical properties of alloys. Such so-called "microalloying" additions have been widely applied to various alloy systems. For example, microalloying elements such as Nb, V and Ti in low carbon steels; i.e. high strength low alloy (HSLA) steels, are utilized to produce fine carbide and/or nitride precipitates during thermomechanical processing, resulting in the tensile strength to levels over 1200MPa[24]. In Al-Cu alloys, furthermore, it is well known that trace elements of Sn, In and Cd increase both the rate and extent of age-hardening at elevated aging temperatures due to the finer and more uniform dispersion of the θ'(Al_2Cu) phase[25-27]. Therefore, the enhanced T_1 phase precipitation by the combined Mg and Ag addition to Al-Li-Cu alloys may be also an example of the success of improved properties of alloys by microalloying additions.

As for the effects of microalloying elements on the δ' phase formation, only few attempts have been made compared with those for Al-Cu alloys. In general, the small difference of lattice parameters between the δ' phase (a=0.401-0.4038nm) and Al (a=0.40496nm) is well recognized to be responsible for the low mechanical strength of Al-Li alloys because of a small coherent strain around δ' particles. As is the structurally analogous case of γ'/γ in Ni-base superalloys, therefore, microalloying additions may improve the mechanical properties of Al-Li alloys. Baumann *et al.*[28] reported that small additions of Ag and Zn increase both the δ'/α lattice misfit and δ' solvus temperature because of the preferential partitioning of these elements within the δ' phase. Sato *et al.*[29] also investigated the δ' phase stability in Al-Li alloys containing Ag, Au and Mg and concluded that the preferential partitioning of these additional elements inside the δ' phase markedly affects to increase the solvus temperature and coarsening rate of the particles. However, these investigations mainly address the microstructure changes induced by microalloying additions rather than the improved mechanical properties of Al-Li alloys.

Even for the phase decomposition kinetics, such a microalloying addition affects to a great extent. For example, Sn, In and Cd additions to Al-Cu alloys markedly reduce or inhibit the low-temperature aging by suppressing the GP zone formation, unlike the case of high-temperature aging described above. This pronounced retardation has been explained in terms of the so-called vacancy trapping effect proposed by Kimura *et al.*[30], in which these additional atoms preferentially trap quenched-in excess vacancies available for Cu diffusion. This proposed effect is on the basis of experimentally obtained binding energies between a solute atom and a vacancy in the corresponding dilute Al alloys[31-37] (Table 1.2). Although higher values of Sn-, In- and Cd-Vacancy pairs in Table 1.2 certainly suggest the probability of the above mechanism, these values are always pointed out to be doubtful because quenching experiments based on the residual electrical resistivity can not follow clustering of solute atoms during quenching operation[38-40]. In fact, reinvestigated binding energies with special attention to the prevention of the solute atom clustering[41] are extremely smaller than previously reported ones as shown with brackets ( ) in Table 1.2. Therefore, a theoretical approach based on characteristic quantities of each element becomes extremely effective in predicting the role of an arbitrary microalloying element.

1.1.4 Prediction of role of microalloying elements using computer simulation

Because of the recent rapid progress in computer hardware, a new field in materials science "Computational Materials Science" has been advanced based on the possibility of performing computer simulations of large systems. At present, such the computer simulation technology is widely applied to inquiries into various physical phenomena occurring in solid materials. In general, a direct detection of phase transformations occurring in alloys; e.g. diffusion of solute atoms, nucleation and growth of precipitates and preferential partitioning of additional elements, is significantly difficult using any available experimental methods. A computer simulation using a Monte Carlo method[42] is an alternative powerful tool to elucidate the mechanisms because the method can reproduce atomistic events spatially and temporally for arbitrary alloy systems. Soisson *et al.*[43] performed a Monte Carlo simulation of Cu atom clustering in α-Fe to follow the microstructural evolution of the morphology, composition and size distribution of Cu atom clusters. Ikeda *et al.*[44, 45] qualitatively ascribed electrical resistivity changes of an Al-4.5mol%Zn alloy to size distributions of Zn atom clusters obtained from a Monte Carlo simulation. Furthermore, Saito *et al.*[46] applied the simulation to ordering of the γ' phase in commercial Ni-base superalloys in order to predict preferential substitution sites of some alloying elements.

The simultaneous reaction of clustering and ordering processes in the Al-Li system can be also investigated. Okuda *et al.*[9] reproduced the phase decomposition of an Al-Li binary alloy on a Monte Carlo simulation using an extended pair interaction model[47, 48], in which pair interactions between second nearest neighbors are also taken into account in

Table 1.2 Reported values of binding energy, $E^{b}_{s\text{-}v}$, between a solute atom, s , and a vacancy, v , in the dilute Al alloy.

Solutes	$E^{b}_{s\text{-}v}$ / eV	References	Solutes	$E^{b}_{s\text{-}v}$ / eV	References
Li	0.26	[26]	Sn	0.22	[27]
Cu	0.05	[27]	Cd	0.18	[27]
Mg	0.19	[27]	In	0.25	[27]
Zn	0.10	[28]	Fe	0.24	[29]
Ag	0.08	[29]	Mn	0.15	[31]
Si	0.23	[27]	Zr	0.24	[32]
Ge	0.22	[30]			
Cu	(0.03 ±0.02)	[36]	Ag	(0.01 ±0.01)	[36]
Mg	(0.04 ±0.03)	[36]	Si	(0.07 ±0.01)	[36]
Zn	(0.02 ±0.03)	[36]			

addition to those between nearest neighbors. Under this pair interaction model, most stable atomic configurations become a mixture of ordered structures in the disordered matrix if nearest and second nearest neighbor interactions have negative and positive values, respectively. Therefore, a Monte Carlo simulation using the extended pair interaction model[47, 48] is considered to be effective even in inquiries the effects of microalloying additions to Al-Li alloys.

1.2 Objectives of the present thesis

The objectives of the present thesis are ① to elucidate the role of microalloying elements on the mechanical strength and precipitate microstructures of Al-Li-Cu alloys, and also ② to propose a new high strength Al-Li-Cu alloy based on a theoretical prediction from the results of a Monte Carlo simulation.

The results of transmission electron microscopy (TEM) reveal that the simultaneous formation of some precipitates takes place at various aging temperatures in multicomponent Al-Li-Cu alloys. In this work, the effects of various microalloying elements are investigated first in the cases of simple Al-Cu and Al-Li binary alloy. Comparison between the quantitative kinetics determined from the electrical resistivity changes and the microstructure evolution directly observed in the computer simulation gives useful information concerning both the macroscopic and atomistic phase decomposition behaviors in the investigated alloys. The utilized simulation model based on a Monte Carlo method[49] assumes a rigid fcc lattice in order to reflect atom configurations in Al alloys as exactly as possible. All simulation parameters, which significantly affect the obtained simulation results, were derived from characteristic thermodynamic or kinetic quantities of each element. Not only good agreement between the experimental and theoretical tendencies but also first prediction of the effects of previously never reported microalloying elements is a most important result obtained in the present thesis.

From the results of the above simple Al-Cu and Al-Li binary alloys, furthermore, the effects of microalloying additions to multicomponent Al-Li-Cu alloys are discussed. The obtained simulation results are well classified in terms of the characteristic features of microalloying elements. In particular, a small amount of Mg succeeds in the improvement of the mechanical strength of the ternary alloy because of the simultaneous strong interaction with Li and Cu atoms. The proposed simulation model can provide reasonable mechanisms on the accelerated precipitation, which is entirely responsible for the increased mechanical strength in the Mg-added Al-Li-Cu alloys. The theoretical prediction on the roles of microalloying elements leads to a concept for alloy designing of new high strength Al-Li-Cu alloys.

1.3 Outline of the present thesis

Chapter 1 General Introduction

In this chapter, a brief review on some advantages of Al-Li alloys as a new light material, pronounced effects of microalloying elements and theoretical approaches using a computer simulation has been first presented. Objectives and straightforward outline of the present thesis are also described in the following sections.

Chapter 2 Mechanical Properties and Precipitate Microstructures of Al-Li-Cu Alloys with Microalloying Elements of Mg and Ag

In this chapter, the pronounced effects of a simultaneous addition of Mg and Ag on the mechanical properties and precipitate microstructures of an Al-Li-Cu-Zr alloy have been investigated under various aging conditions. The obtained results are significantly dependent on applied aging temperatures, which promote a simultaneous formation of the precipitates observed in the Al-Cu, Al-Li and Al-Li-Cu alloy systems. This leads to the reason why the present thesis is divided into the following chapters.

Chapter 3 Computer Simulation Models and Derivation Method of Parameters

In this chapter, a Monte Carlo method is briefly introduced first with its several advantages. Fundamentals and conditions of the utilized simulation models, quantitative analysis procedure of simulation microstructures and comparison method with actual aging times are also described in the following sections. The derivation method of utilized simulation parameters, which are determined by the knowledge of experimental thermodynamic or kinetic quantities, are proposed in Section 3.3. Finally, the calculation method of electrical resistivity from obtained simulation results is shown to establish the reliability of this simulation model by comparing with experimentally measured electrical resistivity changes.

Chapter 4 Microstructure Evolution of Cu Atom Clustering and Kinetics of Low-Temperature Precipitation in Al-Cu Alloys with Microalloying Elements

In this chapter, the effects of third additional elements on the kinetics of the GP zone formation in an Al-Cu alloy have been experimentally investigated in the temperature range from 278 to 373K. In particular, the effects of small amount of Mg were examined in detail from both viewpoints of the nucleation and growth of GP zones. A Monte Carlo simulation using only nearest neighbor pair interactions was performed to examine the microstructural evolution of Cu atom clusters resulting in the GP zone formation. Comparison between the quantitative kinetics determined from the resistivity changes and the microstructural evolution directly observed in the simulation gives important information on both the macroscopic phase decomposition kinetics and the microstructural formation mechanism of Cu clusters in Al-Cu alloys containing various additional elements.

Chapter 5 Microstructure Evolution of Li Atom Ordering and Kinetics of Low-Temperature Precipitation in Al-Li Alloys with Microalloying Elements

In this chapter, the effects of third additional elements on the kinetics of low-temperature precipitation in an Al-Li alloy have been experimentally investigated at temperatures from 278 to 373K. The obtained resistivity changes well demonstrate each phase decomposition stage previously observed in Al-Li alloys. The extended Monte Carlo simulation, in which pair interactions between up to second nearest neighbor atoms are taken into account, was performed to examine the microstructural evolution of ordered structures resulting in the δ' phase precipitation. Comparison between the quantitative kinetics determined from the resistivity changes and the microstructural evolution directly observed in the simulation can make clear the relationships between the macroscopic phase decomposition kinetics and the microstructural formation mechanism of the δ' phase in Al-Li alloys containing various additional elements.

Chapter 6 Microstructure Evolution of Solute Atom Clusters and Kinetics of Low-Temperature Precipitation in Al-Li-Cu Alloys with Microalloying Elements

In this chapter, the effects of various additional elements on the age-hardening behavior and precipitate microstructures of an Al-Li-Cu-Zr alloy have been investigated in the temperature range from 278 to 373K. In particular, the effect of small additional Mg, which plays an important role in the accelerated low-temperature precipitation of the quaternary alloy, was quantitatively examined by electrical resistivity measurement. From the atomistic analysis using a Monte Carlo simulation, the characteristic transformation mechanism in Al-Li-Cu-Zr alloys is discussed in the comparison with the simple Al-Cu (Chapter 4) and Al-Li (Chapter 5) binary alloys.

Chapter 7 Nucleation Mechanism of T_1 Phase Precipitation in Al-Li-Cu Alloys

In this chapter, the effects of various additional elements on the age-hardening behavior and precipitate microstructures of an Al-Li-Cu-Zr alloy have been investigated in the temperature range from 403 to 523K. In particular, a small addition of Mg, which is most effective in improving the mechanical properties of the quaternary alloy, is focused and closely related to the nucleation mechanism of the T_1 phase. From the difference in the T_1 phase distributions between three quenching conditions; i.e. W.Q.(water-quench), D.Q.(direct-quench) and S.Q.(step-quench), heterogeneous nucleation sites for the T_1 phase are discussed in terms of both solute atom clusters and point defects aggregates. The Monte Carlo simulation taken into account the effects of quenched-in excess vacancies can well reproduce the proposed mechanism of the T_1 phase nucleation.

Chapter 8 Prediction of Effects of Microalloying Elements and Application to Alloy Designing of New Al-Li-Cu Base Alloys

In this chapter, the obtained simulation results in the previous chapters were classified in terms of characteristic properties of each microalloying element added to an Al-Cu, Al-Li or Al-Li-Cu alloy. From the theoretical prediction on the roles of microalloying elements, furthermore, a concept for alloy designing of new high strength Al-Li-Cu alloys is proposed. The concept is composed of the control of Cu and Mg contents, selection of microalloying elements and optimization of applied solution treatment temperatures. As a consequence of these alloy designing methods, the highest tensile strength of 656MPa in the L (longitudinal) direction is achieved in a newly developed Al-Li-Cu-Mg-Ag-Zr-Zn-Mn alloy.

Chapter 9 Conclusions

In this chapter, conclusion remarks of the present thesis are summarized from the results in each chapter.

The flowchart representing outline of the present thesis is shown in Fig.1.5.

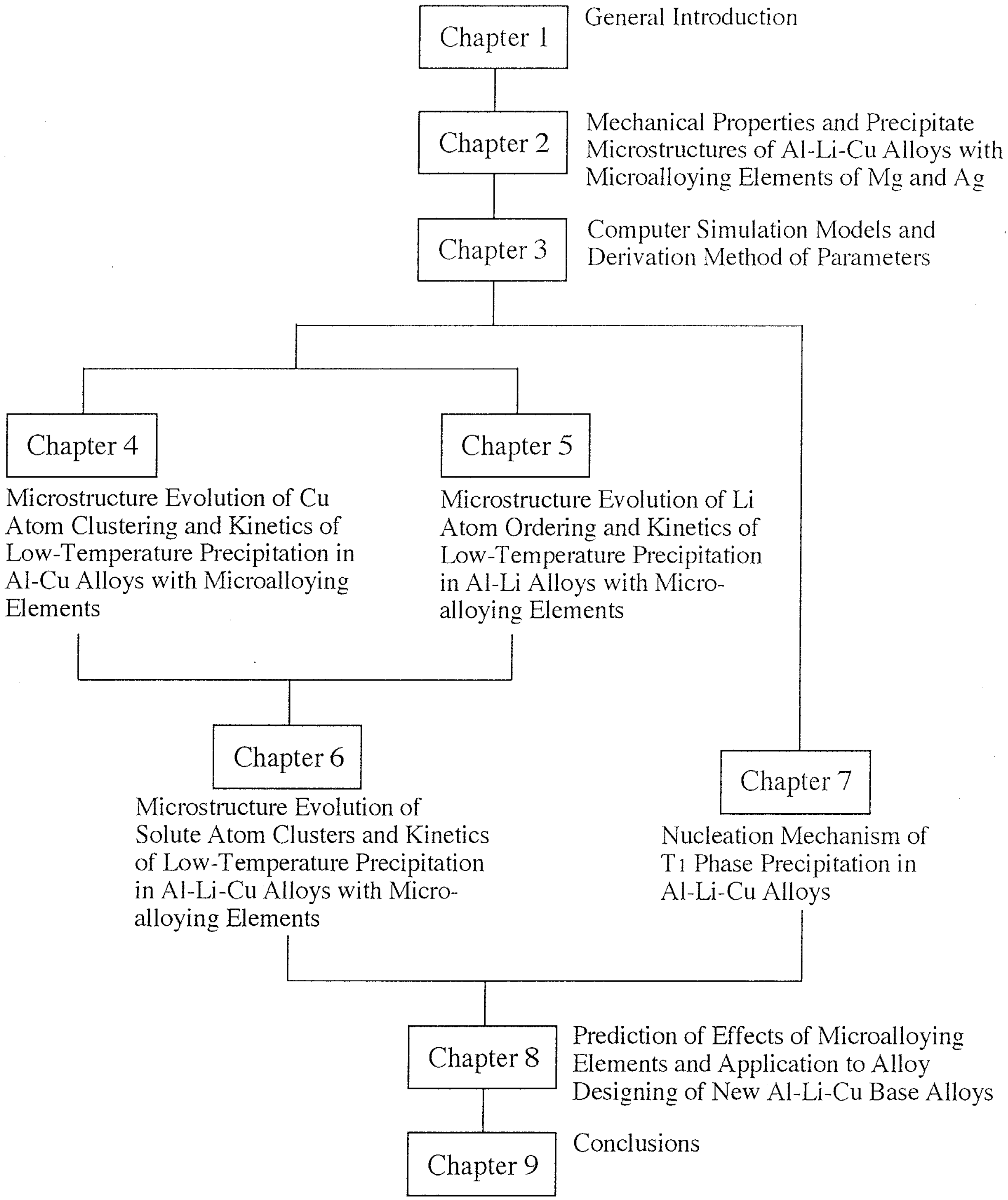

Fig. 1.5 Outline of the present thesis.

References

[1] ASM Handbook: **Vol.2**, *Properties and Selection: Nonferrous Alloys and Special-Purpose Materials*, ed. by J.R.Davis, (1990), p.178.

[2] M.Furukawa, Y.Miura and M.Nemoto: Bulletin of Japan Inst. Metals, **23** (1984), 172.

[3] B.Noble, S.J.Harris and K.Dinsdale: Acta metall. mater., **45** (1997), 2069.

[4] P.D.Pitcher, D.S.McDarmaid C.J.Peel and G.Hall: Proc. 6th Int. Al-Li Conf., (1991), 235.

[5] A.G.Khachaturyan, T.F.Lindsey and J.W.Morris, Jr.: Metall. Trans. A, **19A** (1988), 249.

[6] B.J.Shaiu, H.T.Li and H.Y.Lee and H.Chen: Metall. Trans. A, **21A** (1990), 1133.

[7] M.S.Yu and H.Chen: *Kinetics of Ordering Transformations in Metals*, Ed. H.Chen and V.K.Vasudevan, The Minerals, Metals & Mater. Society, (1992), p.307.

[8] T.Sato and A.Kamio: Mater. Trans., JIM, **31** (1990), 25.

[9] H.Okuda and K.Osamura: Acta metall. mater., **42** (1994), 1337.

[10] H.Suzuki, M.Kanno and N.Hayashi: J. Jpn. Inst. Light Metals, **32** (1982), 88.

[11] F.W.Gayle, W.T.Tack, F.H.Heubaum and J.R.Pickens: Proc. 6th Int. Al-Li Conf., **Vol.1** (1991), 203.

[12] F.W.Gayle, F.H.Heubaum and J.R.Pickens: Scripta Metall., **24** (1990), 79.

[13] W.T.Tack, F.H.Heubaum and J.R.Pickens: Scripta Metall., **24** (1990), 1685.

[14] J.R.Pickens, F.H.Heubaum, T.J.Langan and L.S.Kramer: Proc. 5th Int. Al-Li Conf., **Vol.3** (1987), 1397.

[15] T.J.Langan and J.R.Pickens: Proc. 5th Int. Al-Li Conf., **Vol.2** (1987), 691.

[16] I.J.Polmear and R.J.Chester: Scripta Metall., **23** (1989), 1213.

[17] V.D.Scott, S.Kerry and R.L.Trumper: Mater. Sci. and Tech., **3** (1987), 827.

[18] J.R.Pickens, F.H.Heubaum, T.J.Langan and L.S.Kramer: Proc. 5th Int. Al-Li Conf., **Vol.3** (1987), 1397.

[19] H.Suzuki, M.Kanno and N.Hayashi: J. Jpn. Inst. Light Metals, **32** (1982), 577.

[20] V.D.Scott, S.Kerry and R.L.Trumper: Mater. Sci. and Tech., **3** (1987), 827.

[21] G.Itoh, Q.Cui and M.Kanno: Mater. Sci. and Eng. A, **A221** (1996), 128.

[22] H.Suzuki, M.Kanno and N.Hayashi: J. Jpn. Inst. Light Metals, **32** (1982), 88.

[23] R.J.Rioja and E.A.Ludwiczak: Proc. 3th Int. Al-Li Conf., (1985), 471.

[24] For example, M.Katsumata, O.Ishiyama, T.Inoue and T.Tanaka: Mater. Trans., JIM, **32** (1991), 715.

[25] H.K.Hardy: J. Inst. Metals, **78** (1950-51), 169.

[26] Y.Baba: Mater. Trans., JIM, **10** (1969), 188.

[27] I.J.Polmear and H.K.Hardy: J. Inst. Metals, **84** (1955-56), 23.

[28] S.F.Baumann and D.B.Williams: Proc. 2nd Int. Al-Li Conf., TMS of AIME, New York, (1984), p.17.

[29] T.Sato and A.Kamio: Proc. 4th Int. Conf. on Aluminum Alloys, Georgia Inst. of Tech., Atlanta, (1994), p.169.

[30] H.Kimura and R.R.Hasiguti: Acta metall., **9** (1961), 1076.

[31] K.S.Raman and E.S.D.Das: Scripta Metall., **4** (1970), 291.

[32] A.J.Perry and E.M.Entwitsle: Phil. Mag., **18** (1968), 1085.

[33] G.Rivaud, J.P.Riviere and J.Grilhe: Scripta Metall., **6** (1972), 65.

[34] L.F.Mondolfo: *Aluminum Alloys: Structure and Properties*, BUTTER WORTHS, London, (1976).

[35] B.Kishore and K.I.Vasu: Scripta Metall., **5** (1971), 999.

[36] G.W.Hond, A.F.Quenneville, R.J.Schultz and M.L.Swanson: Crystal Lattice Defects, **Vol.2** (1971), p.243.

[37] M.Ohta and F.hashimoto: Trans. Japan Inst. Metals, **6** (1965), 9.

[38] S.Fujikawa, K.Hirano and Y.Baba: Bulletin of Japan Inst. Metals, **7** (1968), 495.

[39] M.Doyama: Journal of Nuclear Materials, **69&70** (1978), 350.

[40] K.Hirano: J. Japan Inst. Light Metals, **29** (1979), 249.

[41] M.Koike, K.Furukawa, J.Takamura, H.Hira, N.Yamamoto and F.Nakamura: *Point Defects and Defect Interactions in Metals*, Proc. Yamada Science Foundation, University of Tokyo Press, (1982), p.457.

[42] N.Metropolis, A.W.Rosenbluth, M.N.Rosenbluth, A.H.Teller and E.Teller: J. Chem. Phys., **21** (1953), 1087.

[43] F.Soisson, A.Barbu and G.Martin: Acta mater., **44** (1996), 3789.

[44] H.Ikeda and H.Matsuda: J. Japan Inst. Metals, **48** (1984), 8.

[45] H.Ikeda and H.Matsuda: J. Japan Inst. Metals, **49** (1985), 423.

[46] Y.Saito and H.Harada: Mat. Sci. and Eng., **A223** (1997), 1.

[47] M.J.Richards and J.W.Cahn: Acta metall., **19** (1971), 1263.

[48] H.Ino: Acta metall., **26** (1978), 827.

[49] N.Metropolis, A.W.Rosenbluth, M.N.Rosenbluth, A.H.Teller and E.Teller: J. Chem. Phys., **21** (1953), 1087.

Chapter 2

Mechanical Properties and Precipitate Microstructures of Al-Li-Cu Alloys with Microalloying Elements of Mg and Ag

2.1 Introduction

Lithium is the lightest metallic element found in nature and its addition to aluminum significantly reduces density. According to the equilibrium phase diagram in Fig.1.1, furthermore, alloys based on the Al-Li system are of age-hardening type because of a marked change in Li solubility in Al with temperature change. When Al-Li alloys are quenched from the α single-phase region into the $\alpha+\delta$ two-phase region, therefore, phase decomposition of the supersaturated solid solution occurs although a somewhat complicated sequence is followed[1]. The transient metastable δ'(Al_3Li) phase, which has a $L1_2$-type ordered structure coherent with the Al matrix, is well-known to be responsible for the age-hardenability of the alloys. Plastic deformation in the Al-Li binary alloys strengthened by the δ' phase, however, takes place easily due to the superlattice dislocation mechanism, in which dislocations tend to move in pairs on a particular slip plane because of a compensation for anti-phase boundaries(APB) within the δ' particles. This deformation mechanism results in a low ductility and low fracture toughness of the Al-Li alloys because the stress concentration at grain boundaries induced by the dislocation pileup eventually leads to grain boundary failure. Therefore, the δ' phase is not worth while to be utilized as the strengthening phase in commercial Al-Li alloys over a wide range application to structural components.

The addition of alloying elements is an effective method to improve the mechanical strength of Al-Li alloys due to some mechanisms; i.e. solid-solution hardening, precipitation hardening and dispersion hardening. As a major additional element in Al-Li alloys, Cu has been utilized to produce new strengthening phases such as GP zone, θ'(Al_2Cu) and T_1(Al_2LiCu) in addition to the δ' phase. Zr has been also added to retard recrystallization resulting in a decreased grain size, which is caused by the dispersoid formation of fine β' (Al_3Zr) particles. In a fabrication process, however, such the developed Al-Li alloys; e.g. the registered 2090(Al-Li-Cu-Zr), 2091, 8090 and 8091(Al-Li-Cu-Mg-Zr) alloys, must be inevitably subjected to the stretch temper by 3-7% prior to artificial aging treatments to promote the homogeneous precipitation of the above strengthening phases (i.e. T8 temper condition). Since this pre-worked temper is quite unpractical especially for the fabrication of large component parts, however, further attempts have been also conducted to obtain the same mechanical properties without stretching as those of the T8 temper alloys on the basis of additions of microalloying elements. These attempts led to the introduction of new 2094, 2095, 2096 and 2195 alloys, which contain small amounts of Mg and Ag to stimulate the transgranular precipitation of the T_1 phase with the high number density[2-4], in the early 1990s. These alloys are expected to be a promising material for aerospace application; e.g. cryogenic tankage of booster systems, because conventional T6 temper conditions can provide the excellent mechanical strength over 700MPa(UTS)[3, 5, 6], which is the highest one among all ingot metallurgy(I/M) aluminum alloys. As for the mechanism of the accelerated T_1 phase precipitation by the combined addition of Mg and Ag, the detailed discussion is made in Chapter 7.

In this chapter, the pronounced effects of a simultaneous addition of Mg and Ag on the mechanical properties and precipitate microstructures of an Al-5.0%Li-2.3%Cu-0.04%Zr (mol%) alloy have been investigated under various aging conditions using hardness and electrical resistivity measurements, tensile test and transmission electron microscopy. The obtained results are significantly dependent on applied aging temperatures, which promote the simultaneous formation of some precipitates observed in the Al-Cu, Al-Li and Al-Li-Cu alloy systems. This leads to the reason why the present thesis is divided into the following chapters.

2.2 Experimental Procedures

2.2.1 Preparation of materials

The alloys utilized in this chapter were supplied by Alithium Limited. Two types of alloys were prepared from high-purity materials under Ar gas atmosphere followed by continuous casting. The chemical compositions of the alloys are listed in Table 2.1. For

Table 2.1 Chemical compositions of the alloys utilized in this chapter (mol%).

Alloys	Li	Cu	Mg	Ag	Zr	Al
(Mg+Ag)-added	5.27	2.33	0.553	0.0972	0.0471	bal.
Mg-free	5.23	2.39	0.002	0.0948	0.0443	bal.

simplicity, an Al-5.3%Li-2.4%Cu-0.04%Zr alloy containing 0.5%Mg and 0.1%Ag (mol%) is designated as (Mg+Ag)-added alloy, whereas the equivalent alloy containing only 0.1mol%Ag is designated as Mg-free alloy, in this chapter.

2.2.2 Fabrication process

The ingots were homogenized at 723K for 86.4ks, then scalped, and hot- and cold-rolled to 1.6mm-thick sheets after re-heating at 773K for 21.6ks. Solution treatments were carried out in a salt bath at 778K for 1.8ks followed by water quenching at ~298K. The subsequent aging treatments were performed at temperatures from 278 to 523K for various aging times. In this work, the room temperature designated as RT always stands for ~298K. The above fabrication process is illustrated in Fig.2.1.

2.2.3 Hardness measurement

The specimens for hardness measurement were cut from the fabricated sheets with dimensions of 10mm × 10mm × 1.6mm. After various heat treatments, each specimen was mechanically polished using #100-#1200 emery papers and 0.3-1.0μm alumina particle buffing. For the Al alloys containing substantial amounts of Li, the surface of the specimens was removed by 0.1mm in thickness at least to eliminate the regions of Li loss induced during the above solution treatment[7]. Micro Vickers testing machine was utilized for hardness measurement of as-polished specimens with a 500g load. The hardness of each specimen was determined as an average value of five tested points out of seven ones.

2.2.4 Tensile test

The specimens for tensile test were prepared from 1.0mm-thick sheets with a gauge length of 25mm in the longitudinal direction. The shape and size of tensile specimen are illustrated in Fig.2.2. The tensile test was performed at a constant strain rate of 1.3×10^{-4}/s at RT with a Instron-type tensile test machine. In this work, at least three specimens were tested to obtain reliable values of 0.2% yield stress(0.2% Y.S.), ultimate tensile strength(UTS) and elongation(Elo.).

2.2.5 Electrical resistivity measurement

The wires for electrical resistivity measurement were prepared by drawing with dimensions of ϕ1.0mm × 300mm^1. After various heat treatments, all wire specimens were quickly quenched into water at ~298K followed by the immersion in liquid nitrogen at ~77K. The electrical resistivity measurement was carried out by the usual four-probe

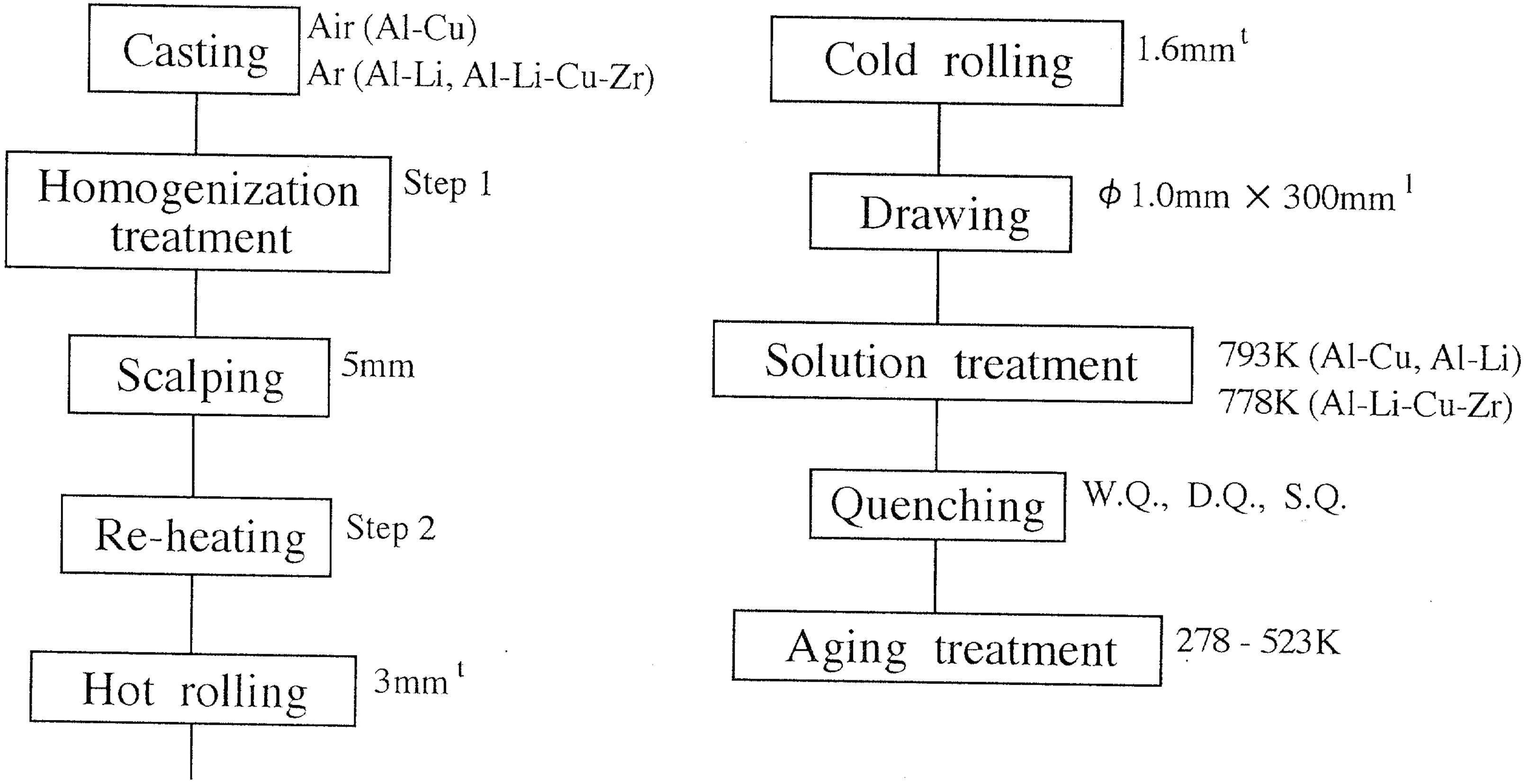

Fig. 2.1 Flowchart for preparing alloy specimens.

potentiometric technique. The value of electrical resistivity, ρ, was calculated using the following equation;

$$\rho = (V_m / I_{st}) \cdot (A / L) \tag{2.1}$$

where

V_m : Measured potential difference (in mV)
I_{st} : Constant current of electricity (120mA)
A : Cross-sectional area of the wire (0.785mm^2)
L : Gauge length (300mm).

The overall accuracy of measured electrical resistivities was assessed to be within ± 0.02% using a standard resistor.

2.2.6 Transmission electron microscopy

The foils for transmission electron microscopy (TEM) were prepared by a twin-jet polishing technique in a solution of 20vol.% nitric-acid and 80vol.% methanol at ~250K. TEM observation was performed at an accelerating voltage of 200kV with both JEM200CX and JEM3010 transmission electron microscopes. High resolution images of precipitate microstructures were taken using 000 transmitted beam and two or four diffracted beams along one excited direction under the axial illumination condition. Since the maximum contrast is generally obtained at a quarter of the extinction distance, very thin regions of specimens were observed. The size distribution and number density of some precipitates were determined from bright field TEM micrographs by estimating the foil thickness due to an equal thickness fringe method.

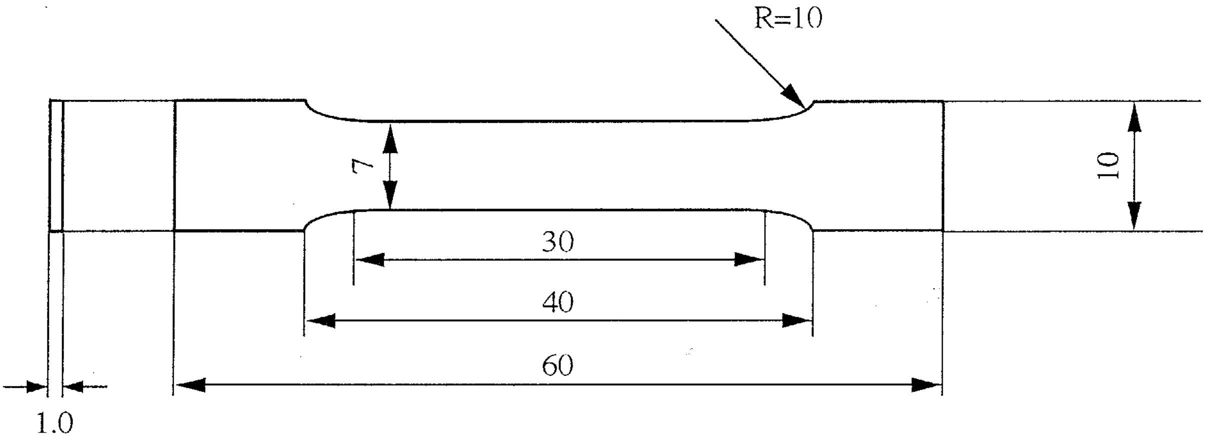

Fig.2.2 Shape and dimensions of specimen for tensile test.

2.3 Precipitation behavior of low-temperature aging

2.3.1 Hardness changes

The isothermal aging curves of hardness are illustrated in Fig.2.3 for the (Mg+Ad)-added and Mg-free(i.e. Ag-added) alloys aged at RT to 373K. With increasing aging time, the (Mg+Ad)-added alloy exhibits a rapid and pronounced hardening to reach over HV150 at all aging temperatures. Although higher aging temperatures; e.g. 373K, eventually attain almost identical values of hardness, on the other hand, the rate of hardness-increase in the Mg-free alloy is obviously decreased compared with that in the (Mg+Ag)-added alloy. The difference of aging response between the two alloys is also revealed from the results of tensile test.

2.3.2 Tensile properties

Figure 2.4 shows longitudinal tensile properties of the (Mg+Ag)-added and Mg-free(i.e. Ag-added) alloys under both the as-quenched and naturally aged conditions. It is obvious that a small addition of Mg markedly increases the age-hardenability of naturally aged Al-Li-Cu-Zr alloys resulting in the excellent strength-ductility combination of 307MPa (0.2%Y.S.), 523MPa(UTS) and 14.6%(Elo.) after 1814ks aging. Such the pronounced difference in mechanical properties can be well interpreted by comparing their precipitate microstructures.

2.3.3 Transmission electron micrographs

Figure 2.5(a) and (b) shows the bright field TEM images, including the corresponding diffraction patterns, for the (Mg+Ag)-added and Mg-free(i.e. Ag-added) alloys aged at RT. The electron diffraction pattern of the (Mg+Ag)-added alloy exhibits continuous diffuse streaks toward the $\langle 100 \rangle$ direction together with superlattice reflections, indicating the presence of a mixture of fine GP(1) zones and the δ' phase (and/or its precursory structures) (Fig.2.5(a)). In contrast, the diffraction pattern of the Mg-free alloy reveals almost no precipitates even after 2.7×10^4 ks aging (Fig.2.5(b)) similarly to that of the naturally aged (Mg+Ag)-added alloy in the early stage of aging; i.e. until about 1 ks. At higher aging temperatures, however, GP(1) zones are also detected even in the Mg-free alloys with the coexisting δ' phase, as revealed in the TEM micrograph of the Mg-free alloy aged at 373K for 5.4×10^3 ks (Fig.2.5(c)). These results indicate that a small addition of Mg to Al-Li-Cu-Zr alloys markedly affects the formation rates of GP(1) zones and/or the δ' phase resulting in the faster increase in the hardness (Fig.2.3).

2.3.4 Electrical resistivity changes

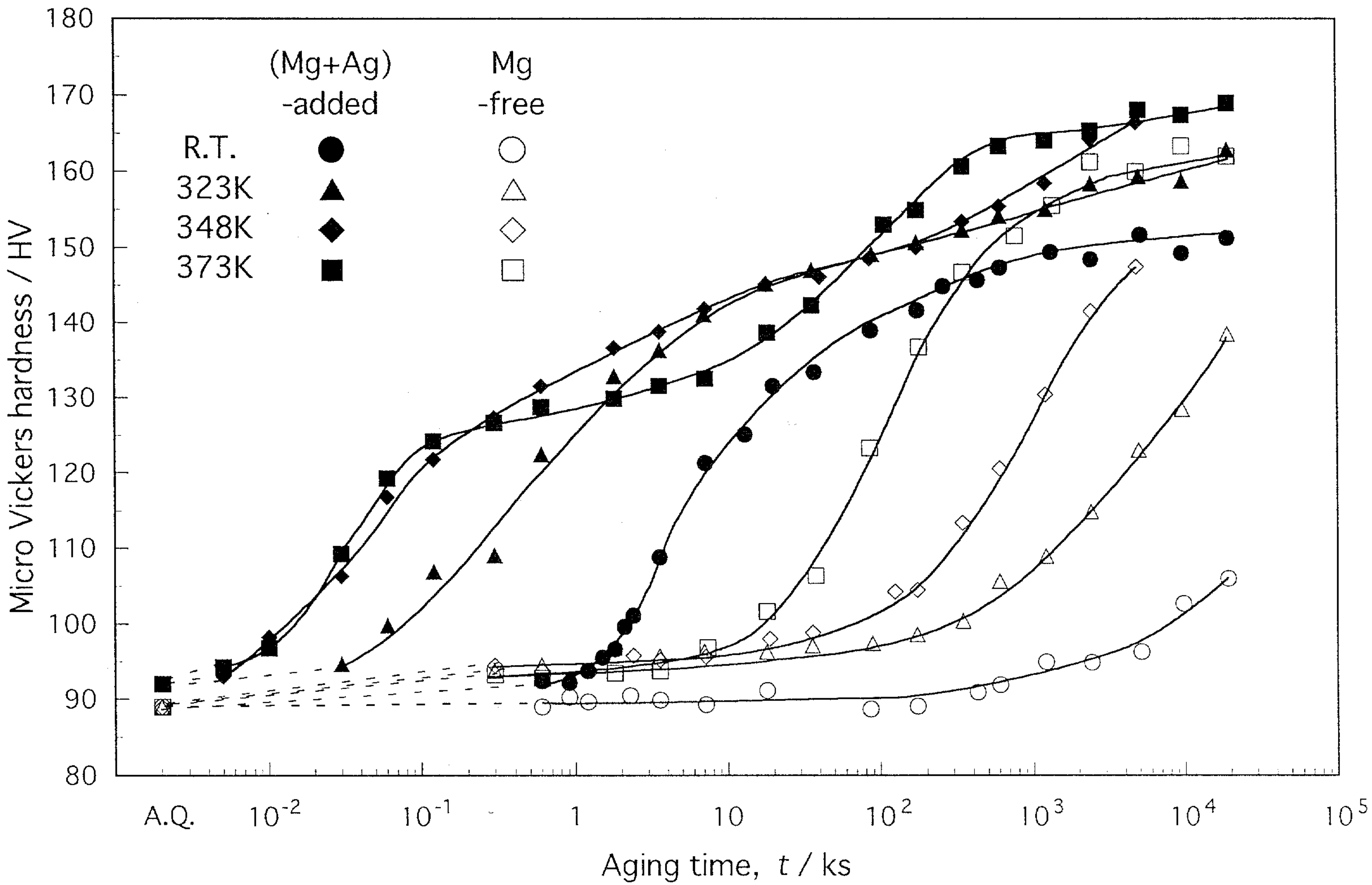

Fig.2.3 Isothermal aging curves of hardness for (Mg+Ag)-added and Mg-free alloys aged at RT(~298K) to 373K.

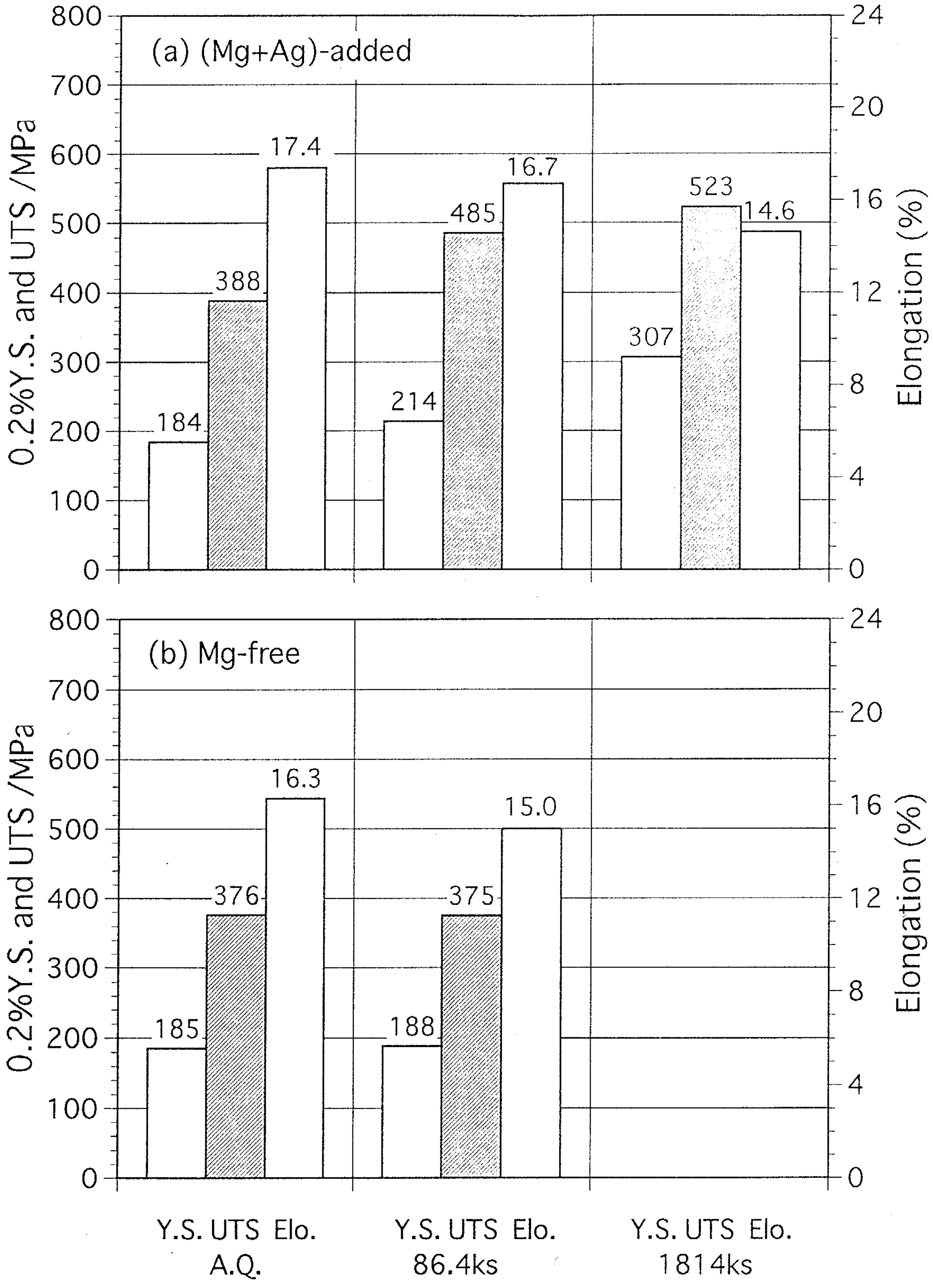

Fig. 2.4 Longitudinal tensile properties of (a) (Mg+Ag)-added and (b) Mg-free alloys as-quenched(A.Q.) and aged at RT for 86.4 and 1814ks.

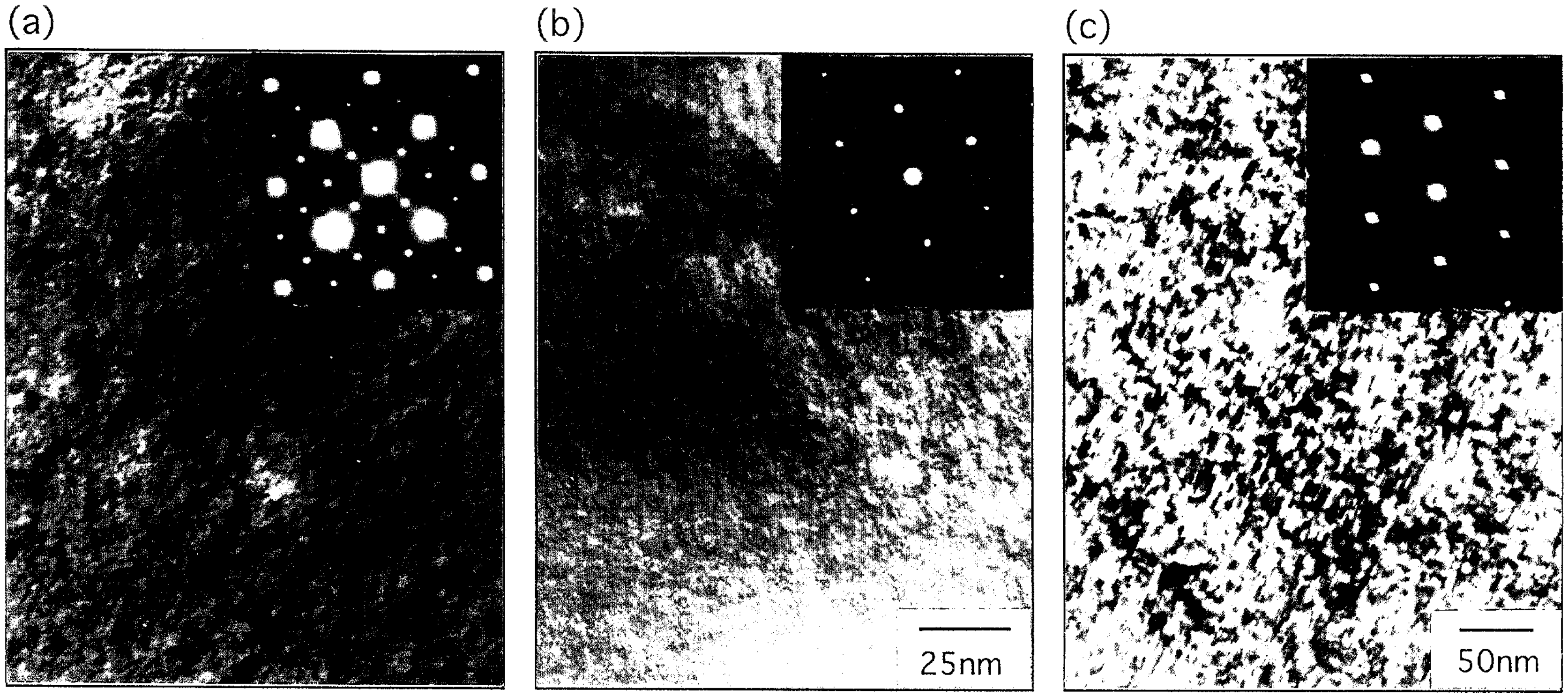

Fig.2.5 Electron micrographs with diffraction patterns for (Mg+Ag)-added alloys aged at RT for 864ks(a), Mg-free alloy aged at RT for 2.7×10^{4}ks(b) and 373K for 5.4×10^{3}ks(c).

Electrical resistivity measurement is capable of the more detailed quantitative analysis of the precipitation kinetics. Figure 2.6 illustrates the electrical resistivity changes of the (Mg+Ag)-added and Mg-free(i.e. Ag-added) alloys aged at 278 to 373K. The difference in as-quenched resistivities between them almost originates in the ~0.55mol%Mg addition because its calculated contribution to ρ is ~2.5nΩm using a reported value of ρ_s^0= 4.6nΩm/mol%Mg[8]. Except for the 278K aging of the Mg-free alloy, both alloys clearly display a two-stage increase in resistivity; i.e. first, a stage of gradual increase and second, a stage of rapid increase. In this work, the first stage is designated as Stage 1, whereas the subsequent is designated as Stage 2. In general, it is well recognized that Al-Cu binary alloys exhibit one-stage increase in resistivity from just after quenching at low aging temperatures, whereas Al-Li binary alloys also display a rapid increase in ρ from the early stage of low-temperature aging. Regardless of the small addition of Mg, therefore, anomalous two-stage increase observed in Fig.2.6 is regarded as a characteristic feature of Al-Li-Cu alloys, which strongly suggests the simultaneous precipitation of GP(1) zones and the δ' phase (and/or its precursory structures).

For the kinetics of phase decomposition in Al-Li-Cu alloys, Mg addition obviously shortens the transition time from Stage 1 to Stage 2, t_S, as indicated in Fig.2.6. The acceleration of the Stage 2 precipitation, which is also revealed in the age-hardenability of the (Mg+Ag)-added alloy (Fig.2.3), is well explained by the enhanced formation of GP(1) zones from the results of the precipitate microstructures in Fig.2.5. In contrast, it is quite natural to consider that the Stage 1 precipitation is attributed to the growth of the δ' phase and/or its precursory structures. In this work, in order to elucidate the detailed effects of various additional elements, Chapters 4 and 5 are assigned to the simple cases of Al-Cu and Al-Li binary alloys. From the revealed roles of microalloying elements in these alloys, furthermore, the mechanism of the accelerated Stage 2 precipitation by the Mg addition is discussed in detail in Chapter 6 again.

2.4 Precipitation behavior of high-temperature aging

2.4.1 Hardness changes

Hardness changes during isothermal aging at 403 to 523K are illustrated in Fig.2.7 for the (Mg+Ag)-added and Mg-free(i.e. Ag-added) alloys. The small addition of Mg obviously shortens the time to attain peak hardness and also increases the value of peak hardness at all aging temperatures; e.g. as much as ~HV50 at 433K. The difference in the age-

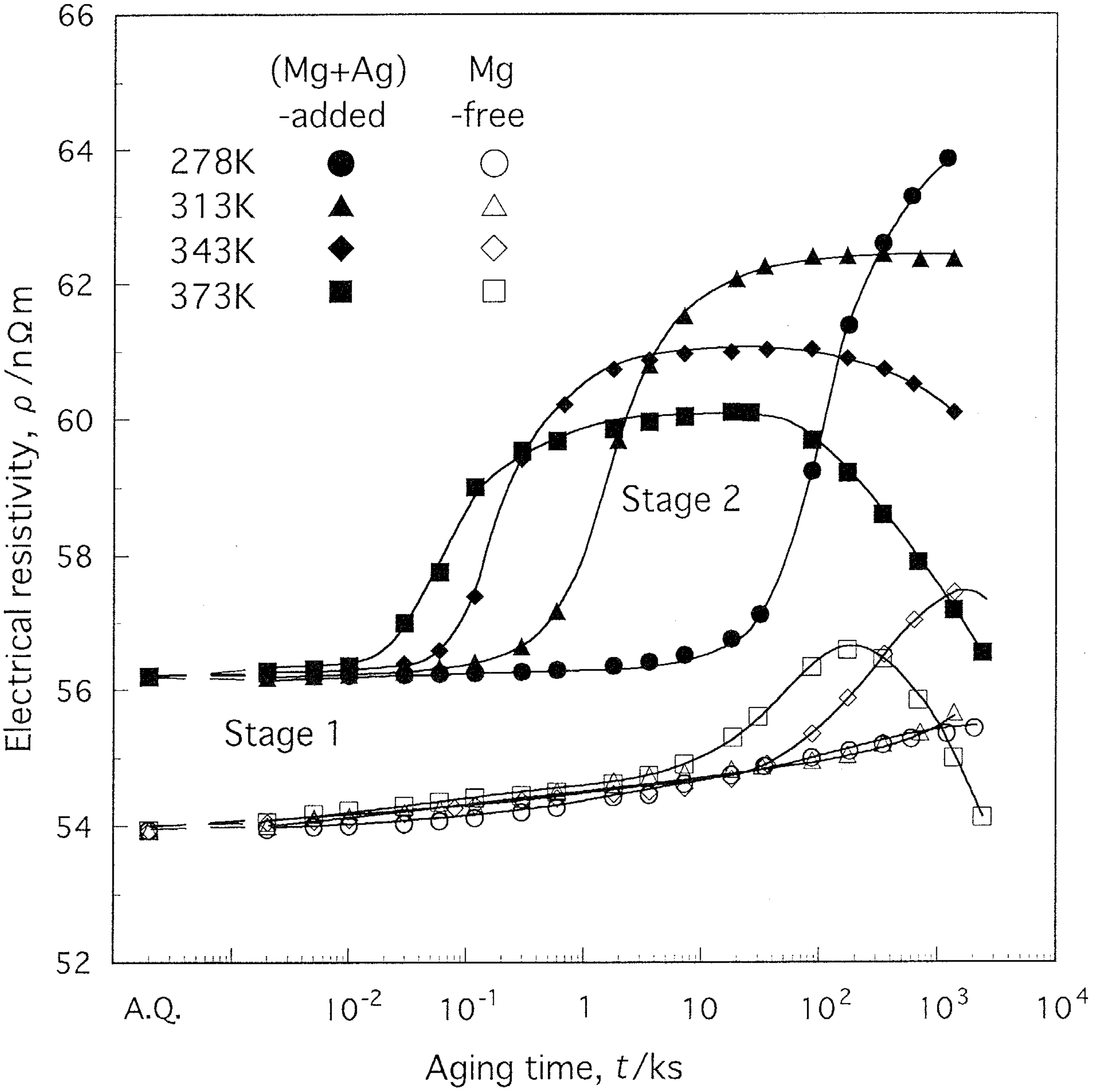

Fig.2.6 Changes in electrical resistivity of (Mg+Ag)-added and Mg-free alloys aged at 278 to 373K after quenching from 778K.

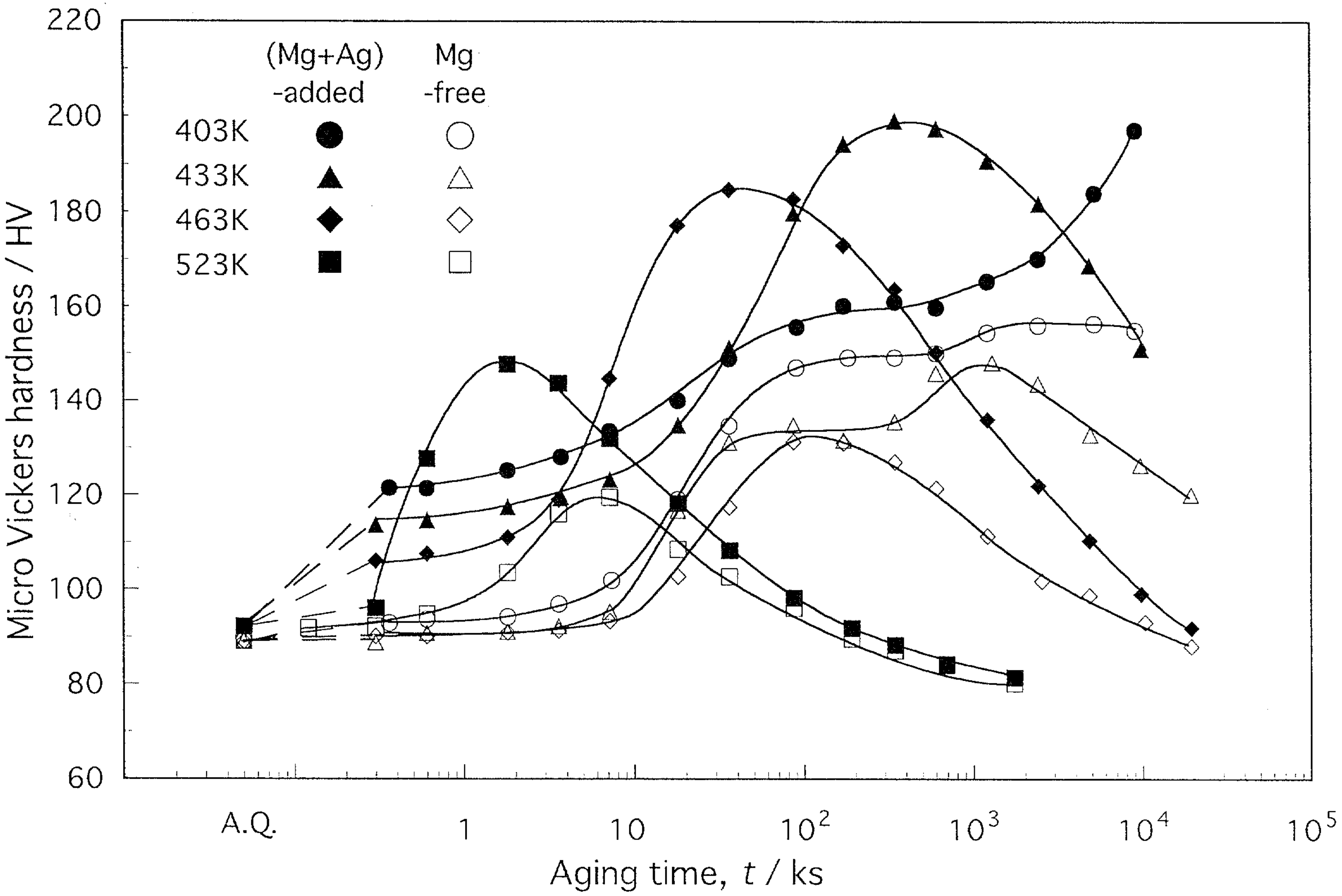

Fig. 2.7 Isothermal aging curves of hardness for (Mg+Ag)-added and Mg-free alloys aged at 403 to 523K.

hardenability is also revealed by the mechanical strength of the two alloys.

2.4.2 Tensile properties

Figure 2.8 shows longitudinal tensile properties of the (Mg+Ag)-added and Mg-free(i.e. Ag-added) alloys aged at 433 to 463K. Each aging condition provides almost peak hardness of the two alloys as illustrated in Fig.2.7. It is obviously seen that a small addition of Mg yields higher values of mechanical strength compared with that of the Mg-free alloys, resulting in an excellent properties for commercial applications of the (Mg+Ag)-added alloys. This pronounced effect of Mg addition can be well explained in terms of microstructural changes during aging.

2.4.3 Transmission electron micrographs

Figure 2.9 shows the bright field TEM images for the (Mg+Ag)-added and Mg-free(i.e. Ag-added) alloys aged at 433K for 346ks. The electron diffraction patterns of both alloys exhibit continuous streaks toward the $\langle 100\rangle$ direction with intensity maxima at every fourth between fundamental 200 spots, indicating the presence of plate-like GP(2) zones. The microstructure of the (Mg+Ag)-added alloy also reveals the high number density of the T_1 phase on the $\{111\}$ habit planes, which provides both continuous streaks toward the $\langle 111\rangle$ direction and 1/3, 2/3 220 spots in the corresponding diffraction patterns. In the Mg-free alloy, however, the T_1 phase are observed heterogeneously at subgrain boundaries with the coarsened precipitate size and low precipitate number density. The pronounced difference in the precipitate microstructures clearly shows that a small addition of Mg markedly stimulates the transgranular formation of the T_1 phase resulting in the higher mechanical strength of Al-Li-Cu-Zr alloys. The similar results are obtained in the precipitate microstructures of the 463K aging as illustrated in Fig.2.10. Figure 2.11 shows precipitate size distributions of the (Mg+Ag)-added and Mg-free alloys under the above two aging conditions. Table 2.2 summarizes observed precipitates in the two alloys aged at RT to 523K. It is obviously confirmed that the small addition of Mg to Al-Li-Cu-Zr alloys significantly accelerates the T_1 phase formation at above ~400K, whereas strengthening phases of the Mg-free alloys are still GP zones and the θ' phase with the coarsened T_1 phase only at subgrain boundaries. It should be also emphasized in Table 2.2 that metastable phase regions remain unchanged regardless of Mg addition at most of investigated aging temperatures. The mechanism of the enhanced T_1 phase precipitation by the Mg addition is discussed in detail in Chapter 7.

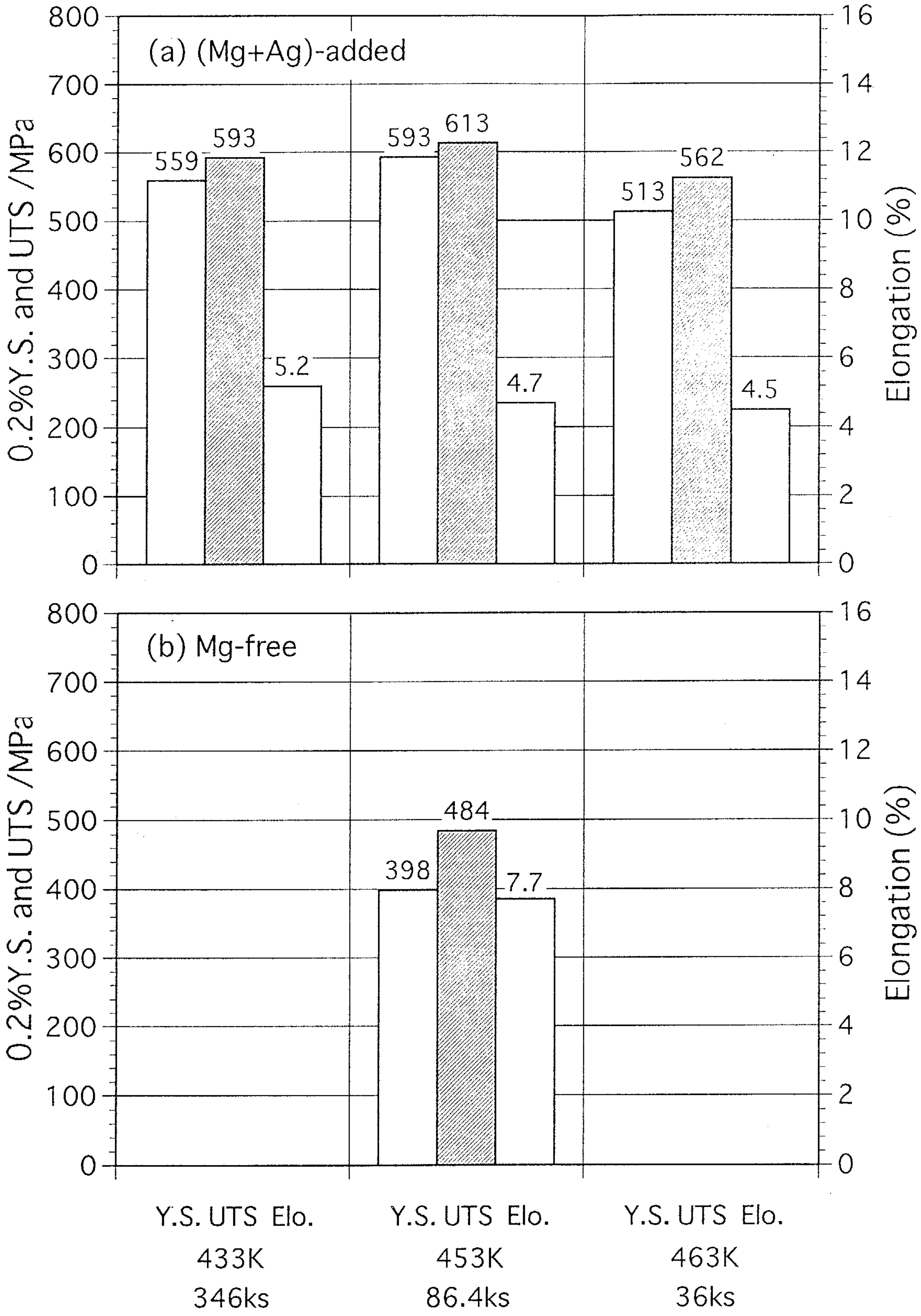

Fig. 2.8 Longitudinal tensile properties of (a) (Mg+Ag)-added and (b) Mg-free alloys aged at 433K for 346ks, 453K for 86.4ks and 463K for 36ks.

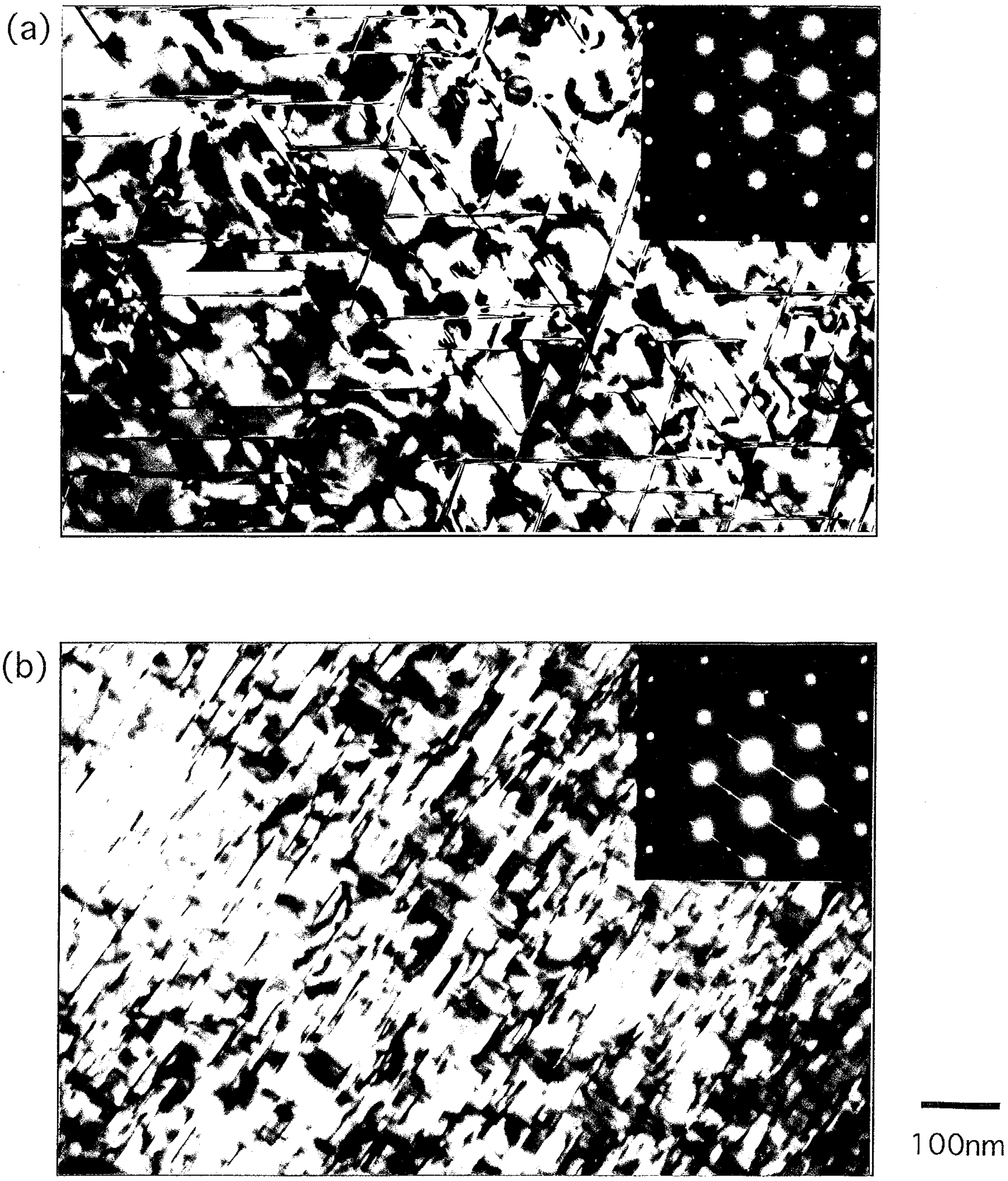

Fig.2.9 Electron micrographs with diffraction patterns for (Mg+Ag)-added (a) and Mg-free (b) alloys aged at 433K for 346ks.

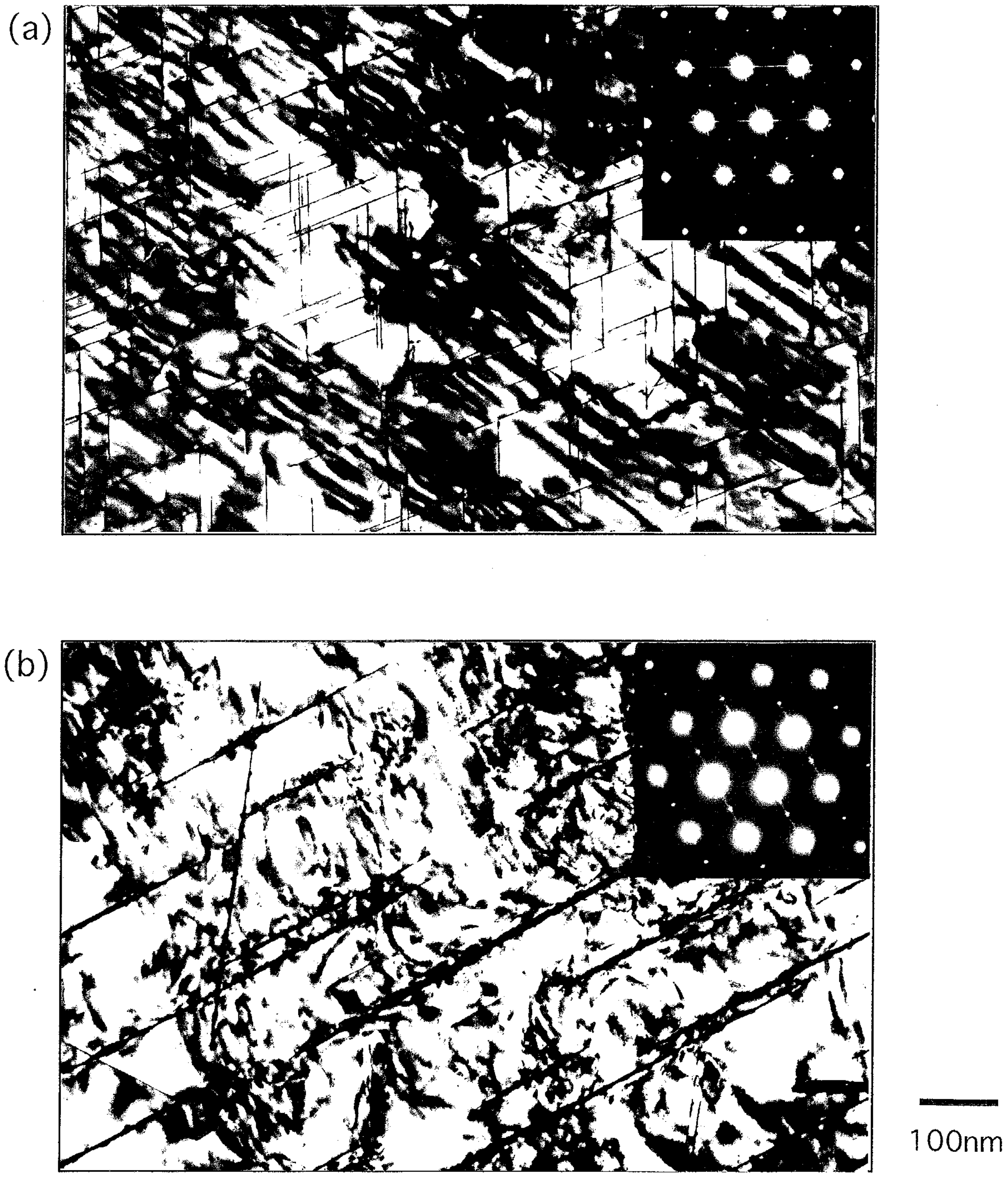

Fig.2.10 Electron micrographs with diffraction patterns for (Mg+Ag)-added (a) and Mg-free (b) alloys aged at 463K for 36ks.

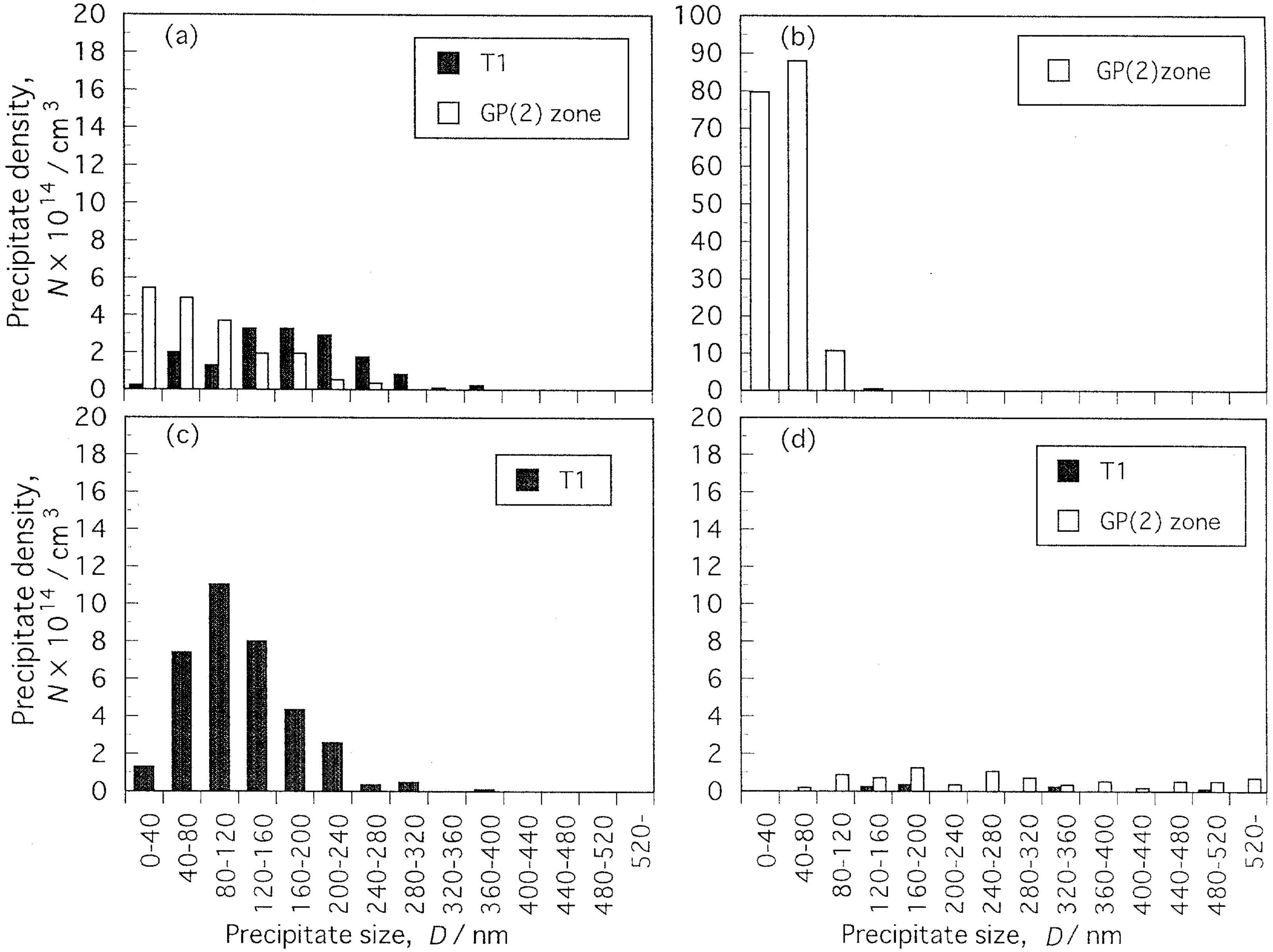

Fig. 2.11 Precipitate size distributions for (Mg+Ag)-added and Mg-free alloys aged at either 433K for 346ks(a, b) or 463K for 36ks(c, d).

Table 2.2 Precipitates observed in (Mg+Ag)-added and Mg-free (i.e. Ag-added) alloys aged at temperatures from RT to 523K. The precipitates in brackets ( ) are of low density and T_1 phase in brackets [ ] is only detected at subgrain boundaries.

Aging temperature / K	Aging time / ks	(Mg+Ag)-added alloy	Mg-free alloy
298(RT)	8.6×10^{2}	δ', GP(1) zone	(δ')
	2.4×10^{4}	δ', GP(1) zone	(δ'), (GP(1) zone)
373	1.8×10^{3}	δ', GP(1) zone	δ', GP(1) zone
403	1.8×10^{3}	δ', GP(1) zone	δ', GP(1) zone
	9.7×10^{3}	δ', GP(2) zone, T_1, GPB(2) zone	———
433	3.6×10	δ', GP(1) zone	δ', GP(1) zone
	3.5×10^{2}	δ', GP(2) zone, T_1	δ', GP(2) zone, [T_1]
	1.9×10^{4}	———	(δ'), θ', [T_1]
463	7.2	T_1	(δ'), GP(2) zone
	3.6×10	T_1	δ', GP(2) zone, [T_1]
	1.9×10^{4}	T_1	(δ'), θ', [T_1]
523	9.0×10^{-1}	T_1	[T_1]
	1.8	T_1	[T_1]

2.5 Conclusions

The mechanical properties and precipitate microstructures of both an Al-5.0%Li-2.3%Cu-0.04%Zr (mol%) alloy and the equivalent alloy containing 0.55mol%Mg and 0.01mol%Ag were investigated at aging temperatures ranging from 278 to 523K using hardness and electrical resistivity measurements, tensile test and transmission electron microscopy. The obtained results are summarized as follows.

(1) Both alloys exhibit a two-stage increase in hardness and electrical resistivity at below ~373K. The first gradual-increase stage, Stage 1, is attributed to the growth of the δ' phase and/or its precursory structures, whereas the subsequent rapid-increase stage, Stage 2, corresponds to the GP(1) zone formation.

(2) A small addition of Mg to the Al-Li-Cu-Ag-Zr alloy markedly accelerates the GP(1) zone formation resulting in the faster increase in both hardness and electrical resistivity.

(3) The small amount of additional Mg also stimulates the T_1 phase precipitation resulting in the enhanced age-hardening at elevated aging temperatures higher than ~400K.

(4) In contrast, the microstructures of the Mg-free alloys consist of GP zones and/or the θ' phase with the coarsened T_1 phase only at subgrain boundaries.

References

[1] A.G.Khachaturyan, T.F.Lindsey and J.W.Morris, Jr.: Metall. Trans. A, **19A** (1988), 249.

[2] T.J.Langan and J.R.Pickens: Proc. 5th Int. Al-Li Conf., **Vol.2** (1987), 691.

[3] J.R.Pickens, F.H.Heubaum, T.J.Langan and L.S.Kramer: Proc. 5th Int. Al-Li Conf., **Vol.3** (1987), 1397.

[4] I.J.Polmear and R.J.Chester: Scripta Metall., **23** (1989), 1213.

[5] F.W.Gayle, F.H.Heubaum and J.R.Pickens: Scripta Metall., **24** (1990), 79.

[6] W.T.Tack, F.H.Heubaum and J.R.Pickens: Scripta Metall., **24** (1990), 1685.

[7] H.Ueda, A.Matsui, M.Furukawa, Y.Miura and M.Nemoto: J. Jpn. Inst. Metals, **49** (1985), 562.

[8] T.Fujita and T.Ohtsuka: J. Low Temp. Phys., **29** (1977), 333.

Chapter 3
Computer Simulation Models and Derivation Method of Parameters

3.1 Introduction

Because of the recent rapid progress in computer hardware, a new field in materials science has been advanced due to the possibility of performing computer simulations of large systems. At present, such computer simulation technologies are widely applied to make clear various phenomena in solid materials; e.g.

① Calculation of phase diagrams by Cluster Variation Method(CVM) and study of configurational thermodynamics and kinetics by Path Probability Method (PPM)[1-7],

② Alloy design based on Molecular-Orbital theory[8-11],

③ Predictions of structural stability and compound formation by extended Huckel method[12-15],

④ Phase decomposition analysis based on discrete type Non-Liner Diffusion Equation[16-20]

and

⑤ Modeling of microstructure evolution using Monte Carlo method[21-24].

Among them, the Monte Carlo simulation is a most powerful method especially to inquire into the microscopic behavior occurring in alloys because the method can visualize such atomistic events as nucleation and growth of precipitates for arbitrary alloy systems. Soisson *et al.*[21] performed a Monte Carlo simulation of Cu atom clustering in α-Fe to follow the microstructural evolution of the morphology, composition and size distribution of Cu atom clusters. Ikeda *et al.*[22, 23] qualitatively ascribed electrical resistivity changes of an Al-4.5mol%Zn alloy to size distributions of Zn atom clusters obtained from a Monte Carlo simulation. Furthermore, Saito *et al.*[24] applied the simulation to ordering of the γ' phase in commercial Ni-base superalloys in order to predict preferential substitution sites of some alloying elements.

Any above computer simulation, however, requires a number of assumptions and simplifications in the model in order either to shorten the simulation time or to solve equations analytically. Therefore, the modeling of simulations is a quite important problem to obtain reliable simulation results. In this work, a kinetic Ising model[25] with interactions up to second nearest neighbors on the fcc lattice was adopted to reflect the atom configurations in Al as exactly as possible. All simulation parameters, which significantly affect the obtained simulation results, were derived from known thermodynamic or kinetic quantities.

In this chapter, the Monte Carlo method is briefly introduced first with its several advantages. Fundamentals and conditions of utilized simulation model are described in the following section. Both the quantitative analysis of simulation microstructures and the comparison with actual aging times are also made. Section 3.3 describes a derivation method of the utilized simulation parameters, which are determined by the knowledge of experimental thermodynamic or kinetic quantities. The calculation method of electrical resistivity from the obtained structural parameters is finally proposed to establish the reliability of the simulation results by comparing with experimentally measured electrical resistivity changes.

3.2 Simulation models

3.2.1 Monte Carlo method

Since Metropolis *et. al*[26] first proposed a so-called "Monte Carlo" method for the study of thermodynamical properties of substances consisting of interacting individual molecules, the method has been extensively applied to various physical phenomena concerning statistical mechanics. The Monte Carlo method is based on a stochastic process in a given system, which generates a Boltzmann-weighted chain of the concerned configurations, resulting in the powerful method to follow microstructural changes even in solid materials. In particular, phase decompositions in alloys are quite convenient in applying this method because thermally activated vacancy jumps mostly control their kinetics and formation behavior. In this work, dynamical evolutions of some precipitates involving both clustering and ordering reactions are investigated using a standard Metropolis algorithm[26]. Several advantages of this method are pointed out as follows:

① Atomistic events during phase decompositions; e.g. diffusion of solute atoms, nucleation and growth of precipitates, can be visualized spatially and temporally from the quite early stage of aging.

② No information such as critical nucleus size, shape and composition of precipitates and distinction between nucleation and growth stages is required.

③ The simulation results are entirely ascribed to utilized simulation parameters.

④ The structural parameters characterizing obtained simulation microstructures; e.g. residual solute atom concentrations in the matrix, average size and number density of precipitates, can be easily evaluated using the cluster analysis method[27, 28].

3.2.2 Conditions of utilized simulation model

Computer simulations were performed on a rigid fcc lattice with 25×25×25 unit cells (i.e. 132651 lattice points) by a conventional Monte Carlo method[26]. Periodic boundary conditions were also adopted to eliminate a limitation of the above simulation size. Figure 3.1 shows the algorithm of the simulation procedure performed in this work based on the Monte Carlo method. As an initial microstructure of the simulation system, all lattice sites are occupied at random by Al atoms, Cu or Li atoms and third elemental atoms with the corresponding alloy composition. The realistic diffusion of these atoms always takes place via vacancies with the concentration of $\sim 1.5 \times 10^{-4}$, which approximately agrees with the equilibrium vacancy concentration in pure Al at 793K[29]. This postulates that the investigated phase decomposition evolves without diminishing quenched-in excess vacancies during the simulation. The exchange of a randomly selected vacancy with one of its nearest neighbor atoms is allowed if the transition probability, W, is greater than a randomly generated number, x, between 0 and 1. The value of W is calculated from the symmetrical solution[30]:

$$W = \exp(-\Delta E / RT) / [1 + \exp(-\Delta E / RT)], \qquad (3.1)$$

where ΔE is the energy difference between atom configurations before and after the exchange, R is the gas constant and T is the simulated temperature. As a straightforward example, the calculation method of ΔE in a two-dimensional square lattice is illustrated in Fig.3.2. In this work, the normalized total attempt times by the number of vacancies refer to the simulation time in Monte Carlo steps(MCs) because actual diffusion of vacancies takes place simultaneously.

3.2.3 Structural parameters characterizing simulation microstructures

Structural parameters characterizing simulation microstructures were followed as a function of Monte Carlo steps(MCs) using the cluster analysis method[27, 28]. In this work, a cluster was defined as a solute atom aggregate containing either two and more than two solute atoms for clustering process, or more than six solute atoms within one unit cell of a $L1_2$-type ordered structure for ordering process. Therefore, residual solute concentrations in the matrix, Cs, can be obtained from either the concentration of isolated solute atoms surrounded by Al atoms (clustering process) or solute atom aggregates containing less than seven solute atoms within one $L1_2$-type unit cell (ordering process), respectively. The number density of precipitates, N, in the unit of m^{-3} is estimated from the number of solute

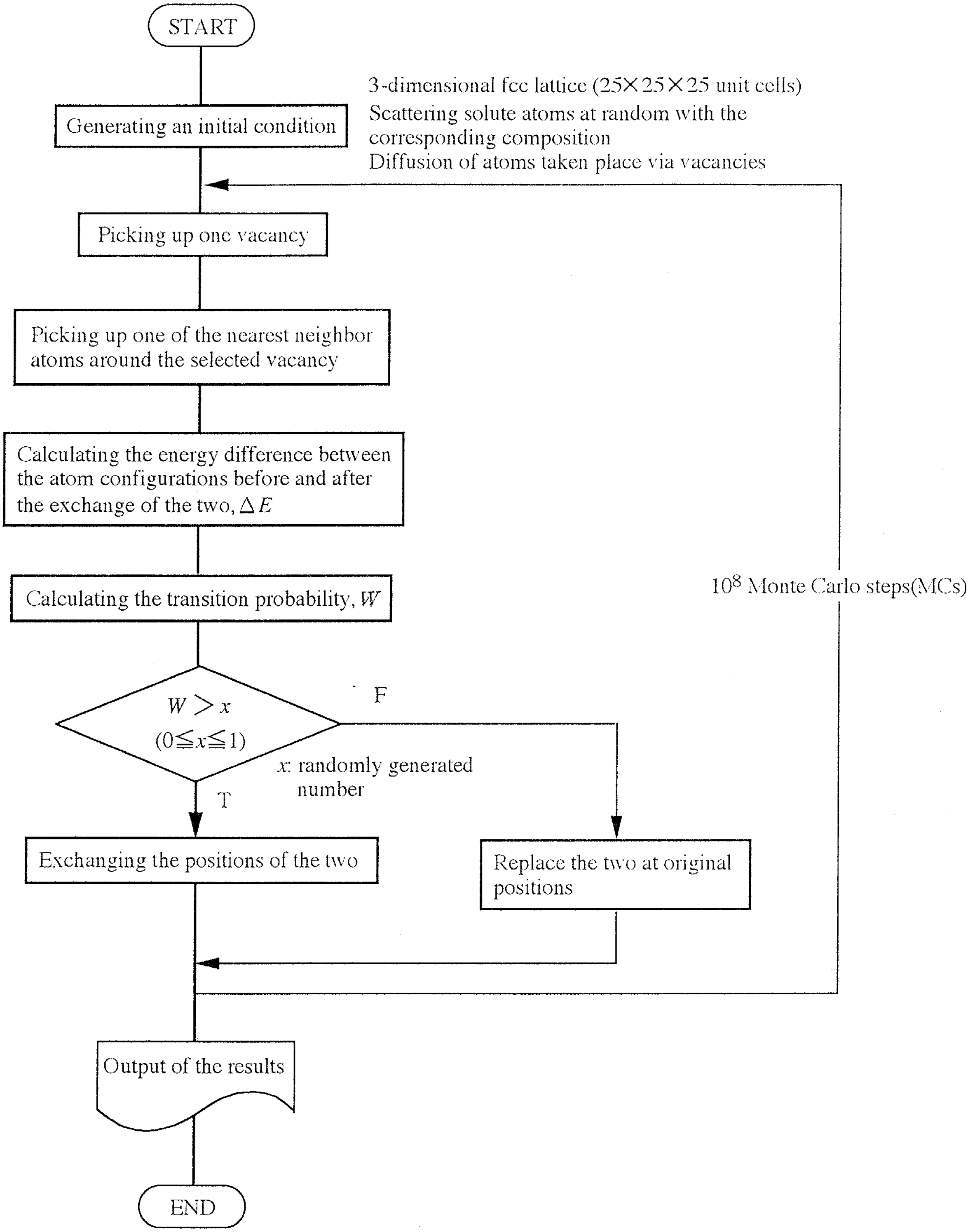

Fig.3.1 Algorithm of the simulation procedure using the Monte Carlo method performed in this work.

Energy difference between atom configurations before and after an exchange, $\Delta E = E_{aft} - E_{bef}$

○ Al

● Cu

none Vacancy

Before the exchange

$$E_{bef} = (3\times\varepsilon_{\text{Al-Cu}} + \varepsilon_{\text{Cu-V}}) + (2\times\varepsilon_{\text{Al-V}} + 2\times\varepsilon_{\text{Cu-V}})$$

After the exchange

$$E_{aft} = (3\times\varepsilon_{\text{Al-V}} + \varepsilon_{\text{Cu-V}}) + (2\times\varepsilon_{\text{Al-Cu}} + \varepsilon_{\text{Cu-V}} + \varepsilon_{\text{Cu-Cu}})$$

Fig.3.2 Calculation method of energy difference between atom configurations before and after an exchange, ΔE, on a two-dimensional square lattice.

atom clusters within the simulation system, whereas the average size of precipitates, n, is defined as the number of solute atoms inside one cluster. As for the simulation of ordering processes, furthermore, the degree of short-range order (SRO), s, is evaluated from the neighborhood relationship around atoms. Such atomistic events as the preferential vacancy trapping by some elemental atoms and the substitution of third additional elements within the ordered structure are also quantitatively estimated during the Monte Carlo simulation.

3.2.4 Comparison between MCs and actual aging time

It is quite essential to compare the simulation time defined above with the actual aging time experimentally subjected to alloys. In this work, as an effective scaling method between them, self-diffusion of Al was investigated using the same simulation models as illustrated in Fig.3.3. Figure 3.4 quantitatively shows the variation in concentration profiles of marked Al atoms, which originally settled in one side ($x<0$) and gradually migrate through an interface ($x=0$) to the other side ($x>0$) in Fig.3.3, as a function of Monte Carlo steps(MCs). These profiles can be analytically expressed by solving Fick's second law,

$$C(x, MCs) = (1/2)\left\{1 - \mathrm{erf}(x / 2\sqrt{Dt})\right\} \tag{3.2}$$

using the following boundary conditions; i.e. $C=1$ (100mol%) at $x<0$ and $C=0$ (0mol%) at $x>0$. Here, $C(x$, MCs) is the concentration of marked Al atoms on one atomic layer with the distance from the interface, x, at an arbitrary MCs, D is the self-diffusion coefficient at a fixed temperature and 'erf' stands for the usual error function. Taking into account the fact that the simulation for self-diffusion of Al is independent of simulated temperatures, scaling constants between MCs and actual aging time, m, can be assessed by comparing the estimated diffusion coefficient at each simulated temperature with experimentally reported one. In this work, the increased self-diffusion coefficient by quenched-in excess vacancies, D^*

$$\begin{aligned} D^* &= D_0 \exp(-Q/RT_a) \times \left\{\exp(-E_F/RT_S)/\exp(-E_F/RT_a)\right\} \\ &= D_0 \exp\left\{(-Q+E_F)/RT_a\right\} \exp(-E_F/RT_S) \end{aligned} \tag{3.3}$$

where

Pre-exponential factor: $D_0 = 1.71 \times 10^{-4}$ m^2/s
Activation energy for self-diffusion: Q =142kJ/mol
Gas constant: R =8.3145J/mol · K
Formation energy of a vacancy: E_F =64.6kJ/mol(0.67eV)[31]
Solution-treatment temperature: T_S =793K.

was utilized as the experimental coefficient, D, in eq.(3.2). Table 3.1 summarizes the evaluated scaling constants, m, together with the diffusion coefficients at Ta in both the

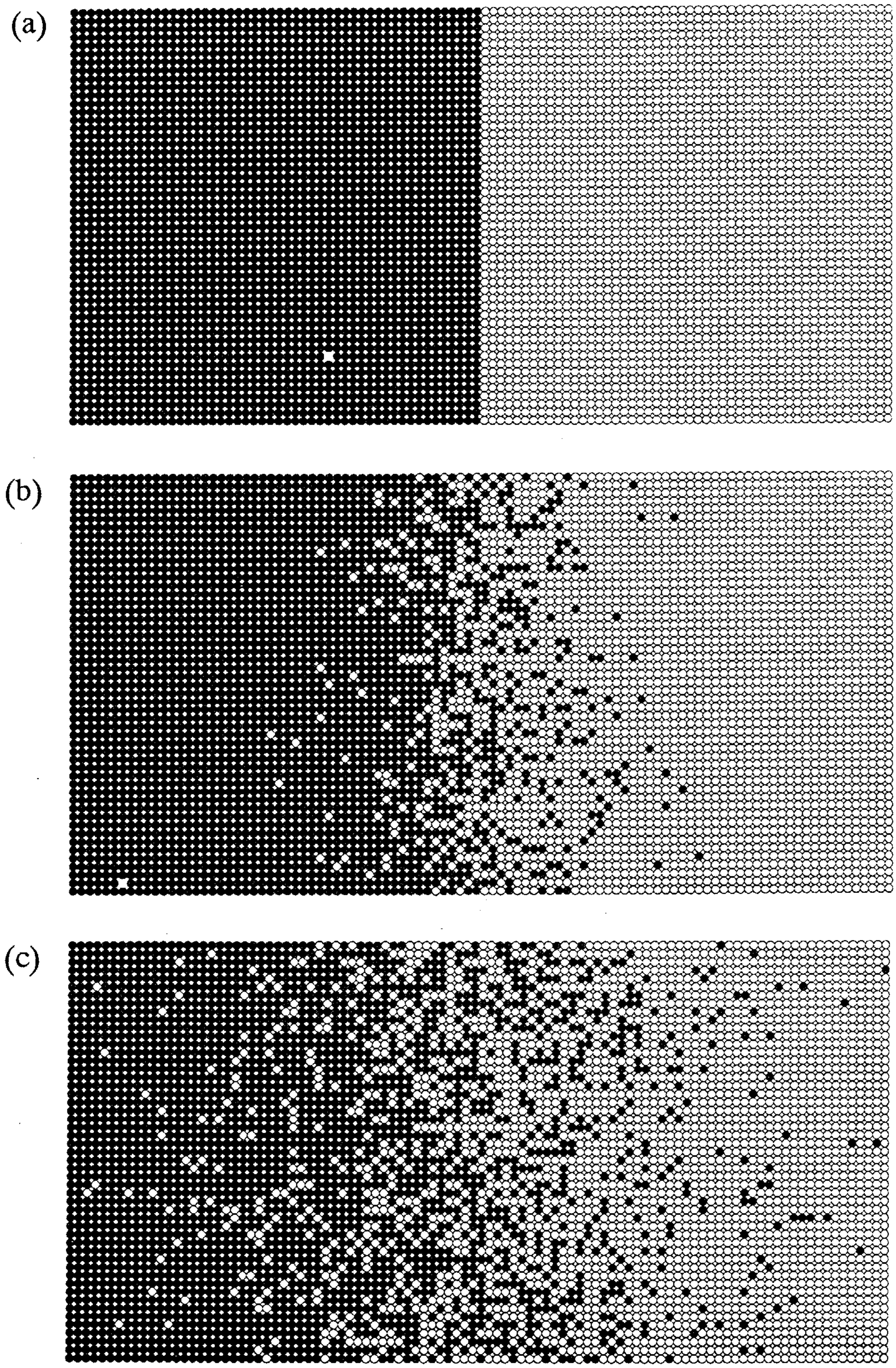

Fig.3.3 Dynamical evolution of marked Al atoms, which originally settled in one side and gradually migrate through an interface to the other side, on one atomic layer of (001) plane during self-diffusion for 1MCs(a), 2.5×10^5MCs(b) and 2.5×10^7MCs(c). The open and solid circles represent unmarked Al and marked Al atoms, respectively.

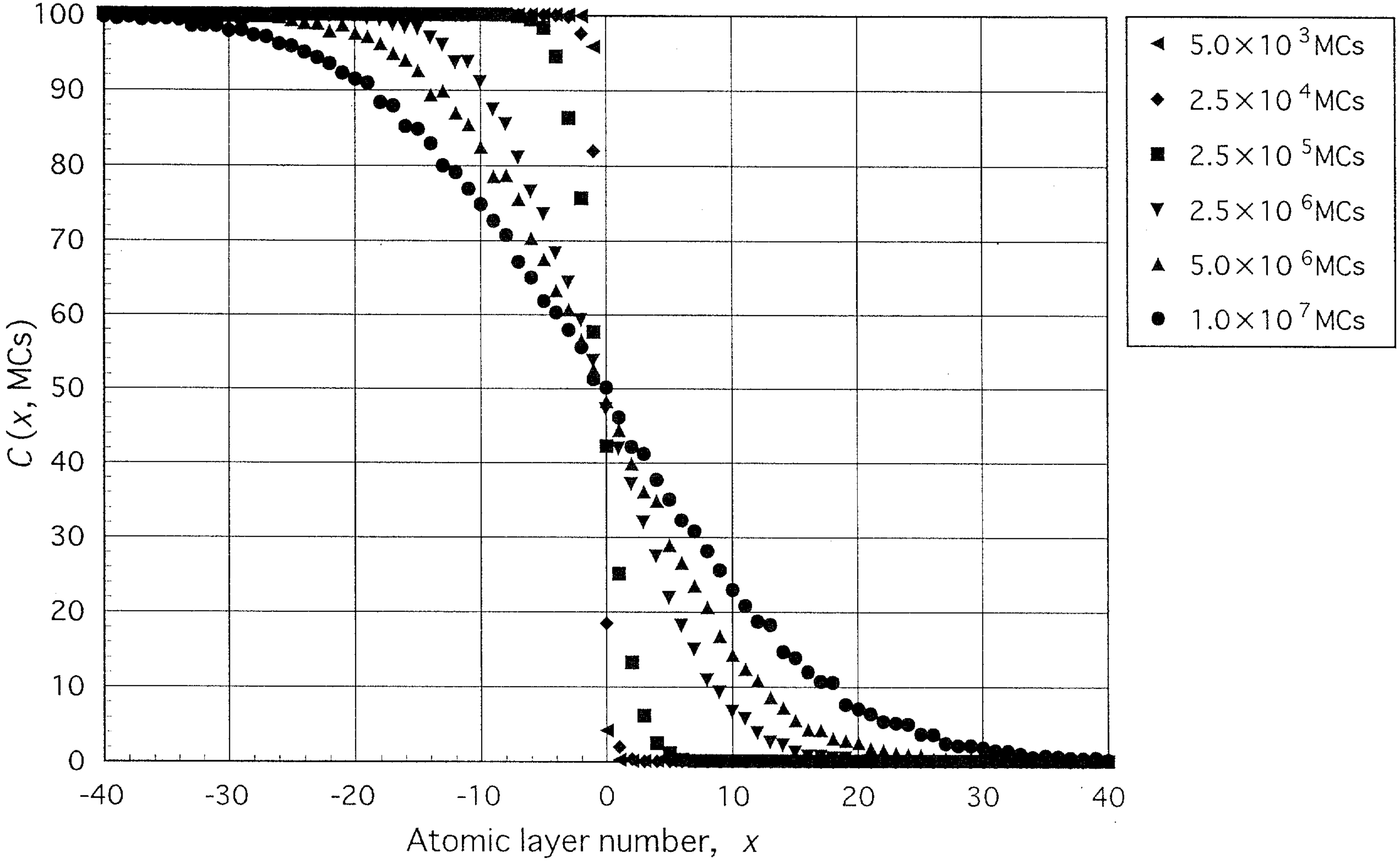

Fig.3.4 Variation in concentration plofile of marked Al atoms, which originally settled in one side (x<0) and gradually migrates through an interface (x=0) to the other side (x>0) as a function of MCs, on one atomic layer with a distance from the interface during self-diffusion of Al.

Table 3.1 Diffusion coefficients at aging temperatures, *Ta* , both in the equilibrium state, D_{eq} , and the accerelated state by quenched-in excess vacancies, D^* , and obtained scaling constants between Monte Carlo steps(MCs) and actual aging times, *m* .

Aging temperature, *Ta* / K	Diffusion coefficient at *Ta* in the equilibrium state, D_{eq} / m^2s^{-1}	Diffusion coefficient at *Ta* in the acceretated state, D^* / m^2s^{-1}	Scaling constant, *m* / s・MCs^{-1}
273	1.2×10^{-31}	1.5×10^{-23}	3.2×10^{-2}
313	3.4×10^{-28}	1.2×10^{-21}	4.1×10^{-4}
343	4.1×10^{-26}	1.6×10^{-20}	3.0×10^{-5}
373	2.2×10^{-24}	1.4×10^{-19}	3.5×10^{-6}
400	4.9×10^{-23}	7.5×10^{-19}	6.5×10^{-7}
500	2.5×10^{-19}	7.8×10^{-17}	6.0×10^{-9}

equilibrium state, D_{eq}, and accelerated state by quenched-in excess vacancies, D^*. The actual aging time performed in this Monte Carlo simulation is exponentially shortened with increasing aging temperature, Ta. In the simulation at 273K, however, it is sufficiently reasonable to correlate the temporal evolution of 10^7MCs with actual aging time of $\sim 10^7$s, not $\sim 3.2 \times 10^5$s in Table 3.1, if continuous decrease in vacancy concentration due to the vacancy-sink mechanism is taken into account. This relationship; i.e. 1MCs is almost equal to 1s at 273K, is confirmed again in Chapters 4-6 by the comparison between electrical resistivity changes experimentally measured and evaluated from the simulation results.

3.3 Derivation method of simulation parameters

The study of phase decompositions in alloys using a Monte Carlo method requires an accurate estimation of interatomic interactions. In this work, all interactions are restricted up to second nearest neighbors and also derived from known thermodynamic or kinetic quantities. Tables 3.2 and 3.3 summarize experimental values of the cohesive energy, E_{coh}[32], formation energy of a vacancy, E^F_V[31] and nearest neighbor interatomic distance, r^{pure}_{ii}[32], in pure metals. The values of maximum solubility limits, C_j^{max}, and the corresponding temperatures, T_j^{max}, in the equilibrium phase diagrams for Al-*j*, Cu-*j*, Li-*j* and Mg-*j* binary alloys[33, 34] are listed in Tables 3.4-3.7. The derivation method of utilized pair interactions is as follows.

3.3.1 Pair interaction between same atom species

Pair interaction between same atom species, ε_{ii}, is estimated from the phenomenological Lennard-Jones type potential of the following form:

$$\varepsilon_{ii} = \varepsilon_{ii}^{pure}[(r_{ii}^{pure}/r)^8 - 2(r_{ii}^{pure}/r)^4], \qquad (3.4)$$

where a pair interaction between *i-i* atoms in the pure metal, ε^{pure}_{ii}, is evaluated from

$$\varepsilon_{ii}^{pure} = 2E_{coh}/z. \qquad (3.5)$$

The exponents of repulsive and attractive terms in eq.(3.4); i.e. 8 and 4, are previously reported values for pure metals[3, 35]. Figure 3.5(a) illustrates the variations in ε_{ii} with the interatomic distance, r, for Al-Al and Cu-Cu pairs. Note that a slightly larger value of ε_{CuCu} than the most stable $\varepsilon^{pure}_{CuCu}$ is utilized in this simulation when Cu-Cu pairs are formed on the Al lattice sites having the nearest neighbor interatomic distance r^{pure}_{AlAl}= 0.2864nm.

3.3.2 Pair interaction between different atom species

Table 3.2 Experimental values of cohesive energy, E_{coh}, and formation energy of a vacancy, $E^{\mathrm{F}}_{\mathrm{v}}$, in pure metals[30, 31].

I A	II A	III A	IV A	V A	VI A	VII A	VIII			I B	II B	III B	IV B	V B	VI B	VII B
H				X Upper Lower	: Element : Cohesive energy, E_{coh} / kJmol^{-1} : Formation energy of a vacancy, $E^{\mathrm{F}}_{\mathrm{v}}$ / eV											
Li 158 0.480	Be 320 —											B 561 —	C 711 —	N 474 —	O 251 —	F 81.0 —
Na 107 0.335	Mg 145 0.58											Al 327 0.67	Si 446 —	P 331 —	S 275 —	Cl 135 —
K 90.1 0.34	Ca 178 —	Sc 376 —	Ti 468 1.27	V 512 2.2	Cr 395 2.0	Mn 282 —	Fe 413 1.6	Co 424 1.34	Ni 428 1.79	Cu 336 1.28	Zn 130 0.54	Ga 271 —	Ge 372 —	As 285.3 —	Se 237 —	Br 118 —
Rb 82.2 —	Sr 166 —	Y 422 —	Zr 603 >1.5	Nb 730 2.6	Mo 658 3.24	Tc 661 —	Ru 650 —	Rh 554 —	Pd 376 1.70	Ag 284 1.11	Cd 112 0.46	In 243 0.52	Sn 303 0.51	Sb 265 1.4	Te 211 —	I 107 —
Cs 77.6 —	Ba 183 —	La 431 ~1	Hf 621 —	Ta 782 2.9	W 859 3.6	Re 775 —	Os 788 —	Ir 670 —	Pt 564 1.35	Au 368 0.93	Hg 65 —	Tl 182 0.46	Pb 196 0.58	Bi 210 0.35	Po 144 —	At — —

Table 3.3 Crystal structure and nearest neighbor interatomic distance, r^{pure}_{ii}, in pure metals[31].

X	: Element
Upper	: Crystal structure
Lower	: Interatomic distance, r^{pure}_{ii} / Å

I A	II A	III A	IVA	V A	VIA	VIIA	VIII			I B	II B	III B	IVB	V B	VIB	VIIB
H hcp																
Li bcc 3.023	Be hcp 2.22											B tet —	C hex 1.54	N hex —	O cub —	F mon 1.44
Na bcc 3.659	Mg hcp 3.20											Al fcc 2.864	Si dia 2.35	P cub —	S orh —	Cl tet 2.02
K bcc 4.525	Ca fcc 3.95	Sc hcp 3.25	Ti hcp 2.89	V bcc 2.62	Cr bcc 2.50	Mn cub 2.24	Fe bcc 2.48	Co hcp 2.50	Ni fcc 2.49	Cu fcc 2.56	Zn hcp 2.66	Ga Orh 2.44	Ge dia 2.45	As rhm 3.16	Se hex 2.32	Br orh —
Rb bcc 4.837	Sr fcc 4.30	Y hcp 3.55	Zr hcp 3.17	Nb bcc 2.86	Mo bcc 2.72	Tc hcp 2.71	Ru hcp 2.65	Rh fcc 2.69	Pd fcc 2.75	Ag fcc 2.89	Cd hcp 2.98	In tet 3.25	Sn(β) tet 3.02	Sb rhm 2.91	Te hex 2.86	I orh 3.54
Cs bcc 5.235	Ba bcc 4.35	La hex 3.73	Hf hcp 3.13	Ta bcc 2.86	W bcc 2.74	Re hcp 2.74	Os hcp 2.68	Ir fcc 2.71	Pt fcc 2.77	Au fcc 2.88	Hg rhm 3.01	Tl hcp 3.46	Pb fcc 3.50	Bi rhm 3.07	Po cub 3.34	At — —

Table 3.4 Maximum solubility of each element, C_j^{max}, in pure Al and the corresponding temperature, T_j^{max}[32, 33].

I A	II A	III A	IV A	V A	VI A	VII A	VIII			I B	II B	III B	IV B	V B	VI B	VII B
H																
Li 13.9 873	Be 0.299 917											B	C	N	O	F
Na	Mg 18.6 723											Al	Si 1.59 850	P	S —	Cl
K	Ca <0.03 873	Sc 0.210 913	Ti 0.748 938	V 0.319 933.5	Cr 0.37 934.5	Mn 0.902 931.5	Fe 0.025 928	Co >0.01 930	Ni 0.11 912.9	Cu 2.48 821	Zn 49.1 716	Ga 8.82 299.6	Ge 2.00 693	As —	Se 3.1E-3 933	Br
Rb	Sr —	Y 0.052 912	Zr 0.083 933.5	Nb 0.064 934.4	Mo 0.070	Tc	Ru —	Rh	Pd —	Ag 23.9 839	Cd 0.113 922	In 0.045 912	Sn 2.3E-3 501.3	Sb —	Te —	I
Cs	Ba —	La 9.7E-3 913	Hf 0.186 935	Ta 0.037 941	W 0.024 933.5	Re —	Os	Ir <0.1 923	Pt —	Au 0.061 923	Hg —	Tl —	Pb 0.026 931.5	Bi 0.026 930	Po	At

X : Element
Upper : Maximum solubility, C_j^{max}, in Al / mol%
Lower : Corresponding temperature, T_j^{max} / K

— Practically insoluble

Table 3.5 Maximum solubility of each element, C_j^{max}, in pure Cu and the corresponding temperature, T_j^{max}[32, 33].

I A	II A	III A	IV A	V A	VI A	VII A	VIII			I B	II B	III B	IV B	V B	VI B	VII B
H																
Li 22.1 453.5	Be 13.7 1138											B	C	N	O	F
Na	Mg 6.93 999											Al 19.6 1308	Si 11.4 1123	P	S 2.4×10^{-2} 1340	Cl
K	Ca —	Sc —	Ti 7.81 1158	V 0.125 1358	Cr 0.891 1350	Mn ※	Fe 4.64 1369	Co 7.51 1385	Ni ※	Cu	Zn 38.3 727	Ga 20.6 893	Ge 11.6 1097	As 6.83 958	Se —	Br
Rb	Sr —	Y —	Zr 0.120 1245	Nb 0.103 1353	Mo	Tc	Ru	Rh ※	Pd ※	Ag 4.87 1052	Cd 2.07 822	In 10.9 847	Sn 9.13 793	Sb 5.83 918	Te —	I
Cs	Ba	La —	Hf 0.394 1261	Ta	W	Re	Os	Ir 8.08 1411	Pt ※	Au ※	Hg	Tl 1241 0.278	Pb —	Bi 3.0×10^{-3} 543.6	Po	At

X	: Element
Upper	: Maximum solubility, C_j^{max}, in Cu / mol%
Lower	: Corresponding temperature, T_j^{max} / K

— Practically insoluble

※ Completely miscible in each other

Table 3.6 Maximum solubility of each element, C_j^{max}, in pure Li and the corresponding temperature, T_j^{max}[32, 33].

I A	II A	III A	IV A	V A	VI A	VII A	VIII			I B	II B	III B	IV B	V B	VI B	VII B
H																
Li	Be —											B	C	N	O	F
Na —	Mg 75.5 861											Al —	Si —	P	S —	Cl
K	Ca —	Sc	Ti	V	Cr —	Mn	Fe —	Co	Ni	Cu 0.01 453.1	Zn 1.49 434	Ga —	Ge —	As	Se —	Br
Rb	Sr —	Y	Zr	Nb	Mo	Tc	Ru	Rh	Pd —	Ag 9.14 418.5	Cd 18.0 528	In 0.2 452	Sn —	Sb	Te —	I
Cs	Ba —	La	Hf	Ta	W	Re	Os	Ir	Pt	Au 0.7 428	Hg	Tl —	Pb —	Bi —	Po	At

X : Element
Upper : Maximum solubility, C_j^{max}, in Li / mol%
Lower : Corresponding temperature, T_j^{max} / K

— Practically insoluble

Table 3.7 Maximum solubility of each element, C_j^{max}, in pure Mg and the corresponding temperature, T_j^{max}[32, 33].

ⅠA	ⅡA	ⅢA	ⅣA	ⅤA	ⅥA	ⅦA	Ⅷ			ⅠB	ⅡB	ⅢB	ⅣB	ⅤB	ⅥB	ⅦB
H																
Li 18.3 861	Be											B	C	N	O	F
Na	Mg											Al 11.77 710	Si —	P	S	Cl
K	Ca 0.817 789.5	Sc 15.0 983	Ti	V	Cr	Mn 0.985 926	Fe	Co	Ni —	Cu —	Zn 2.40 613	Ga 3.49 698	Ge —	As	Se	Br
Rb	Sr 3.1×10^{-2} 858	Y 3.40 840.4	Zr 1.04 926.6	Nb	Mo	Tc	Ru	Rh	Pd	Ag 3.83 745	Cd ※	In 19.4 757	Sn 3.35 834.2	Sb —	Te	I
Cs	Ba 2.0×10^{-3} 907	La	Hf	Ta	W	Re	Os	Ir	Pt	Au 9.9×10^{-2} 848	Hg 1.20 721	Tl 15.4 678.3	Pb 7.75 739.2	Bi 1.12 826	Po	At

X : Element
Upper : Maximum solubility, C_j^{max}, in Cu / mol%
Lower : Corresponding temperature, T_j^{max} / K

— Practically insoluble
※ Completely miscible in each other

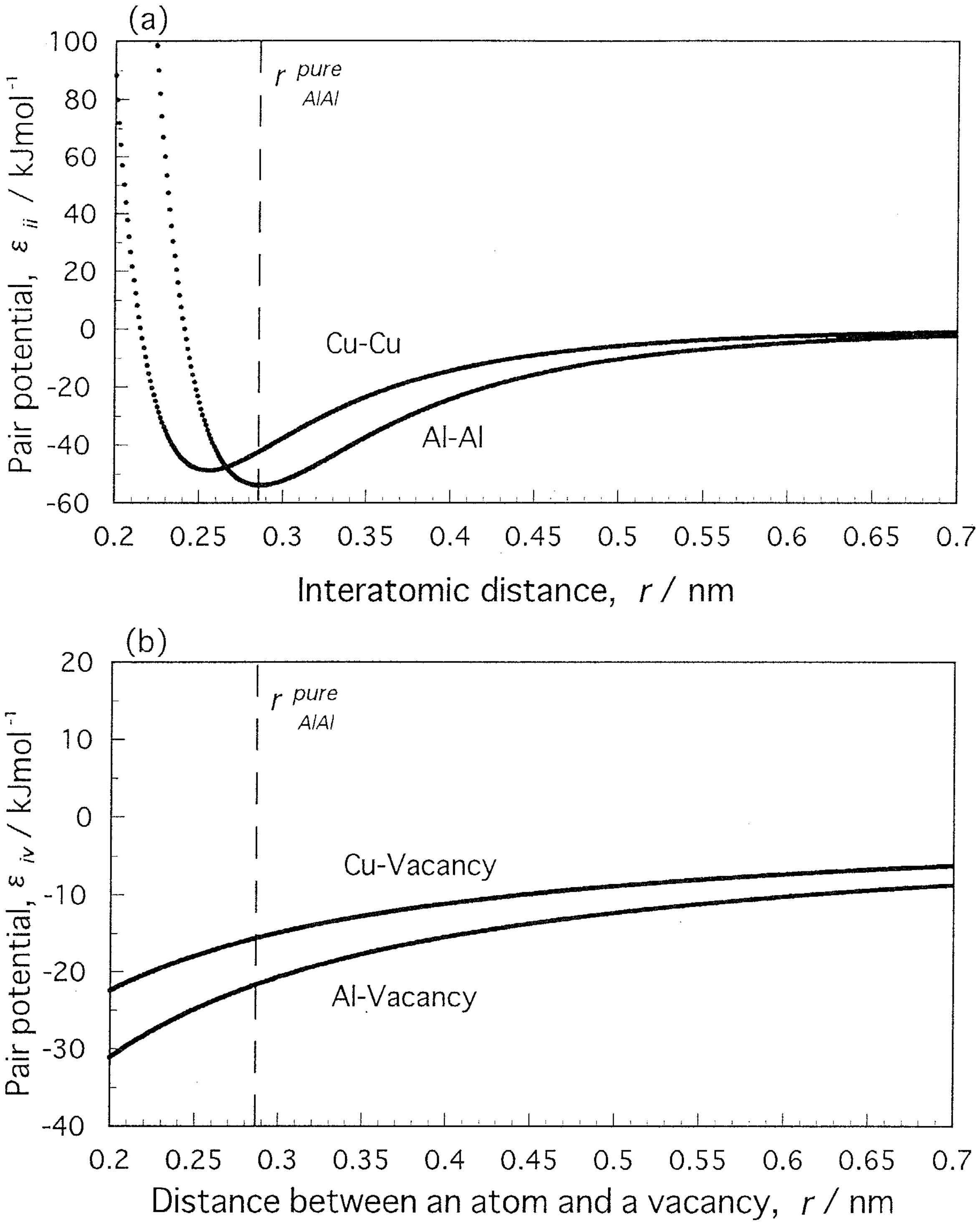

Fig.3.5 Variations in assumed pair interactions between same atom species, ε_{ii}(a) and between an atom and a vacancy, ε_{iv}(b) as a function of the distance between them. The vertical broken lines represent an interatomic distance of an arbitrary pair located on Al lattice sites.

In contrast, pair interaction between different atom species, ε_{ij}, is obtained from an interaction parameter derived from the corresponding equilibrium phase diagram, ε_{dia}:

$$\varepsilon_{ij} = \varepsilon_{dia} + (\varepsilon_{ii} + \varepsilon_{jj})/2. \tag{3.6}$$

In the case of the phase decomposition with clustering reaction, the value of ε_{dia} is exactly equal to the ordering parameter, V_{ij}, which is introduced in Chapter 4, because the derivation method is based on a regular solution approximation. In general, the free energy change in mixing, ΔG_{mix}, in a regular solution of *i-j* binary alloys is expressed as follows:

$$\begin{aligned} \Delta G_{mix} &= \Delta H_{mix} - T\Delta S_{mix} \\ &= \Omega x_i x_j + RT(x_i \ln x_i + x_j \ln x_j) \end{aligned} \tag{3.7}$$

where

$$\Omega = N_a z\varepsilon. \tag{3.8}$$

Here, x_i and x_j refer to mol-fractions of i and j atoms; i.e. $x_i+x_j=1$, ε an interaction parameter and Na Avogadro's number. Under the condition of a solid solution having the maximum j concentration, C_j^{max}, in i at the corresponding temperature, T_j^{max}, the following relationship can be approximately assumed:

$$d\Delta G_{mix} / dx_i = \Omega(x_j - x_i) + RT(\ln x_i - \ln x_j) = 0, \tag{3.9}$$

because the free energy change ΔG_{mix} becomes almost minimum. Therefore, interaction parameters derived from the equilibrium phase diagrams, ε_{dia}, can be obtained by the following equation:

$$\begin{aligned} \varepsilon_{dia} &= RT(\ln x_i - \ln x_j)/ N_a z(x_i - x_j) \\ &= RT_j^{\max}(\ln(1 - c_j^{\max}) - \ln c_j^{\max})/ N_a z(1 - 2c_j^{\max}). \end{aligned} \tag{3.10}$$

3.3.3 Pair interaction between an atom and a vacancy

Pair interaction between an atom and a vacancy, ε_{iv}, is estimated from the assumed potential (i.e. 0-1 type Lennard-Jones potential) of the form;

$$\varepsilon_{iv} = -\varepsilon_{iv}^{pure}(r_{ii}^{pure} / r). \tag{3.11}$$

Here, 'ghost' pair interaction between an i atom and a vacancy in the pure metal, ε^{pure}_{iv}, is evaluated from

$$\varepsilon_{iv}^{pure} = (E_v^F + E_{coh}) / z, \tag{3.12}$$

as derived by Doyama *et al.*[36]. Figure 3.5(b) illustrates the variations in ε_{iv} with the distance between an elemental atom and a vacancy, r, for Al-Vacancy and Cu-Vacancy pairs. Note that no repulsive force works between them under this assumption.

3.3.4 Assumptions for derived pair interactions

The utilized pair interactions for the Monte Carlo simulation are summarized in Table 3.8. All parameters are assumed to be independent of both the composition and temperature of the simulated alloys. This implies that the simulation model adopted in this work does not take into account the entropy term, resulting in the Pseudo-Ground State analysis[37-39]. Despite such the simplification, however, the success of the performed simulations is proved because basic physical features of the investigated phase decompositions can be sufficiently followed. The precipitate-matrix interfacial energy is not also taken into account because of its less influence on the obtained simulation results except for the morphology of precipitates.

As for the elements having bcc structure such as Li, Fe, Cr and V, the coordination number, z, was regarded as not 8 but 12 because the interatomic distance between second nearest neighbor atoms is rather close to that between nearest neighbor atoms, as previously pointed out by Doyama et al.[36]. Similar approximation was also applied to Sn having bct structure. The simulation for the Si-added alloys was not unfortunately performed because of an open question as to whether a pair interaction between Si-Si atoms estimated from a diamond structure, $\varepsilon^{pure}_{SiSi}$, can be utilized as a Si-Si pair interaction on the Al lattice sites.

3.4 Comparison between experimental and Monte Carlo simulation results

It is also necessary to establish the reliability of the simulation results obtained in this work by comparing with experimental results. Electrical resistivity changes are quite convenient for this comparison because structural parameters such as Cs, N and n can produce calculated increments in electrical resistivity, $\Delta\rho_{Cal}$, using the following relationship;

$$\Delta\rho_{Cal} = \sum_{S} Cs\rho_S^0 + Ng(n), \tag{3.13}$$

where ρ_s^0 and $g(n)$ stand for contributions to electrical resistivity by residual solute atoms per 1mol% and one cluster with average size n. This equation implies that the superimposition of the decreased residual solute concentrations and increased size and number density of precipitates, which are represented in the first and second terms on the right-hand side of eq.(3.13) respectively, attributes to change in electrical resistivity during phase decomposition occurring in alloys. In this work, the comparison between electrical resistivity curves experimentally obtained and evaluated from the simulation results is made to reveal the effectiveness of the utilized simulation models. Table 3.9 shows reported values of electrical resistivity increments by residual solute atoms in aluminum, ρ_s^0[40-46]. As for the function $g(n)$, furthermore, the following relationship is assumed;

Table 3.8 Pair interactions between same atom species, ε_{ii} , between different atom species, ε_{ij} , and between a solute atom and a vacancy, ε_{iv} , utilized in this simulation (in kJ/mol).

	ε_{ii} , ε_{ij}						
	Al	Cu	Mg	Li	Zn	Ag	Sn
Al	-54.5	-49.3	-34.5	-37.9	-36.4	-49.6	-47.4
Cu	—	-48.5	-32.2	-35.7	-33.4	-45.5	-46.6
Mg	—	—	-16.8	—	—	—	—
Li	—	—	—	-24.4	—	—	—
Zn	—	—	—	—	-20.3	—	—
Ag	—	—	—	—	—	-47.3	—
Sn	—	—	—	—	—	—	-47.7
Vacancy	-21.9	-15.8	-10.3	-11.8	-6.03	-14.8	-24.2
	ε_{iv}						

Table 3.9 Reported values of increment in electrical resistivity by residual solute atoms in the dilute Al alloy, ρ_s^0.

Elements	ρ_s^0 / nΩm · mol^{-1}	References	Elements	ρ_s^0 / nΩm · mol^{-1}	References
Cu	8.0	[39]	Sn	9.0	[43]
Mg	4.6	[40]	Si	6.7	[44]
Zn	2.4	[41]	Zr	58.0	[43]
Ag	13.4	[41]	Ge	8.6	[45]
Li	8.38	[42]			

$g(n) = (2.1 \times 10^{-35})n^{0.8}$ for plate-like GP zone in Al-Cu alloys (3.14)

and

$g(n) = (2.5 \times 10^{-35})n^{0.8}$ for spherical δ' phase in Al-Li alloys. (3.15)

The equation(3.14) for Al-Cu alloys is derived from an experimentally obtained linear relationship between average zone diameter and increment in ρ by one zone in Fig.3.6[47]. In contrast, the equation(3.15) for Al-Li alloys is a proposed relationship by comparing calculated resistivity changes from the obtained simulation results with experimentally measured ones.

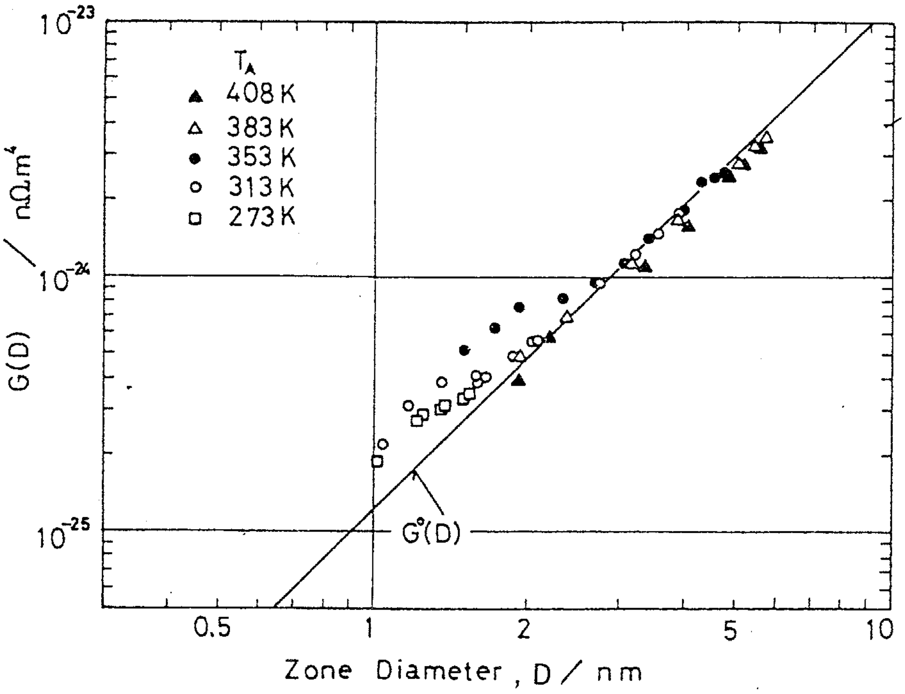

Fig.3.6 Change in scattering power of one GP zone in Al-Cu alloys, G(D), as a function of average zone diameter experimentally determined by simultaneous measurements of small-angle X-ray scattering(SAXS) intensities and electrical resistivity changes during aging at T_A [47].

References

[1] H.Yamauchi and R.Kikuchi: Bulletin of Japan Inst. Metals, **22** (1983), 399.

[2] C.Sigli and J.M.Sanchez: CALPHAD, **8** (1984), 221.

[3] J.M.Sanchez, J.R.Barefoot, R.N.Jarrett and J.K.Tien: Acta Metall., **32** (1984), 1519.

[4] T.Mori: Bulletin of Japan Inst. Metals, **28** (1989), 268.

[5] M.Enomoto, H.Harada and M.Yamazaki: CALPHAD, **15** (1991), 143.

[6] N.Onodera, T.Abe and T.Yokokawa: Acta Metall., **42** (1994), 887.

[7] T.Mohri: Bulletin of Japan Inst. Metals, **33** (1994), 1416.

[8] H.Adachi and S.Imoto: Bulletin of Japan Inst. Metals, **17** (1978), 490.

[9] M.Morinaga, N.Yukawa and H.Adachi: Bulletin of Japan Inst. Metals, **23** (1984), 911.

[10] M.Morinaga, N.Yukawa and H.Adachi: Bulletin of Japan Inst. Metals, **27** (1988), 165.

[11] R.Ninomiya, H.Yukawa and M.Morinaga: J. Japan Inst. Light Metals, **44** (1994), 171.

[12] S.Yamamoto, M.Mizuno and H.Kobayashi: J. Japan Inst. Metals, **57** (1993), 402.

[13] S.Yamamoto, T.Wakabayashi and H.Kobayashi: J. Japan Inst. Metals, **57** (1993), 1367.

[14] S.Yamamoto: J. Japan Inst. Light Metals, **44** (1994), 733.

[15] M.Takeda and H.Oka and I.Onaka: Phys. stat. sol. (a), **132** (1992), 305.

[16] A.Takeuchi, T.Koyama, T.Kozakai and T.Miyazaki: J. Japan Inst. Metals, **54** (1990), 1177.

[17] A.Takeuchi, T.Koyama, T.Moriya and T.Miyazaki: J. Japan Inst. Metals, **56** (1992), 1242.

[18] A.Takeuchi, T.Koyama and T.Miyazaki: J. Japan Inst. Metals, **57** (1993), 492.

[19] T.Koyama, T.Miyazaki and M.Doi: J. Japan Inst. Metals, **60** (1996), 553.

[20] T.Koyama, T.Miyazaki, M.Doi, A.M.Mebed and T.Moriya: J. Japan Inst. Metals, **60** (1996), 560.

[21] F.Soisson, A.Barbu and G.Martin: Acta mater., **44** (1996), 3789.

[22] H.Ikeda and H.Matsuda: J. Japan Inst. Metals, **48** (1984), 8.

[23] H.Ikeda and H.Matsuda: J. Japan Inst. Metals, **49** (1985), 423.

[24] Y.Saito and H.Harada: Mat. Sci. and Eng., **A223** (1997), 1.

[25] K.Kawasaki: Phys. Rev., **145** (1966), 224.

[26] N.Metropolis, A.W.Rosenbluth, M.N.Rosenbluth, A.H.Teller and E.Teller: J. Chem. Phys., **21** (1953), 1087.

[27] J.Hoshen and R.Kopelman: Phys. Rev., **B14** (1976), 3438.

[28] S.Sakamoto and F.Yonezawa: *Kotai Butsuri* (Solid State Physics), **24** (1989), 219.

[29] R.W.Siegel: J. Nuclear Materials, **69&70** (1978), 117.

[30] R.J.Glauber: J. Math. Phys., **4** (1963), 294.

[31] Landolt-Bornstein: *Numerical Data and Functional Relationship in Science and Technology*, **Vol.25**, *Atomic Defects in Metals*, ed. by H.Ullmaier, Springer-Verlag, Berlin, (1991).

[32] C.Kittel: *Introduction to Solid State Physics*, 5th edition John Wiley & Sons, Inc., New York, (1976), p.74.

[33] Landolt-Bornstein: *Numerical Data and Functional Relationship in Science and Technology*, **Vol.5**, *Phase Equilibria, Crystallographic and Thermodynamic Data of Binary Alloys*, ed. by O.Madelung, Springer-Verlag, Berlin, (1991).

[34] ASM Handbook: **Vol.3**, *Alloy Phase Diagrams*, ed. by H.Baker, Materials park, Ohio, (1992).

[35] R.Furth: Proc. Roy. Soc., **183A** (1944), 87.

[36] M.Doyama and J.S.Koehler: Acta metall., **24** (1976), 871.

[37] H.Hosoda, T.Shinoda, T.Suzuki and Y.Mishima: J. Japan Inst. Metals, **58** (1994), 483.

[38] H.Hosoda, T.Sato, T.Tezuka, Y.Mishima and A.Kamio: J. Japan Inst. Metals, **58** (1994), 865.

[39] H.Hosoda, A.Kamio, T.Suzuki and Y.Mishima: J. Japan Inst. Metals, **60** (1996), 793.

[40] F.J.Kedves, L.Gergely, M.Hordos and E.Kovacs-Csetenyi: Phys. Stat. Sol. (a), **13** (1972), 685.

[41] T.Fujita and T.Ohtsuka: J. Low Temp. Phys., **29** (1977), 333.

[42] J.Takamura: *Lattice Defects in Quenched Metals*, Academic Press, New York, (1965), 521.

[43] S.Fujikawa, Y.Izeki and K.Hirano: Scripta Metall., **20** (1986), 1275.

[44] F.R.Fickett: Cryogenics, **11** (1971), 349.

[45] S.Fujikawa, Y.Nogi and K.Hirano: J. Japan Inst. Light Metals, **29** (1979), 331.

[46] S.Fujikawa and Y.Izeki: Metall. Trans. A, **24A** (1993), 277.

[47] K.Osamura, N.Otsuka and Y.Murakami: Phil. Mag. B, **45** (1982), 583.

Chapter 4

Microstructure Evolution of Cu Atom Clustering and Kinetics of Low-Temperature Precipitation in Al-Cu Alloys with Microalloying Elements

4.1 Introduction

Apart from industrial interests, the formation mechanism and kinetics of Guinier-Preston zones(GP zones) observed in Al-Cu alloys still attract much attention among scientists because definitive conclusions have not been reached yet despite a wide prevalence of Al-Cu base commercial alloys. The first evidence of the zones was independently found in the late 1930s by Guinier[1] and Preston[2] using different X-ray techniques, and since then several models for GP zones have been proposed[3-8]. The model by Gerold[5] describing GP zones as single-layer platelets of Cu atoms coherent with the {100} planes of the matrix has been widely accepted although the existence of small amounts of multi-layer GP zones were also reported[9-11]. As for the formation mechanism of GP zones, however, little is still known because a direct detection of Cu atom clusters, which are rapidly formed from supersaturated solid solutions prior to GP zones, is significantly difficult using any available experimental methods. For example, it has been normally regarded that the activation energy for the nucleation of GP zones is practically almost negligible. As described in Chapter 6, however, Al-Cu alloys containing substantial amounts of Li are found to exhibit a distinct stage of the GP(1) zone nucleation with an activation energy of 85.5kJ/mol. A further addition of Mg are also found to decrease the activation energy due to the heterogeneous nucleation effect with the aid of Mg/Cu/Vacancy complexes. These results indicate that some additional elements significantly change the nucleation behavior of GP zones in Al-Cu alloys. Therefore, it is quite important to elucidate the roles of various additional elements on the formation behavior of GP zones especially from the nucleation point of view.

On the other hand, many investigations have been reported on the growth kinetics of GP zones in Al-Cu alloys containing various trace elements[12]. As a consequence of hot arguments in the early 1970s, it is widely believed that the elements having high binding energies with vacancies such as Sn, In and Cd markedly retard the growth rate of GP zones due to the so-called vacancy trapping effect proposed by Kimura *et al.*[13]. However, reported binding energies between a solute atom and a vacancy in the dilute Al alloys

(Table 1.2) are always pointed out to be doubtful because quenching experiments based on residual electrical resistivities can not follow microstructural changes occurring in alloys during quenching operation[14-16]. The transition elements having low solubility limits in Al; e.g. Fe, Mn and Zr, are also well-known to suppress the coarsening rate of GP zones because of an increased number density of insoluble compounds, which act as vacancy sinks and/or consumption places of dissolved Cu atoms. Except for the influence of Zr in dilute Al-Cu-Mg alloys[17], however, no consideration has been given to any effect of these transition elements in the solution state. As for a small addition of Mg, furthermore, Entwistle *et al.* [18] suggested that Al-4mass%Cu alloys containing higher than 0.1mass%Mg exhibit the enhanced formation of GP zones resulting in an increased hardness because of the accelerated diffusion of Cu atoms with the aid of mobile Cu/Mg/Vacancy groups. Wyss *et al.*[19] also proposed that the acceleration of the GP zone formation in a naturally aged Al-2.6mol%Cu-0.18mol%Mg alloy is attributed to Mg-Vacancy clusters, which may enhance the GP zone nucleation by increasing the number of nucleation sites and/or the frequency of nuclei formation. However, these proposed mechanisms are recognized to a lesser extent because of a slightly confusion of both the nucleation and growth behavior of GP zones.

In order to investigate the formation behavior of GP zones in detail, microstructure evolution should be followed although it is rather difficult experimentally. A computer simulation using a reliable model is an alternative powerful method to elucidate microscopic events occurring in alloys. In particular, the simulation using a Monte Carlo method is capable of reproducing the atomistic behavior such as the nucleation and growth of precipitates entirely depending on utilized simulation parameters. Therefore, a theoretical approach based on characteristic quantities of each element becomes quite effective in predicting the effects of microalloying elements in Al-Cu alloys.

In this chapter, the effects of third additional elements on the kinetics of the GP zone formation in an Al-1.8mol%Cu alloy have been experimentally investigated in the temperature range from 278 to 373K using electrical resistivity measurement. In particular, the effects of small additional Mg were examined in detail from both viewpoints of the nucleation and growth of GP zones because the problem relating to the Mg addition is still under debate. A Monte Carlo simulation using reasonable pair interactions was also performed to examine the microstructural evolution of Cu atom clusters resulting in the GP zone formation. Comparisons between the quantitative kinetics determined by the resistivity changes and the microstructural evolution directly observed in the simulation give important information on both the macroscopic transformation kinetics and the microstructural formation mechanism of Cu clusters in Al-Cu alloys containing various additional elements.

4.2 Experimental procedures

The alloys utilized in this chapter were prepared from high-purity elemental ingots; i.e. 99.99%Al, 99.9%Mg, 99.99%Zn, 99.9%Ag, 99.9%Sn and 99.999%Si, and master alloys; i.e. Al-33.3%Cu, Al-18.5%Li and Al-4.77%Zr (in mass%). The melting of these alloys was carried out under air atmosphere followed by permanent mould casting. The chemical compositions of the alloys are listed in Table 4.1. The concentrations of impurity elements such as Fe and Ti are lower than 0.01mass% in all alloys. The elements added to an Al-1.8%Cu alloy are 0.3%Mg, 0.3%Li, 0.3%Zn, 0.3%Ag, 0.01%Sn, 0.3%Si and 0.05%Zr (in mol%). For simplicity, an alloy containing a small amount of additional element, *x*, is designated as *x*-added alloy in this chapter.

All the ingots were homogenized at 723K for 36.4ks and rolled down to 1.6mm-thick sheets through hot- and cold-rolling. Solution treatments were carried out in a salt bath at 793K for 1.8ks followed by water quenching at ~298K. The subsequent aging treatments were performed at temperatures from 278 to 373K for various aging times. In this work,

Table 4.1 Chemical compositions of the alloys utilized in this chapter (mol%).

Alloys	Cu	Mg	Li	Zn	Ag	Sn	Si	Zr	Al
Al-Cu	1.74	—	—	—	—	—	—	—	bal.
Mg-added	1.83	0.273	—	—	—	—	—	—	bal.
Li-added	1.74	—	0.32	—	—	—	—	—	bal.
Zn-added	1.75	—	—	0.297	—	—	—	—	bal.
Ag-added	1.75	—	—	—	0.294	—	—	—	bal.
Sn-added	1.74	—	—	—	—	0.0068	—	—	bal.
Si-added	1.85	—	—	—	—	—	0.325	—	bal.
Zr-added	1.79	—	—	—	—	—	—	0.0485	bal.

the room temperature designated as RT always stands for ~298K. The above fabrication process is shown in Fig.2.1. The experiments in this chapter; i.e. electrical resistivity measurement and transmission electron microscopy, were made in the same manner described in Chapter 2.

4.3 Effects of microalloying elements

4.3.1. Transmission electron micrographs

Figure 4.1 shows the bright field TEM images with diffraction patterns for the Al-Cu, Mg-, Si-, Zn-, Ag-, Sn- and Li-added alloys aged at 373K for 604.8ks. The corresponding diffraction patterns confirm that the structure very finely observed in all micrographs is of GP(1) zones, which is formed on the {100} planes of the matrix having about 10-20nm in diameter. The strain field around GP(1) zones indicated by image contrasts is responsible for the age-hardenability of the alloys due to the precipitate strengthening. Although a slightly increased diameter is observed in the Mg- and Sn-added alloys, no significant difference of the precipitate microstructures is detected among the investigated alloys.

4.3.2. Electrical resistivity changes

The electrical resistivity measurement has been commonly made to follow the phase decomposition behavior occurring in alloys because of both its high sensitivity to microstructure changes and its capability to be measured from the quite early stage of aging. Osamura *et al.*[20, 21] attributed anomalous increases in electrical resistivity during low-temperature aging in Al-Zn and Al-Cu alloys to the increased Bragg scattering with increasing size and number density of GP zones. The increments in electrical resistivity from the as-quenched values during aging at 278K are shown in Fig.4.2 for the Al-Cu, Mg-, Si-, Zn-, Ag-, Sn-, Zr- and Li-added alloys. From just after quenching all alloys display a monotonous increase in ρ due to the rapid formation of GP(1) zones, then gradually decrease to show a maximum resistivity, $\rho_{\max}$. From the comparison between the rates of resistivity-increase in the early stage of aging, Mg obviously retards the GP zone formation, which is never reported previously, similarly to the well-known cases of Sn and Zr.

4.3.3. Quantitative analysis of phase decomposition kinetics

The retardation of the GP zone formation in the Mg-added alloy is confirmed by the quantitative analysis using Johnson-Mehl-Avrami equation[22-25]:

$$y = 1 - \exp[-(kt)^n], \qquad (4.1)$$

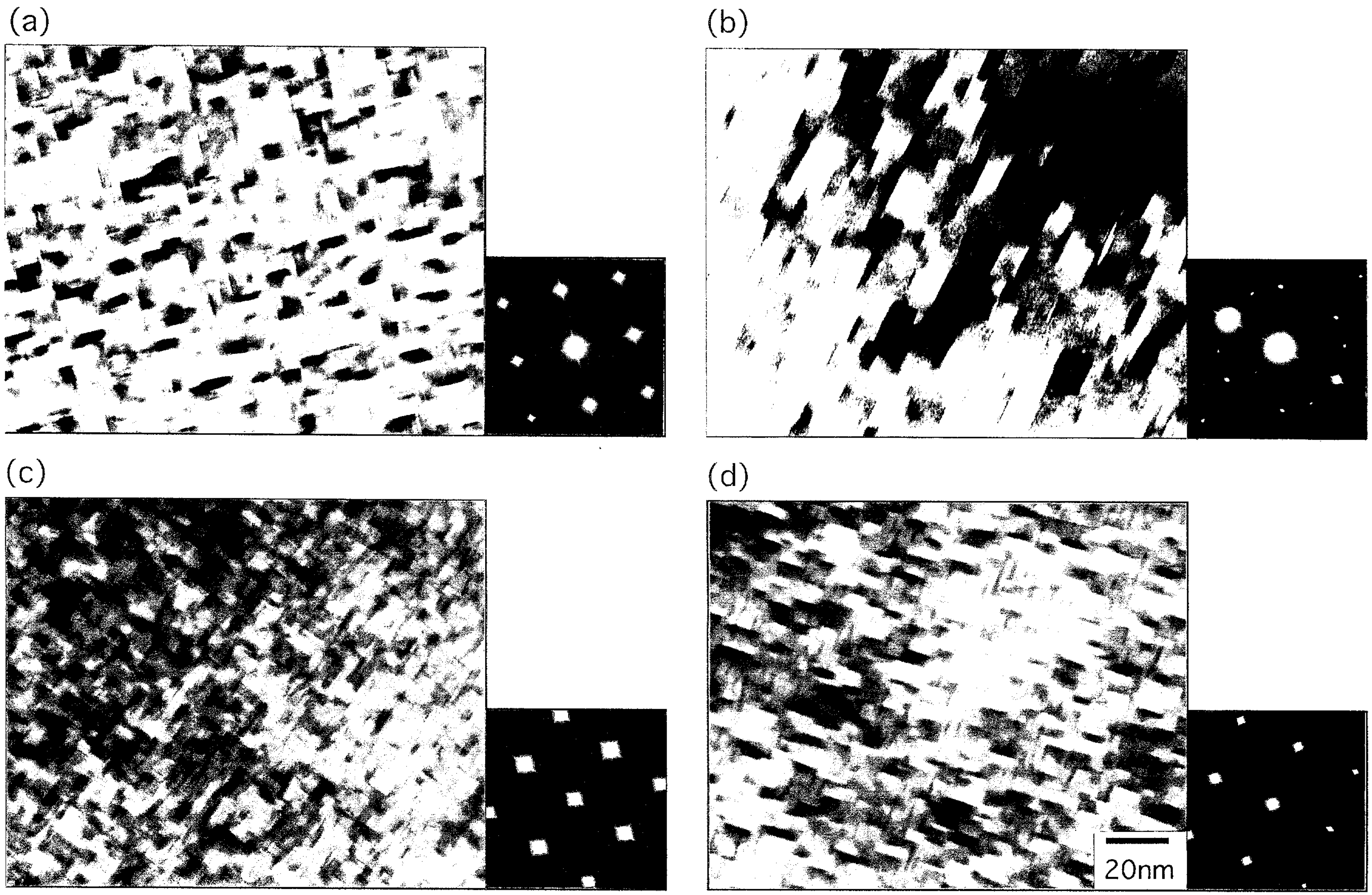

Fig. 4.1 Electron micrographs with diffraction patterns for (a)Al-Cu, (b) Mg-added, (c)Si-added and (d)Zn-added alloys aged at 373K for 604.8ks.

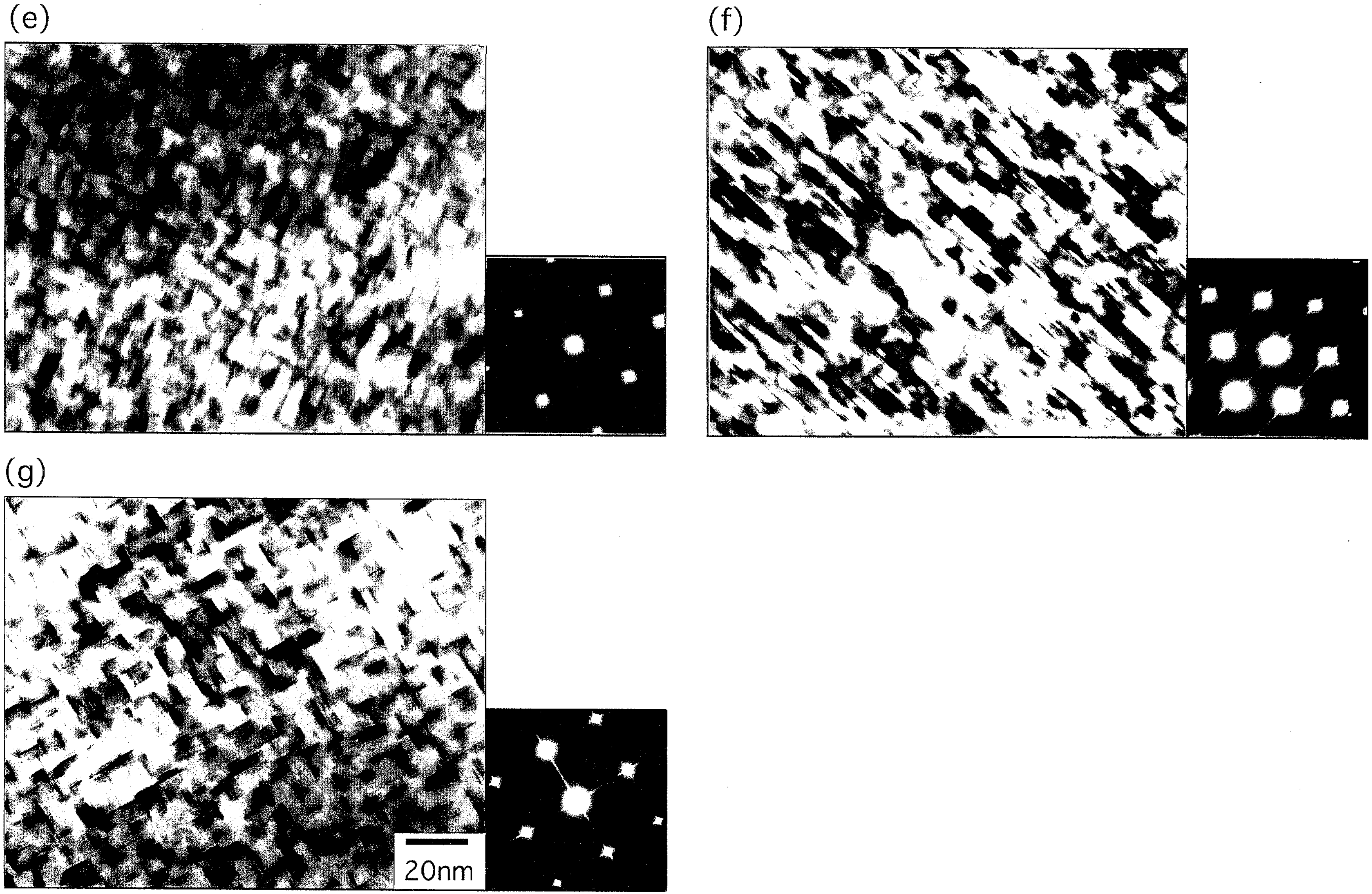

Fig. 4.1 Continued; (e)Ag-added, (f)Sn-added and (g)Li-added alloys aged at 373K for 604.8ks.

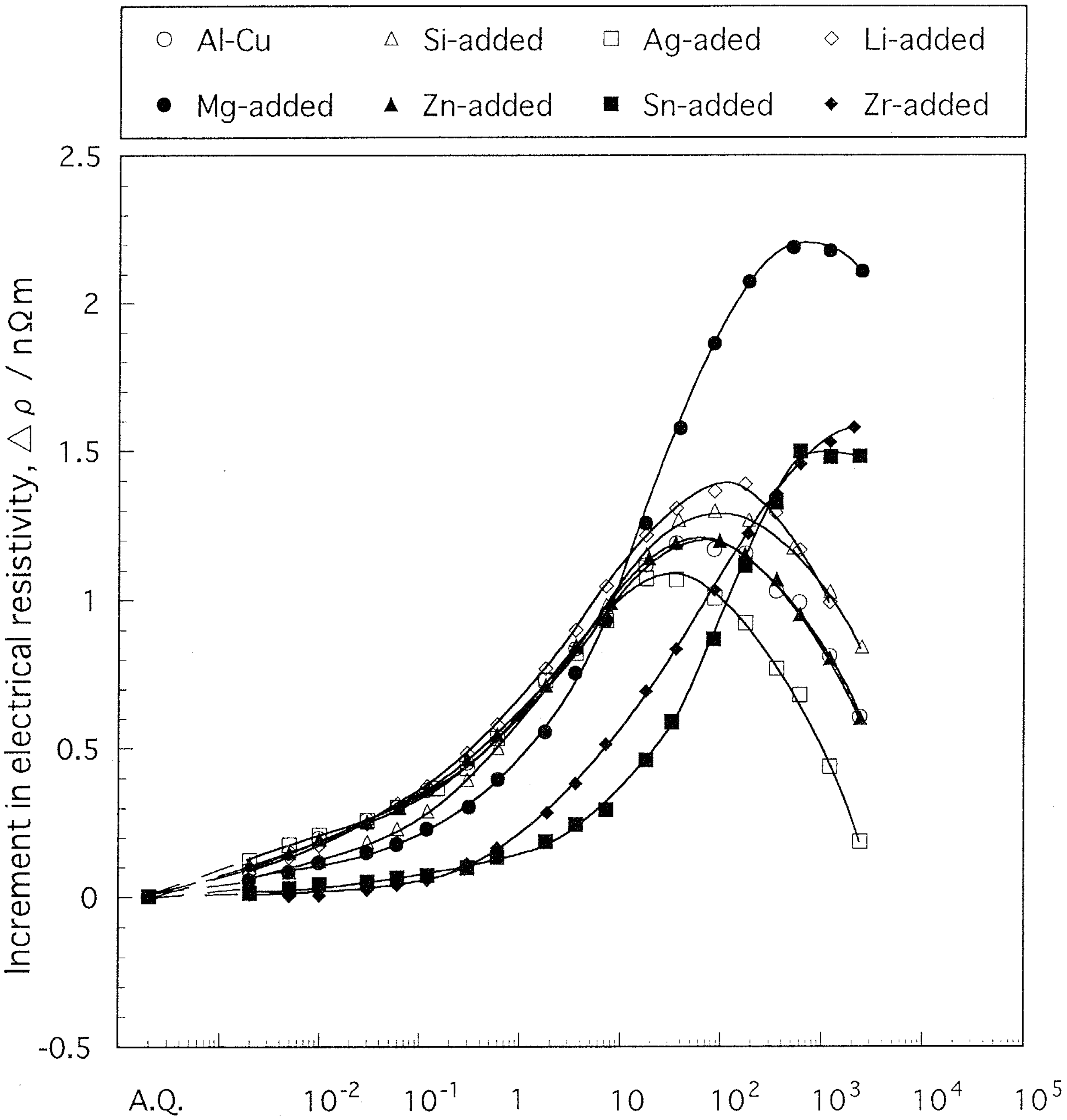

Fig.4.2 Increments in electrical resistivity from as-quenched values during aging at 278K for the Al-Cu alloys containing various additional elements.

where n is the power related to the transformation mechanism, and k is the rate constant at a fixed temperature. In the following analysis, eq.(4.1) is rewritten as below by taking the logarithms:

$$\ln\ln[1/(1-y)] = n\ln t + n\ln k. \qquad (4.2)$$

In this work, the transformed fraction, y, is defined as

$$y = (\rho_t - \rho_0)/(\rho_{\max} - \rho_0), \qquad (4.3)$$

where ρ_0, ρ_t, $\rho_{\max}$ are the resistivities at the as-quenched state, at time t and at the maximum, respectively. The definition represented in eq.(4.3) is sufficiently reasonable because the electrical resistivity during natural aging in an Al-1.8mol%Cu alloy linearly increases with increasing average diameter of zones, not integrated intensity related to the volume fraction of zones[26], as illustrated in Fig.4.3. From the linear relationship indicated by the straight line, a value of resistivity at arbitrary aging time, ρ_t, allows a determination of the average number of Cu atoms composed in one plate-like zone with the corresponding diameter, D. Thus, y is considered to be the degree of Cu condensation compared with the number of Cu atoms inside one zone providing a maximum resistivity, $\rho_{\max}$.

Figure 4.4 shows the variations in $\ln\ln[1/(1-y)]$ with $\ln t$ derived from the electrical resistivity changes in Fig.4.2. The corresponding straight lines through plotted points provide almost identical tangents; i.e. n=~0.35, indicating that the same decomposition mechanism works in all alloys. On the other hand, the rate constants, k, for the Mg-, Sn- and Zr-added alloys are significantly smaller than those for the Al-Cu, Zn- and Ag-added alloys as revealed by their intercepts on the $\ln\ln[1/(1-y)]$ axis. This implies that small amounts of Mg, Sn and Zr markedly suppress the GP zone formation, whereas Zn and Ag additions exert almost no influence on the phase decomposition kinetics of Al-Cu alloys. It is further shown in Fig.4.3 that the additions of Si and Li also show a weak tendency to suppress the GP zone formation as previously reported[12]. The similar results are obtained for other aging temperatures lower than 373K.

In general, the plots of $\ln k$ against reciprocal aging temperatures, $1/T$, provide an apparent activation energy for the precipitate formation, Q^*, according to the following relationship:

$$k = A\exp(-Q^*/RT),$$

i.e.,

$$\ln k = -(Q^*/RT) + \ln A, \qquad (4.4)$$

where R is the gas constant, A is a constant containing the jump frequency of vacancies

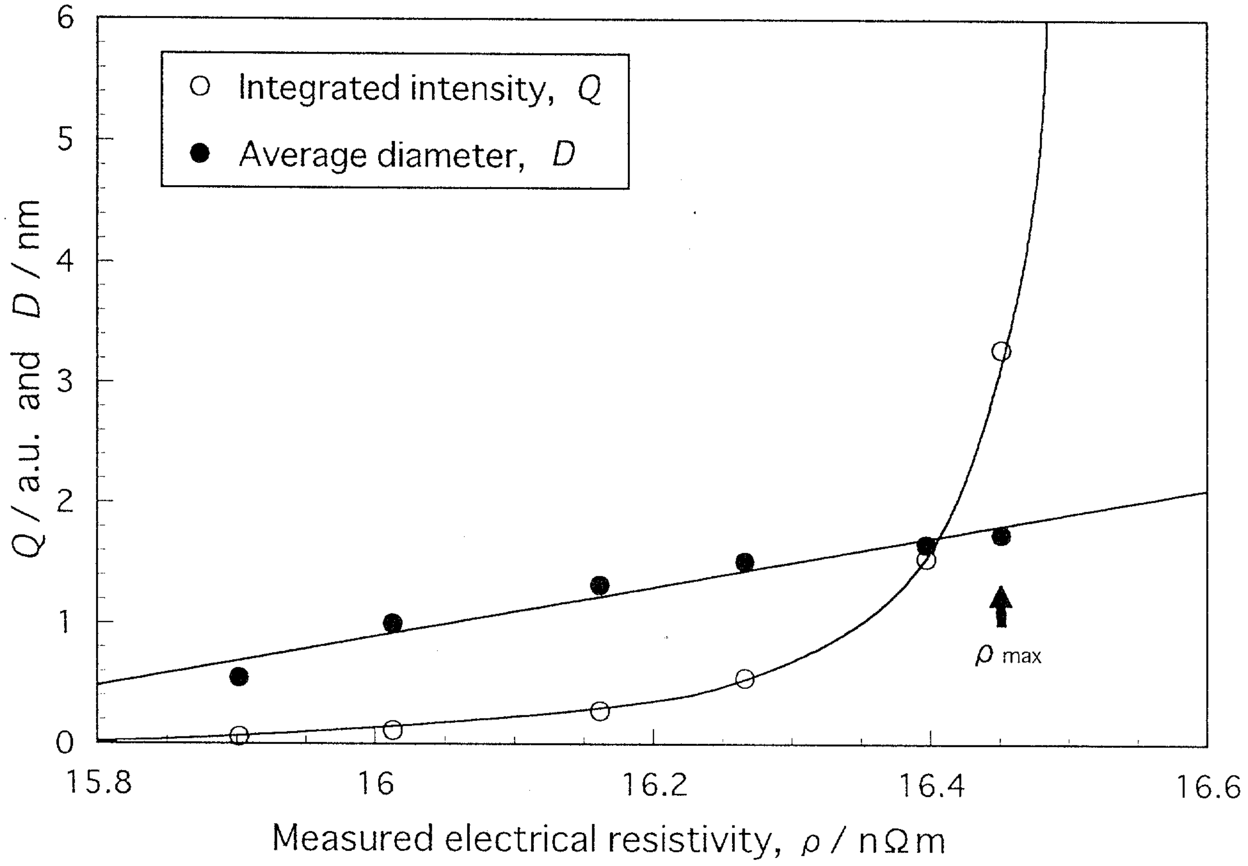

Fig.4.3 Variations in integrated intensity, Q , and average diameter , D, of GP zones in a naturally aged Al-1.8mol%Cu alloy with experimentally measured electrical resistivity, ρ .

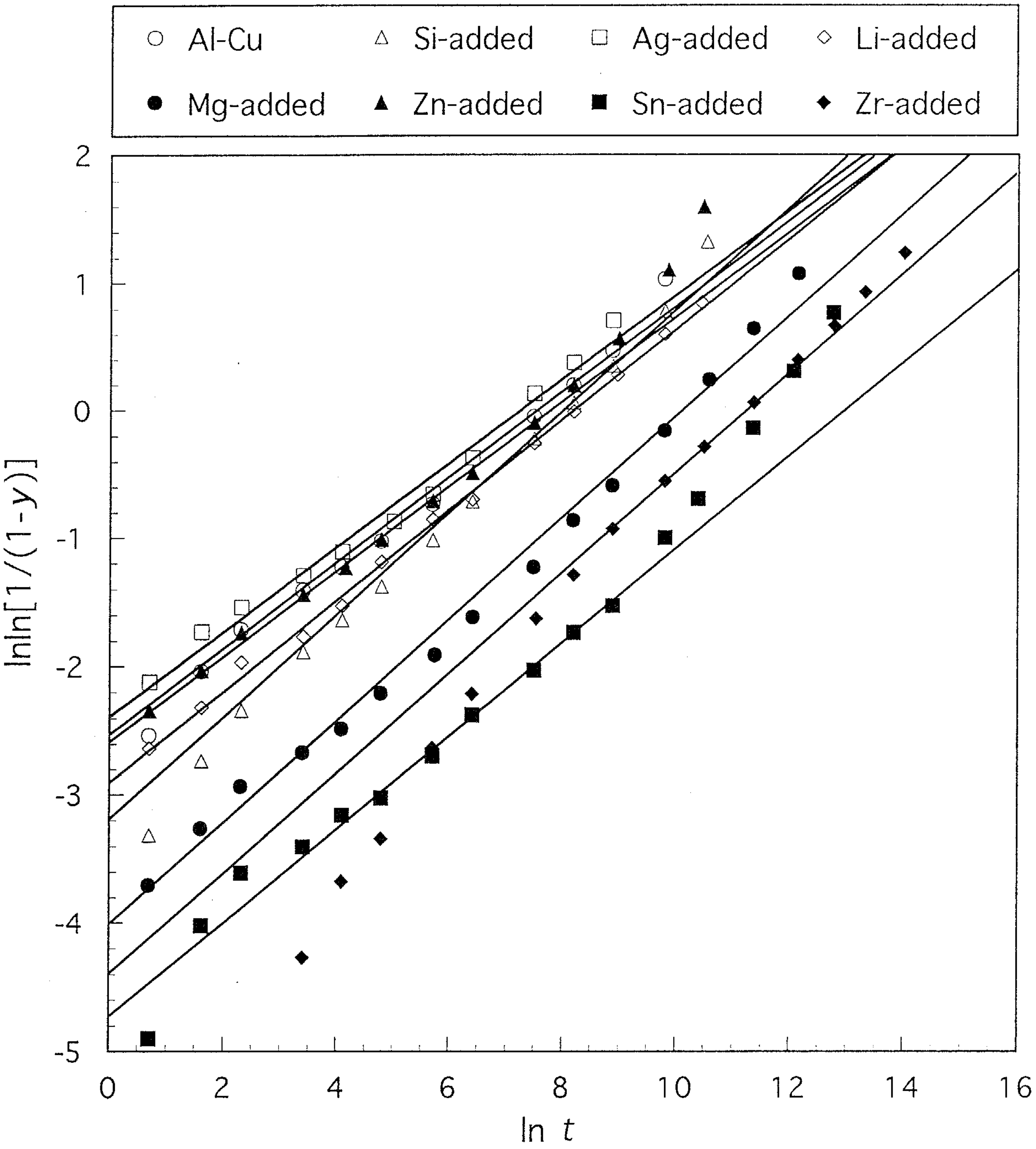

Fig.4.4 Variations in lnln[1/(1- y)] with ln t for the Al-Cu alloys containing various additional elements aged at 278K.

and the nucleation frequency of precipitates. From the Arrhenius plots in Fig.4.5, Q^* are determined to be ~54kJ/mol for the Al-Cu, Zn- and Ag-added alloys, 70.8kJ/mol for the Mg-added alloy and 84.6kJ/mol for the Sn-added alloy, respectively. Although these values are slightly larger than previously reported activation energies for the growth of GP zones; e.g. 48.2kJ/mol(0.5eV) for an Al-4mass%Cu alloy and 67.5-77.2kJ/mol(0.7-0.8eV) for an Al-4mass%Cu-0.025mass%Sn alloy[13], it can be concluded that Mg is also classified to be an element which markedly retards the GP zone formation as is the well-known case of Sn. However, two questions still remain unsolved; i.e. which stage of nucleation and growth attributes to the retardation of the GP zone formation and why contradictory results[18, 19] were reported on the effect of Mg addition. Monte Carlo simulation is likely capable of providing alternative useful suggestions to them.

4.4. Simulated microstructures

4.4.1. Derivation method of parameters

In general, phase decompositions after quenching from the solid solution range to a two-phase field can be divided into two categories; i.e. clustering and ordering reactions. The ordering parameter based on a pair interaction model;

$$V_{ij} = \varepsilon_{ij} - (\varepsilon_{ii} + \varepsilon_{jj})/2 \tag{4.5}$$

can predict which reaction of the two actually occurs in the supersaturated solid solution. Here, ε_{ij}, ε_{ii} and ε_{jj} are pair interactions between different atom species, *i-j*, and same atom species, *i-i* and *j-j*, derived in Chapter 3. In the case of $V_{ij}>0$ the alloy exhibits a tendency to form solute atom clusters in the solvent matrix, whereas in the case of $V_{ij}<0$ the alloy is inclined to form intermetallic compounds consisting of the constituent elements. As represented in the equilibrium phase diagram, the Al-Cu system is obviously classified in the latter group resulting in a negative ordering parameter between Al and Cu atoms. As for the formation of metastable GP zones in Al-Cu alloys, however, the former clustering reaction should be applied because GP zone is widely believed to comprise Cu atoms only. Therefore, it is quite natural to estimate the simulation parameter between Al and Cu atoms by utilizing the metastable phase diagram of the Al-Cu system, which is symmetrically balanced between the solid solution of Al and GP zones of ~100% Cu atoms at low temperatures. The utilized simulation parameters for Al-Cu alloys containing various third additional elements are summarized in Table 4.2. Note that only nearest neighbor interactions are taken into account and all parameters have positive values because of the pair interaction model under a regular solution approximation.

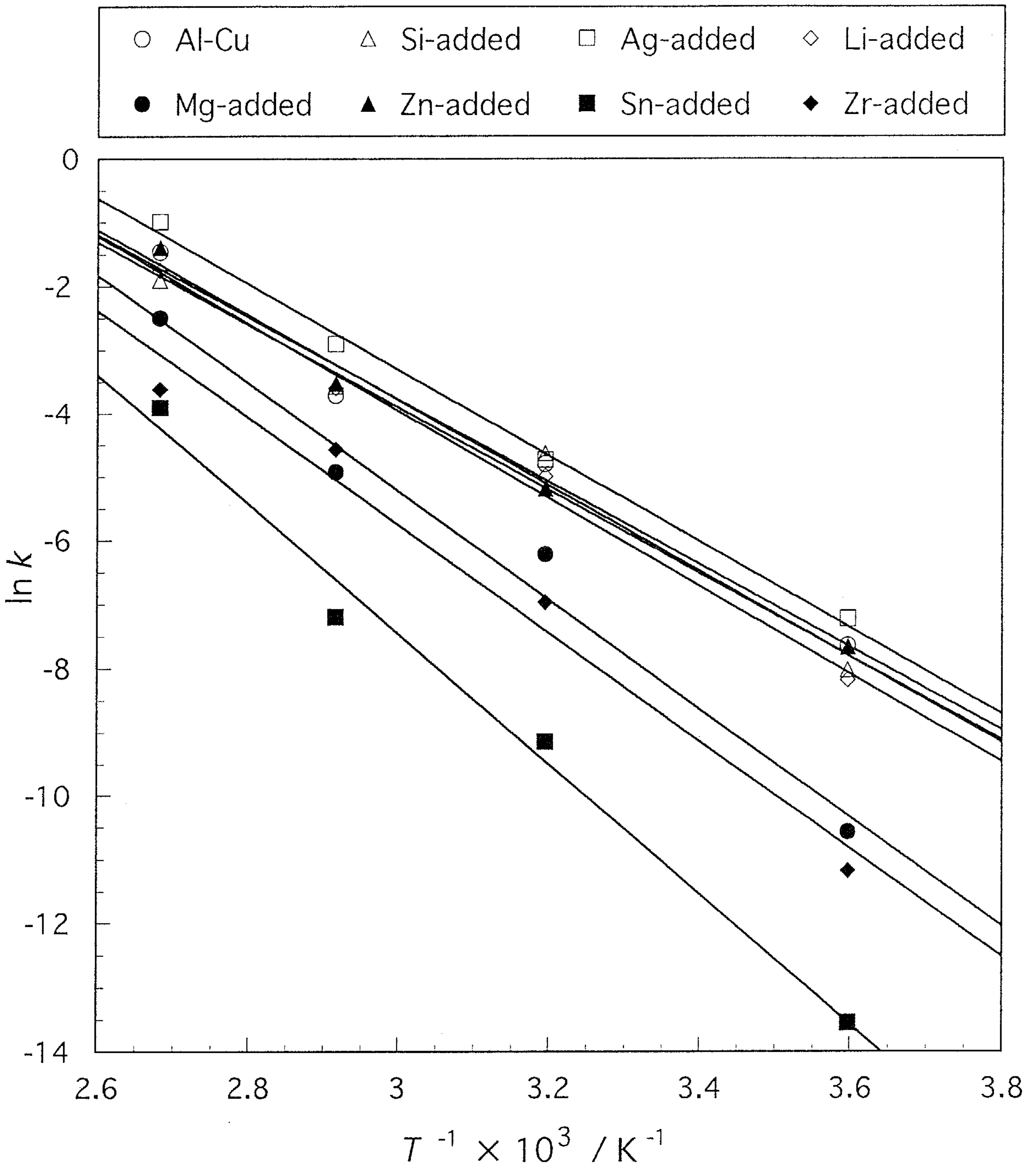

Fig.4.5 Arrhenius plots of ln k values against reciprocal aging temperatures for the Al-Cu alloys containing various additional elements.

4.4.2. Precipitate morphologies

Figure 4.6(a)-(c) illustrates the evolution of Cu atom distributions on one atom layer of the (001) plane in the Al-Cu alloy simulated at 273K. The utilized simulation program is described in Appendix. At the beginning of the simulation, Cu atoms indicated by black circles are homogeneously distributed throughout the Al matrix indicated by yellow circles, then gradually constitute the extensive volume fraction of Cu clusters due to a positive value of ε_{AlCu}. In this simulation, the morphology of Cu clusters are not disk-shaped but unshaped close to spherical, unlike actual GP zones observed in Al-Cu alloys, because the elastic effect induced by the difference in atomic radii between Al and Cu atoms is not considered. This simplification, however, is reasonable enough because three-dimensional Cu atom clusters are reported to be actually observable prior to the formation of plate-like GP zones on high resolution lattice images of an Al-1.6mol%Cu alloy[27, 28]. Another reason for the simplification is that the GP zone formation is believed to be governed by the rate of the diffusion-controlled growth rather than that of the interface-controlled growth. In fact, the obtained Q^* value for the Al-Cu alloy; i.e. ~54kJ/mol, supports the diffusion-controlled reaction because the value is well in agreement with previously reported activation energies for the migration of vacancies, 42-67kJ/mol[29-33]. Therefore, the difference in the shape of Cu clusters is considered to play no noteworthy part here in the kinetics of the GP zone formation.

Table 4.2 Ordering parameters utilized in the simulation of Al-Cu alloys containing various third additional elements, X (in kJ/mol). It should be noted that only nearest neighbor interactions are taken into account.

	Third additional elements, X							
	Cu	Mg	Li	Zn	Ag	Sn	Cd	In
Al	2.20	1.18	1.53	0.992	1.29	3.71	4.34	4.88
Cu	—	0.500	0.709	1.03	2.40	1.54	2.29	1.58
Vacancy	0.860	-8.50	-6.50	-2.29	2.16	-9.50	-6.53	-16.4
	V_{iv}							

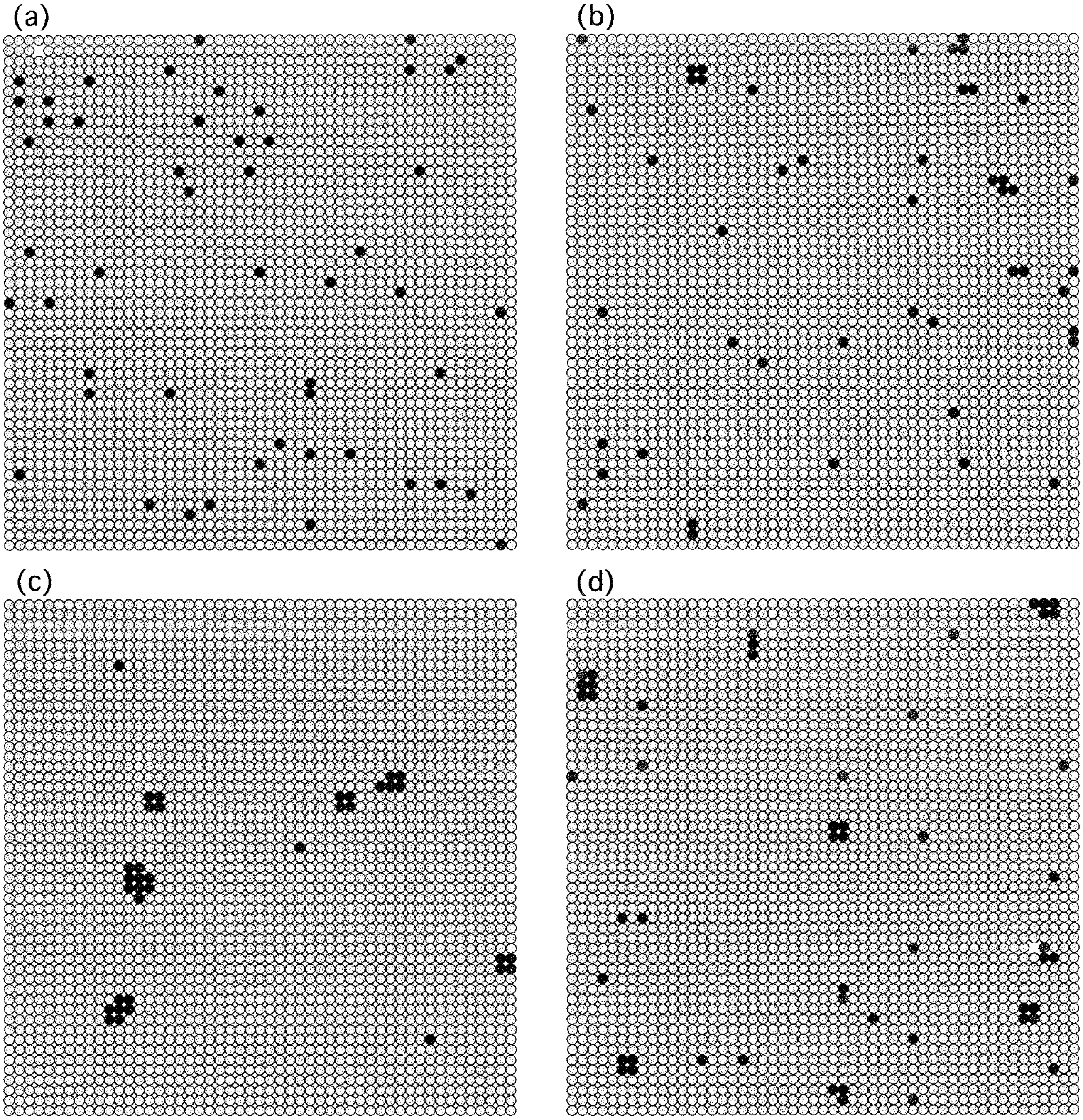

Fig.4.6 Dynamical evolution of solute atom distributions on one atom layer of (001) plane during 273K simulation of Al-Cu alloy for 1MCs(a), 1×10^5 MCs(b) and 5×10^6MCs(c) and Mg-added alloy for 5×10^6MCs(d). The yellow, black and red circles represent Al, Cu and Mg atoms, respectively.

4.4.3. Variations in structural parameters

(a) Residual solute concentration in the matrix

As a typical example of the effects of third additional elements, Fig.4.7 shows variations in residual solute concentrations in the Al matrix, *Cs*, during dynamical evolution for the Al-Cu, Ag- and Mg-added alloys simulated at 273K. Although the incidental formation of dimer and trimer clusters slightly decreases the initial solute concentrations, net Cu concentrations are almost identical in the three alloys. As Monte Carlo step(MCs) proceeds, however, the Ag-added alloy displays a monotonous decrease in the residual Cu concentration at the same rate as the Al-Cu alloy, whereas the Mg-added alloy exhibits an obvious retardation of Cu atom clustering. The similar simulation results are obtained for other alloys; i.e. the elements having larger ordering parameters with a vacancy, $V_{v\text{-}x}$, such as Zn, Ti, Co, Fe and Cr are classified in the former group, whereas the elements having smaller $V_{v\text{-}x}$ such as Li, Sn, In and Cd in the latter one. This classification is clearly illustrated along the vertical axis in Fig.4.8 and is well consistent with the experimental results previously reported[12] as summarized in Table 4.3. As for the contradictory effects of Mg in Table 4.3, it can be concluded from the obtained results that a small amount of Mg affects to suppress the formation of Cu clusters as is the well-known cases of Sn, In and Cd. The retardation of the Cu cluster formation by Mg addition is simply explained in terms of the so-called vacancy-trapping effect proposed by Kimura *et al.*[13]. Figure 4.9 shows the variations in the average number of nearest neighbor Ag or Mg atoms around one vacancy during the simulations of the Ag- and Mg-added alloys. The increased formation of Mg-Vacancy pairs in the Mg-added alloy suggests the decreased diffusion rate of Cu atoms due to the preferential vacancy trapping by Mg atoms. Such situations can be frequently observed in atom configurations during the simulation.

(b) Number density and average size of clusters

Figure 4.10 shows the variations in number density, *N*, and average size, *n*, of clusters during dynamical evolution of the Al-Cu, Ag- and Mg-added alloys simulated at 273K. The difference in the initial *N* values between the Al-Cu and the ternary alloys arises from the formation of dimer and trimer clusters containing Ag or Mg atoms which are formed by chance at the beginning of the simulation. With increasing Monte Carlo step(MCs), *N* of the Mg-added alloy increases more slowly than those of the Al-Cu and Ag-added alloys, then gradually decreases to show a higher maximum due to the competitive growth among clusters. The average size of Cu clusters is significantly smaller in the Mg-added alloy than those of the Al-Cu and Ag-added alloys. The similar simulation results are obtained in

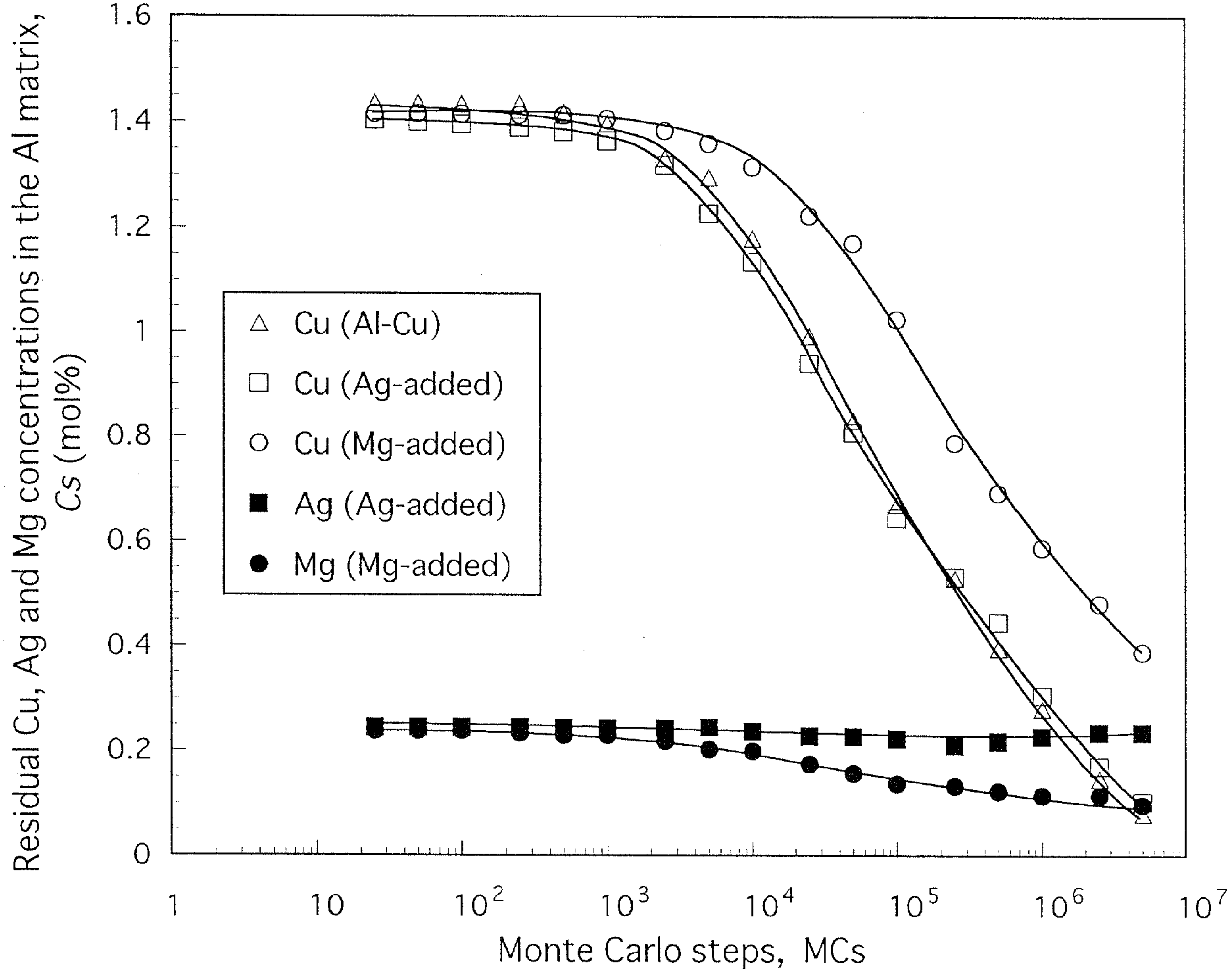

Fig.4.7 Variations in residual Cu, Ag and Mg concentrations in the Al matrix, *Cs*, with Monte Carlo steps(MCs) for Al-Cu, Ag- and Mg-added alloys simulated at 273K.

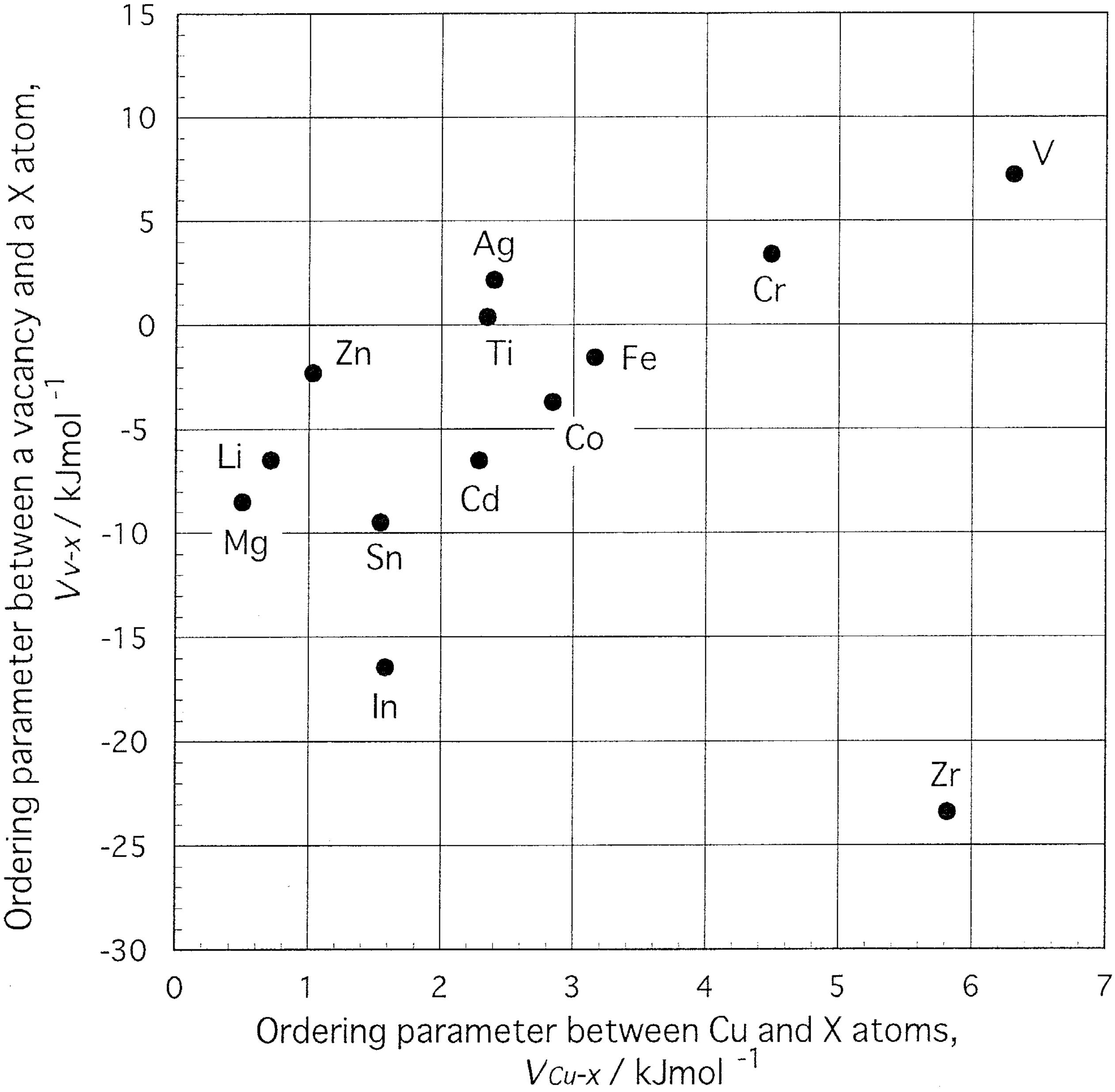

Fig.4.8 Relationships between $V_{V\text{-}X}$ and $V_{Cu\text{-}X}$ for various elemental atoms, X ($V_{V\text{-}X}$: ordering parameter between a vacancy and a X atom, $V_{Cu\text{-}X}$: ordering parameter between Cu and X atoms).

Table 4.3 Effects of additional elements in the solution state on the kinetics of GP zone formation in Al-Cu alloys.

I A	II A	III A	IV A	V A	VI A	VII A	VIII			I B	II B	III B	IV B	V B	VI B	VII B
H																
Li ● ●	Be ●											B	C	N	O	F
Na —	Mg ○ ●											Al	Si — ●	P	S	Cl
K	Ca	Sc	Ti —	V — —	Cr —	Mn	Fe —	Co —	Ni —	Cu	Zn — —	Ga —	Ge ●	As	Se	Br
Rb	Sr	Y	Zr ● ●	Nb —	Mo	Tc	Ru	Rh	Pd	Ag — —	Cd ● ●	In ● ●	Sn ● ●	Sb —	Te	I
Cs	Ba	La	Hf	Ta —	W — —	Re	Os	Ir	Pt	Au —	Hg —	Tl —	Pb — ●	Bi —	Po	At

X	: Element
Upper	: Experimental result previously reported
Lower	: Result obtained in this work

○ accelarates GP zone formation

— has little or no effect

● suppresses due to the Vacancy-trapping mechanism

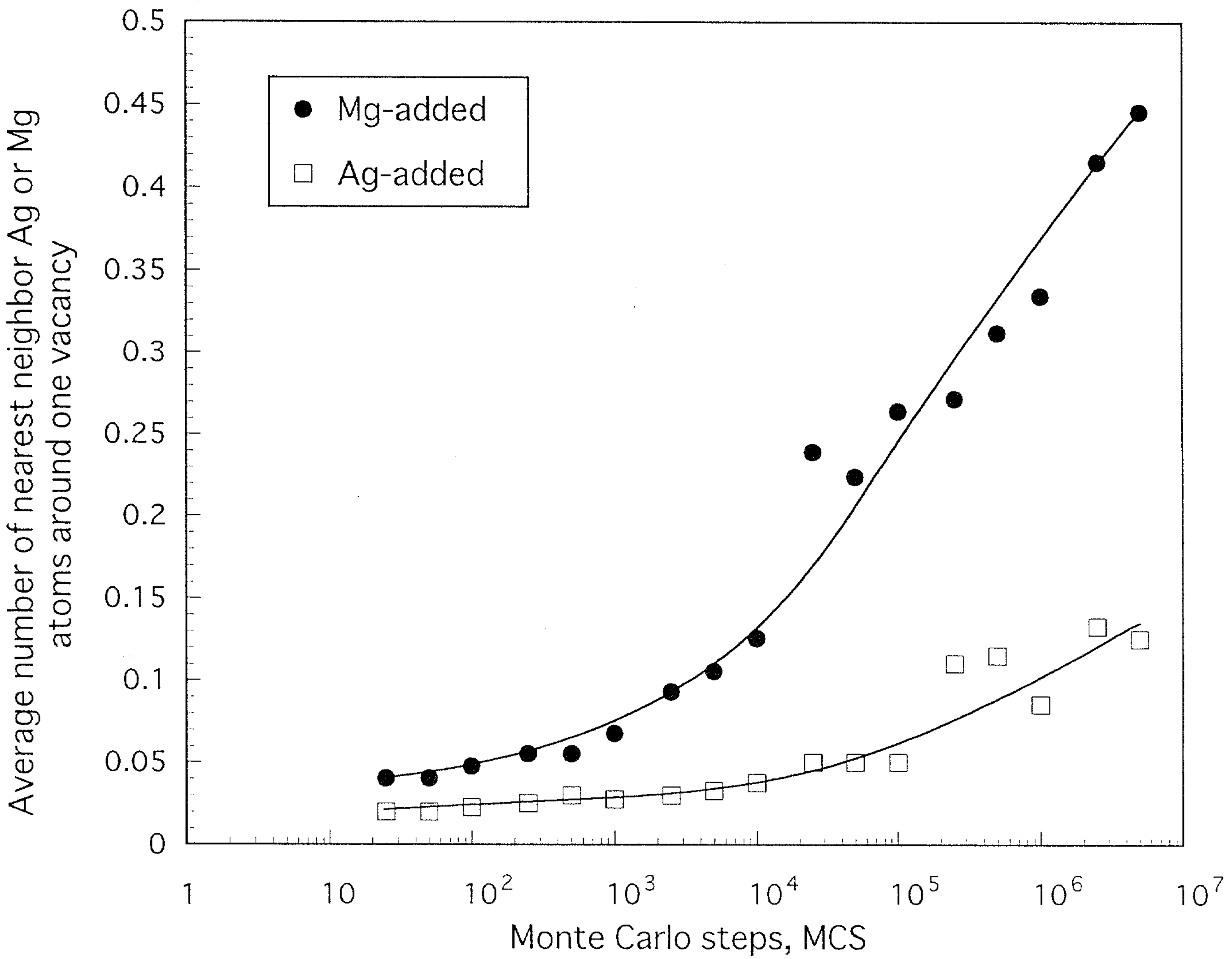

Fig.4.9 Variations in average number of nearest neighbor Ag or Mg atom around one vacancy with Monte Carlo steps for Ag- and Mg-added alloys simulated at 273K.

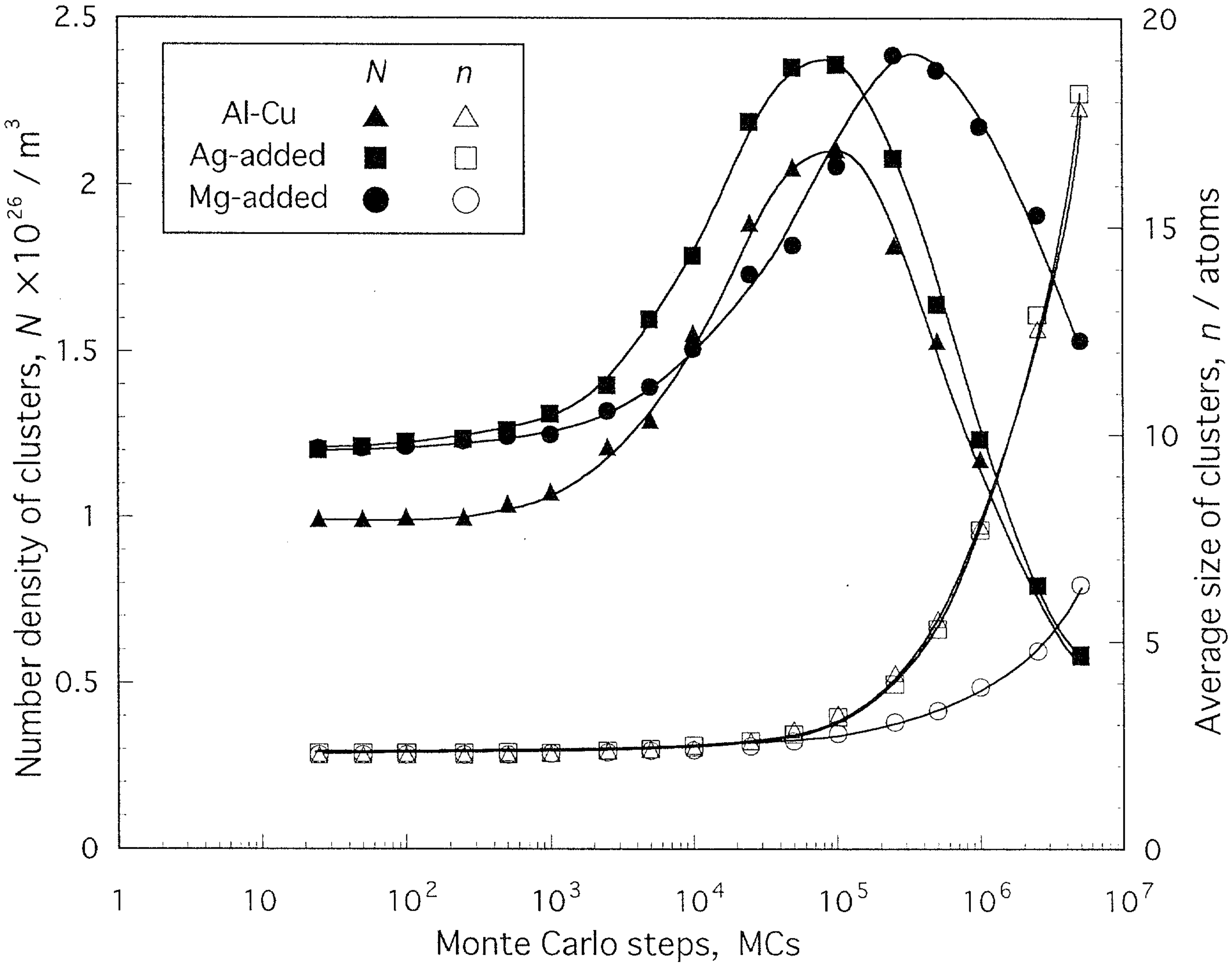

Fig.4.10 Variations in number density, *N*, and average size, *n*, of clusters with Monte Carlo steps(MCs) for Al-Cu, Ag- and Mg-added alloys simulated at 273K.

other alloys; i.e. Zn, Ti, Co, Fe and Cr have almost no effect to change the microstructure evolution of Al-Cu alloys, whereas Sn, In, Cd and Li are regarded as the elements which markedly suppress the growth rate of Cu clusters.

(c) Partitioning behavior of additional elements

As for the partitioning behavior of third additional elements, however, the Mg-added alloy alone forms the extremely increased number density of Mg-containing clusters compared with other alloys, as suggested by the higher decreasing-rate of the residual Mg concentration in Fig.4.7. This can be seen more clearly in Fig.4.11, which shows the variations in the average number of nearest neighbor Cu atoms around either one Mg atom or one Ag atom during the simulations of the Ag- and Mg-added alloys. The increased number of Mg-Cu pairs in the Mg-added alloy suggests that a small amount of Mg in Al-Cu alloys significantly affects the nucleation behavior of GP zones, for example, due to the heterogeneous nucleation effect. The combined consideration with the preferential partitioning of vacancies next to Mg atoms(Fig.4.9) results in the formation of Mg/Cu/Vacancy complexes in the Mg-added alloy. In fact, these Mg/Cu/Vacancy complexes are frequently observed during the simulation as illustrated in the solute atom distribution of the Mg-added alloy simulated at 273K for 5×10^6MCs (Fig.4.6(d)). Note that Mg atoms, indicated by red circles, have a strong tendency to coexist with Cu atoms inside clusters due to the high Cu-Mg interaction. This tendency is smaller in the Li-, Zn-, Sn- and In-added alloys and smallest in the other alloys, as suggested by ordering parameters between Cu and the elemental atoms, $V_{Cu\text{-}x}$, in Fig.4.8 (see along the horizontal axis).

4.5 Comparison between experimental and Monte Carlo simulation results

In general, changes in electrical resistivity during the GP zone formation are believed to take place by the superimposition of the increases in size and number density of zones and the decrease in residual solute concentrations in the matrix. From structural parameters obtained in the simulation, therefore, the calculated increments in electrical resistivity, $\Delta\rho_{Cal}$, can be estimated using eq.(3.13). Except for the Zn-added alloy, the changes in $\Delta\rho_{Cal}$ illustrated in Fig.4.12 are well consistent with experimentally measured changes in Fig.4.2. Although the cause of the discrepancy in the Zn-added alloy is not fully understood, one of probable reasons is a change of the function $g(n)$ due to the addition of third elements. In fact, Hiraoka *et al.*[34] reported that a scattering power of one GP zone in Al-Zn alloys is slightly changed by third additional elements. As far as the other alloys are concerned,

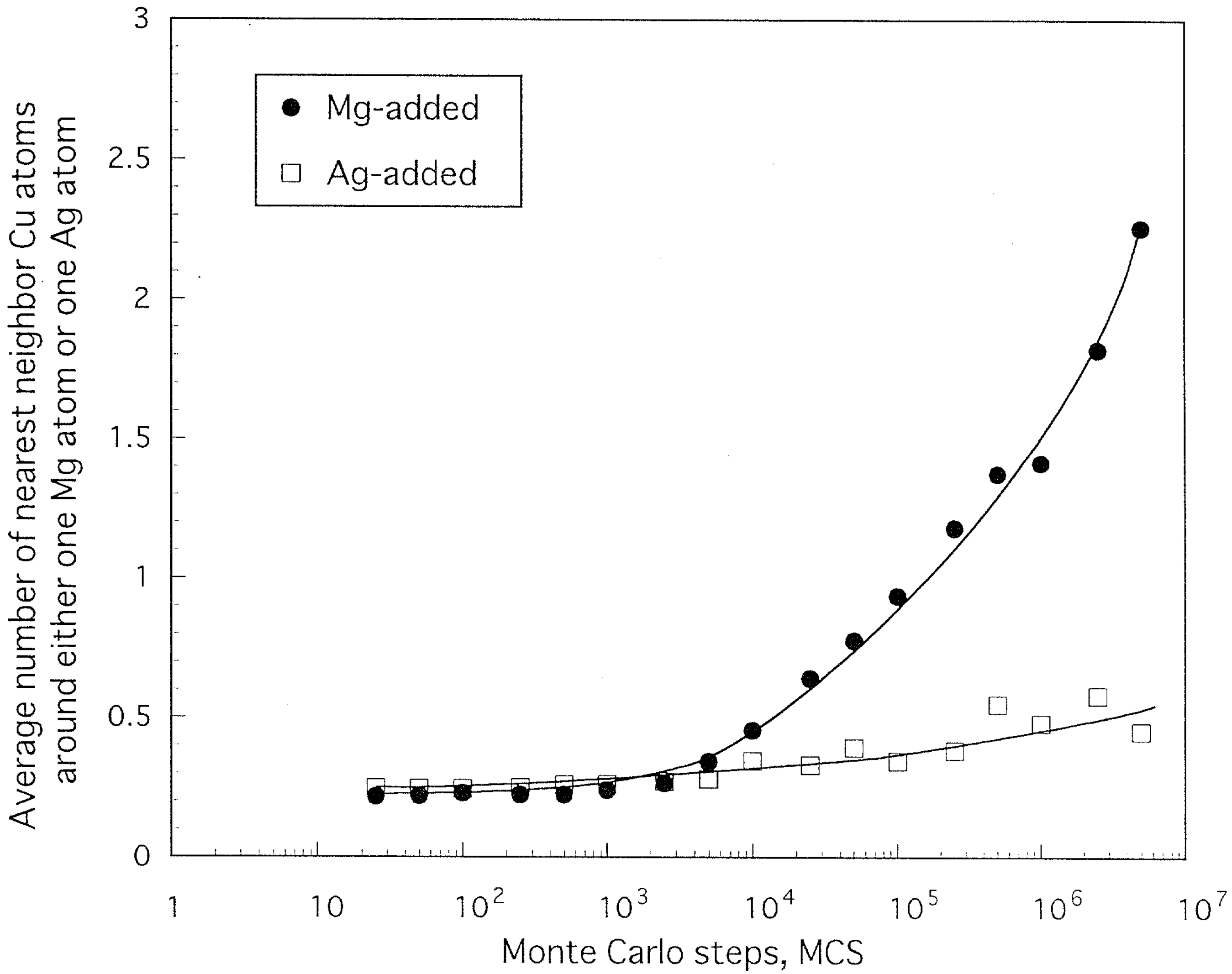

Fig.4.11 Variations in average number of nearest neighbor Cu atoms around either one Mg atom or one Ag atom with Monte Carlo steps for Ag- and Mg-added alloys simulated at 273K.

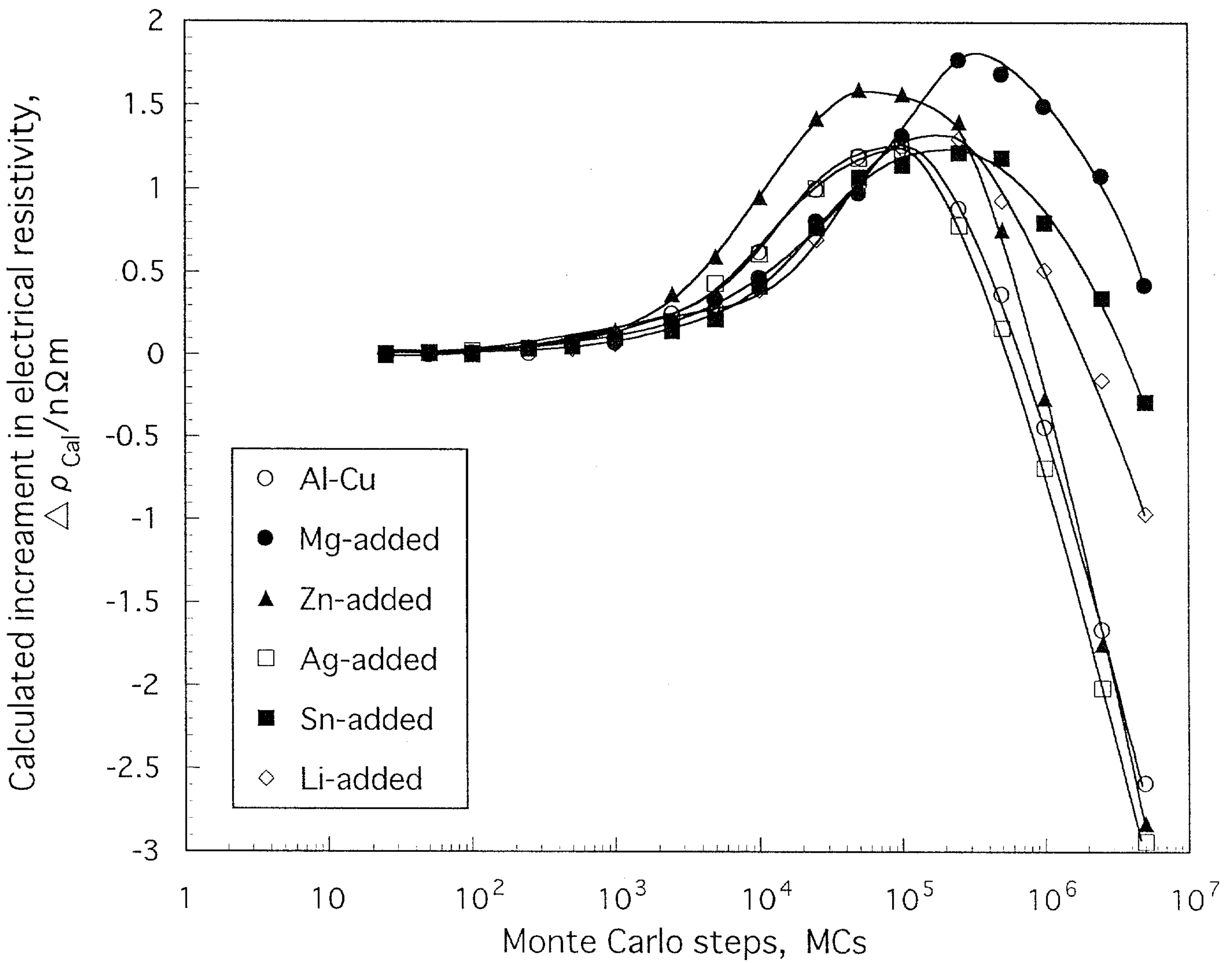

Fig.4.12 Calculated increments in electrical resistivity, $\Delta\ \rho_{Cal}$, obtained from the Monte Carlo simulation at 273K for Al-Cu, Mg-, Zn-, Ag-, Sn- and Li-added alloys.

however, the following tendencies are revealed from the simulation results obtained in this work. A small addition of Ag to Al-Cu alloys exerts no marked influence on the formation kinetics of GP zones due to no significant interaction between Ag and Cu atoms, as revealed by the similar microstructure evolution to the Al-Cu alloy. On the other hand, additions of Mg, Sn and Li markedly decrease the growth rate of GP zones because of the so-called vacancy trapping mechanism[13], resulting in a slower increase in electrical resistivity. Only in the Mg-added alloy, however, the extremely increased number density of clusters containing Mg atoms (and/or some vacancies) are formed due to the considerably high Cu-Mg interaction. This implies that a small amount of Mg in Al-Cu alloys significantly affects the nucleation behavior of GP zones, for example, due to the heterogeneous nucleation effect with the aid of Mg/Cu/Vacancy complexes. This effect is more clearly revealed in the case of Al-Cu alloys containing substantial amounts of Li as described in Chapter 6.

4.6 Conclusions

The effects of third additional elements on the formation behavior of GP zones were investigated for an Al-1.8%Cu (in mol%) alloy aged at temperatures from 278 to 373K. The elements added to the binary alloy are 0.3%Mg, 0.3%Si, 0.3%Zn, 0.3%Ag, 0.3%Li, 0.05%Zr and 0.01%Sn (in mol%). Comparisons between the quantitative kinetics determined by the electrical resistivity changes and the microstructure evolution during the Monte Carlo simulation give important information on both the macroscopic transformation behavior and the detailed formation mechanism of Cu clusters. The obtained results are as follows:

(1) Small additions of Mg and Li to Al-Cu alloys markedly retard the GP zone formation as is the well-known case of Sn. This is because that these additional atoms preferentially trap free-vacancies available for Cu diffusion to form clusters; i.e. the so-called vacancy-trapping mechanism, due to their relatively high interactions with vacancies. Such situations can be frequently observed in atom configurations during the simulation.

2) In contrast, additions of Ag and Zn exert no marked influence on the kinetics of the GP zone formation in Al-Cu alloys. This is explained by no significant interactions between these elemental atoms and Cu atoms, resulting in the similar microstructure evolution of Cu clusters to that in the binary alloy.

(3) Only in the Al-Cu alloy containing Mg, however, the extremely increased number

density of clusters containing Mg atoms (and/or some vacancies) are observed during the simulation. This implies that a small amount of Mg in Al-Cu alloys significantly affects the nucleation behavior of GP zones, for example, due to the heterogeneous nucleation effect with the aid of Mg/Cu/Vacancy complexes.

References

[1] A. Guinier: Ann. Phys., **12** (1939), 161.
[2] G.G.Preston: Phil. Mag., **26** (1938), 855.
[3] A. Guinier: Acta Cryst., **5** (1952), 121.
[4] J.M.Silcock, T.J.Heal and H.K.Hardy: J. Inst. Metals, **82** (1953-54), 239.
[5] V.Gerold: Z. Metallk., **45** (1954), 599.
[6] K.Toman: Acta Cryst., **10** (1957), 187.
[7] K.Doi: Acta Cryst., **13** (1960), 45.
[8] D.R.James and G.L.Liedl: Acta Cryst., **18** (1965), 678.
[9] X.Auvray, P.Georgopoulos and J.B.Cohen: Acta metall., **29** (1981), 1061.
[10] T.Sato and T.Takahashi: Trans. Japan Inst. Metals, **23** (1982), 461.
[11] K.Hono, T.Satoh and K.Hirano: Phil. Mag. A, **53** (1986), 495.
[12] For example, L.F.Mondolfo: *Aluminum Alloys: Structure and Properties*, BUTTER WORTHS, London, (1976), p.265.
[13] H.Kimura and R.R.Hasiguti: Acta metall., **9** (1961), 1076.
[14] S.Fujikawa, K.Hirano and Y.Baba: Bulletin of Japan Inst. Metals, **7** (1968), 495.
[15] M.Doyama: Journal of Nuclear Materials, **69&70** (1978), 350.
[16] K.Hirano: J. Japan Inst. Light Metals, **29** (1979), 249.
[17] S.Ozbilen and H.M.Flower: Acta matall., **37** (1989), 2993.
[18] K.M.Entwistle, J.H.Fell and Kang Il Koo: J. Inst. Metals, **91** (1962-63), 84.
[19] R.K.Wyss and R.E.Sanders,Jr.: Metall. Trans. A, **19A** (1988), 2523.
[20] K.Osamura, Y.Hiraoka and Y.Murakami: Phil. Mag., **28** (1973), 809.
[21] K.Osamura, N.Otsuka and Y.Murakami: Phil. Mag., **45** (1982), 583.
[22] W.A.Johnson and R.F.Mehl: Trans. AIME, **135** (1939), 416.
[23] M.Avrami: J. Chem. Phys., **7** (1939), 1103.
[24] M.Avrami: J. Chem. Phys., **8** (1940), 212.
[25] M.Avrami: J. Chem. Phys., **9** (1941), 177.
[26] T.Sato, T.Murakami, Y.Amemiya, H.Hashizume and T.Takahashi: Acta metall., **36** (1988), 1335.

[27] H.Fujita and C.Lu: Mater. Trans., JIM, **33** (1992), 892.

[28] H.Fujita and C.Lu: Mater. Trans., JIM, **33** (1992), 897.

[29] W.De Sorbo, H.N.Treaftis and D.Turnbull: Acta metall., **6** (1958), 379.

[30] D.Turnbull, H.S.Rosenbaum and H.N.Treaftis: Acta metall., **8** (1960), 277.

[31] D.Turnbull and R.L.Corima: Acta metall., **8** (1960), 747.

[32] T.J.Koppenaal and M.F.Fine: J. Appl. Phys., **32** (1961), 781.

[33] H.Kimura, R.Kimura and R.R.Hasiguti: Acta metall., **10** (1962), 607.

[34] Y.Hiraoka, K.Osamura and Y.Murakami: J. Japan Inst. Metals, **40** (1976), 1134.

Chapter 5

Microstructure Evolution of Li Atom Ordering and Kinetics of Low-Temperature Precipitation in Al-Li Alloys with Microalloying Elements

5.1 Introduction

Al-Li base alloys have been received considerable attention as a new light material in the 21st century because of their excellent combination of high specific strength and low density. These properties are of great interest particularly to aerospace, aviation, automobile and high-speed transportation industries where weight reduction is significantly important. The high strength of Al-Li alloys is primarily achieved by the precipitation of the metastable δ ' phase, which is homogeneously formed in a spherical morphology prior to the equilibrium δ (AlLi) phase. The δ ' phase has a $L1_2$-type ordered structure coherent with the Al matrix with the composition of Al_3Li. Deformation behavior of the Al-Li alloys strengthened by the δ ' phase is generally accepted in the following manners. In the under-aged condition, δ ' particles are cut by pair moving dislocations (i.e. superlattice dislocations) so that the passage of the second dislocation can compensate the increased anti-phase boundary (APB) energy formed by the passage of the first one. In the over-aged condition, on the other hand, dislocations move away by the by-pass mechanism leaving Orowan loops at the δ ' particles. These results indicate that the coherent strain and APB energies are extremely essential to improve the mechanical properties of Al-Li alloys. The additions of third elements are quite effective to change these properties, for example, as is the well-known case of the γ '/ γ misfit modification by various transition elements in Ni base superalloys. Baumann *et al.*[1] reported that small additions of Ag and Zn increase both the δ '/ α (matrix) lattice misfit and the δ ' solvus temperature because of the preferential partitioning of these elements within the δ ' phase. Sato *et al.*[2] also investigated the δ ' phase stability of the Al-Li alloys containing Ag, Au and Mg and concluded that the preferential partitioning of these additional elements inside the δ ' phase markedly affects to increase both the solvus temperature and coarsening rate of the particles. In the early stage of aging, however, little is known about the effects of additional elements to Al-Li alloys.

As for the phase decomposition sequence of Al-Li alloys, a somewhat complicated behavior is observed in supersaturated solid solutions during aging. In general, phase decompositions in quenched alloys can be divided into two categories; i.e. clustering and ordering processes. The ordering parameter V_{ij} based on a pair interaction model is usually utilized to describe which process takes place in the supersaturated solid solution. If $V_{ij}>0$, the alloy exhibits a tendency toward clustering or else (i.e. $V_{ij}<0$) toward ordering. In the case of Al-Li alloys, however, the simultaneous reaction of clustering and ordering processes has been suggested to take place. Khachaturyan *et al.*[3] made a theoretical investigation on the precipitation paths of quenched Al-Li alloys using a mean-field thermodynamic model. Their theoretical analysis predicts that disordered solid solution congruently orders, then decomposes into two ordered regions with different Li concentrations by either a secondary spinodal mechanism or a classical nucleation and growth process. As a consequence of the decomposition process, the final microstructure consisting of ordered δ' particle and the disordered matrix is achieved because Li-lean regions eventually disorder due to the instability with respect to the composition and/or the degree of order. The free energy change during the phase decomposition process is schematically illustrated in Fig.5.1. Chen *et al.*[4, 5] investigated in-situ decomposition paths of Al-Li binary alloys by simultaneous measurements of small-angle X-ray scattering (SAXS) intensities and X-ray diffraction (XRD) intensities of superlattice reflections using a synchrotron radiation. Their experimental results revealed that congruent ordering precedes decomposition because in the quite early stage of aging (e.g. 0.2s aging at 458K) only XRD {100} superlattice reflections emerged, whereas no noticeable SAXS scattering intensity could be detected. Sato *et al.*[6] directly observed uniformly developed ordered structures in the as-quenched state and ordered domains separated by disordered regions in the subsequent aging stage using high resolution electron microscopy. The proposed phase decomposition sequence by Khachaturyan *et al.*[3], therefore, appears to be sufficiently probable. The similar reactions are reported to be observable in the Fe-Al[7], Fe-Be[8, 9] and Cu-Zn[10] systems. Such simultaneous reactions of clustering and ordering processes can be interpreted by an extended pair interaction model[11, 12], in which pair interactions between second nearest neighbor atoms are taken into account in addition to those between nearest neighbor atoms. Under this model, the most stable atomic configuration becomes a mixture of ordered structures in the disordered matrix if nearest and second nearest neighbor interactions have negative and positive values, respectively. Therefore, a Monte Carlo simulation using the extended pair interaction model[11, 12] is considered to be sufficiently effective to investigate the phase decomposition behavior of Al-Li alloys containing various additional elements.

In this chapter, the effects of third additional elements on the kinetics of the low-

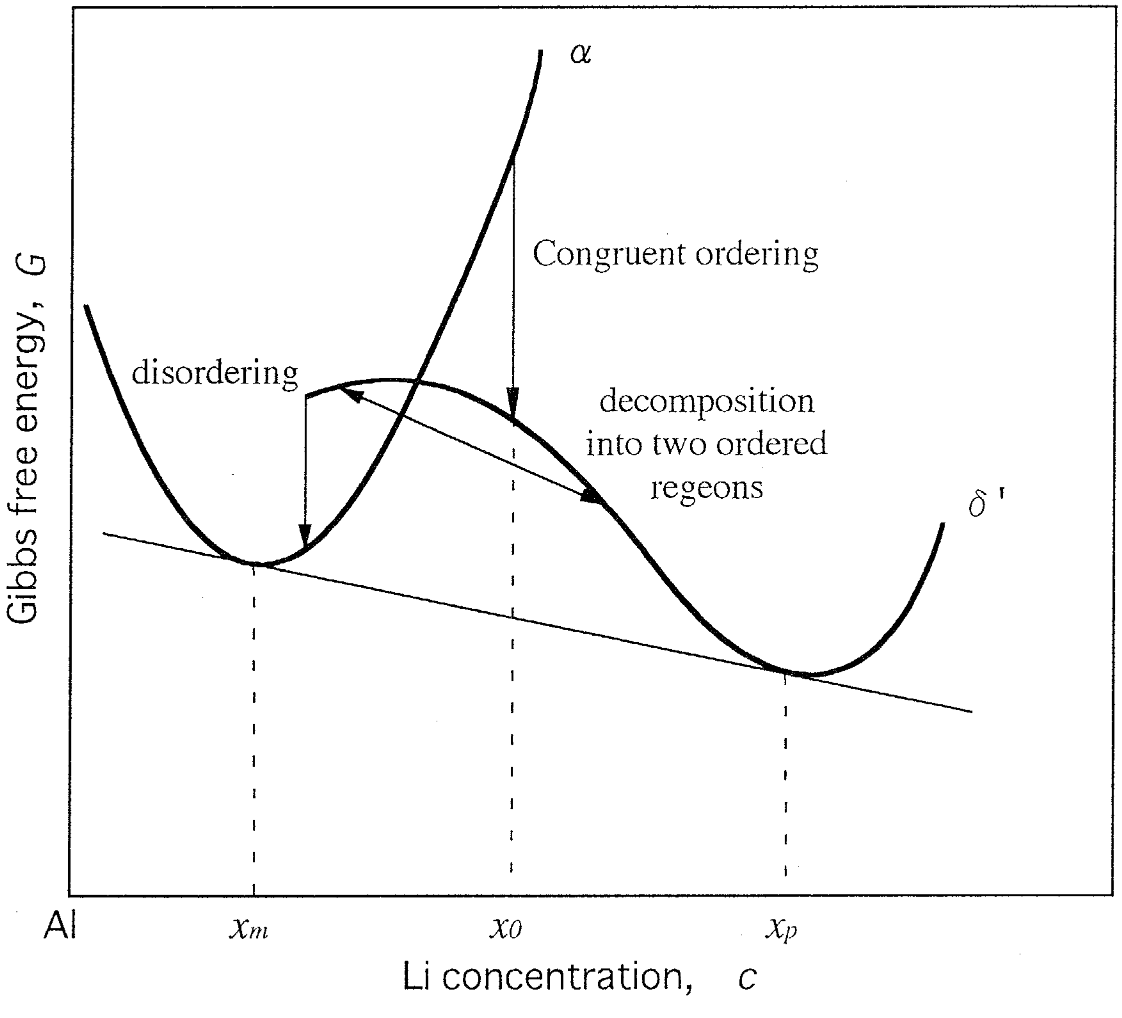

Fig.5.1 Schematic representation of the thermodynamic model in the as-quenched Al-Li system proposed by Khachaturyan *et al.* [5]. The disordered solution continuously separates the ordered δ ' phase and α phase via both congruent ordering and decomposition into two ordered regions .

temperature precipitation in an Al-5.3mol%Li alloy have been experimentally investigated in the temperature range from 278 to 373K using electrical resistivity measurement. The measured resistivity changes are well correlated with each stage of the previously reported phase decomposition sequence in Al-Li alloys. A Monte Carlo simulation, in which pair interactions between up to second nearest neighbor atoms are taken into account, was also performed to examine the microstructure evolution of ordered structures resulting in the δ ' phase. Comparisons between the quantitative kinetics determined by the resistivity changes and the microstructure evolution directly observed in the simulation can make clear the relationship between the macroscopic transformation kinetics and the microstructural formation mechanism of the δ ' phase in Al-Li alloys containing various additional elements.

5.2 Experimental procedures

The alloys utilized in this chapter were prepared from high-purity elemental ingots; i.e. 99.99%Al, 99.9%Mg, 99.9%Ag and 99.999%Si, and master alloys; i.e. Al-18.5%Li and Al-33.3%Cu (in mass%). The melting of these alloys was carried out under Ar gas atmosphere followed by permanent mould casting. The chemical compositions of the alloys are listed in Table 5.1. The concentrations of impurity elements such as Fe and Ti are lower than 0.01mass% in all alloys. The elements added to an Al-(7.8-9.5)%Li alloy are 0.25%Cu, 0.25%Mg, 0.25%Ag and 0.3%Si (in mol%). For simplicity, an alloy containing a small amount of additional element, x, is designated as x-added alloy in this chapter.

All the ingots were homogenized by two steps at temperatures in Table 5.2 and fabricated to 1.6mm-thick sheets through hot- and cold-rolling. Solution treatments were carried out in a salt bath at 793K followed by water quenching at ~298K. For Al-Li base alloys, various solution-treatment times were applied in order to adjust Li concentrations in the matrix because the significant difference in residual Li concentrations is inevitably induced among the alloys during the above preparation process. The success of such the adjustment treatment can be quantitatively verified from as-quenched values of the electrical resistivity by assuming that the concentrations of third additional elements remain unchanged through the fabrication process as those of the ingots in Table 5.1. This treatment is quite effective in investigating the true effect of third additional elements in Al-Li alloys containing equivalent Li concentrations. The subsequent aging treatments were carried out at temperatures from 278 to 473K for various aging times. In this work, the room temperature designated as RT always stands for ~298K. The above fabrication process is shown in

Table 5.1 Chemical compositions of the alloys utilized in this chapter (mol%).

Alloys	Li	Cu	Mg	Ag	Si	Al
Al-Li	7.87	—	—	—	—	bal.
Cu-added	8.58	0.235	—	—	—	bal.
Mg-added	9.50	—	0.289	—	—	bal.
Ag-added	8.00	—	—	0.261	—	bal.
Si-added	8.73	—	—	—	0.332	bal.

Table 5.2 Conditions of homogenization treatment applied to each alloy.

Alloys	Homogenization Step 1	Homogenization Step 2
Al-Li	773K, 172.8ks	—
Cu-added	778K, 86.4ks	793K, 86.4ks
Mg-added	778K, 86.4ks	793K, 86.4ks
Ag-added	778K, 86.4ks	793K, 86.4ks
Si-added	793K, 172.8ks	848K, 86.4ks

Fig.2.1. The experiments in this chapter; i.e. electrical resistivity measurement and transmission electron microscopy, were made in the same manner described in Chapter 2.

5.3 Effects of microalloying elements

5.3.1 Transmission electron micrographs

As a typical example, Fig.5.2 shows the dark field TEM micrographs showing the well-developed δ' phase for the Al-Li, Mg- and Ag-added alloys aged at 473K for 345.6ks. In all alloys, spherical particles with the average size of ~30nm are observed distributing homogeneously throughout the Al matrix. Some δ' particles are observed as if they are in contact with each other, however, these particles are probably separated toward the *Z* direction (thickness direction) of the specimen. Although the change in the precipitate number density between the three alloys may indicate a somewhat effect of small additional Mg or Ag, it is impossible to discuss the tendency in detail because of a scatter of the obtained TEM microstructures.

5.3.2 Electrical resistivity changes

In order to verify whether the adjustment of Li concentrations among the investigated alloys is achieved or not, as-quenched values of the electrical resistivity, ρ_0, are quantitatively estimated by assuming that the concentrations of third additional elements remain unchanged through the fabrication process as those of the ingots in Table 5.1. Table 5.3 shows both values of experimentally measured ρ_0 and the corresponding residual Li concentration, *Cs*, in the as-quenched Al-Li, Cu-, Mg-, Ag- and Si-added alloys. The contributions to electrical resistivity by 1mol% residual solute atoms in Al are adopted to be previously reported values in Table 3.8. By adjusting solution-treatment times, almost identical values of *Cs* are obtained around 5.3mol% among all alloys. This adjustment treatment, therefore, is quite effective in investigating the true effect of third additional elements in the Al-Li alloys containing equivalent Li concentrations. Figure 5.3 illustrates the increments in electrical resistivity from as-quenched values during aging at 278K for the Al-Li, Cu-, Mg-, Ag- and Si-added alloys. From just after quenching all alloys display a two-stage increase in ρ without any incubation time due to the rapid formation of low-temperature precipitates in Al-Li alloys, as previously reported at aging temperatures below 383K[6, 13]. This two-stage increase suggests that several structural changes occur during phase decomposition in Al-Li alloys. As for the effects of third additional elements, furthermore, the Mg-added alloy alone reveals a tendency to retard the decomposition rate of Al-Li

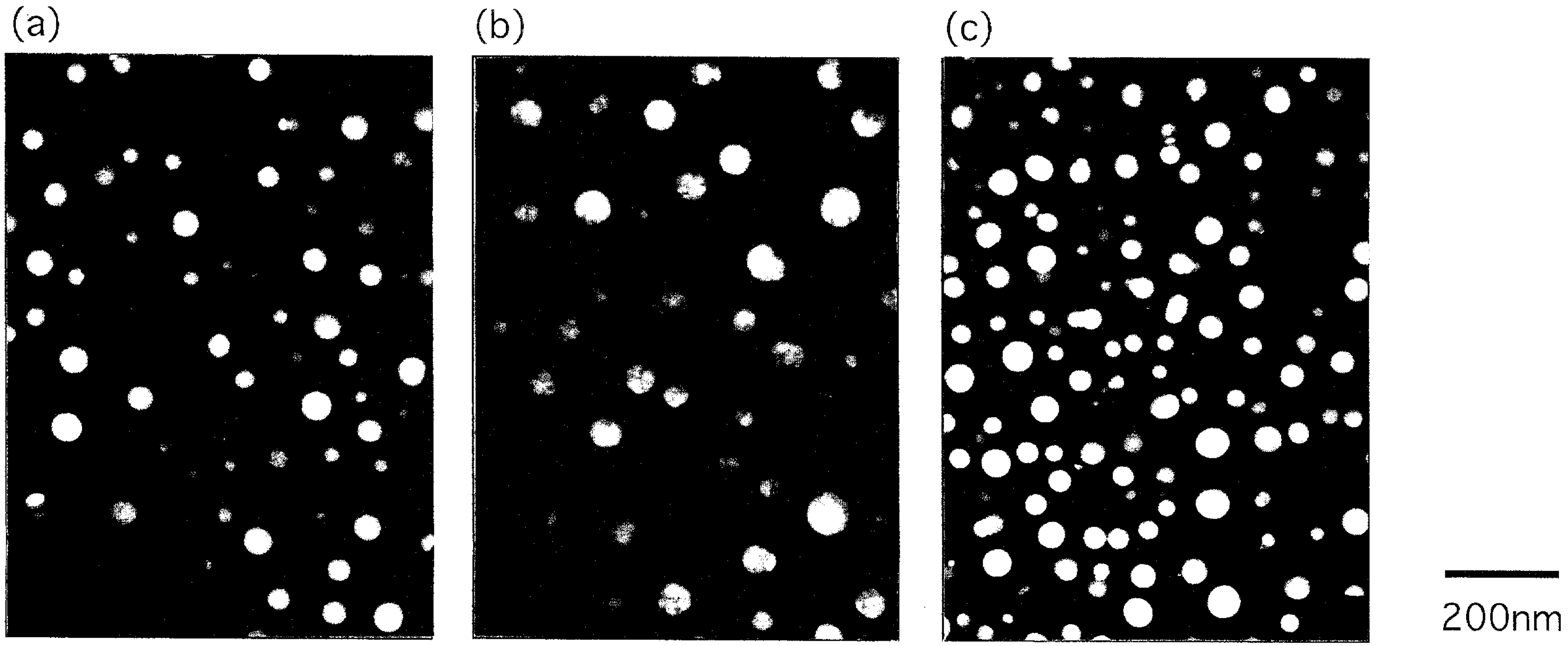

Fig.5.2 Dark field TEM micrographs for Al-Li(a), Mg-added(b) and Ag-added(c) alloys aged at 473K for 346ks.

Table 5.3 As-quenched values of electrical resistivity , ρ_0, and corresponding Li concentration, *Cs* , for each alloy.

Alloys	Subsequent aging temperature, *Ta* / K	As-quenched electrical resistivity, ρ_0 / nΩm	Corresponding Li concentration, *Cs* / mol%
Al-Li	278	47.75	5.45
	323	46.4	5.29
	373	47.21	5.38
Cu-added	278	49.66	5.45
	323	47.13	5.15
	373	48.01	5.25
Mg-added	278	49.83	5.54
	323	48.77	5.41
	373	47.58	5.27
Ag-added	278	50.71	5.38
	323	48.62	5.13
	373	50.98	5.42
Si-added	278	49.46	5.39
	323	47.51	5.15
	373	48.71	5.30

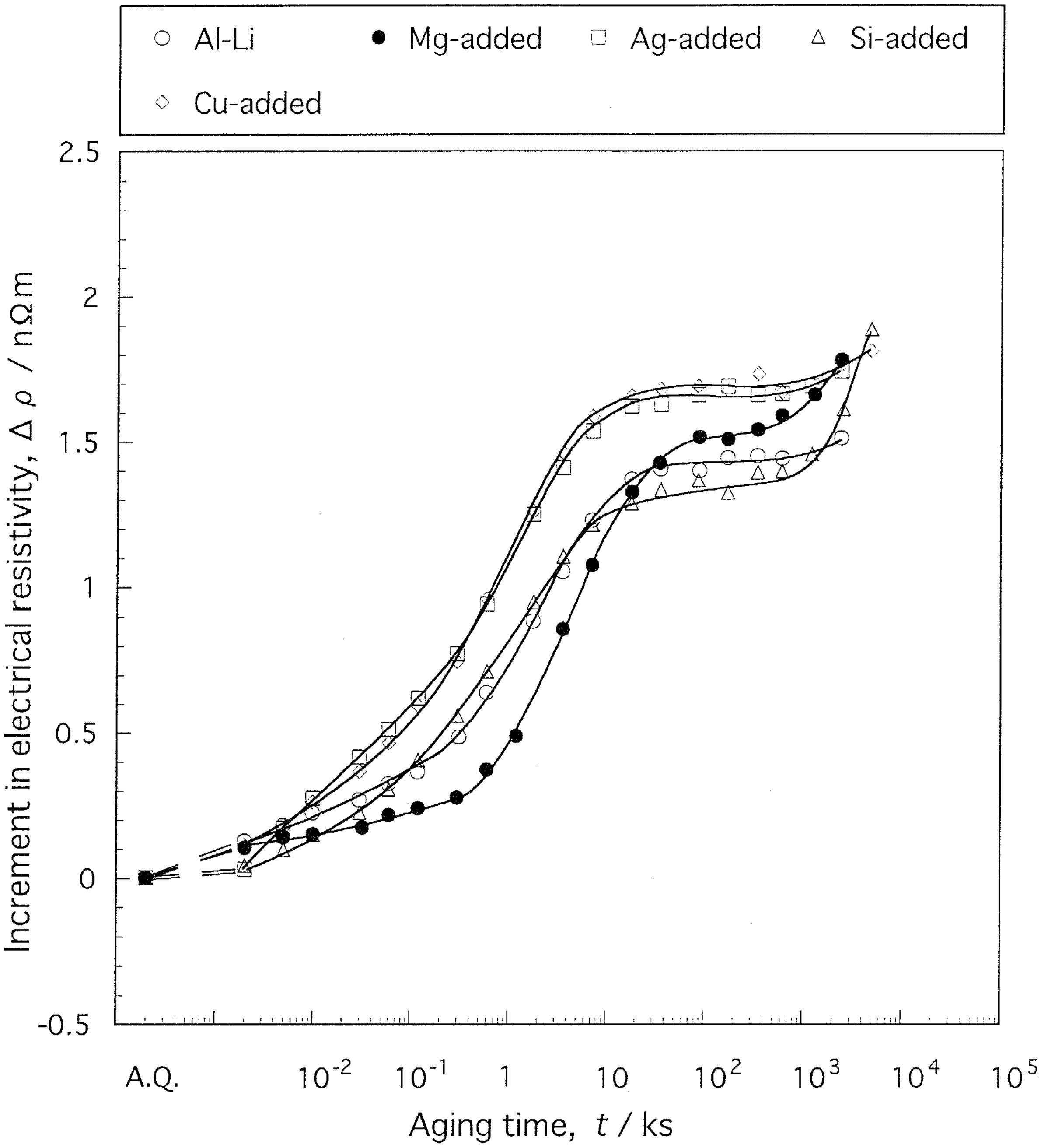

Fig.5.3 Increments in electrical resistivity from as-quenched values during aging at 278K for the Al-Li alloys containing various additional elements.

alloys, as suggested in the early stage of aging in Fig.5.3. The similar result is obtained for other aging temperatures lower than 373K.

5.3.3 Quantitative analysis of phase decomposition kinetics

The detailed quantitative analysis of the phase decomposition kinetics in Al-Li alloys containing various additional elements was made using Johnson-Mehl-Avrami equation in eq.(4.1). Figure 5.4 illustrates the variations in $\ln\ln[1/(1-y)]$ with $\ln t$ derived from the electrical resistivity changes at 278K in Fig.5.3. All the investigated alloys obviously possess two separated stages, which are represented by two straight lines having different tangents n, during the electrical resistivity changes. These stages are well associated with the phase decomposition sequence in Al-Li alloys proposed by Khachaturyan *et al.* [3]; i.e.

① Decomposition stage of uniformly ordered structures into two ordered phases: i.e. Li-rich and Li-lean phases, by either a secondary spinodal mechanism or a classical nucleation and growth process

and

② Simultaneous stage of both the decomposition of the Li-rich phase into the δ' phase, in which the composition and the degree of order have increased, and the subsequent growth of the δ' particles,

respectively. In fact, at the corresponding aging time to each stage, Sato *et al.* [6] directly observed uniformly developed ordered structures and the subsequent ordered domains using high resolution electron microscopy. These precipitates are generally regarded as precursory structures of the δ' phase, resulting in the two-stage increase in electrical resistivity changes. It is further shown in Fig.5.4 that a small amount of Mg significantly suppresses the formation of low-temperature precipitates in Al-Li alloys, as revealed by a smaller rate constant k obtained from its intercept on the $\ln\ln[1/(1-y)]$ axis. Therefore, the Mg-added alloy alone can exhibit a stage of congruently ordering throughout the Al matrix as represented by a broken straight line in Fig.5.4. The first experimental detection of the congruent ordering stage is entirely attributed to the slower phase decomposition rate caused by a relatively low Li concentration(~5.3mol%), low aging temperature(278K) and small addition of Mg. Si also has a similar but smaller effect compared with Mg, whereas Cu and Ag exert almost no influence on the decomposition rate of Al-Li alloys.

In the same manner as Al-Cu alloys in Chapter 4, rate constants k for the first increasing stage are Arrhenius-plotted against reciprocal aging temperatures, $1/T$, in order to evaluate apparent activation energies, Q^*, for the low-temperature precipitation in the investigated Al-Li base alloys. The slopes of the corresponding straight lines in Fig.5.5

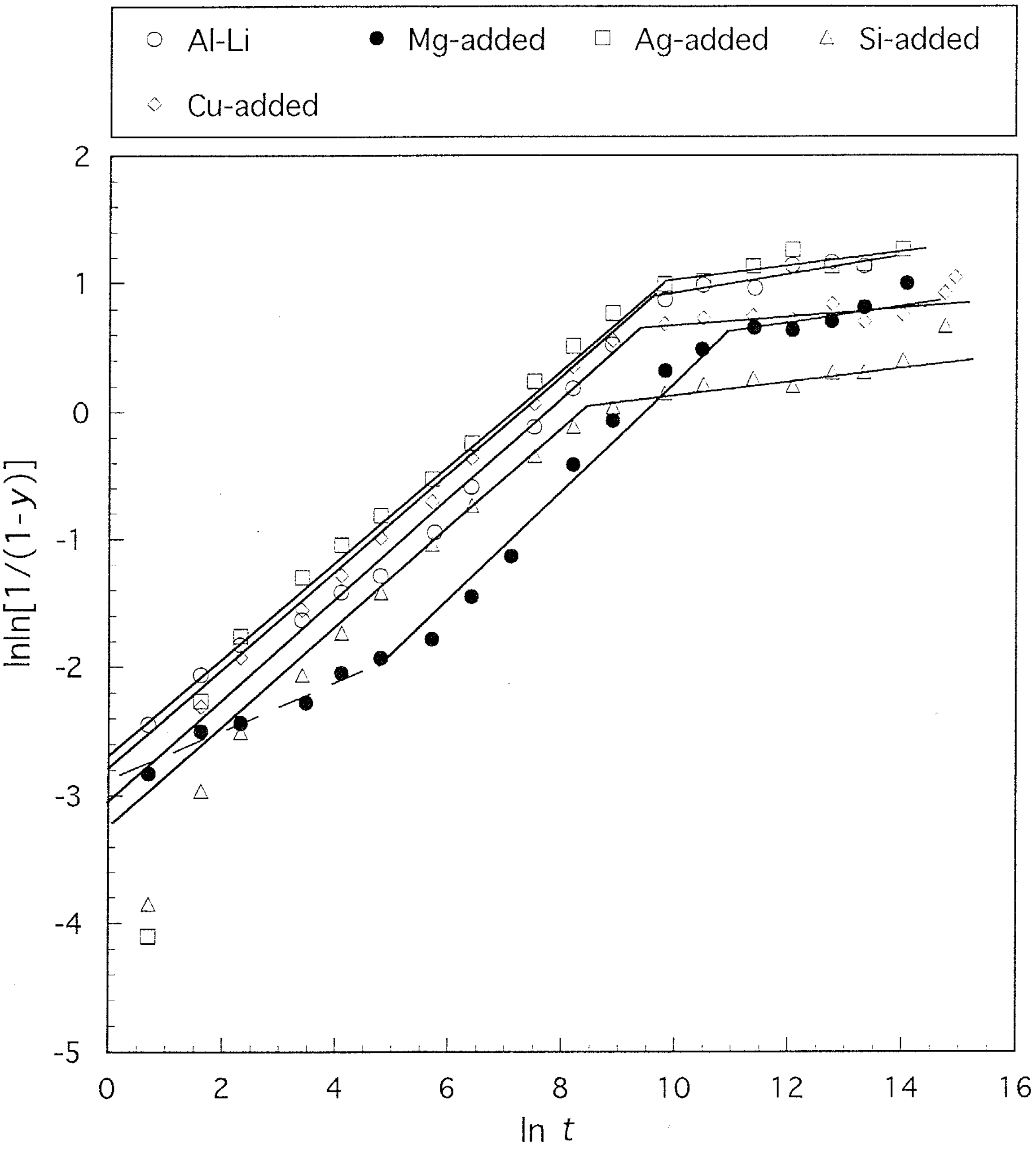

Fig.5.4 Variations in lnln[1/(1- y)] with ln t for the Al-Li alloys containing various additional elements aged at 278K.

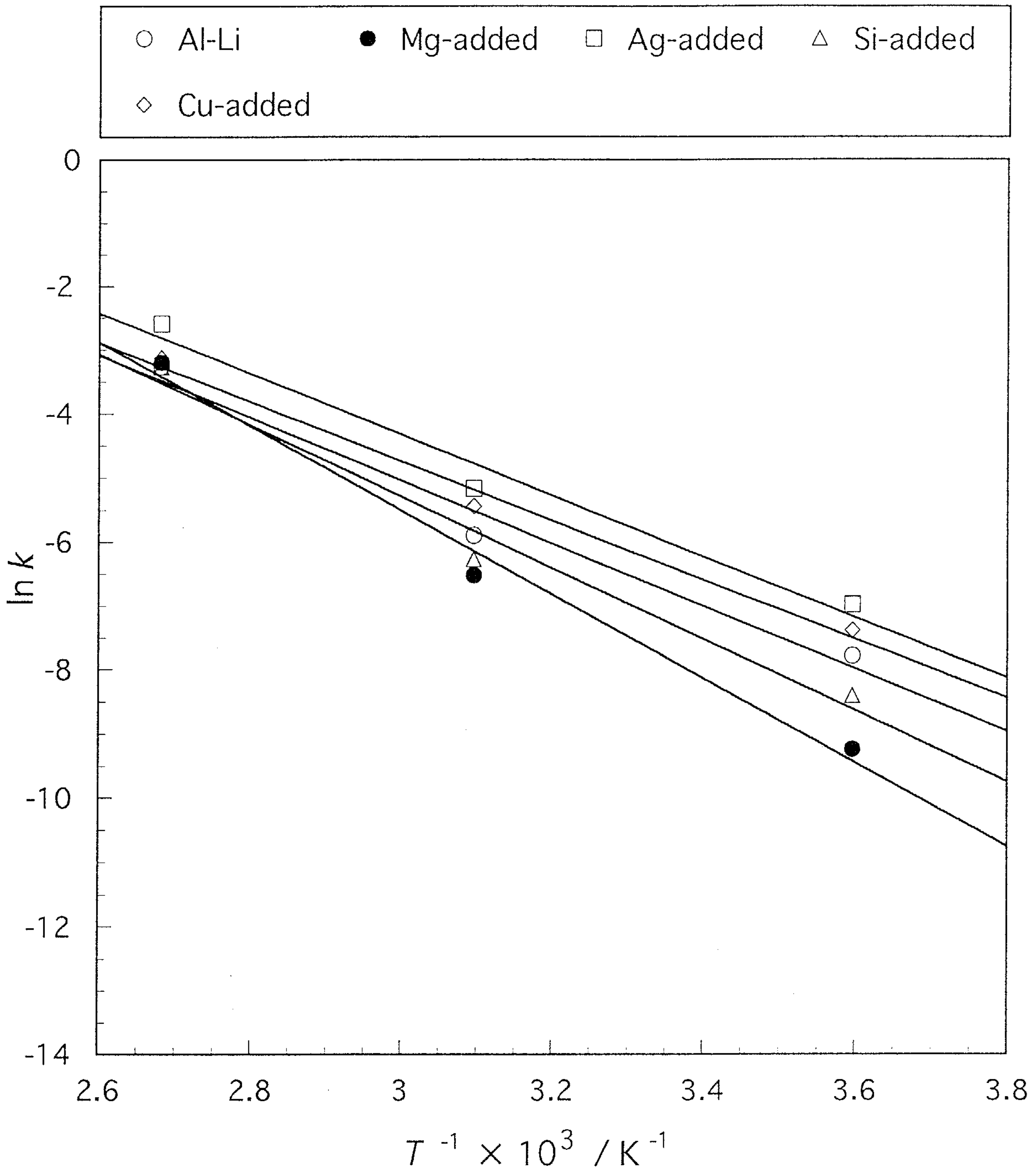

Fig.5.5 Arrhenius plots of ln *k* values against reciprocal aging temperatures for the Al-Li alloys containing various additional elements.

give the values of Q^* to be ~40kJ/mol for the Al-Li, Cu- and Ag-added alloys, 46.2kJ/mol for the Si-added alloy and 54.5kJ/mol for the Mg-added alloy, respectively. These values are extremely smaller than previously reported activation energies in the early stage of low-temperature aging; e.g. 67.5kJ/mol for an Al-6.25mol%Li alloy[13] and 67.3kJ/mol (0.7eV) for an Al-6.72mol%Li alloy[14]. This significant discrepancy is presumably attributed to the difference in the Li concentrations between the alloys utilized in this work (i.e. Al-5.3mol%Li) and in the previously performed studies[13, 14]. In fact, Shaiu *et al.*[4] pointed out a fairly strong compositional dependence of the activation energies because activation energies for the growth of the δ' phase were assessed to be 103.5kJ/mol(21.5kcal/mol) for an Al-7mol%Li alloy and 143.0kJ/mol (29.7kcal/mol) for an Al-12mol%Li alloy. From the above estimated activation energies, however, it can be qualitatively concluded that a small addition of Mg or Si retards the formation rate of low-temperature precipitates in Al-Li alloys.

5.4. Simulated microstructures

5.4.1 Derivation method of parameters

As for the simulation of ordering processes, both nearest and second nearest neighbor interactions are taken into account for the calculation of ΔE values, unlike the case of the simulation of clustering processes in Chapter 4. In general, phase decompositions of quenched alloys can be divided into two categories; i.e. clustering and ordering processes. The ordering parameter V_{ij} based on a pair interaction model,

$$V_{ij} = \varepsilon_{ij} - (\varepsilon_{ii} + \varepsilon_{jj})/2 \tag{5.1}$$

is usually utilized to describe which process occurs in the supersaturated solid solution. If $V_{ij}>0$ the alloy exhibits a tendency toward clustering or if $V_{ij}<0$ that toward ordering. Here, ε_{ij}, ε_{ii} and ε_{jj} are pair interactions between different atom species and same atom species derived in Chapter 3. In the case of Al-Li alloys, however, the simultaneous reaction of clustering and ordering processes is reported to take place. Ino[12] took into account two types of pair interactions with opposite signs between nearest and second nearest neighbor atoms,

$$\begin{aligned} V_{ij}^1 &= \varepsilon_{ij}^1 - (\varepsilon_{ii}^1 + \varepsilon_{jj}^1)/2 < 0 \\ V_{ij}^2 &= \varepsilon_{ij}^2 - (\varepsilon_{ii}^2 + \varepsilon_{jj}^2)/2 > 0 \end{aligned} \tag{5.2}$$

in order to explain microstructures consisting of both B2-type ordered regions and compositional modulated regions observed in an Fe-23mol%Be alloy[9]. The negative nearest neighbor interaction, V_{ij}^1, contributes in forming the ordered structures, whereas the positive second nearest neighbor interaction, V_{ij}^{2}, contributes in decomposing into two regions of varying Be concentrations. The extended pair interaction model[11, 12], therefore, appears to be applicable enough to the phase decomposition of Al-Li alloys. In this work, the nearest neighbor interaction between Al and Li atoms was estimated from the heat of solution, ΔH^{0}, by Miedema's semi-empirical formula[15] together with the cohesive energies of pure metals. Figure 5.6 shows ordering parameters between nearest neighbor Al and j atoms, $V_{Al\text{-}j}^{1}$, against those between nearest neighbor j atoms, $V_{j\text{-}j}^{1}$. Here, the values of $V_{Al\text{-}j}^{1}$ are calculated from

$$V_{Al-j}^{1} = (E_{Coh}^{Al} + E_{Coh}^{j} + \Delta H^{0}) / z \qquad (5.3)$$

because the following equation can be assumed when 1mol% solute elemental atoms, j , are substantially solved in a solvent, i, at infinite dilution;

$$(z_i / 2)\varepsilon_{ii} + (z_j / 2)\varepsilon_{jj} = z_{ij}\varepsilon_{ij} - \Delta H^{0}. \qquad (5.4)$$

The straight line ($V_{Al\text{-}j}^{1}=0$) in Fig.5.6, at which the state of supersaturated solid solutions is most stable, divides all elements j into two categories; i.e. the elements forming ~100%j atom clusters in Al ($V_{Al\text{-}j}^{1}>0$) and the elements having intermetallic compounds with Al ($V_{Al\text{-}j}^{1}<0$). It should be emphasized that this classification completely corresponds to actual equilibrium phase diagrams for Al-j binary alloys. The utilized simulation parameters for Al-Li alloys containing various third additional elements are summarized in Table 5.4. Note that only parameter between nearest neighbor Al and Li atoms has a negative value of -1.17kJ/mol, whereas other ones using a regular solution approximation are positive. This set of parameters for nearest and second nearest neighbor Al and Li atoms is quite close to that for phase diagram calculation of the Al-Li binary system using the cluster variation method (CVM)[16, 17]; i.e. $V_{Al\text{-}Li}^{1}$=-1.75kJ/mol (-210k_B) and $V_{Al\text{-}Li}^{2}$=0.873kJ/mol (105k_B) (k_B is Boltzman's constant). Therefore, the utilized simulation parameters in this work; $V_{Al\text{-}Li}^{1}$=-1.17kJ/mol and $V_{Al\text{-}Li}^{2}$=0.669kJ/mol, are sufficiently reasonable to describe the phase decomposition of Al-Li alloys.

5.4.2. Precipitate morphologies

Figure 5.7(a)-(c) illustrates atom configurations on consecutive three layers normal to the [001] direction in the Al-Li alloy simulated at 273K for 5×10^{6}MCs. Unlike the case of Al-Cu alloys in Chapter 3, L1$_2$-type ordered structures are formed throughout the Al matrix, indicated by yellow circles, with a high number density of the precipitates. The ordered structures are composed of alternately arranged Li atoms, indicated by purple circles, along the [100] and [010] directions on one (001) layer and sandwiched between

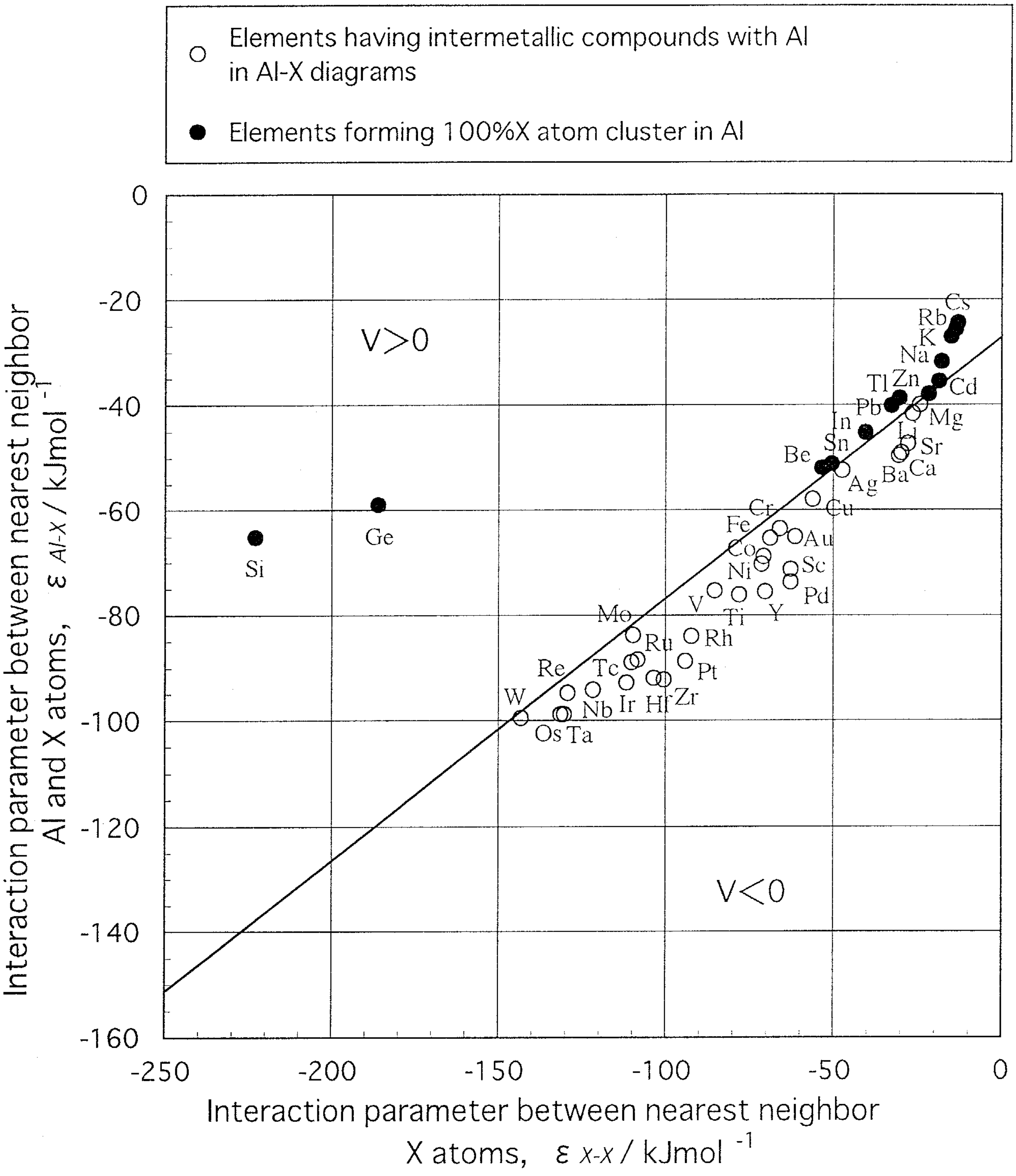

Fig.5.6 Relationships between ε_{Al-X} and ε_{X-X} for various elemental atoms, X. ε_{Al-X} and ε_{X-X} represent estimated interaction parameters between nearest neighbor Al-X atoms and X-X atoms, respectively.

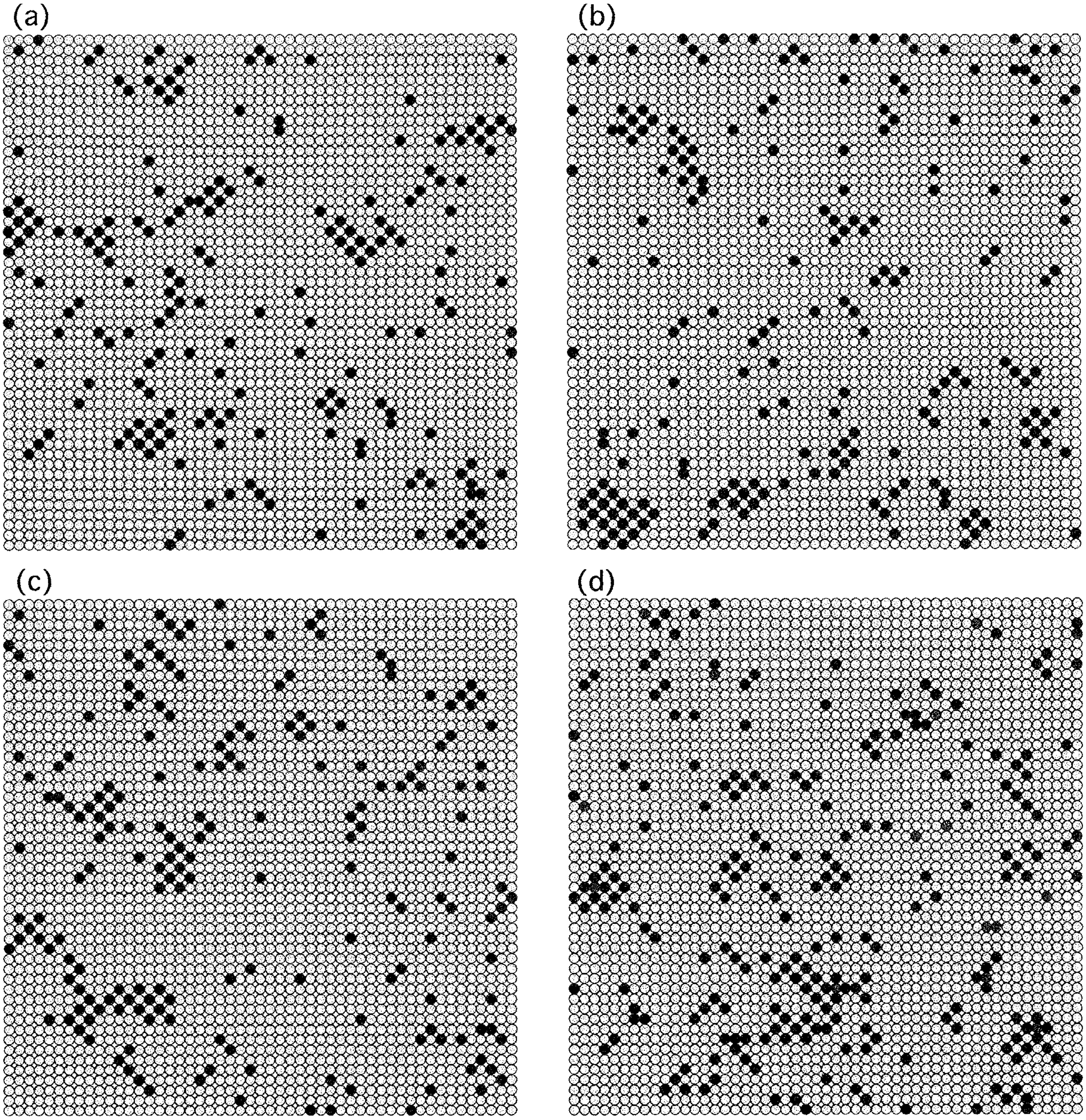

Fig.5.7 Atom configurations after 273K simulation for 5×10^{6}MCs both on consecutive three atom layers normal to the [001] direction of Al-Li alloy(a)-(c) and on one (001) plane of Ag-added alloy(d). The yellow, purple and red circles represent Al, Li and Ag atoms, respectively.

the regions consisting of only Al atoms on its upper and lower layers. The morphology of the ordered structures are almost close to spherical, which is well consistent with that of the δ ' phase observed in Al-Li alloys. As for the simulation of Al-Li alloys, therefore, the simplified simulation model by ignoring elastic effects of precipitates is sufficiently reasonable because the difference in lattice parameters between the fcc Al matrix (a=0.40496nm) and the δ ' phase(a=0.401-0.4038nm) is quite small.

5.4.3. Variations in structural parameters

(a) Short-range order parameters

In the case of the phase decomposition with ordering, the degree of order as well as the composition also changes during aging. In this work, the degree of short-range order (SRO) was quantitatively estimated from the neighborhood relationship around atoms. In general, the Warren-Cowley SRO parameter for i th neighbor, s_i, in an A-B binary alloy is defined as follows[18, 19];

$$s_i = 1 - \left(P_i^{AB} / c_B\right) \qquad (5.5)$$

where P_i^{AB} and c_B denote both the conditional probability of finding B atoms at ith neighbor positions when there is an A atom at the origin and the atomic fraction of B atoms in the alloy. If A and B atoms are completely ordered in the alloy, s_i is identically unity, whereas

Table 5.4 Ordering parameters utilized in the simulation of Al-Li alloys containing various third additional elements, X (in kJ/mol). The values in upper and lower columns represent ones between nearest and second nearest neighbor atoms, respectively.

		Third additional elements, X							
		Li	Mg	Cu	Zn	Ag	Cd	Au	In
Al	$V_{Al\text{-}X}{}^{1}$	-1.17	1.18	2.20	0.992	1.29	4.34	4.74	4.88
	$V_{Al\text{-}X}{}^{2}$	0.669	0.516	0.963	0.434	0.564	1.90	2.07	2.14
Li	$V_{Li\text{-}X}{}^{1}$	—	1.32	0.790	1.30	0.814	0.867	1.49	1.95
	$V_{Li\text{-}X}{}^{2}$	—	0.578	0.346	0.569	0.356	0.379	0.652	0.853
Vacancy	$V_{V\text{-}X}$	-6.50	-8.50	0.860	-2.29	2.16	-6.53	-2.80	-16.4
						V_{iv}			

the case of s_i =0 represents the statistical arrangement of these atoms. In this work, the SRO parameters up to the second nearest neighbors are followed during dynamical evolution for the Al-Li alloy simulated at 273K as illustrated in Fig.5.8. It is seen that s_1 monotonously decreases, which means that incidentally formed nearest neighbor Li pairs rapidly dissolve, whereas s_2 obviously displays a two-stage increase; i.e. early rapid increasing stage and the subsequent saturated stage. These stages presumably correspond to both the decomposition stage of uniformly ordered structures into two ordered regions and the subsequent growth stage of Li-rich regions, respectively. This classification is in agreement with experimental results of electrical resistivity changes in Section 5.3.3. Under this simulation model, unfortunately, the stage of congruent ordering could not be reproduced.

(b) Residual solute concentration in the matrix

As a typical example of the effects of third additional elements, Fig.5.9 shows the variations in residual solute concentrations in the Al matrix, *Cs*, during dynamical evolution for the Al-Li, Cu- and Mg-added alloys simulated at 273K. Although the incidental formation of clusters containing more than seven solute atoms slightly decreases the initial solute concentrations, net Li concentrations are almost identical in the three alloys. With increasing Monte Carlo step(MCs), however, the Cu-added alloy displays a monotonous decrease in the residual Li concentration at the same rate as the Al-Li alloy, whereas the Mg-added alloy exhibits an obvious retardation of Li atom segregation. The similar simulation results are obtained for other alloys; i.e. Ag, Zn and Au are classified in the former group, whereas Cd and In in the latter one. This classification is entirely ascribed to the utilized ordering parameters with a vacancy, $V_{v\text{-}x}$, as suggested along the vertical axis in Fig.5.10. Table 5.5 summarizes the comparison between experimental results obtained from electrical resistivity measurement and theoretical ones based on the Monte Carlo simulation. Not only good agreement between them but also first prediction for previously never reported elements is a most important result obtained in the present thesis. The pronounced retardation of the low-temperature precipitation in Al-Li alloys by Mg, Cd and In additions is simply explained in terms of the decreased diffusion rate of Li atoms due to the preferential vacancy trapping by these additional atoms. Such situations can be frequently observed in atom configurations during the simulation. Even in Al-Li alloys, therefore, Mg, Cd and In are regarded as the elements showing the vacancy-trapping effect[20], as well as the case of Al-Cu alloys containing these elements in Chapter 4.

(c) Number density and average size of ordered structures

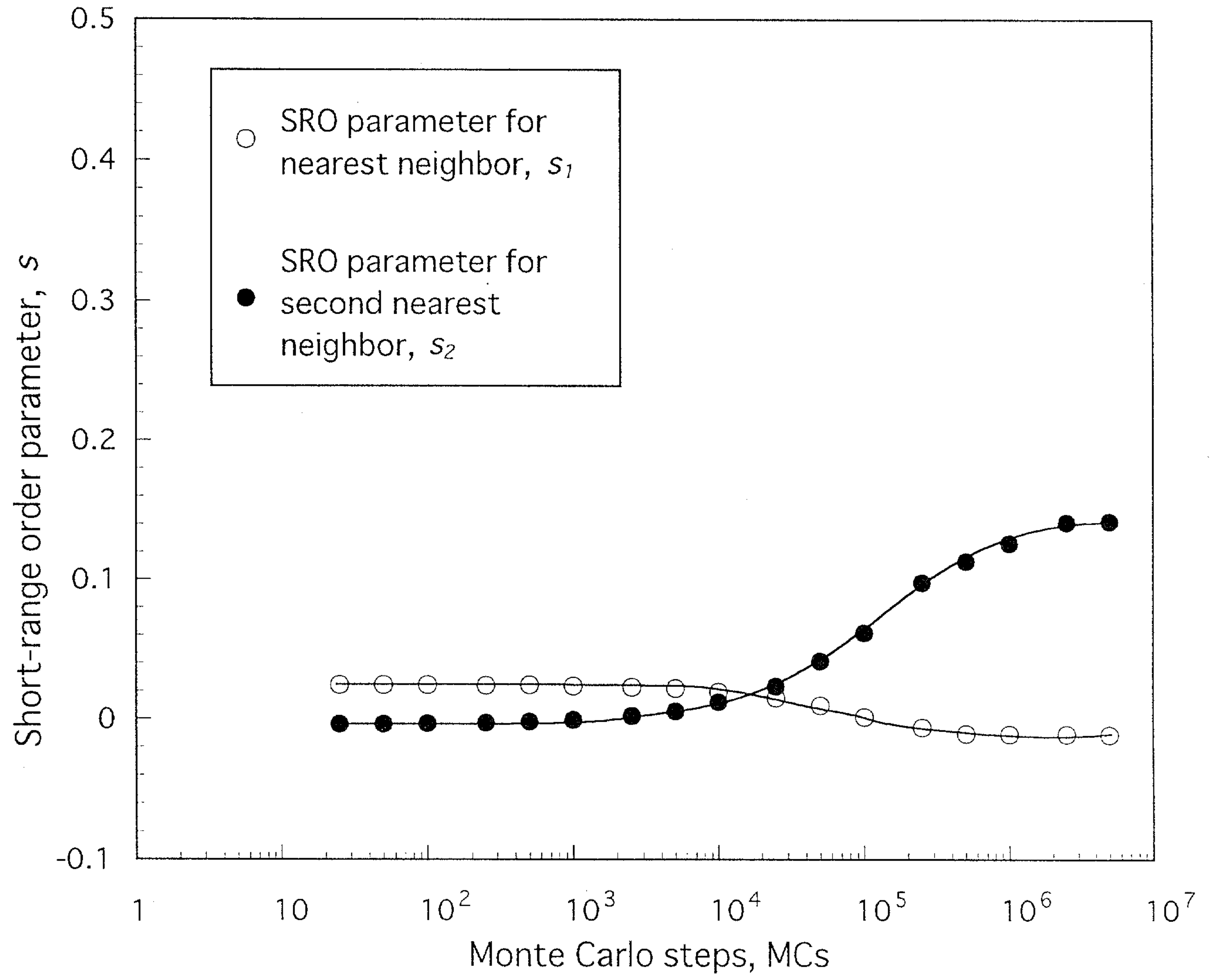

Fig.5.8 Variations in Warren-Cowley short-range order(SRO) parameters for nearest (s_1) and second nearest (s_2) neighbors with Monte Carlo steps(MCs) for Al-Li alloy simulated at 273K.

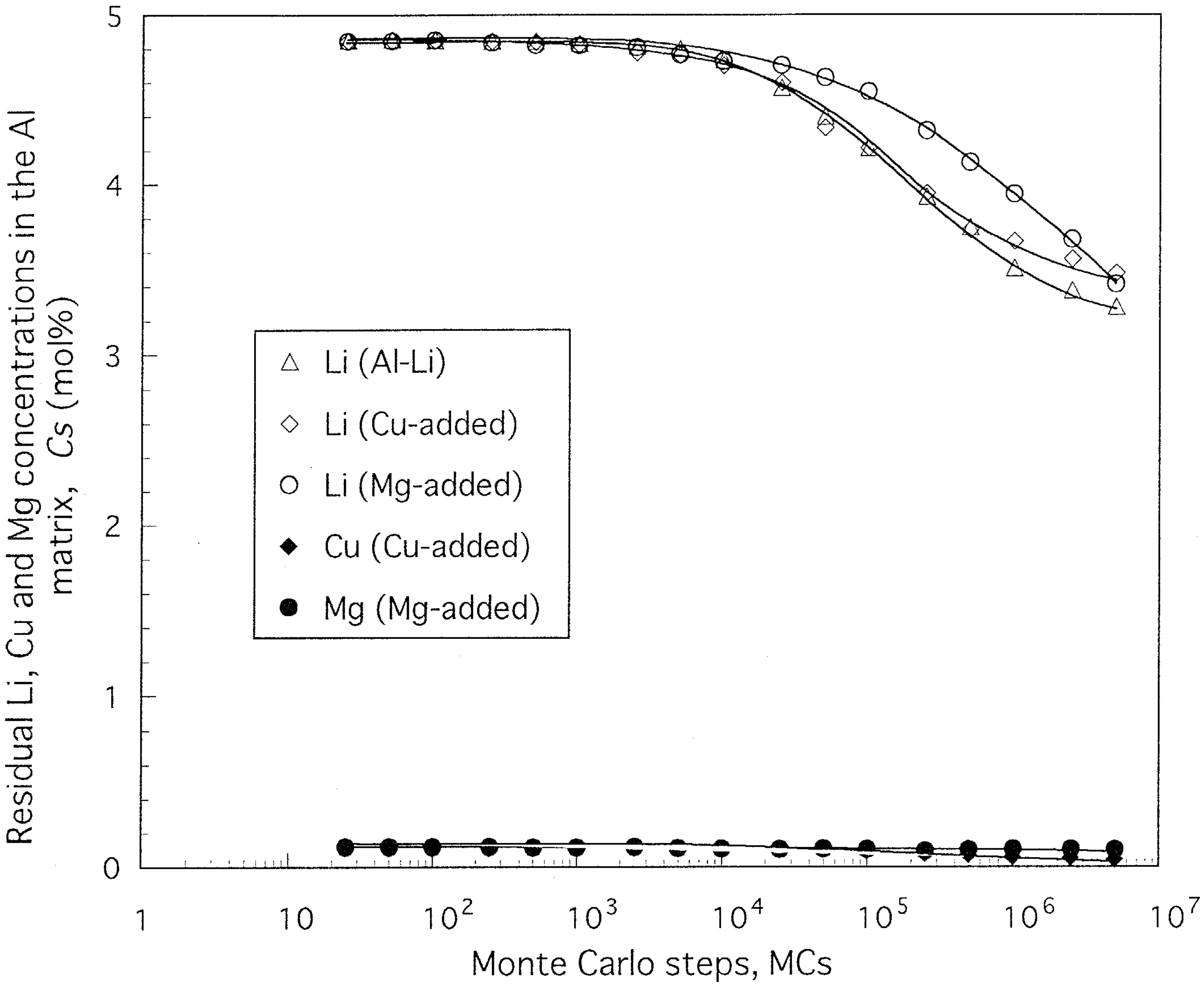

Fig.5.9 Variations in residual Li, Cu and Mg concentrations in the Al matrix with Monte Carlo steps(MCs) for Al-Li, Cu- and Mg-added alloys simulated at 273K.

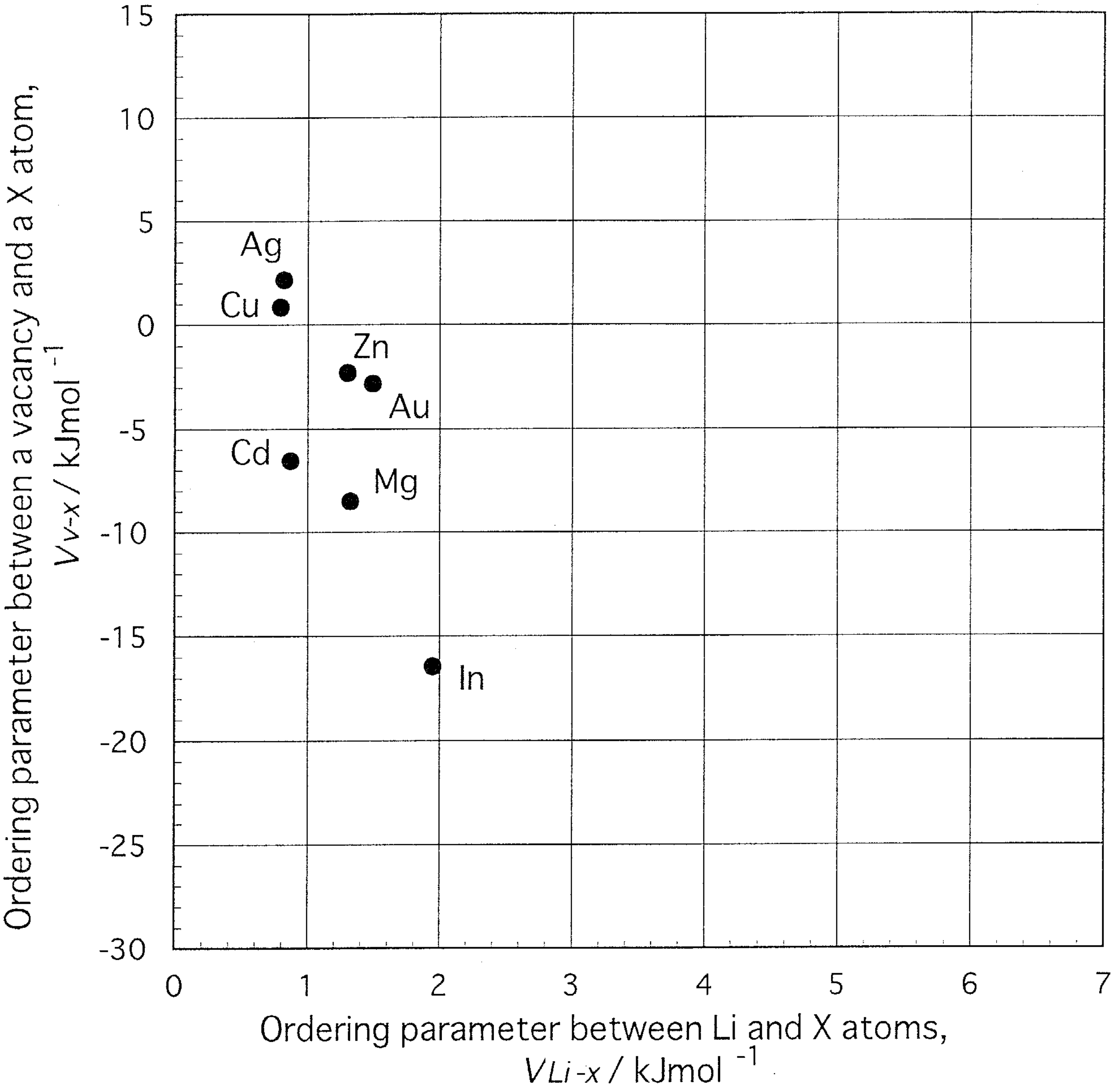

Fig.5.10 Relationships between $V_{v\text{-}x}$ and $V_{Li\text{-}x}$ for various elemental atoms, x ($V_{v\text{-}x}$: ordering parameter between a vacancy and a x atom, $V_{Li\text{-}x}$: ordering parameter between Li and x atoms).

Table 5.5 Effects of additional elements in the solution state on the kinetics of low-temperature precipitation in Al-Li alloys.

I A	II A	III A	IV A	V A	VI A	VII A	VIII			I B	II B	III B	IV B	V B	VI B	VII B
H																
Li	Be											B	C	N	O	F
Na	Mg ● ●											Al	Si ●	P	S	Cl
K	Ca	Sc	Ti	V	Cr	Mn ■	Fe	Co	Ni	Cu — —	Zn — —	Ga	Ge	As	Se	Br
Rb	Sr	Y	Zr	Nb	Mo	Tc	Ru	Rh	Pd	Ag — —	Cd ●	In ●	Sn	Sb	Te	I
Cs	Ba	La	Hf	Ta	W	Re	Os	Ir	Pt	Au —	Hg	Tl	Pb	Bi	Po	At

X	: Element
Upper	: Experimental result obtained from the resistivity changes
Lower	: Theoretical result based on this simulation

○ accelarates δ' zone formation

— has little or no effect

● suppresses due to the Vacancy-trapping mechanism

■ suppresses due to increased solvus temperatures

Figure 5.11 shows the variations in number density, N, and average size, n, of ordered structures during dynamical evolution of the Al-Li, Cu- and Mg-added alloys simulated at 273K. The difference in the initial N values between the Al-Li and the ternary alloys arises from clusters containing third additional elements which are formed by chance at the beginning of the simulation. As Monte Carlo step(MCs) proceeds, the Mg-added alloy exhibits the slower increase in N than the Al-Li and Cu-added alloys resulting in an almost identical maximum to the other alloys. As for the average size of ordered structures, on the other hand, no considerable effect on the microstructure evolution of the Al-Li alloy is detected in both the Cu- and Mg-added alloys. The similar simulation results are obtained for other additional elements; i.e. Ag, Zn and Au have almost no influence on the phase decomposition behavior of Al-Li alloys, whereas Cd and In slightly decrease the increasing-rate in the number density of ordered structures. This retardation by the Mg, Cd and In additions is well described in terms of their vacancy trapping effects[20].

(d) Partitioning behavior of additional elements

Even for the investigation of the partitioning behavior of third additional elements, the Monte Carlo simulation utilized in this work is quite available. The decreasing-rate of residual solute concentrations of third additional elements in Fig.5.9 obviously suggests that Cu has a strong tendency toward preferential partitioning within ordered structures compared with Mg. Ag and Cd additions also have the similar tendency as suggested by smaller ordering parameters with Li atoms, $V_{Li\text{-}x}$, along the horizontal axis in Fig.5.10. This tendency of Ag is well in agreement with experimental results using energy dispersive X-ray spectroscopy (EDS)[1, 2]. Recently, Hosoda *et al.*[21] predicted preferential substitution sites of various additional elements within the δ ' phase based on the relative internal energy in the pseudo-ground state. According to their theoretical results, Ag, Zn, Cd, Au, In and Au occupy Al-sites, whereas other transition elements Li-sites, at offstoichiometric compositions where Li concentrations are lower than 25mol%. The straightforward calculation using simulation parameters in Table 5.4 can also give the quantitative estimation of preferential substitution sites of third additional elements. Table 5.6 shows the comparison of total binding energies up to second nearest neighbors around one third additional atom, which occupies Al- or Li-site within the δ ' phase, respectively. It should be noted that the substitution behavior estimated from the utilized simulation parameters is well consistent with the theoretical prediction by Hosoda *et al.* [21] except for the case of Zn addition. Such the substitution behavior can be directly observed in atom configurations during the simulation. As a typical example, the atom configuration on one

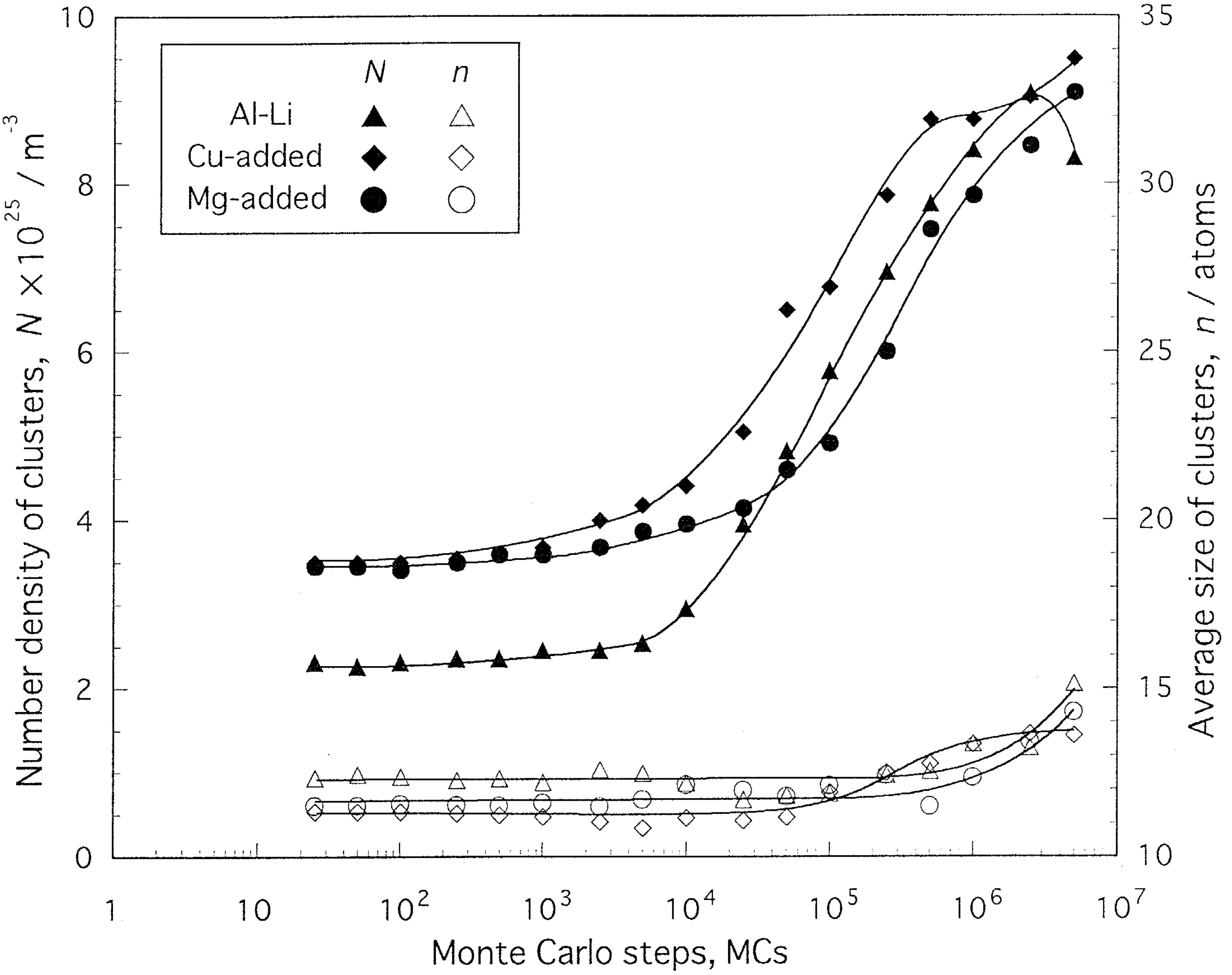

Fig.5.11 Variations in number density, N, and average size, n, of clusters with Monte Carlo steps(MCs) for Al-Li, Cu- and Mg-added alloys simulated at 273K.

Table 5.6 Total binding energies up to second nearest neighbor atoms around one third additional atom, X, which occupies Al- or Li-site within the δ' phase. Comparisons with theoretical prediction by Hosoda *et.al* [21] are also listed.

	Third additional elements, X						
	Mg	Cu	Zn	Ag	Cd	Au	In
Al-site	18.9	40.5	18.2	13.2	21.8	30.3	36.2
Li-site	17.6	34.0	15.3	17.6	54.4	60.8	63.7
This work	Li-site	Li-site	Li-site	Al-site	Al-site	Al-site	Al-site
Hosoda *et. al*	Li-site	Li-site	Al-site	Al-site	Al-site	Al-site	Al-site

(001) plane of the Ag-added alloy is illustrated in Fig.5.7(d). Note that Ag atoms indicated by red circles have a strong tendency to occupy Al-sites within the δ' phase due to the decreased total binding energy in Table 5.6. The preferential partitioning of additional elements may affects the nature of low-temperature precipitates in Al-Li alloys; e.g. the thermal stability and/or lattice misfit with the Al matrix.

5.5 Comparison between experimental and Monte Carlo simulation results

Similarly to the case of Al-Cu base alloys in Chapter 4, calculated increments in electrical resistivity, $\Delta\rho_{Cal}$, were derived using eq.(3.13) from structural parameters obtained in the simulations for the Al-Li base alloys. In the early stage of the phase decomposition in Al-Li alloys, however, the rigorously microstructural evaluation using small-angle X-ray scattering (SAXS) is rather difficult because of both the diffuse precipitate/matrix interface and the non-conserved form of precipitate size distributions[22]. As described in Chapter 3, therefore, the function *g(n)*, which means the contribution to electrical resistivity by one cluster with average size *n*, was assumed to be the relationship of eq.(3.15) by comparing the estimated $\Delta\rho_{Cal}$ curves with experimentally measured ones. The proposed function may provides never experimentally measured relationship between the size of one δ' particle and the corresponding increase in ρ in Al-Li alloys. Figure 5.12 illustrates the variations in $\Delta\rho_{Cal}$ for the Al-Li, Cu-, Mg- and Ag-added alloys simulated at 273K. Although prolonged Monte Carlo steps(MCs) reduce the values of $\Delta\rho_{Cal}$, the Al-Li, Cu- and Mg-added alloys exhibit the similar curves of $\Delta\rho_{Cal}$ to experimentally measured ones in Fig.5.3. The discrepancy in the Ag-added alloy is considered to be responsible for the change of the function *g(n)* caused by additions of third elements. This consideration is supported by the experimental results that additional Ag is preferentially partitioned within the δ' phase in Al-Li alloys[1, 2]. Therefore, it can be concluded from the obtained simulation results that a small addition of Cu, Ag or Zn to Al-Li alloys exerts no marked influence on the formation kinetics of low-temperature precipitates because of no significant interaction between the elemental atom and a vacancy. On the other hand, the additions of Mg, Sn and Li obviously suppress the phase decomposition rate in Al-Li alloys due to the so-called vacancy trapping mechanism[20] resulting in the slower increase in electrical resistivity.

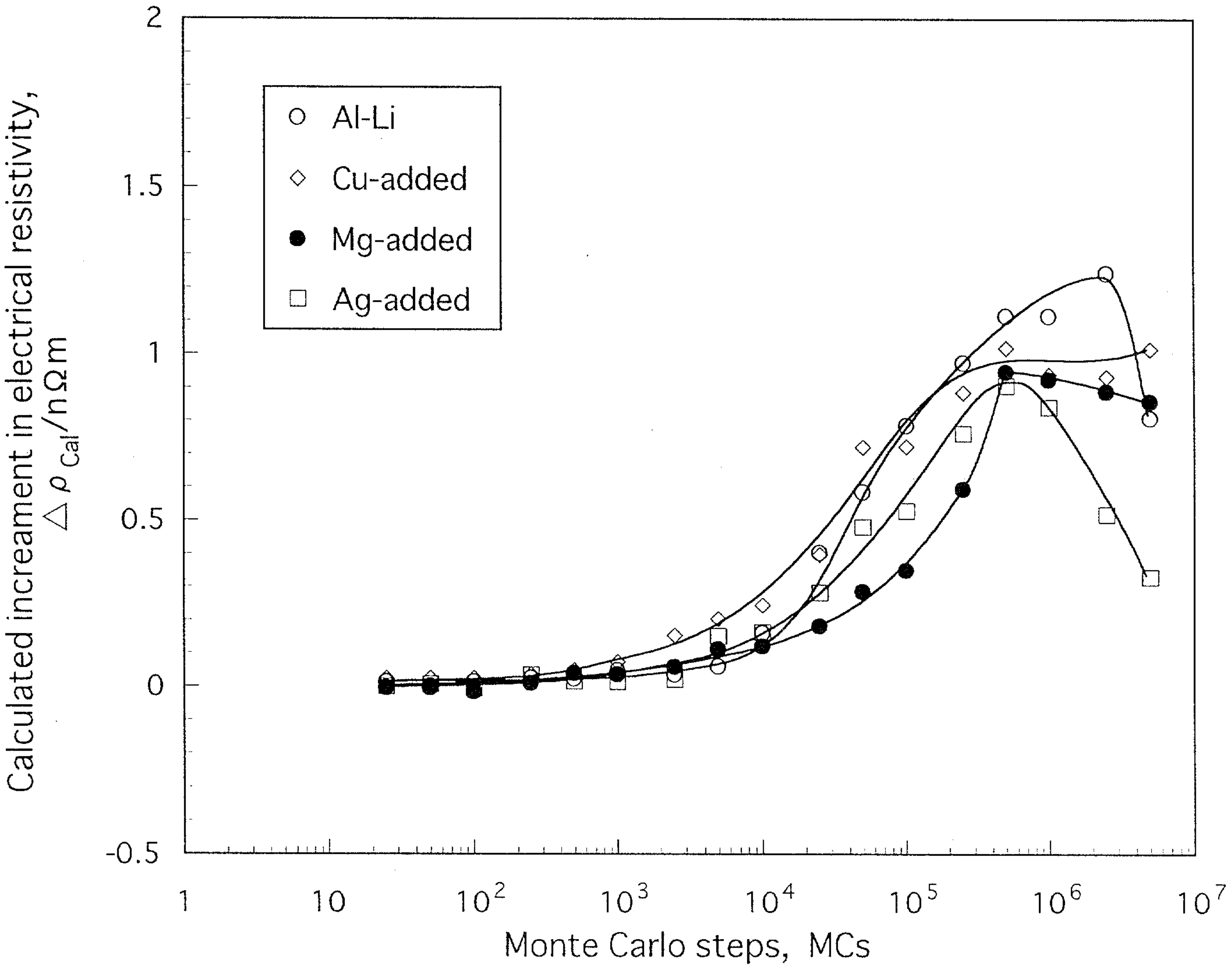

Fig.5.12 Calculated increments in electrical resistivity, $\Delta \rho_{Cal}$, obtained from the Monte Carlo simulation at 273K for Al-Li, Cu-, Mg- and Ag-added alloys.

5.6 Conclusions

The effects of third additional elements on the formation behavior of low-temperature precipitates were investigated for an Al-8mol%Li alloy aged at temperatures from 278 to 373K. The elements added to the binary alloy are 0.25%Cu, 0.25%Mg, 0.25%Ag and 0.3%Si (in mol%). Comparisons between the quantitative kinetics determined by the electrical resistivity changes and the microstructure evolution during the Monte Carlo simulation give important information on both the macroscopic transformation behavior and the detailed formation mechanism of ordered structures. The obtained results are summarized as follows.

(1) A small addition of Mg to Al-Li alloys markedly retards the formation of ordered structures consisting of Al and Li atoms similarly to the case of Al-Cu alloys containing Mg. This is because that Mg atoms preferentially trap free-vacancies available for Li diffusion to form ordered structures; i.e. the so-called vacancy-trapping mechanism, due to the relatively high interaction with a vacancy. Such situations can be frequently observed in atom configurations during the simulation.

(2) In contrast, additions of Ag, Zn and Cu exert no marked influence on the kinetics of the low-temperature precipitation in Al-Li alloys. This is explained by no significant interactions between these elemental atoms and vacancies, resulting in the similar microstructure evolution of ordered structures to that of the binary alloy.

(3) As for the substitution behavior of third additional atoms within the ordered structures, Ag and Cu exhibit a strong tendency toward substituting Al-sites of a $L1_2$-type structure, whereas Mg and Zn have a feasibility of both site substitutions, respectively.

References

[1] S.F.Baumann and D.B.Williams: Proc. 2nd Int. Al-Li Conf., TMS of AIME, New York, (1984), p.17.

[2] T.Sato and A.Kamio: Proc. 4th Int. Conf. on Aluminum Alloys, Georgia Inst. of Tech., Atlanta, (1994), p.169.

[3] A.G.Khachaturyan, T.F.Lindsey and J.W.Morris, Jr.: Metall. Trans. A, **19A** (1988), 249.

[4] B.J.Shaiu, H.T.Li and H.Y.Lee and H.Chen: Metall. Trans. A, **21A** (1990), 1133.

[5] M.S.Yu and H.Chen: *Kinetics of Ordering Transformations in Metals*, Ed. H.Chen and

V.K.Vasudevan, The Minerals, Metals & Mater. Society, (1992), p.307.

[6] T.Sato and A.Kamio: Mater. Trans., JIM, **31** (1990), 25.

[7] S.M.Allen and J.W.Cahn: Acta metall., **24** (1976), 425.

[8] J.Higgins, R.B.Nicholson and P.Wikes: Acta metall., **22** (1974), 201.

[9] Y.Sumitomo, K.Matsuhiro, M.Ura and F.E.Fujita: Report on annual meeting of Japan Inst. Metals, (1971).

[10] H.Kubo, I.Cornelis and C.M.Wayman: Acta metall., **28** (1980), 405.

[11] M.J.Richards and J.W.Cahn: Acta metall., **19** (1971), 1263.

[12] H.Ino: Acta metall.: **26** (1978), 827.

[13] R.Nozato, H.Izawa and H.Tsubakino: J. Japan Inst. Metals, **44** (1980), 1203.

[14] S.Ceresara, A.Giarda and A.Sanchez: Phil. Mag., **35** (1977), 97.

[15] A.K.Niessen, F.R.de Boer, R.Boom, P.F.de Chatel, W.C.M.Mattens and A.R.Miedema: CALPHAD, **7** (1983), 51.

[16] J.S.Garland and J.M.Sanchez: *Kinetics of Ordering Transformations in Metals*, Ed. H.Chen and V.K.Vasudevan, The Minerals, Metals & Mater. Society, (1992), p.207.

[17] H.Okuda and K.Osamura: Acta metall. mater., **42** (1994), 1337.

[18] J.M.Cowley: Phys. Rev., **77** (1950), 669.

[19] J.M.Cowley: Phys. Rev., **120** (1960), 1648.

[20] H.Kimura and R.R.Hasiguti: Acta metall., **9** (1961), 1076.

[21] H.Hosoda, T.Sato, H.Tezuka, Y.Mishima and A.Kamio: J. Japan Inst. Metals, **58** (1994), 865.

[22] H.Okuda: Private communication.

Chapter 6
Microstructure Evolution of Solute Atom Clusters and Kinetics of Low-Temperature Precipitation in Al-Li-Cu Alloys with Microalloying Elements

6.1 Introduction

In the last decade, several types of Al-Li-Cu alloys have been developed with the intention of direct replacement of conventional Al alloys. At the present time, some aircraft parts such as leading edge, floor beam and access panel are already substituted by the 2090 (Al-Li-Cu-Zr) and 8090 (Al-Li-Cu-Mg-Zr) alloys. However, there are also limitations to further wide range applications of the Al-Li-Cu alloys to other structural components; e.g. skin, frame, upper or lower wings of commercial aircrafts. One of the troublesome problems is a decreased toughness of the alloys after prolonged exposure at low temperatures (e.g. 70℃); i.e. lack of thermal stability at around 70℃ (343K). In the case of aerospace application, for example, prolonged thermal exposure during service gradually results in the decreased fracture toughness with the simultaneous increase in strength of the components. To date, some researchers have reported that this unfavorable embrittlement is attributed to Li segregation at grain boundaries[1], new precipitation of the fine δ' phase[2] or change in width of the δ'-precipitation free zone (PFZ)[3]. On the other hand, Noble *et al.*[4] suggested that the embrittlement of the 8090 alloy is mainly caused by the further precipitation of GPB zones, not the δ' formation, because an Al-2.5mass%Li binary alloy exhibits no marked change in the fracture energy during thermal exposure at 343K. These results indicate that thermal stability of Al-Li-Cu alloys appears to be ascribed to a number of low-temperature precipitates which are simultaneously formed in the alloys. Therefore, it also becomes essential to examine the effects of microalloying elements on the low-temperature precipitation of Al-Li-Cu alloys by comparing with the cases of the simple Al-Cu (Chapter 4) and Al-Li (Chapter 5) binary alloys.

Even from a welding point of view, furthermore, it is necessary to make clear the detailed effects of microalloying elements in weldable Al-Li-Cu alloys. In general, there is no doubt that the properties and performance of weldments are greatly influenced by their microstructures formed during welding, depending on the chemical composition and fabricated process of base metals. In the case of heat-treatable alloys, the effects of welding can be divided into five regions with the distance from welding arc as illustrated in

Fig.6.1[5]. Each region exactly reflects temperatures attained during welding, resulting in a joint efficiency of welded parts. In particular, the zones designated as A, B and C in Fig.6.1 are quite important regions to obtain strong joints because as-cast and as-solution treated conditions normally cause the decreased mechanical strength of alloys. Therefore, re-heating treatments after welding operation are an indispensable procedure to bring the mechanical properties of the above zones back to nearly original ones of base metals, although such the temper is unpractical especially to large parts of structural components. The acceleration of the natural aging response by small additional elements is a quite effective method to obtain the excellent joint efficiency without such the trouble postweld treatments.

In this chapter, the effects of various microalloying elements on the age-hardening behavior and precipitate microstructures of an Al-5.0%Li-2.3%Cu-0.04%Zr (mol%) alloy have been investigated in the temperature range from 278 to 373K using hardness measurement and transmission electron microscopy. In particular, the effect of small additional Mg, which plays an important role in the accelerated low-temperature precipitation of the quaternary alloy, was quantitatively examined by electrical resistivity measurement. From the atomistic analysis by a Monte Carlo simulation, furthermore, the characteristic decomposition mechanism in the Al-Li-Cu alloys is discussed in the comparison with the cases of the simple Al-Cu (Chapter 4) and Al-Li (Chapter 5) binary alloys. This mechanism is also based on both the preferential vacancy trapping by some solute atoms and solute atom aggregates closely related to their interatomic interactions.

6.2 Experimental Procedures

The alloys utilized in this chapter were supplied by Alithium Limited. Seven types of alloys were prepared from high-purity materials under Ar gas atmosphere followed by continuous casting. The chemical compositions of the alloys are listed in Table 6.1. The elements added to an Al-5.0%Li-2.3%Cu-0.04%Zr alloy are 0.2%Zn, 0.1%Ag, 0.5%Si, 0.2%Ge, 0.5%Mg and 0.5%Mg+0.1%Ag (in mol%). For simplicity, an alloy containing a small amount of additional element, *x*, is designated as *x*-added alloy in this chapter.

All the ingots were homogenized by two steps; i.e. 723K for 86.4ks and 773K for 21.6ks, and fabricated to 1.6mm-thick sheets through hot- and cold-rolling. Solution treatments were carried out in a salt bath at 778K for 1.8ks followed by water quenching at

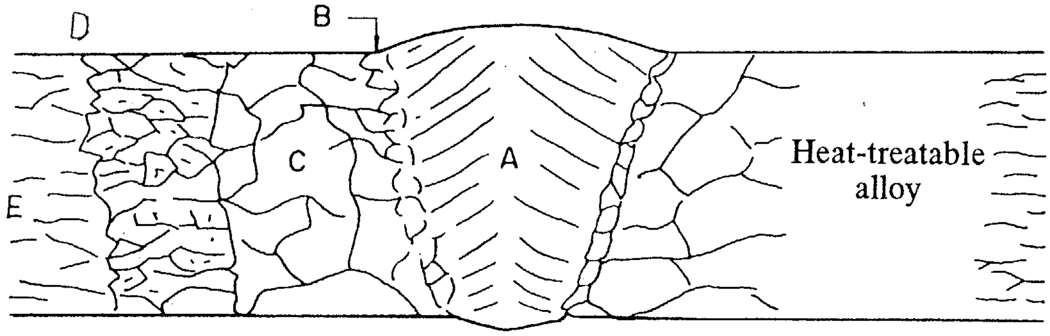

Symbol	Zone	Description
A	Weld metal	Weld bead with as-cast structure where base metal is alloyed with weld metal.
B	Fusion zone	Region where partial melting of the base metal occurs, primarilly at the grain boundaries.
C	Solid solution zone	Region where the heat from welding is high enough to dissolve partially retained in solid solution if cooling is sufficiently rapid.
D	Partially annealed or overaged zone	Region where the heat from welding has caused precipitation and/or coalescence of particles of soluble constituents.
E	Unaffected zone	Region where heating has not affected the structure.

Fig. 6.1 Illustration of a cross section having five characteristic regions formed on welding for heat-treatable alloys.

~298K. The lithium loss during these heat treatments was quantitatively estimated from as-quenched values of the electrical resistivity by assuming that the concentrations of third additional elements remain unchanged through the fabrication process as those in the ingots in Table 6.1. The subsequent aging treatments were performed at temperatures from 278 to 373K for various aging times. In this work, the room temperature designated as RT always stands for ~298K. The above fabrication process is shown in Fig.2.1. The experiments in this chapter; i.e. hardness and electrical resistivity measurements and transmission electron microscopy, were made in the same manner described in Chapter 2.

6.3 Effects of microalloying elements

6.3.1 Hardness changes

The natural aging curves of hardness are illustrated in Fig.6.2 for the Al-Li-Cu-Zr, Ag-, Ge-, Zn-, Si-, Mg- and (Mg+Ag)-added alloys. With increasing aging time, the Mg- and (Mg+Ag)-added alloys display a rapid and pronounced hardening to reach over HV150, which corresponds to the mechanical strength of 526MPa(UTS) and 287MPa(0.2%Y.S.), whereas the Mg-free (i.e. Al-Li-Cu-Zr, Ag-, Ge-, Zn- and Si-added) alloys exhibit almost no age-hardenability within the investigated aging time range. Even in the Mg-free alloys, however, higher aging temperatures result in the increased age-hardening to attain an almost identical value of hardness to that of the (Mg+Ag)-added alloy, as illustrated by the

Table 6.1 Chemical compositions of the alloys utilized in this chapter (mol%).

Alloys	Li	Cu	Zn	Ag	Si	Ge	Mg	Zr	Al
Al-Li-Cu-Zr	5.22	2.35	—	—	—	—	—	0.0441	bal.
Zn-added	4.86	2.39	0.190	—	—	—	—	0.0325	bal.
Ag-added	5.23	2.39	—	0.0948	—	—	—	0.0443	bal.
Si-added	4.70	2.37	—	—	0.508	—	—	0.0295	bal.
Ge-added	4.75	2.33	—	—	—	0.242	—	0.0326	bal.
Mg-added	5.17	2.24	—	—	—	—	0.529	0.0440	bal.
(Mg+Ag)-added	5.27	2.33	—	0.0972	—	—	0.553	0.0471	bal.

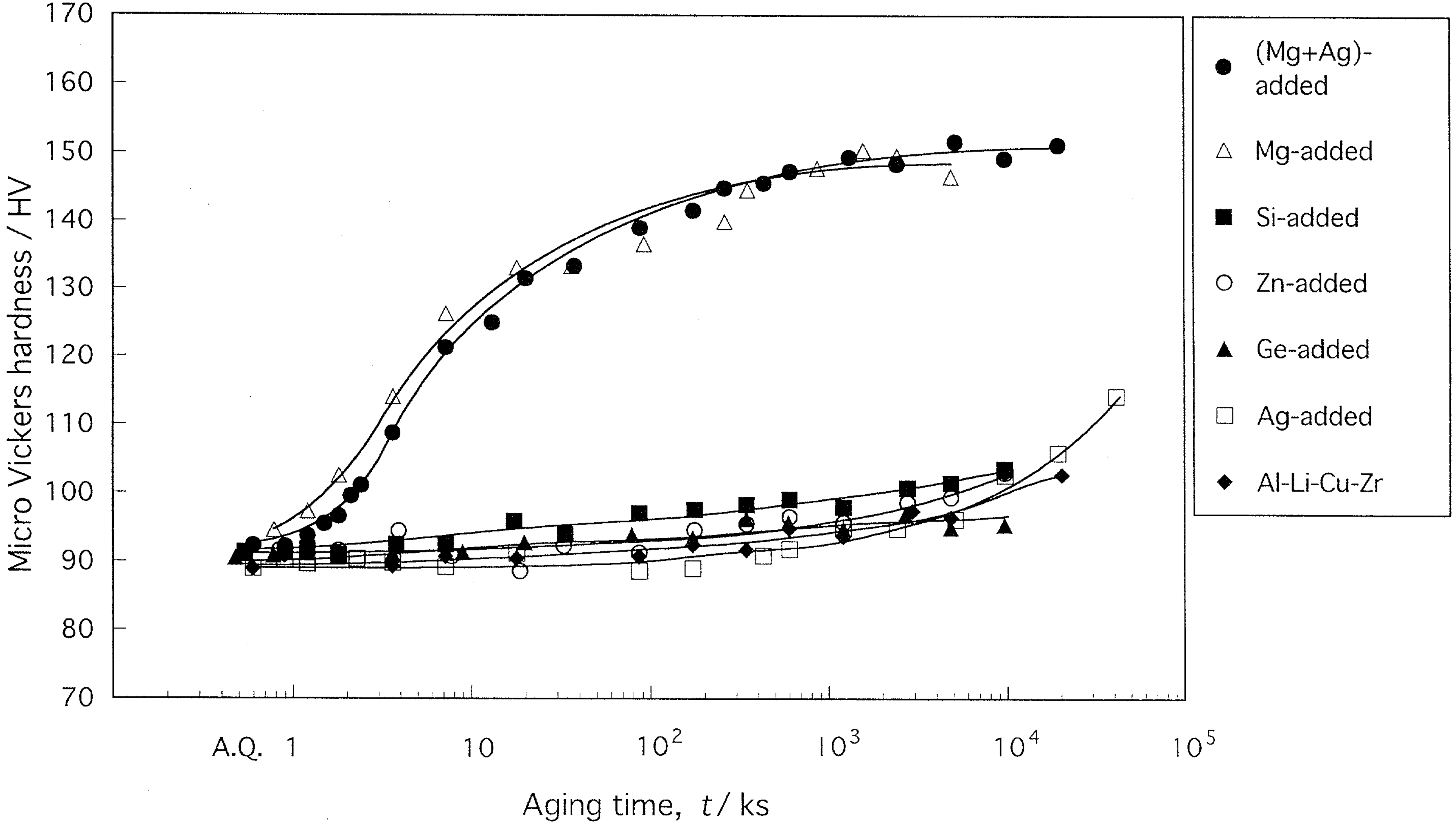

Fig.6.2 Natural aging curves of hardness for the Al-Li-Cu-Zr alloys containing various additional elements.

Mg-free(i.e. Ag-added) alloy aged at 373K in Fig.2.3. The pronounced difference in the rates of hardness-increase between the (Mg+Ag)-added(Mg-added) and Mg-free alloys is well understood by comparing their precipitate microstructures.

6.3.2 Transmission electron micrographs

Figure 6.3 shows the bright field TEM images for the Al-Li-Cu-Zr, Ag-, Ge-, Zn-, Si-, Mg- and (Mg+Ag)-added alloys aged at RT for 864ks. This aging condition gives the extremely large difference in hardness between Mg-containing and Mg-free alloys as illustrated in Fig.6.2. The corresponding diffraction patterns of the Mg- and (Mg+Ag)-added alloys clearly exhibit continuous streaks toward the $\langle 100 \rangle$ direction together with superlattice reflections, indicating the presence of both fine GP(1) zones and the δ ' phase (and/or its precursory structures) (Fig.6.3 (f), (g)). On the other hand, the microstructures of the Mg-free (i.e. Al-Li-Cu-Zr, Ag-, Ge-, Zn- and Si-added) alloys consist of almost no precipitates except for the β ' (Al_3Zr) phase having the Ashby-Brown strain contrast[6] (Fig.6.3(a)-(e)). At higher aging temperatures, however, GP(1) zones can be also detected even in these Mg-free alloys with the coexisting δ ' phase, as revealed in the TEM micrograph of the Mg-free(i.e. Ag-added) alloy aged at 373K for 5.4×10^3 ks (Fig.2.5(c)). These results indicate that a small addition of Mg to Al-Li-Cu-Zr alloys markedly accelerates the formation of GP(1) zones resulting in the faster increase in the hardness (Fig.6.2). In contrast, the addition of Ag, Ge, Zn or Si exerts no marked influence on the age-hardening behavior because of the same precipitation microstructures as that of the quaternary alloy. As for the effects of these additional elements on the precipitation kinetics of the δ ' phase (and/or its precursory structures), the detailed discussion can not be made only from these obtained experimental results (i.e. Figs.6.2 and 6.3).

6.3.3 Electrical resistivity changes

As described in Chapter 2, Al-Li-Cu base alloys clearly display a two-stage increase in electrical resistivity during aging at 278 to 373K irrespective of the presence of additional Mg (Fig.2.6). The plots of resistivity change rates, $d\rho/dt$, against aging times confirm such the two-stage change, which is composed of a monotonous-decrease stage and either anomalous-increase stage ((Mg+Ag)-added) or constant-rate stage (Mg-free(i.e. Ag-added)), as illustrated in Fig.6.4. In this work, the first stage is designated as Stage 1, whereas the subsequent is designated as Stage 2. From the obtained electrical resistivity curves in the preceding chapters, it is already shown that Al-Cu alloys exhibit one-stage increase in ρ from just after quenching at low aging temperatures(Fig.4.2), whereas Al-Li alloys display

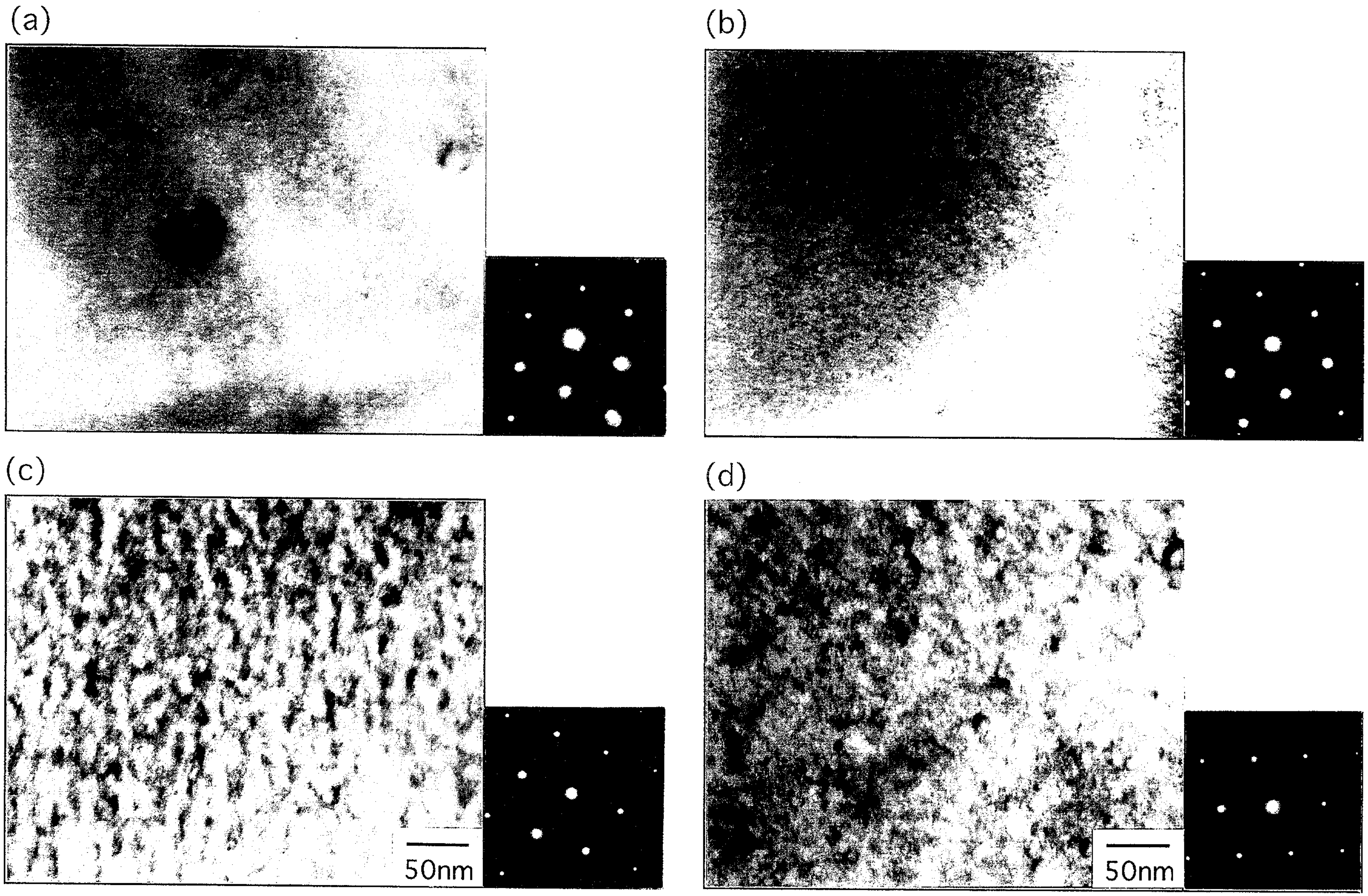

Fig. 6.3 Electron micrographs with diffraction patterns for (a)Al-Li-Cu-Zr, (b)Ag-added, (c)Ge-added and (d)Zn-added alloys aged at RT for 864ks.

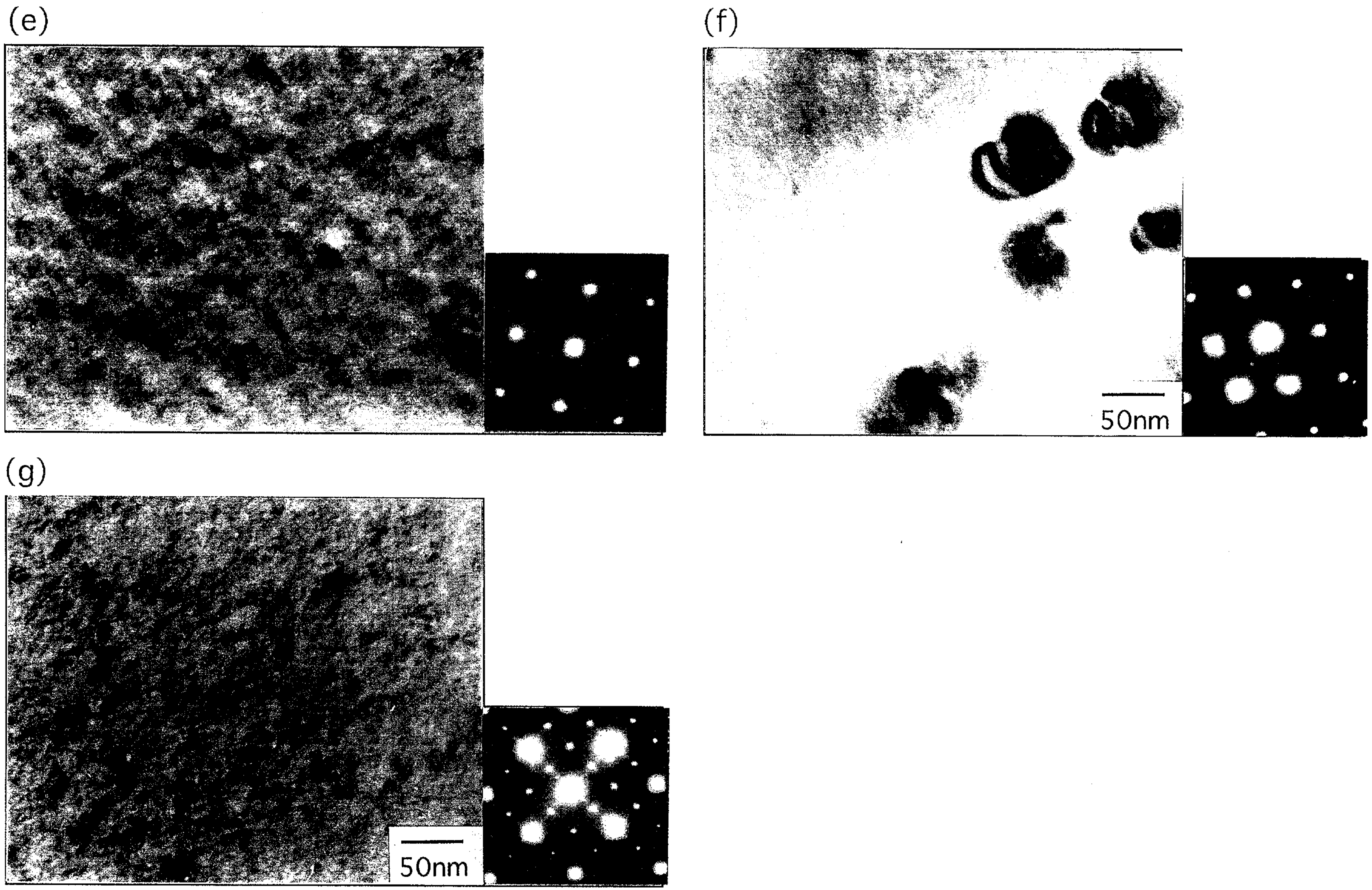

Fig. 6.3 Continued; (e)Si-added, (f)Mg-added and (g)(Mg+Ag)-added alloys aged at RT for 864ks.

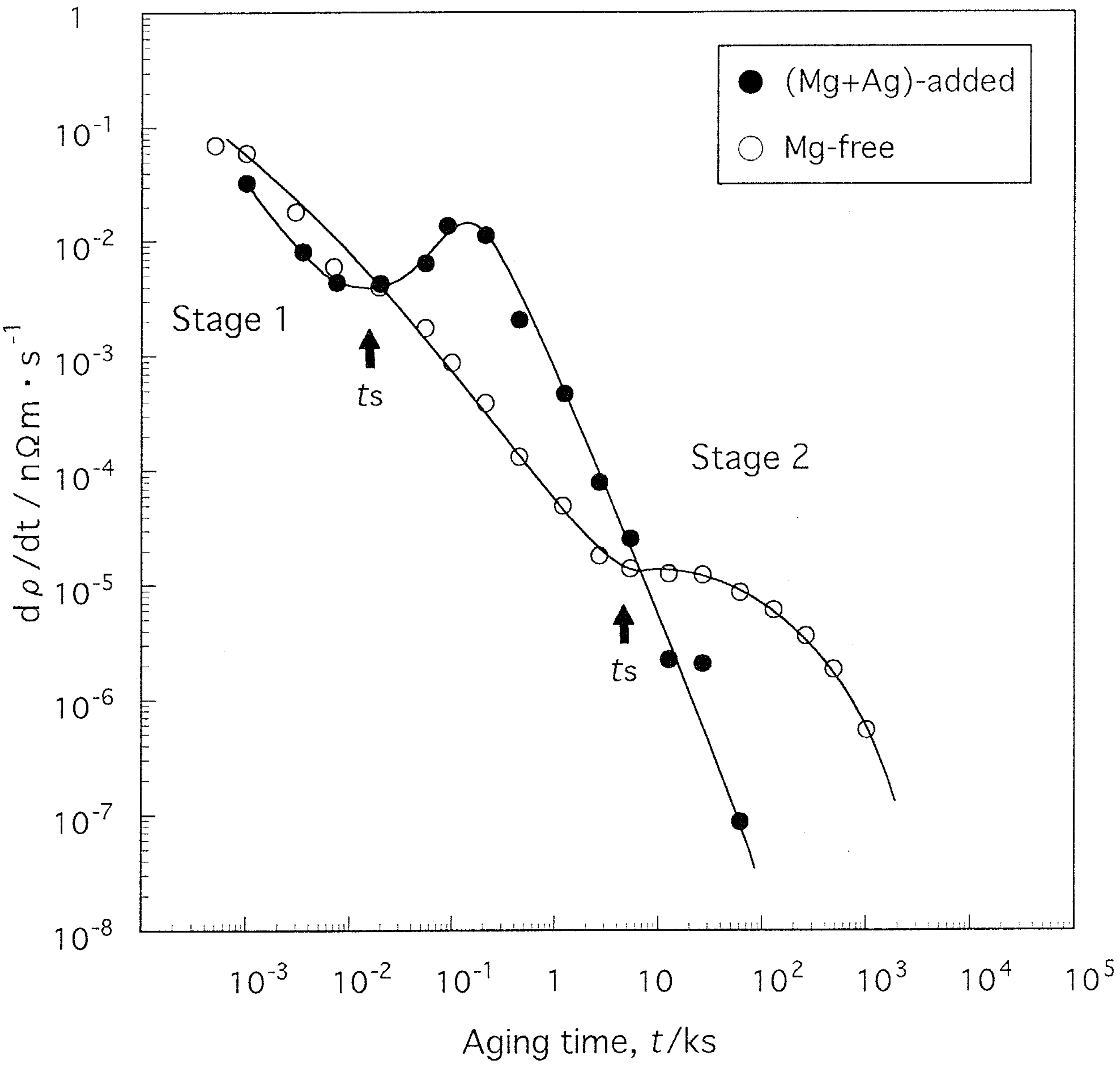

Fig.6.4 Variations in resistivity change rates, $d\rho/dt$, as a function of aging time, t, for (Mg+Ag)-added and Mg-free alloys aged at 343K. The time ts indicates the transition time from Stage 1 to Stage 2.

a rapid increase in the resistivity from the early stage of aging(Fig.5.3). Furthermore, these simple Al-Cu and Al-Li alloys only exhibit a monotonous decrease in dρ/dt within the investigated aging time range. Therefore, the anomalous dρ/dt change observed in Fig.2.6 and Fig.6.4 is regarded as a characteristic feature of Al-Li-Cu alloys, which is closely related to the simultaneous precipitation of GP(1) zones and the δ' phase (and/or its precursory structures).

6.3.4 Quantitative analysis of phase decomposition kinetics

(a) Kinetics of Stage 1 precipitation

The quantitative analysis of the characteristic precipitation in Al-Li-Cu alloys was made using Johnson-Mehl-Avrami equation in eq.(4.1). Figure 6.5 illustrates the variations in lnln[1/(1-y)] of the (Mg+Ag)-added and Mg-free (i.e. Ag-added) alloys derived from the electrical resistivity changes at 343K in Fig.2.6. The plotted points obviously exhibit both one or two straight lines in Stage 1, indicated by solid lines, and one increasing curve in Stage 2, indicated by a broken line, for each alloy. This implies that some structural changes occur even in Stage 1 if the transition time from Stage 1 to Stage 2, t_S, is long enough as is the case of the Mg-free alloy in Fig.6.5. The simple Al-Li(-Mg) alloys in Chapter 5 also exhibit such the two or three regions, which correspond to stages of the phase decomposition sequence in Al-Li alloys, in the relations of lnln[1/(1-y)] to ln$t$ (Fig.5.4). Therefore, it is quite reasonable to assume that the same phase decomposition takes place in both the simple Al-Li(-Mg) and the present Al-Li-Cu(-Mg) alloys because almost identical values of n are estimated; i.e. ~0.42 for the first stage of the Al-Li(-Mg) alloys (Fig.5.4) and ~0.40 for the early Stage 1 of the Al-Li-Cu(-Mg) alloys (Fig.6.5). In fact, the microstructures of the as-quenched (Mg+Ag)-added alloy also reveals the decomposition stage of uniformly ordered structures into two ordered phases as observed in the simple Al-Li alloys[7].

From the intercepts on the lnln[1/(1-y)] axis in Fig.6.5, furthermore, extremely different k values are assessed to be 1.3×10^{-6} s^{-1} and 3.5×10^{-5} s^{-1} for the (Mg+Ag)-added and Mg-free(i.e. Ag-added) alloys, respectively. This implies that a small amount of Mg markedly retards the formation of Stage 1 precipitates, namely precursory structures of the δ' phase, as well as the case of the simple Al-Li(-Mg) alloys in Chapter 5. The similar results are obtained for other aging temperatures as illustrated in Fig.6.6, which shows determined n and k values for the early stage of Stage 1 precipitation against reciprocal aging temperatures. It should be noted that the values of n remain constant at ~0.4 at all

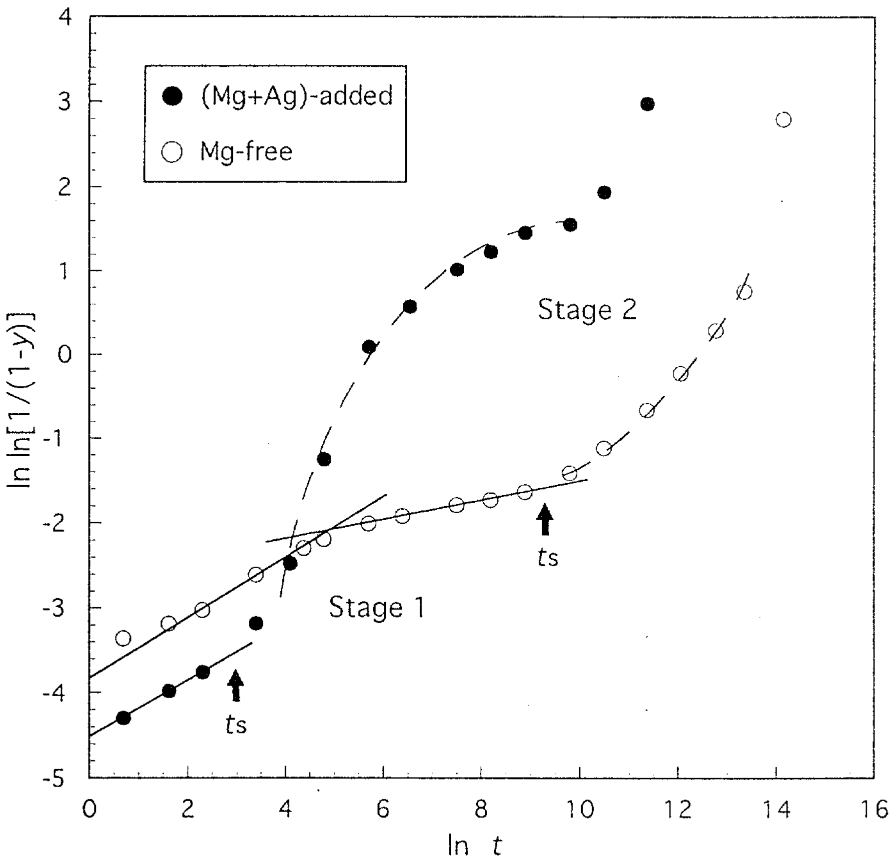

Fig.6.5 Variations in ln ln[1/(1- y)] with ln t for (Mg+Ag)-added and Mg-free alloys aged at 343K, showing two-stage increase.

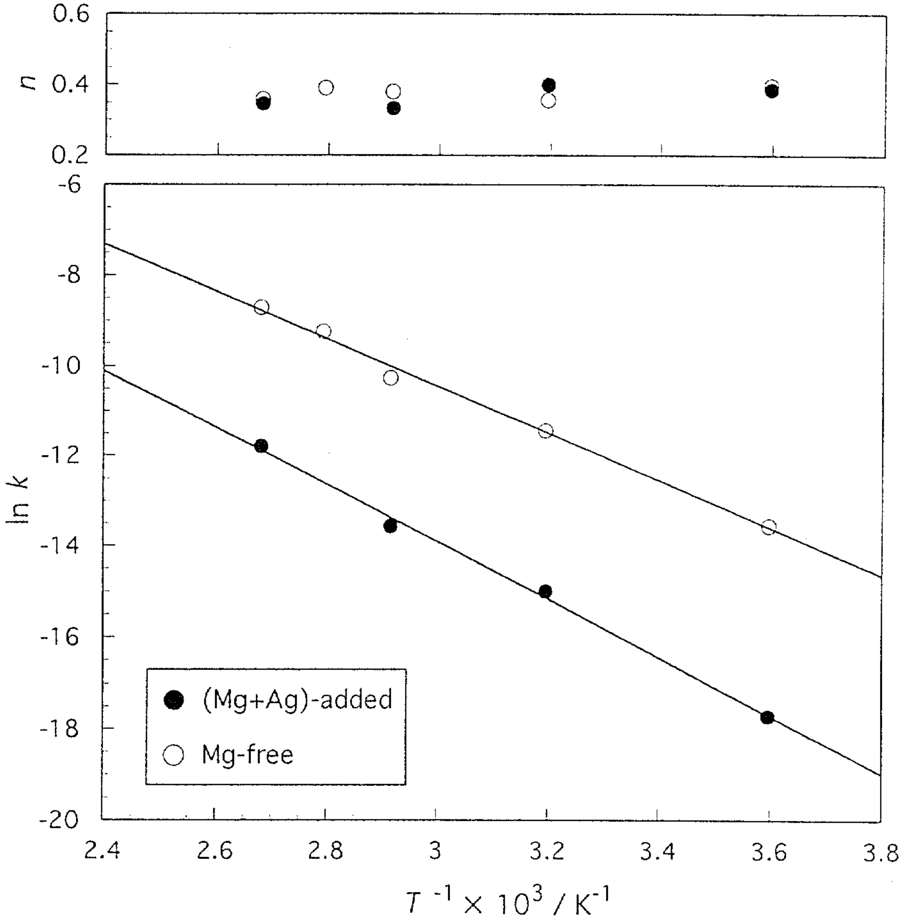

Fig.6.6 Arrhenius plots of n and ln k values in Stage 1 against reciprocal aging temperatures for (Mg+Ag)-added and Mg-free alloys.

investigated temperatures, whereas the values of k for the (Mg+Ag)-added alloy are significantly smaller than those for the Mg-free alloy. The activation energies for the Stage 1 precipitation, $Q^*_{St.1}$, which are estimated from the slopes of the corresponding straight lines in Fig.6.6(b), are 52.7 and 43.6kJ/mol for the (Mg+Ag)-added and Mg-free alloys, respectively. These values are in good agreement with the activation energies for the low-temperature precipitation in the simple Al-Li(-Mg) alloys in Chapter 5; i.e. 54.5kJ/mol for the Al-Li-Mg alloy and 40.7kJ/mol for the Al-Li alloy. Therefore, the small addition of Mg to Li-bearing alloys is found to inevitably retard the phase decomposition rate; e.g. decomposition rate of uniformly ordered structures into two ordered phases.

(b) Kinetics of Stage 2 precipitation

As illustrated in Fig.2.6, on the other hand, the resistivity increments in Stage 2 obviously take place much rapidly in the (Mg+Ag)-added alloy than those of the Mg-free(i.e. Ag-added) alloy. In this work, the precipitation kinetics in Stage 2 was estimated from the transition time from Stage 1 to Stage 2, t_S, at which the value of lnln[1/(1-y)] deviates from each extrapolation line for Stage 1, as indicated by arrows in Fig.6.5. The value of t_S exactly corresponds to the time when the hardness of the two alloys starts to increase at each aging temperature in Fig.2.3. The Arrhenius plots of ln(1/t_S) in Fig.6.7 give the activation energies for the Stage 2 precipitation, $Q^*_{St.2}$, to be 55.5 and 85.5kJ/mol for the (Mg+Ag)-added and Mg-free alloys, respectively. These values are considered to be the activation energies for the GP(1) zone nucleation, not for the growth of GP(1) zones, because GP(1) zones are not detected until t_S at any aging temperatures. This clearly shows that a small amount of Mg markedly accelerates the GP(1) zone formation due to the decreased activation energy for their nucleation resulting in the faster increases in both the hardness and electrical resistivity of Al-Li-Cu alloys. In general, it is difficult to detect experimentally the nucleation behavior of precipitates because of their extremely rapid formation enhanced by quenched-in excess vacancies. In the present alloys, however, it should be noted that coexisting Li atoms play an important role in retarding the GP(1) zone formation due to the preferential vacancy trapping effect[8]. This explains the reason why the activation energies for the GP(1) zone nucleation can be estimated for the first time in the present thesis. Such the vacancy trapping effect by Li atoms is directly observed in the following Monte Carlo simulations.

As for the growth rate of GP(1) zones, however, a small amount of Mg is expected to play a contrary role to the above effect on the GP(1) zone nucleation. As revealed in the case of simple Al-Cu alloys in Chapter 4, the activation energy for the growth of GP(1)

Table 6.2 Nucleation and growth rates of precipitates observed in Mg-free and (Mg+Ag)-added (Mg-added) alloys.

Alloy	Stage 1 (growth of precursor of δ ')	Transition time, t_s (nucleation of GP(1) zones)	Stage 2 (growth of GP(1) zones)
Mg-free	Fast	Late	Fast
(Mg+Ag)-added (Mg-added)	Slow (preferential vacancy trapping by Mg atoms)	Early (Mg/Cu/Vacancy complexes)	Slow (preferential vacancy trapping by Mg atoms)

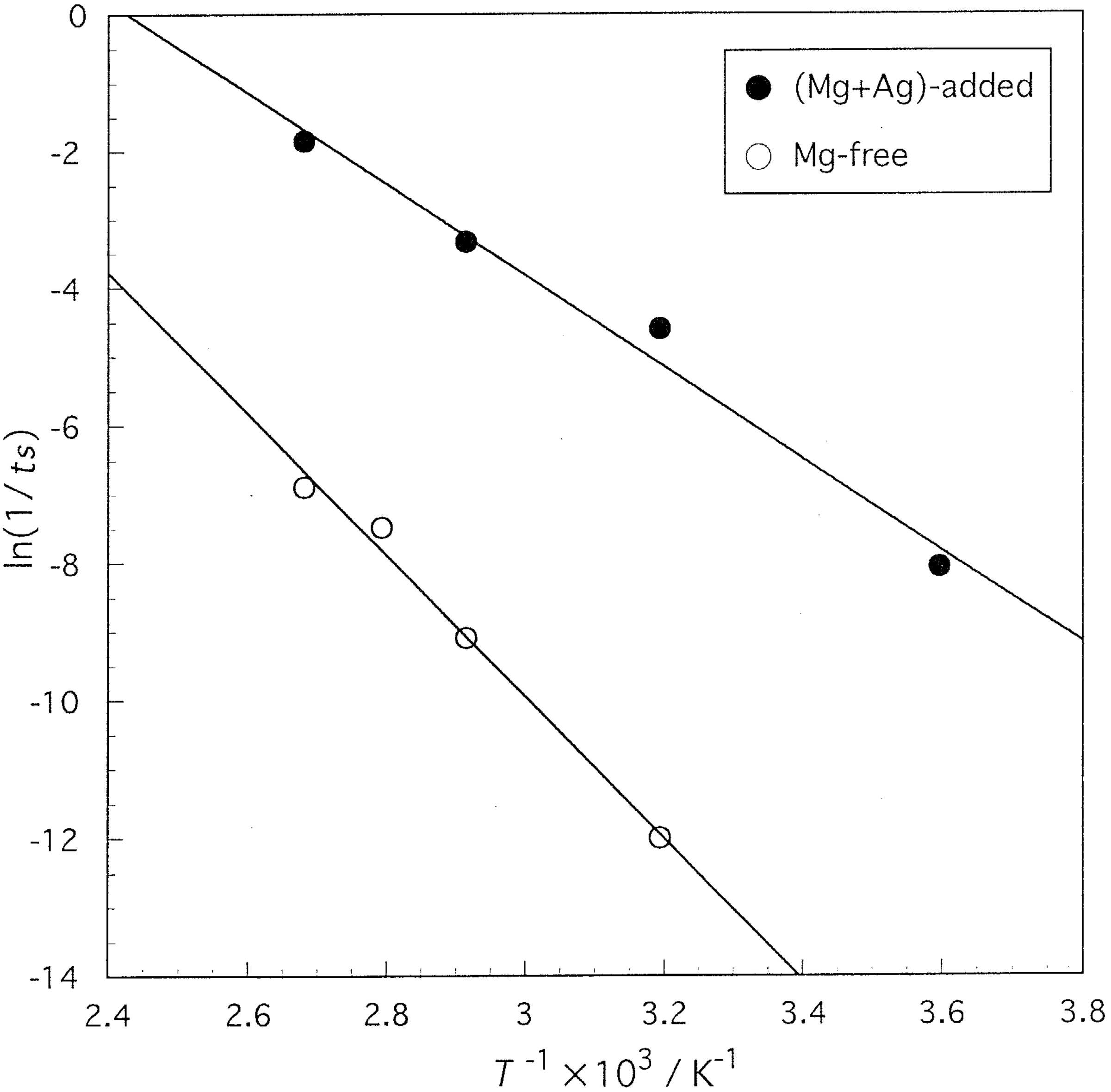

Fig.6.7 Arrhenius plots of ln(1/ ts) against reciprocal aging temperatures for (Mg+Ag)-added and Mg-free alloys.

zones is markedly increased by the small addition of Mg. Therefore, it is quite natural to consider that Mg addition to Al-Li-Cu alloys also exhibits same tendency to retard the growth rate of GP(1) zones even if substantial amount of Li coexists, although such the retardation behavior is not observed during Stage 2 in Fig.2.6 or 6.4. The obtained nucleation and growth rates of each stage-precipitate are summarized in Table 6.2 for the (Mg+Ag)-added(Mg-added) and Mg-free(i.e. Al-Li-Cu-Zr, Ag-, Ge-, Zn- and Si-added) alloys. Note that slightly complicated effects of small additional Mg were experimentally detected for the first time.

6.4. Mechanism of complicated effects of Mg addition

6.4.1 Monte Carlo simulation results

The detailed effects of additional Mg to Al-Li-Cu alloys are verified using a Monte Carlo simulation. In this case, although the utilized simulation models must be extended to treat quaternary alloy systems, the similar conditions described in Chapter 3 can be applied to inquire the low-temperature precipitation in multicomponent Al-Li-Cu-Mg alloys. The utilized simulation parameters between four elemental species are summarized in Table 6.3. Note that only nearest neighbor interactions are taken into account despite the simulation of ordering reaction of the δ' phase and/or its precursory structures. This simplification, however, has little influence on the obtained simulation results for the simultaneous formation of GP zones and the δ' phase except for their morphologies. The utilized Li atom concentration of 4.2mol% in the simulation system was estimated from as-quenched values of the electrical resistivity in the (Mg+Ag)-added alloys; i.e. ~56.2nΩm, by taking into account the effect of Li loss during heat-treatments applied.

Figure 6.8 shows typical atom configurations on one atom layer of (001) plane in the Al-4.2Li-2.4Cu and Al-4.2Li-2.4Cu-0.3Mg (in mol%) alloys simulated at 273K for 5×10^6MCs. Because of a positive ordering parameter between nearest neighbor Li atoms, the extensive volume fraction of Li atom clusters, not ordered structures, is observed as indicated by purple circles. Cu atoms indicated by gray circles are also detected as a relatively low number density of clusters, whose formation rate is remarkably lowered compared with that of Al-Cu binary alloy in Fig.4.6(c). These results indicate that the substantial amount of Li significantly suppresses the GP zone formation by preferentially trapping vacancies available for Cu diffusion, resulting in the formation of the δ' phase and/or its precursory structures. Such the vacancy trapping effect by Li atoms is entirely ascribed to a considerably

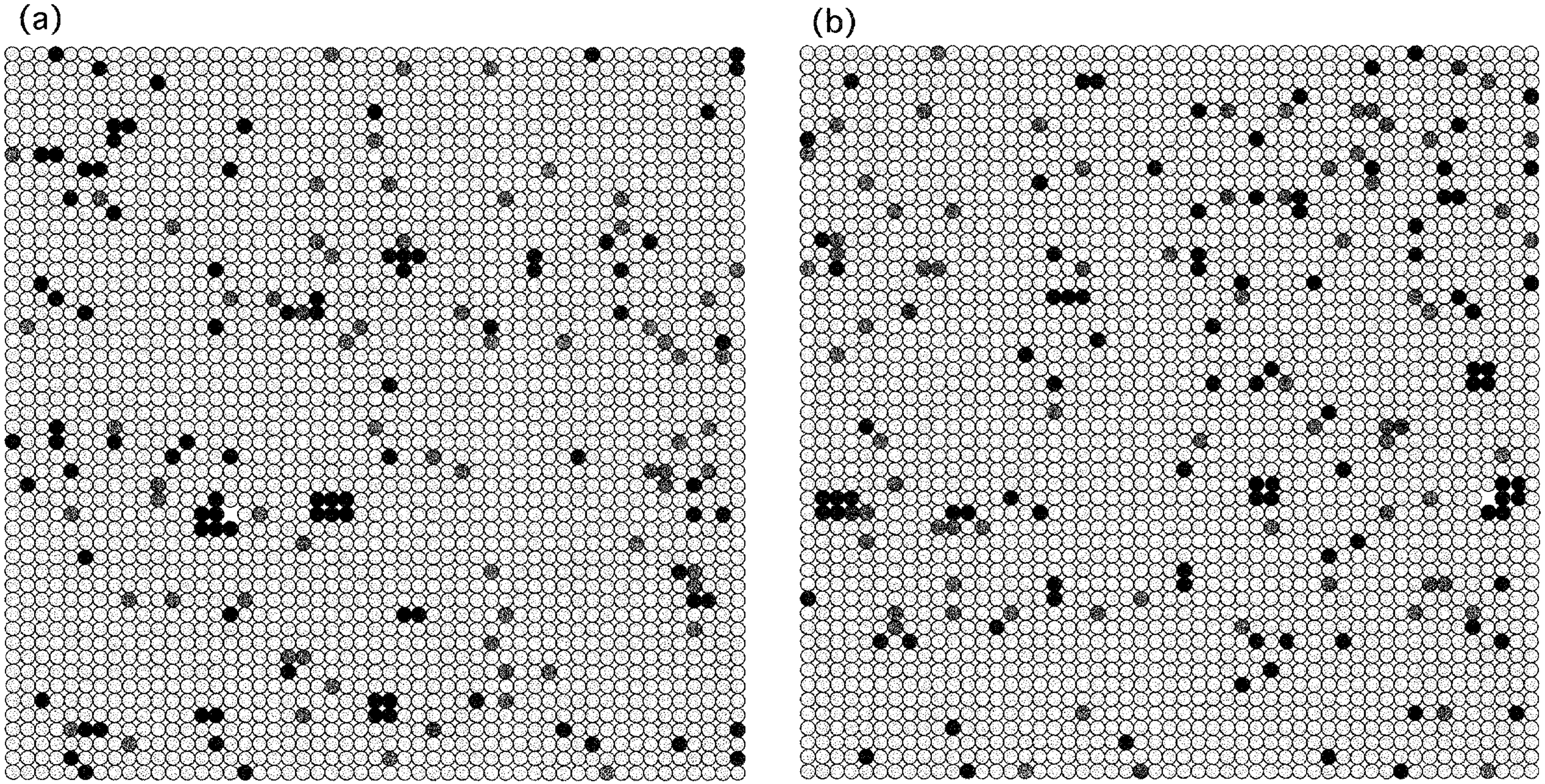

Fig.6.8 Typical atom configurations on one atom layer of (001) plane in Al-Li-Cu(a) and Al-Li-Cu-Mg(b) alloys simulated at 273K for 5×10^6MCs. The yellow, purple, gray and red circles represent Al, Li, Cu and Mg atoms, respectively.

strong Li-Vacancy interaction in Table 6.3 and actually observed during the simulation. Figure 6.9 shows the variations in residual Li, Cu and Mg concentrations in the Al matrix during the simulations at 273K for the Al-Li-Cu and Al-Li-Cu-Mg alloys. As Monte Carlo step(MCs) proceeds, although both alloys display a monotonous decrease in each residual concentration, the small addition of Mg slightly causes the acceleration of Cu atom clustering compared with the Mg-free Al-Li-Cu alloy. This tendency is clearly revealed in the variation in the number density of Cu clusters for the Al-Li-Cu-Mg alloy as illustrated in Fig.6.10. It should be noted that the starting time of the nucleation of Cu atom clusters is obviously shortened by small additional Mg, whereas the variations in number density of Li atom clusters only exhibit a monotonous decrease almost at the same rate in both alloys. These results strongly suggest that a small amount of Mg remarkably enhances the nucleation rate of GP zones with the aid of Mg/Cu pairs and/or Mg/Cu/Vacancy complexes because of the strong tendency of Mg to combine with Cu atoms rather than Li atoms (Table 6.3). Such the effect is revealed in atom configurations of Al-Cu-Mg-Ag alloy in Fig.6.8(b), in which the fourth additional Mg indicated by red circles is frequently detected around Cu atom clusters than Li atom clusters. In contrast, no other additional elements form such complexes with Cu, even if they have strong interactions with vacancies as Ge and Si (Table 1.2), because these elemental atoms preferentially combine with Li atoms, not with Cu atoms, as predicted from characteristic interactions in Figs. 4.8 and 5.10.

Table 6.3 Ordering parameters utilized in the simulation of Al-Li-Cu-Mg alloys (in kJ/mol). It should be noted that only nearest neighbor interactions are taken into account.

	Al	Cu	Mg	Li
Al	—	2.20	1.18	1.53
Cu	—	—	-50.0	0.709
Mg	—	—	—	1.32
Li	—	—	—	—
Vacancy	0	5.00	-8.50	-6.50

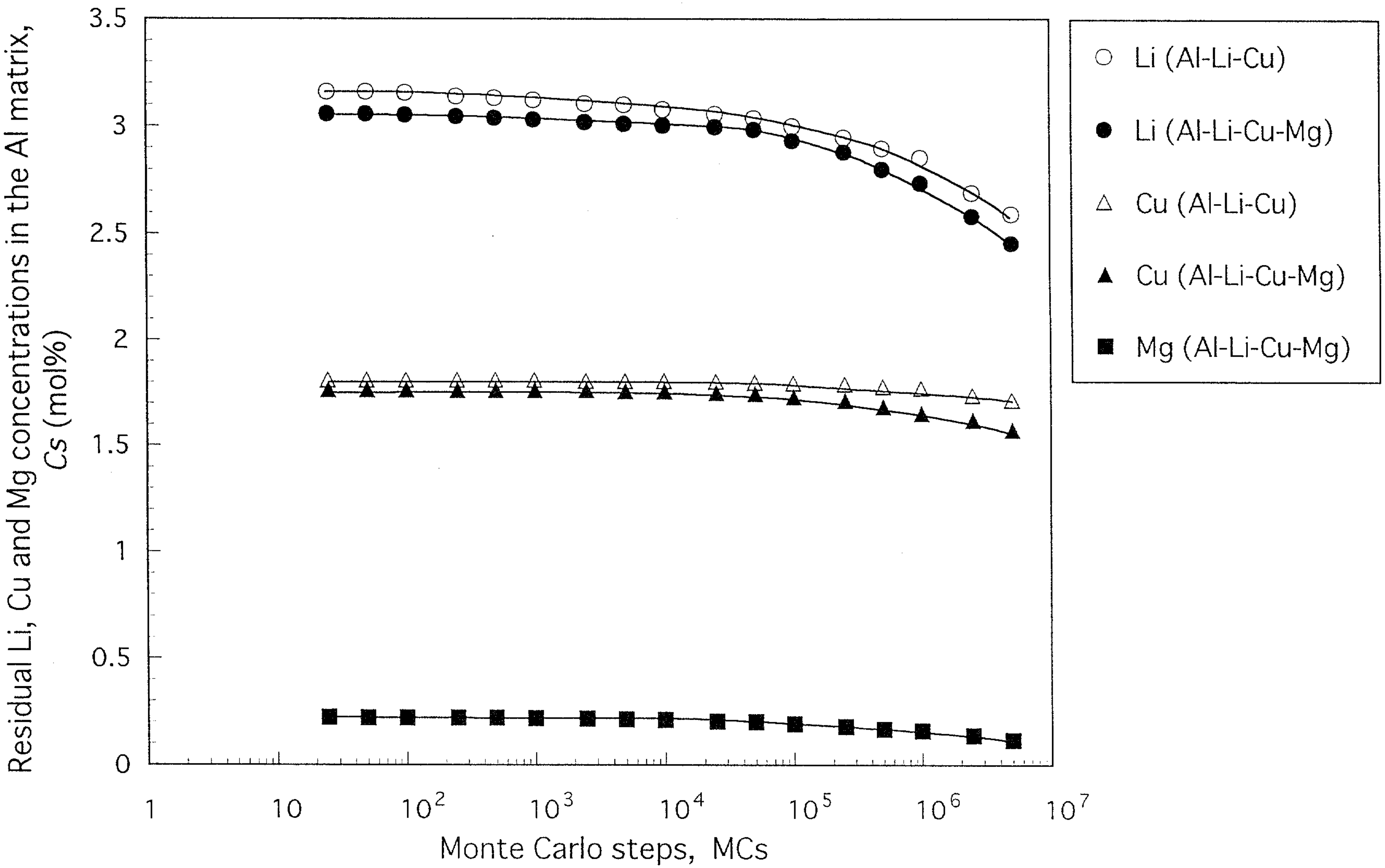

Fig.6.9 Variations in residual Li, Cu and Mg concentrations in the Al matrix, *Cs*, with Monte Carlo steps(MCs) for Al-Li-Cu and Al-Li-Cu-Mg alloys simulated at 273K.

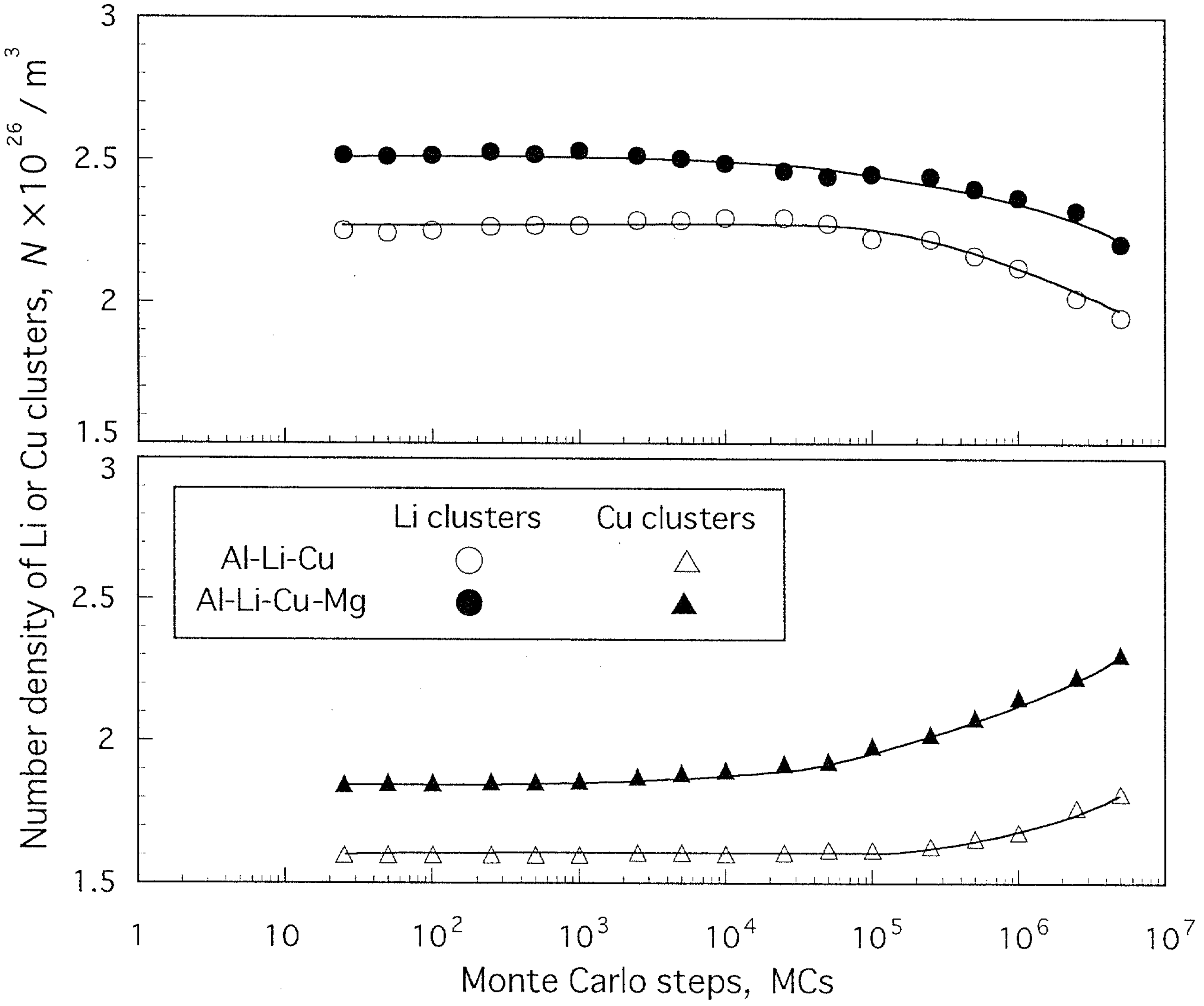

Fig.6.10 Variations in number density, *N*, of Li or Cu clusters with Monte Carlo steps(MCs) for Al-Li-Cu and Al-Li-Cu-Mg alloys simulated at 273K.

6.4.2 Proposed mechanism on accelerated GP zone nucleation by Mg addition

The experimentally obtained effects of Mg addition (Table 6.2) is well explained by taking into account both vacancy-solute atom interactions and solute atom aggregates. As described above, Li atoms, the primary solute in the present alloys, will first trap most of excess vacancies during and/or just after quenching due to the considerably strong Li-Vacancy interaction, resulting in the rapid formation of the δ' phase and/or its precursory structures. This simultaneously suppresses the formation of GP zones because free-vacancies available for Cu diffusion are remarkably decreased. In contrast, the small addition of Mg contributes to lower the growth rate of the δ' phase in Stage 1 by forming numerical Mg/Vacancy pairs because of the strong Mg-Vacancy interaction (Table 6.3). The higher activation energy for the Stage 1 precipitation in the Mg-added alloys, therefore, can be interpreted in terms of the so-called vacancy-trapping effect proposed by Kimura *et al.*[8]. At the same time, Mg also has a strong tendency to combine with Cu atoms as suggested by the utilized ordering parameter in Table 6.3. This indicates that Cu-rich regions for the GP zone formation are easily formed connected with the above Mg/Vacancy pairs resulting in Mg/Cu/Vacancy complexes. This proposed mechanism; i.e. Mg/Cu/Vacancy complex mechanism, most likely attributes to the decreased activation energy for the GP(1) zone nucleation because of the heterogeneous nucleation effect with the aid of Mg/Cu/Vacancy complexes. In fact, Ringer *et al.*[9] directly observed Mg-Cu co-clusters in the early stage of aging in an Al-1.7Cu-0.3Mg(in mass%) alloy using atom probe field ion microscope (APFIM). The proposed mechanism in which Mg/Cu/Vacancy complexes play an important role in the accelerated formation of GP zones, therefore, is considered to be sufficiently probable. In the investigated low-temperature range, furthermore, the simultaneous addition of Ag with Mg unfortunately exerts no marked influence on the precipitation behavior of Mg-added Al-Li-Cu alloys, unlike the case of the elevated-temperatures above ~400K which promote the $T_1(Al_2LiCu)$ phase precipitation as described in Chapter 7.

The increased nucleation rate of GP zones by Mg addition obviously results in the rapid increase in electrical resistivity in Stage 2 as shown in Fig.2.6. In this work, similarly to the cases of the simple Al-Cu (Chapter 4) and Al-Li (Chapter 5) alloys, the calculated electrical resistivity, ρ_{Cal}, was derived from the obtained simulation results for multicomponent Al-Li-Cu-(Mg) alloys using eq.(3.13). Figure 6.11 shows the variations in ρ_{Cal} for the Al-Li-Cu and Al-Li-Cu-Mg alloys simulated at 273K. Although absolute values of both as-quenched resistivity and increasing amount of ρ_{Cal} are still under debate, both alloys exhibit the similar curves of ρ_{Cal} to the experimentally measured ones in

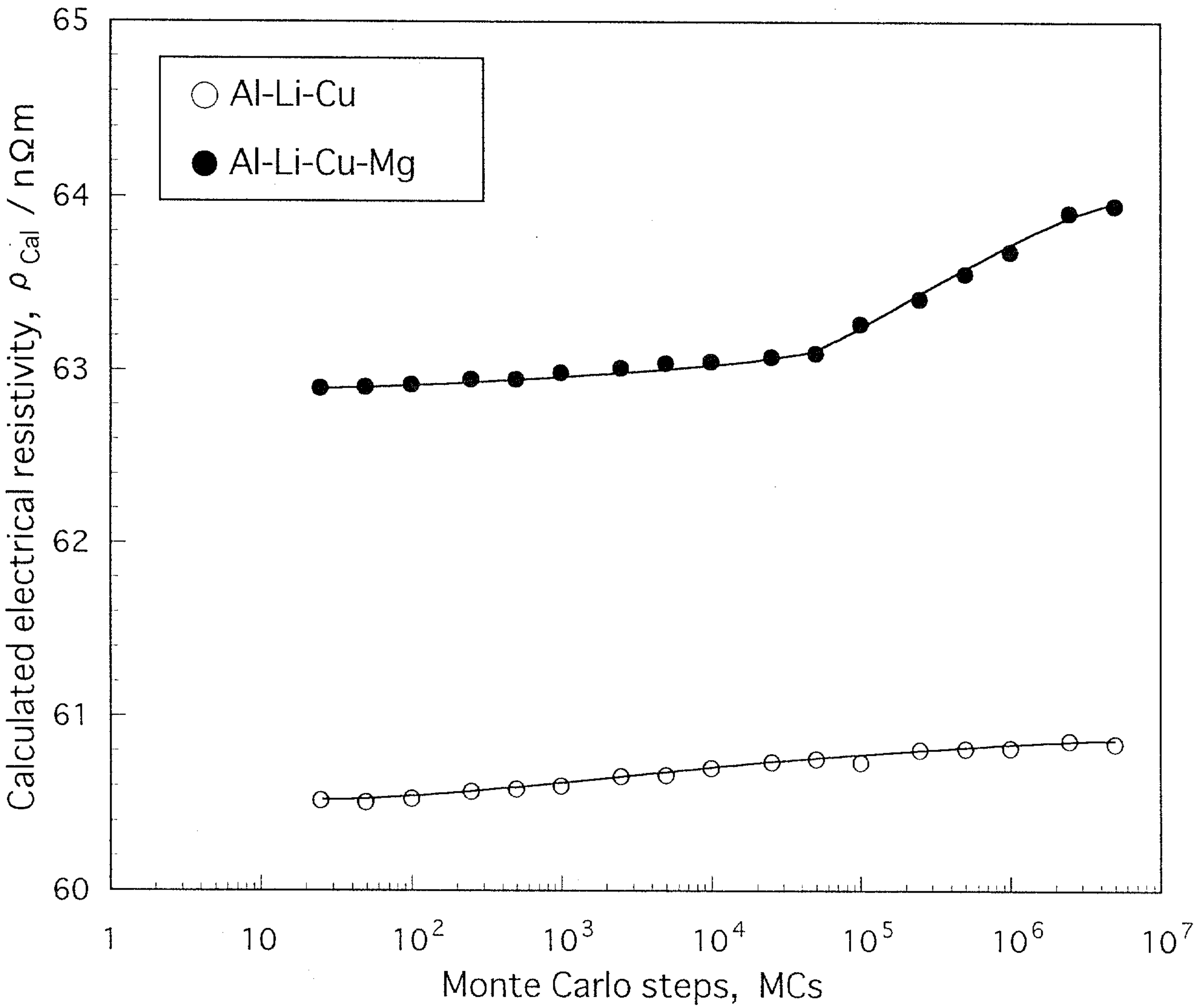

Fig.6.11 Calculated electrical resistivity, ρ_{Cal}, obtained from the Monte Carlo simulation at 273K for Al-Li-Cu and Al-Cu-Li-Mg alloys.

Fig.2.6 even showing the two-stage increase observed in the Mg-added Al-Li-Cu alloys. This agreement is a most important and notable result obtained in the present thesis.

6.5 Conclusions

The effects of microalloying elements on the age-hardening behavior and precipitation microstructures in an Al-5.0Li-2.3Cu-0.04Zr (in mol%) alloy were investigated at aging temperatures ranging from 278 to 373K using hardness and electrical resistivity measurements and transmission electron microscopy. The obtained results are summarized as follows.

(1) Both alloys exhibit a two-stage increase in the hardness and electrical resistivity. The first gradual-increase stage, Stage 1, is attributed to the growth of the δ ' phase and/or its precursory structures, whereas the subsequent rapid-increase stage, Stage 2, corresponds to the GP(1) zone formation consisting of both the nucleation and growth stages.

(2) A small addition of Mg to the Al-Li-Cu-Ag-Zr alloy markedly accelerates the GP(1) zone nucleation resulting in both an enhanced age-hardening and more rapid increase in resistivity at Stage 2. This is well explained by taking into account the important role played by Mg/Cu/Vacancy complexes, which significantly increase the nucleation rate of GP zones with the decreased activation energies.

(3) In contrast, the growth rates of GP(1) zones and the δ ' phase (and/or its precursory structures) are lowered by Mg addition as revealed by higher activation energies in the Mg-added Al-Li-Cu alloys. This is well explained by the pronounced decrease in free-vacancies available for Cu and Li diffusion due to the preferential vacancy trapping by Mg atoms.

References

[1] S.P.Lynch: Mater. Sci. Eng. A, **A136** (1991), 25.

[2] P.D.Pitcher, R.J.Stewart and S.Gupta: Scripta Metall. Mater., **26** (1992), 511.

[3] S.Ohsaki, M.Iino, M.Utsue, K.Kobayashi and T.Sakamoto: J. Jpn. Inst. Light Metals, **45** (1995), 660.

[4] B.Noble, S.J.Harris and K.Dinsdale: Proc. 4th Int. Conf. on Aluminum Alloys, **Vol.2**

(1994), 460.

[5] L.Griffing: *Welding Handbook*, **Section 4**, *Metals And Thier Weldability*, AMERICAN WELDING SOCIETY, Miami, (1972).

[6] M.F.Ashby and L.M.Brown: Phil. Mag. **8** (1963), 1083.

[7] T. Sato and A.Kamio: Mater. Trans., JIM, **31** (1990), 25.

[8] H.Kimura and R.R.Hasiguti: Acta metall., **9** (1961), 1076.

[9] S.P.Ringer, K.Hono, I.J.Polmear and T.Sakurai: Acta mater., **44** (1996), 1883.

Chapter 7
Nucleation Mechanism of T_1 phase precipitation in Al-Li-Cu Alloys

7.1 Introduction

As described in Chapter 2, Al-Li-Cu-Zr alloys containing small amounts of Mg and Ag; e.g. the registered 2094, 2095, 2096 and 2195 alloys, exhibit the excellent mechanical strength compared with the quaternary alloy under the T6 temper condition. The high strength of the (Mg+Ag)-added alloy is obviously responsible for the homogeneous precipitation of the $T_1(Al_2LiCu)$ phase, which is normally formed only at subgrain boundaries in conventional Al-Li-Cu alloys. Although many attempts have been conducted since the (Mg+Ag)-containing alloys were developed as a new high specific strength material[1-3], the mechanism of the accelerated T_1 phase precipitation by the combined Mg and Ag addition is still unclear. One interesting point is why these elements can stimulate the T_1 phase nucleation, nevertheless, whose structure does not consist of them at all. Pickens *et al.*[2] suggested that local ordering structures containing Ag and Mg atoms act as effective nucleation sites for the T_1 phase, similarly to the case of the Ω phase nucleation in Al-Cu-Mg-Ag alloys[4-8]. On the other hand, Suzuki *et al.*[9] pointed out that the T_1 phase nucleation occurs at fine secondary defects which are densely formed in the early stage of aging. Furthermore, the effect of either reduced stacking fault energy of aluminum[10] or some precursory structures; e.g. GP zone[11] and the T_1' phase[12, 13], has been also reported. From both technological and phenomenological points of view, therefore, it is quite important to elucidate the mechanism of the T_1 phase precipitation in the Al-Li-Cu alloys containing small amounts of Mg and Ag.

According to the detailed structure analysis using X-ray and electron diffraction techniques [14-21], the T_1 phase is classified to be of hexagonal structure with a space group most likely of P6/mmm. This thin plate-like precipitate, with a=0.4965nm and c=0.9345nm[16], is observed to lie on four {111} planes in the Al matrix, satisfying the orientation relationships $\{111\}_{Al} \parallel \{0001\}_{T1}$ and $\langle \bar{1}10 \rangle_{Al} \parallel \langle 10\bar{1}0 \rangle_{T1}$. The proposed atom arrangement[16] consists of a stacking sequence of ABABAB..., where A is closed-packed planes with ordered arrangements of Al and Li atoms in 1:2 and 2:1 ratios for alternate A planes, and B is disordered planes with random arrangements of Al and Cu atoms in 1:1 ratio. This proposal implies that the T_1 phase formation inevitably introduces a high number density of stacking faults in the fcc Al matrix; i.e. ABCABABC... . The stacking fault energy of aluminum, however, is generally believed to be so high; e.g. ~ 0.15J/m^2[10], that hexagonal closed-packed (hcp) phases can not directly nucleate on the matrix. Therefore, it becomes necessary to consider the presence of some heterogeneous nucleation sites for the T_1 phase especially by taking into account the roles of microalloying elements and quenched-in excess vacancies.

In this chapter, the effects of various additional elements on the age-hardening behavior and precipitate microstructures of an Al-5.0%Li-2.3%Cu-0.04%Zr (mol%) alloy have been investigated in the temperature range from 403 to 523K using hardness measurement and transmission electron microscopy. In particular, the small addition of Mg, which is most effective in improving the mechanical properties of the quaternary alloy, is focused and closely related to the nucleation mechanism of the T_1 phase. From the difference in the T_1 phase distributions between three quenching conditions; i.e. W.Q.(water-quench), D.Q. (direct-quench) and S.Q.(step-quench), furthermore, heterogeneous nucleation sites for the T_1 phase are discussed in terms of both solute atom clusters and point defects aggregates. The Monte Carlo simulation performed in this work well reproduces the proposed mechanism of the T_1 phase nucleation.

7.2 Experimental Procedures

The alloys utilized in this chapter are same as ones in Chapter 6. The chemical compositions of the alloys are listed in Table 6.1. The elements added to an Al-5.0%Li-2.3%Cu-0.04%Zr alloy are 0.2%Zn, 0.1%Ag, 0.5%Si, 0.2%Ge, 0.5%Mg and 0.5%Mg+0.1%Ag (in mol%). For simplicity, an alloy containing a small amount of additional element, x, is designated as x-added alloy in this chapter.

All the ingots were homogenized by two steps; i.e. 723K for 86.4ks and 773K for 21.6ks, and fabricated to 1.6mm-thick sheets through hot- and cold-rolling. Solution treatments were carried out in a salt bath at 778K for 1.8ks in the same manner as described in Chapter 6. In this chapter, three different quenching treatments were applied to the above alloys. W.Q.(water-quench) is a usual procedure to directly quench solution-treated specimens into water at ~298K. D.Q.(direct-quench) is a procedure to give an aging treatment at temperature Ta directly from quenching bath temperatures Tb (323-523K), whereas S.Q.(step-quench) includes a holding treatment at 673K for 15s during water-quenching from 778K. These quenching treatments are schematically illustrated in Fig.7.1.

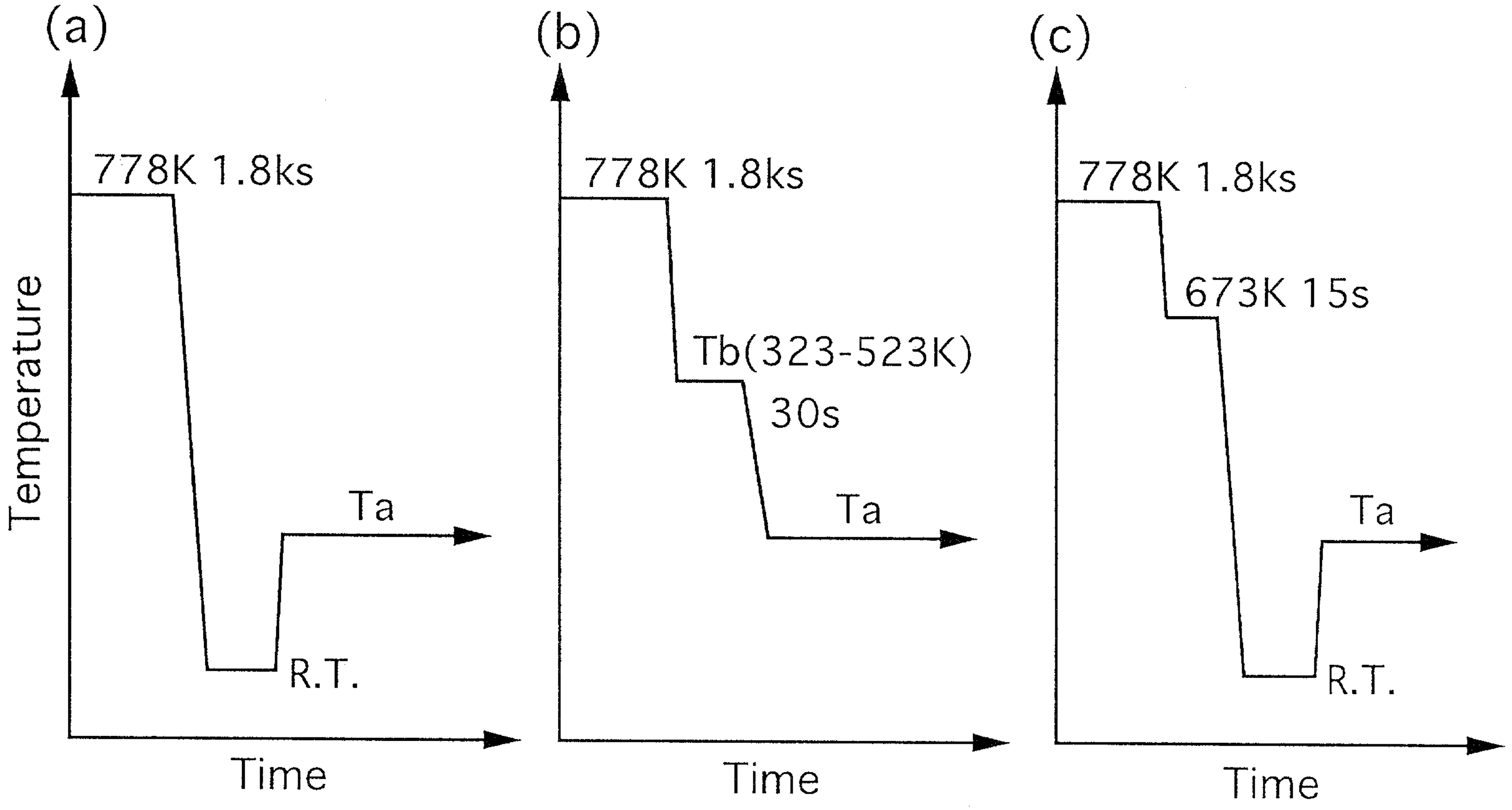

Fig. 7.1 Schematic illustrations of three quenching treatments applied to the Al-Li-Cu-Zr based alloys. (a)W.Q. (water-quench), (b)D.Q. (direct-quench) and (c)S.Q. (step-quench).

The subsequent aging treatments were performed in oil baths at temperatures from 403 to 523K for various aging times. The above fabrication process is shown in Fig.2.1. The experiments in this chapter; i.e. hardness measurement and transmission electron microscopy, were made in the same manner described in Chapter 2.

7.3 Effects of microalloying elements

7.3.1 Hardness changes

Hardness changes during isothermal aging at 433K after W.Q. treatment are shown in Fig.7.2 for the Al-Li-Cu-Zr, Ag-, Ge-, Zn-, Si-, Mg- and (Mg+Ag)-added alloys. The addition of Ag, Ge, Zn or Si to the quaternary alloy exerts almost no marked influence on the values of peak hardness, approximately up to HV10 increase, whereas Mg addition obviously shortens the time to attain peak hardness and also increases the value of peak hardness by ~HV40. The simultaneous addition of Mg and Ag, furthermore, yields the highest value of peak hardness over ~HV200, which corresponds to the mechanical strength of 592MPa(UTS) and 559MPa(0.2%Y.S.) as described in Chapter 2. The similar tendency is also revealed in 463K aging in Fig.7.3. These results indicate that a small addition of Mg to Al-Li-Cu-Zr alloys causes the pronounced increase in the hardness under the T6 temper condition and that the combined addition of Ag with Mg is more effective to increase the mechanical strength of the quaternary alloy.

7.3.2 Transmission electron micrographs

Figure 7.4 shows the bright field TEM images for the Al-Li-Cu-Zr, Ag-, Ge-, Zn-, Si-, Mg- and (Mg+Ag)-added alloys aged at 433K for 346ks after W.Q. treatment. This aging condition provides almost peak hardness for each alloy in Fig.7.2; i.e. T6 temper condition. The electron diffraction patterns of the quaternary, Ag-, Ge-, Zn- and Si-added alloys exhibit continuous streaks toward the ⟨100⟩ direction with intensity maxima at every fourth between fundamental 200 spots, indicating the presence of fine plate-like GP(2) zones with average size of ~60nm(Fig.7.4(a)-(e)). In these Mg-free alloys, the heterogeneous precipitation of the coarsened T_1 phase is also observed only at subgrain boundaries with a low number density. On the other hand, the microstructures of the Mg- and (Mg+Ag)-added alloys reveal a high number density of the T_1 phase on the {111} habit planes, which provides both continuous streaks toward the ⟨111⟩ direction and 1/3, 2/3 220 spots in the corresponding diffraction patterns, with coexisting GP(2) zones (Fig.7.4(f), (g)). The similar results are observed in the precipitate microstructures aged at 463K for 36ks (Figs.7.5).

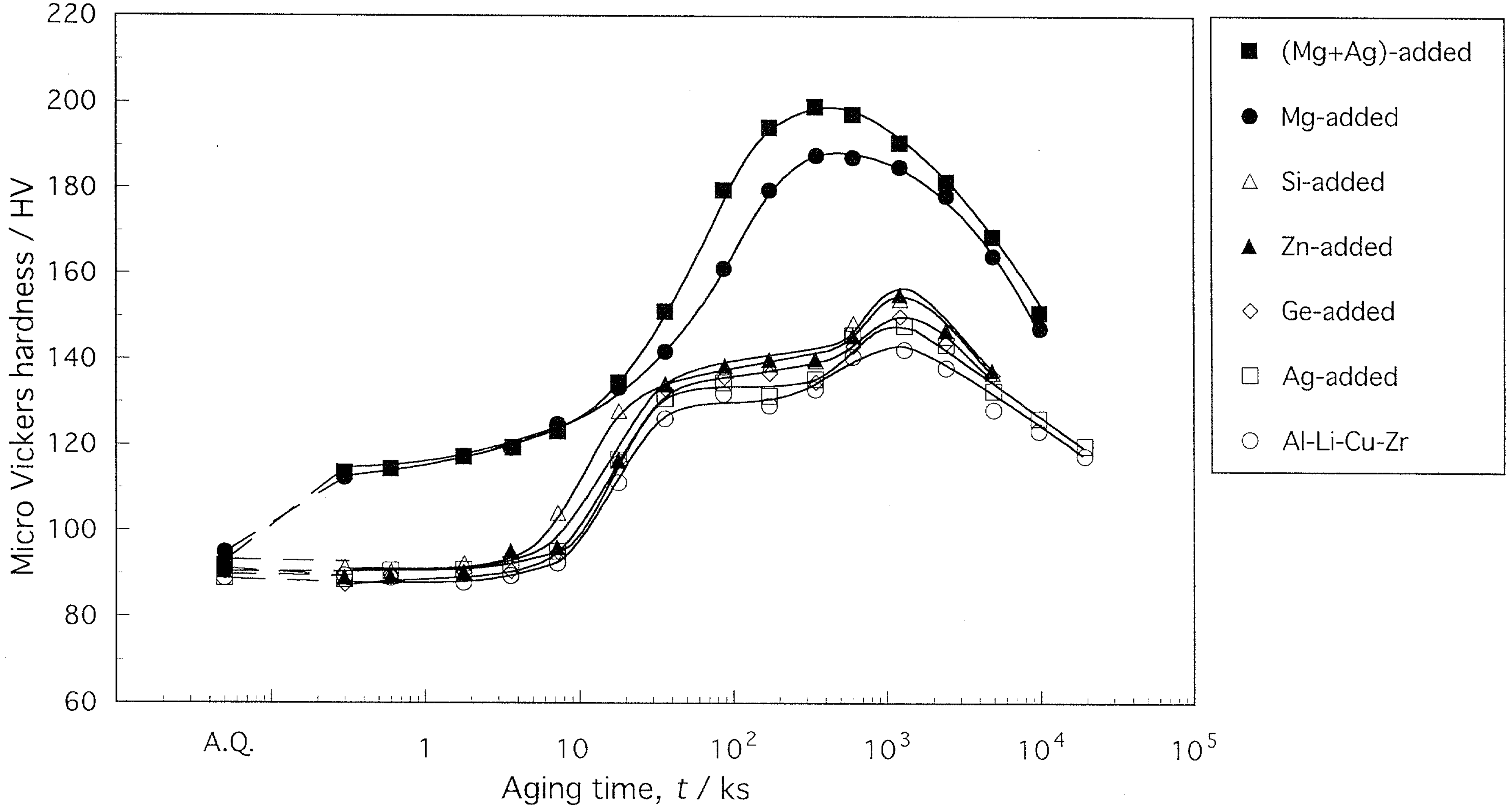

Fig. 7.2 Isothermal aging curves of hardness for Al-Li-Cu-Zr alloys containing various elements. Aging temperature is 433K.

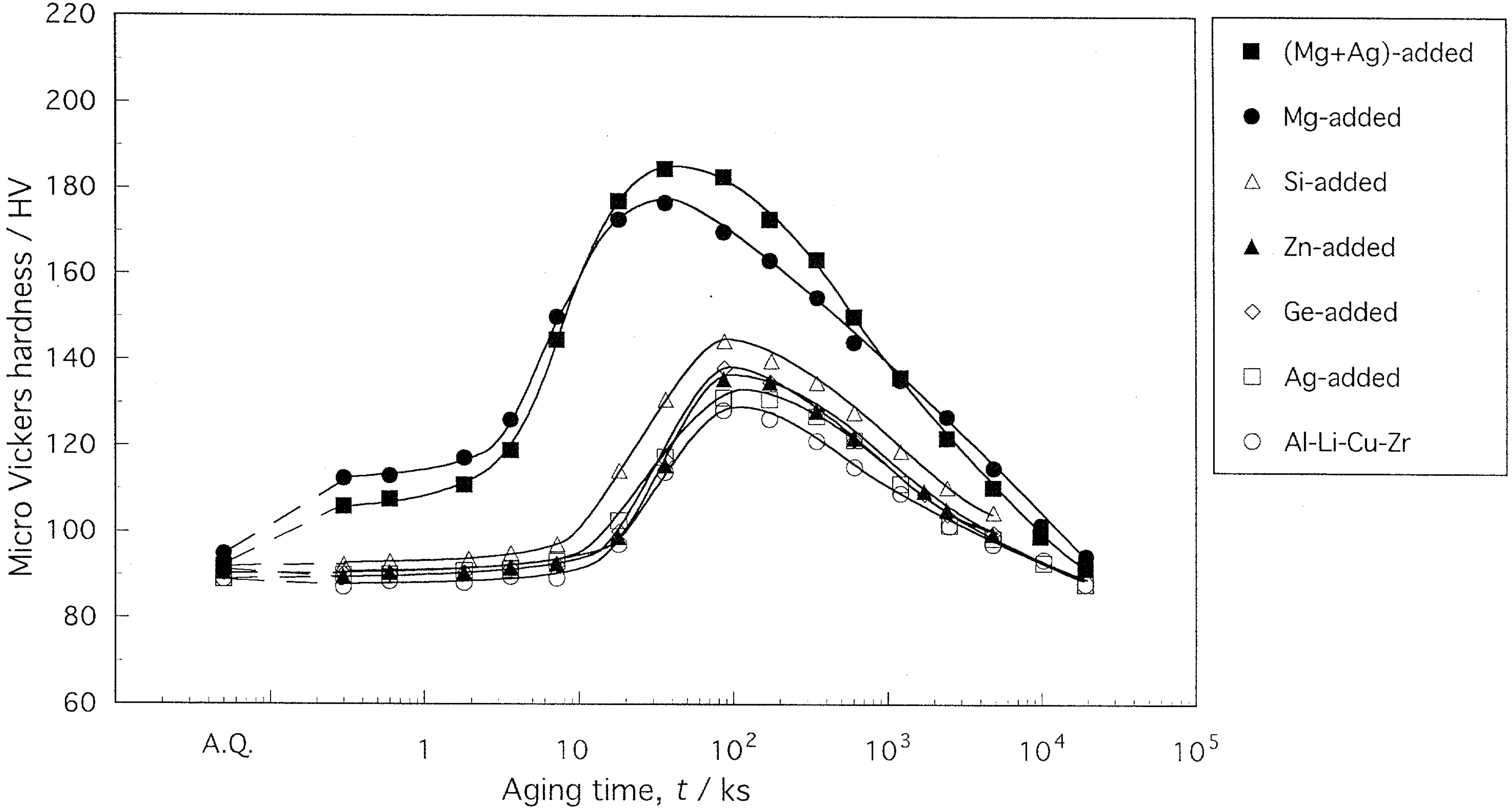

Fig. 7.3 Isothermal aging curves of hardness for Al-Li-Cu-Zr alloys containing various elements. Aging temperature is 463K.

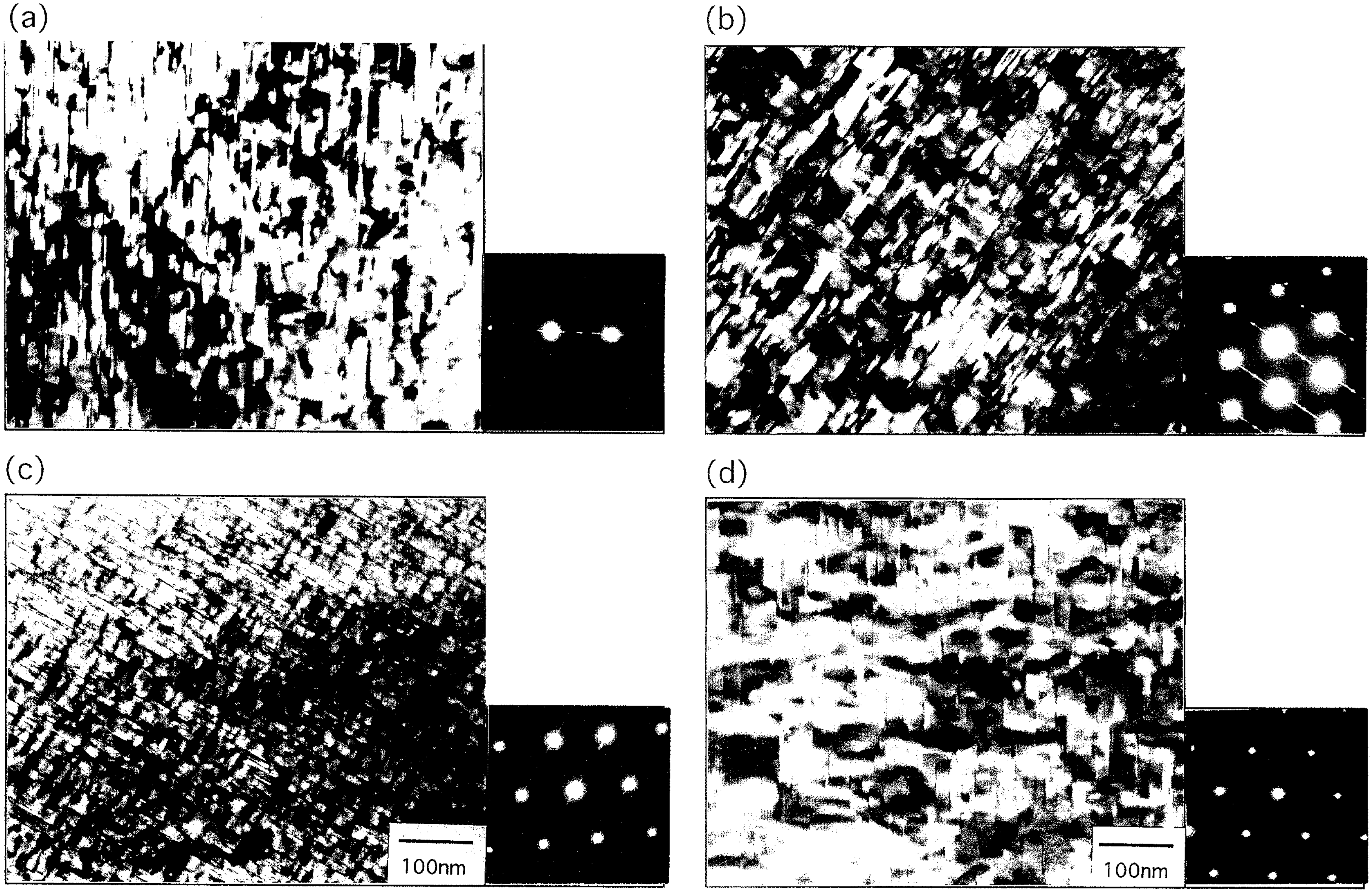

Fig. 7.4 Electron micrographs with diffraction patterns for (a)Al-Li-Cu-Zr, (b)Ag-added, (c)Ge-added and (d)Zn-added alloys aged at 433K for 346ks.

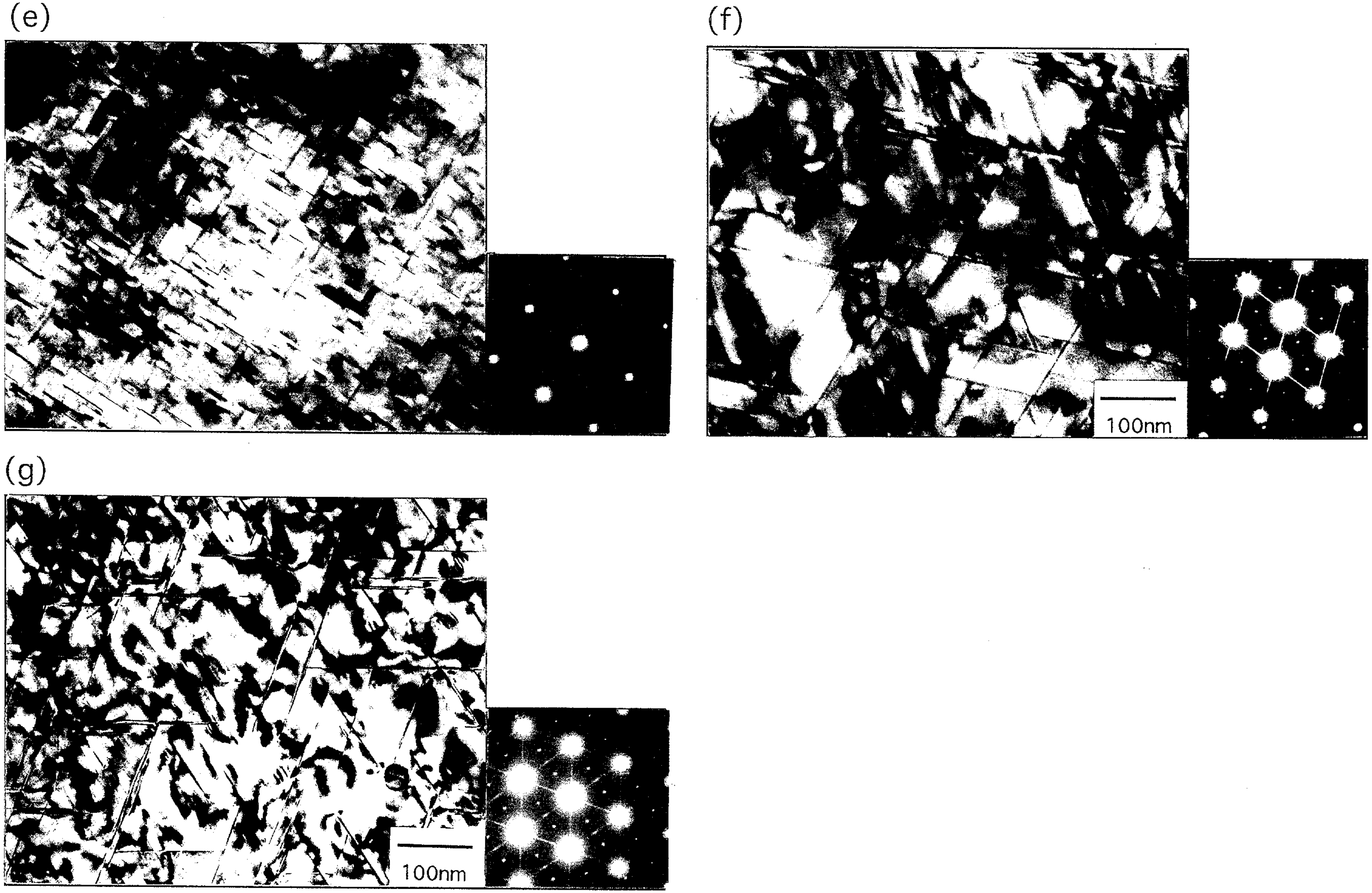

Fig. 7.4 Continued; (e)Si-added, (f)Mg-added and (g)(Mg+Ag)-added alloys aged at 433K for 346ks.

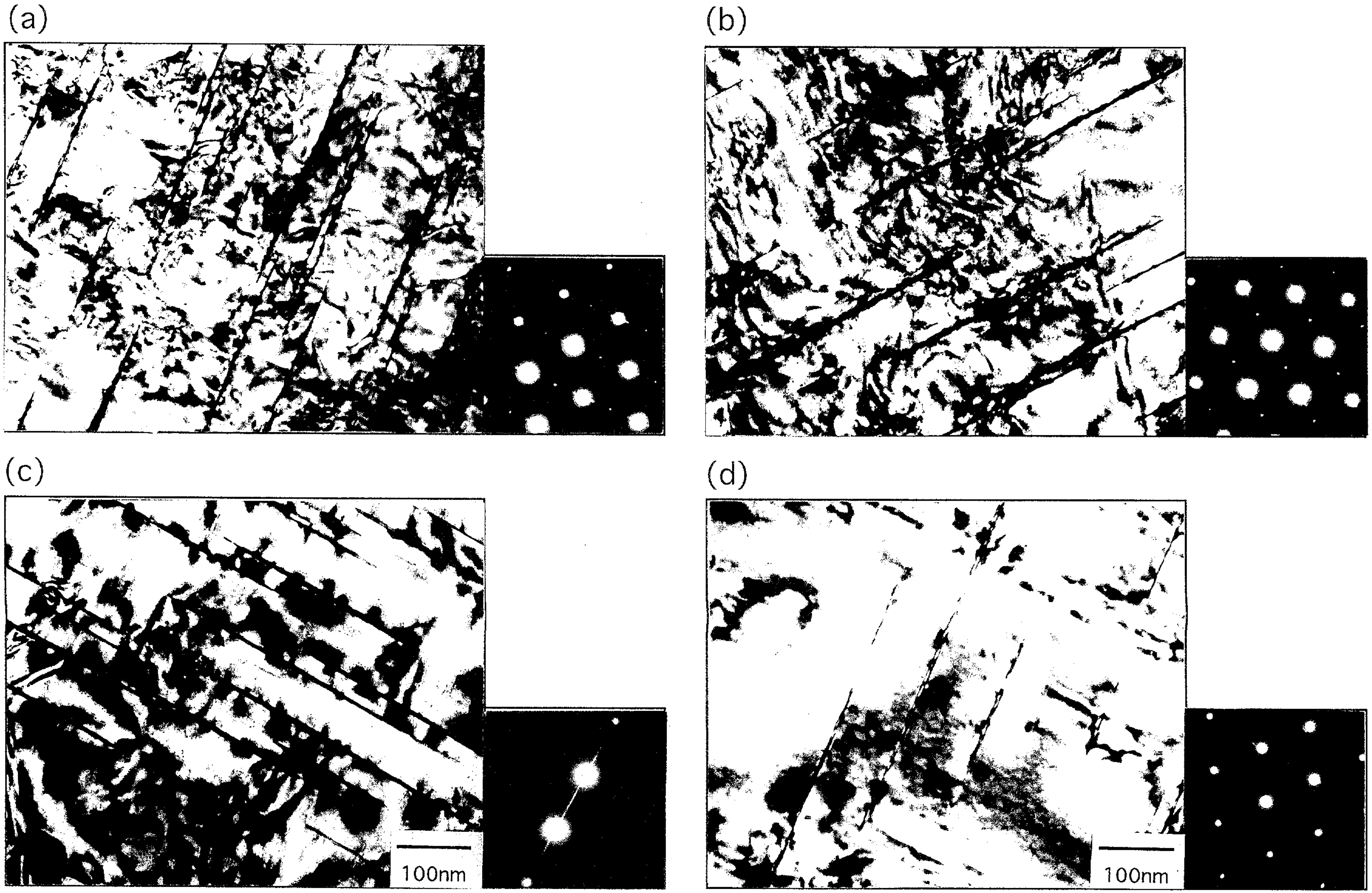

Fig. 7.5 Electron micrographs with diffraction patterns for (a)Al-Li-Cu-Zr, (b)Ag-added, (c)Ge-added and (d)Zn-added alloys aged at 463K for 86.4ks.

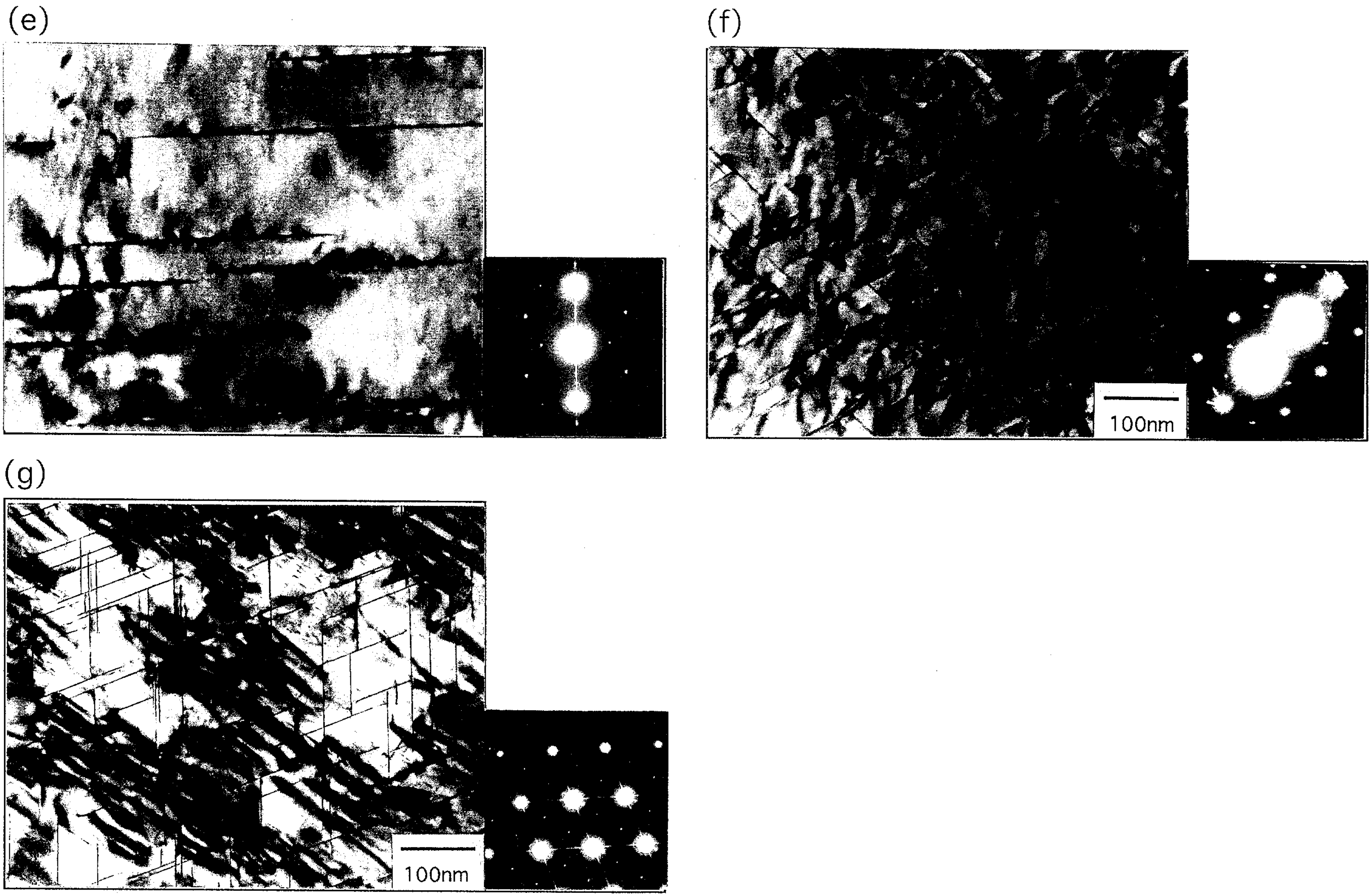

Fig. 7.5 Continued; (e)Si-added, (f)Mg-added and (g)(Mg+Ag)-added alloys aged at 463K for 86.4ks.

From the comparison of observed precipitates in Table 2.2, it is obviously confirmed that the small addition of Mg markedly stimulates the transgranular formation of the T_1 phase, whereas strengthening phases of the Mg-free alloys still remain GP zones with the coarsened T_1 phase only at subgrain boundaries. It should be also emphasized in Table 2.2 that metastable phase fields remain unchanged in both alloys at most of investigated temperatures. Unfortunately, no significant difference in the precipitate microstructures can be detected between the Mg- and (Mg+Ag)-added alloys.

7.4 Effects of quenching conditions

7.4.1 D.Q.(direct-quench) treatment

To date, several mechanisms of the T_1 phase nucleation have been proposed by taking into account the roles of solute atom clusters and metastable precipitates[2, 11-13]. The presence of such precursory structures could be verified by investigating the changes in the precipitate density of the T_1 phase after D.Q.(direct-quench) treatment. Figure 7.6(a) shows the variations in peak hardness with quenching bath temperature, *Tb*, for the (Mg+Ag)-added and Mg-free(i.e. Ag-added) alloys aged at 463K after D.Q. treatment. Here, it should be noted that the (Mg+Ag)-added alloy consists of a high number density of the T_1 phase, whereas strengthening phase of the Mg-free alloy remains GP zones, under this aging condition. Although the peak hardness of the (Mg+Ag)-added alloy gradually decreases with increasing *Tb*, no critical temperature indicated by a discontinuous change in the values of peak hardness is observed, unlike the case of a similarly treated Al-Zn-Mg alloy[22]. This is well explained by the precipitate microstructures of the (Mg+Ag)-added alloys after D.Q. treatment in Fig.7.6(b)-(e), which reveals that the precipitate size distributions of the T_1 phase are almost identical in both cases of *Tb*=RT and *Tb*=523K. Even in the 523K aging, furthermore, the similar continuous decrease in peak hardness is observed in the (Mg+Ag)-added alloy (Fig.7.7(a)), which ascribes to the continuous decrease in the number density of the T_1 phase as illustrated in the precipitate size distributions after D.Q. treatments from *Tb*=RT and *Tb*=523K (Fig.7.7(b)-(e)). These results indicate that no precursory structure of the T_1 phase, which has a certain solvus temperature within the measured *Tb* range, exists unlike the case of an Al-Zn-Mg alloy[22]. This continuous decrease in the T_1 phase precipitation by D.Q. treatment is well explained in terms of the difference in the vacancy concentrations as described in the following section. As for the GP zone formation in the Mg-free alloy, on the other hand, D.Q. treatment has almost no influence as suggested in the variations in peak hardness at both aging temperatures in

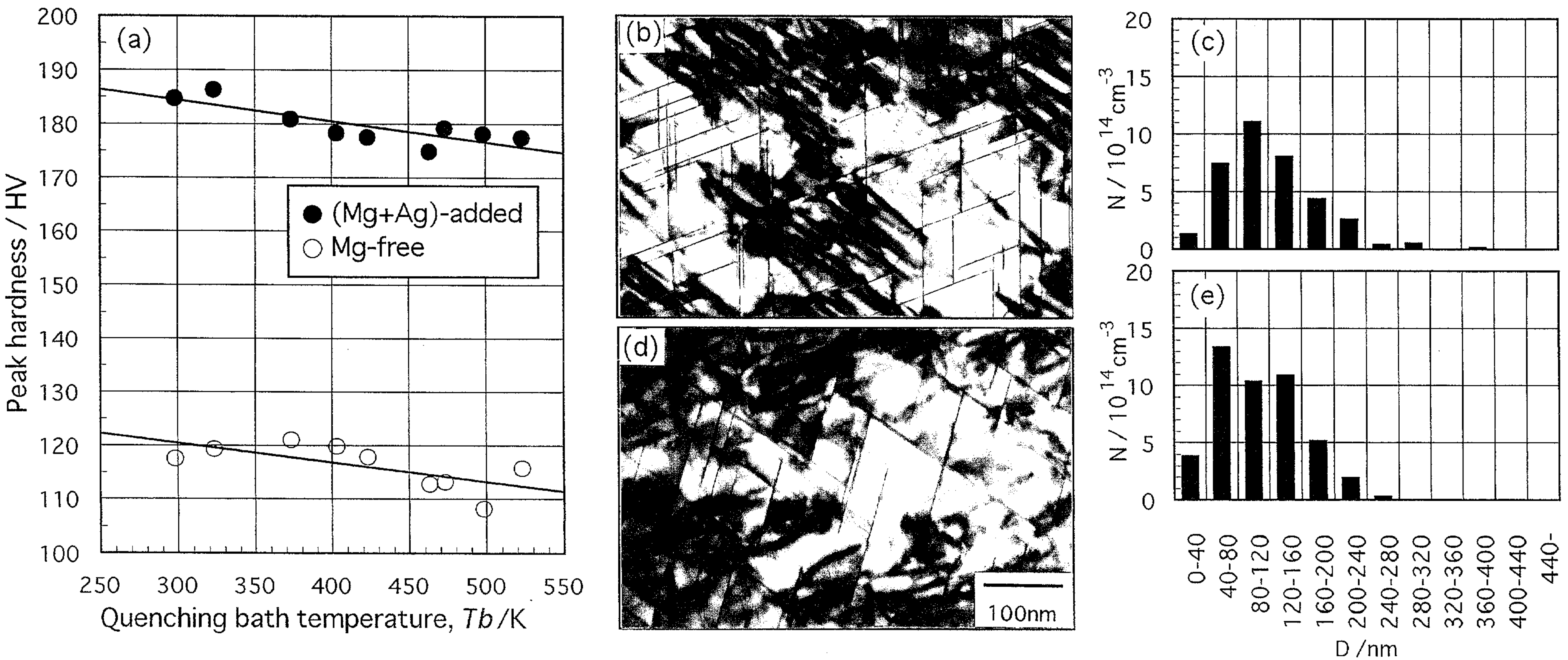

Fig.7.6 Variations of peak hardness in 463K aging with quenching bath temperatures, Tb, for (Mg+Ag)-added and Mg-free alloys (a) and electron micrographs and precipitate size distributions for (Mg+Ag)-added alloys aged at 463K for 36ks after D.Q. treatments from Tb=RT (b,c) and Tb= 523K (d,e) (N: number density of T_1 per unit cm^3, D: size of T_1).

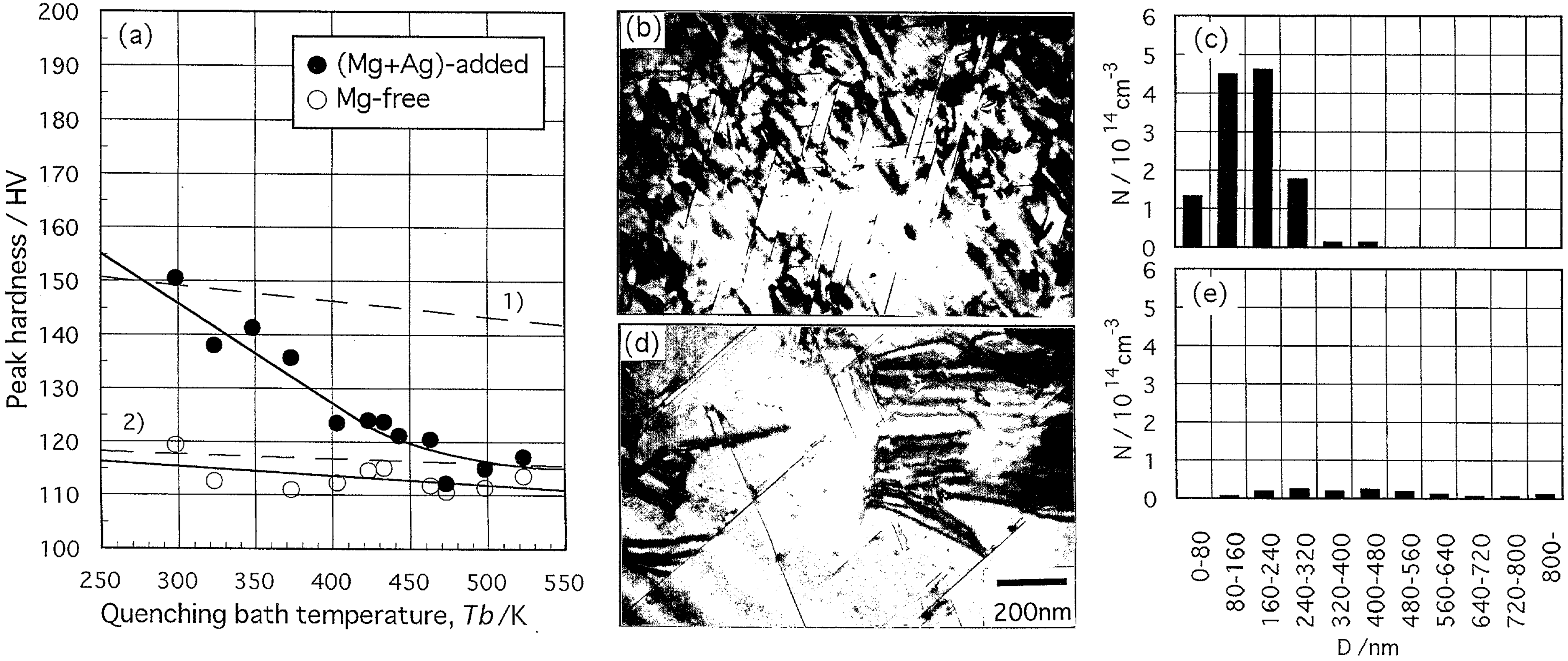

Fig.7.7 Variations of peak hardness in 523K aging with quenching bath temperatures, Tb, for (Mg+Ag)-added and Mg-free alloys (a) and electron micrographs and precipitate size distributions for (Mg+Ag)-added alloys aged at 523K for 1.8ks after D.Q. treatments from Tb=RT (b,c) and Tb=523K (d,e). The broken lines 1) and 2) show predicted hardness changes for the case of Ta<T* and Ta>T*, respectively (Ta: aging temperature, T*: solvus temperature).

Figs.7.6(a) and 7.7(a).

7.4.2 S.Q.(step-quench) treatment

S.Q.(step-quench) treatment was conducted to examine the role of quenched-in excess vacancies on the T1 phase nucleation in Al-Li-Cu alloys. Figure 7.8(a) shows the isothermal aging curves of hardness for the (Mg+Ag)-added and Mg-free(i.e. Ag-added) alloys aged at 463K after both W.Q. and S.Q. treatments. Compared with the Mg-free alloy, the (Mg+Ag)-added alloy after S.Q. treatment drastically decreases the amount of age-hardening rather than that after W.Q. treatment. From the comparison of the TEM micrographs after both quenching treatments (Fig.7.8(b), (d)), the decrease in age-hardenability of the (Mg+Ag)-added alloy after S.Q. treatment is found to arise from the pronounced decrease in the precipitate number density of the T1 phase. This suggests that quenched-in excess vacancies play an important role in the T1 phase nucleation resulting in the higher mechanical strength of the (Mg+Ag)-added alloy. The estimated concentration of quenched-in excess vacancies after S.Q. treatment at 673K is about 1/5~1/10 of that after W.Q. treatment from 778K (i.e. $\sim 10^{-4}$[23]). This ratio well agrees with the amounts of the T1 phase precipitation for the (Mg+Ag)-added alloys after both quenching treatments in Fig.7.8(c), (e). The decrease in the solute atom concentrations during S.Q. treatment is revealed to be negligible using electrical resistivity measurement. Although the decreased electrical resistivity after S.Q. treatment indicates that small amounts of some precipitates are formed at 673K, the decrease is only $\sim 2\text{n}\Omega\text{m}$ compared with that after W.Q. treatment.

7.5 Mechanism of accelerated T1 phase nucleation by Mg addition

7.5.1 Suggestions from experimental results

In general, it is well recognized that semi-coherent precipitates such as the T1 phase are not formed by the homogeneous nucleation but formed heterogeneously because of a decreased energy for nuclei formation. The heterogeneous nucleation sites for semi-coherent precipitates are normally accepted to be ①solute atom clusters, GP zones and some metastable precipitates, and/or ②secondary defects formed of quenched-in excess vacancies; e.g. small clusters of vacancies, voids and dislocation loops. In this work, it is examined first which of the two mechanisms works for the T1 phase nucleation in Al-Li-Cu alloys. Furthermore, the effects of both small amounts of additional elements and quenched-in excess vacancies are discussed based on vacancy-solute atom interactions and solute atom aggregates. Finally, on the basis of the experimental results obtained in this work a mechanism for the T1 phase

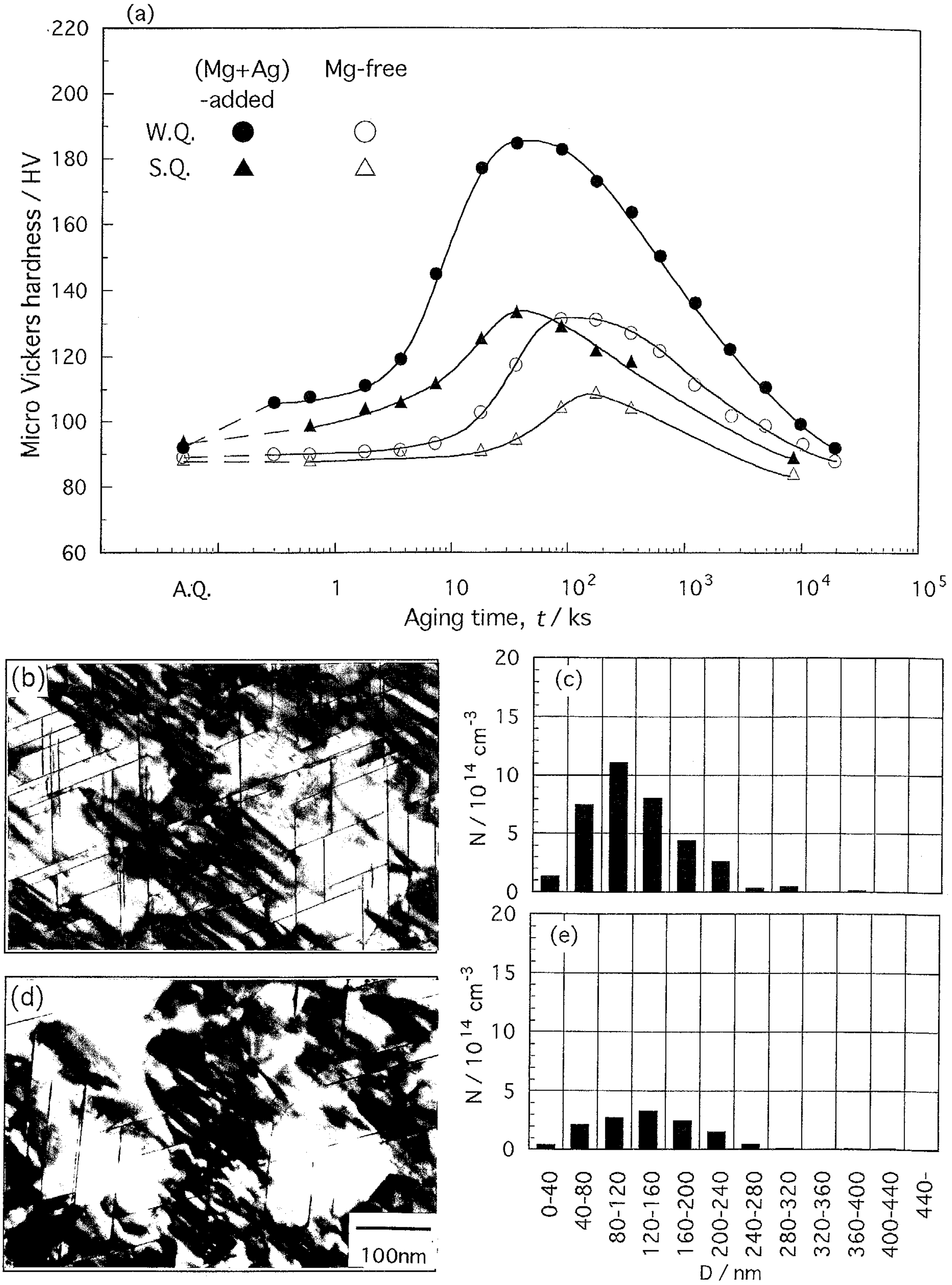

Fig.7.8 Variations of hardness with aging time for 463K aging (a) and electron micrographs and precipitate size distributions for (Mg+Ag)-added alloys aged at 463K for 36ks after W.Q. treatment from 778K (b,c) and S.Q. treatment from 673K (d,e).

nucleation is proposed.

The results of D.Q. treatment described in Section 7.4.1 indicate that no precursory structures of the mechanism ① act as heterogeneous nucleation sites for the T_1 phase. If the mechanism ① is the case, the variation in peak hardness for the (Mg+Ag)-added alloy after D.Q. treatment (Fig.7.7(a)) should be explained in the two cases below, in which two parameters; i.e. aging temperature *Ta* and solvus temperature of the precursory structure *T**, are important to describe the behavior.

i) The case of $Ta < T^*$

If *Ta* is lower than *T**, the precursory structures are sufficiently formed at *Ta*, then, the T_1 phase can nucleate on these precursors resulting in a high number density of the precipitates. Thus, the values of peak hardness remain high at all *Tb* as indicated by the broken line 1) in Fig.7.7(a).

ii) The case of $Ta > T^*$

If *Ta* is higher than *T**, the precursory structures formed at *Tb* will almost dissolve at *Ta*, then, the T_1 phase must nucleate only at subgrain boundaries resulting in a low number density of the precipitates. Thus, the values of peak hardness are low even after D.Q. treatment from low *Tb* as indicated by the broken line 2) in Fig.7.7(a).

Therefore, it is concluded from the above consideration in case i) and case ii) that the continuous decrease in peak hardness as indicated by the solid line in Fig.7.7(a) can not be explained in terms of the mechanism ①.

On the other hand, the results of S.Q. treatment described in Section 7.4.2 indicate that the substantial amount of quenched-in excess vacancies is essential to the T_1 phase nucleation in Al-Li-Cu alloys. This strongly suggests the presence of secondary defects of the mechanism ②, which act as heterogeneous nucleation sites for the T_1 phase. However, even if W.Q. treatment is applied to the Mg-free(i.e. Ag-added) alloys to introduce higher vacancy concentrations, the T_1 phase remains heterogeneous in distribution as illustrated in Fig.7.4(f), (g). Therefore, both the substantial amounts of vacancies and small additional Mg are necessary to stimulate the T_1 phase nucleation resulting in the higher number density of the precipitates. A Monte Carlo simulation can inquire visually into such the atomistic events even including vacancies.

7.5.2 Monte Carlo simulation results

The detailed analysis of the T_1 phase nucleation was made using nearest neighbor interactions for quaternary alloy systems. In this case, however, in order to investigate the effect of small additional Ag, the Al-Cu-Mg-Ag quaternary system was applied to the Monte Carlo simulation. The ignorance of Li has little influence on the inquiry into the T_1 phase nucleation because only Mg addition can stimulate the transgranular precipitation of the T_1 phase. The utilized simulation parameters for the Al-(Li)-Cu-Mg alloys are summarized in Table 7.1. Note that the interaction of divacancy, ε_{vv} is also introduced because quenched-in excess vacancies play an important role in the T_1 phase nucleation as described above. The value of ε_{vv} is estimated from previously reported binding energies of divacancy; i.e. 10.6-28.9kJ/mol (0.11-0.3eV)[23-26], whereas the vacancy concentration in the simulation system is assumed to be $\sim 7.5 \times 10^{-4}$, which is five times higher than that of pure Al at 793K (i.e. $\sim 1.5 \times 10^{-4}$). This increased vacancy concentration is ascribed to the preferential vacancy trapping by solute atoms at the solution temperature, resulting in the higher number density of secondary defects; e.g. small clusters of vacancies, voids and dislocation loops, formed in the subsequent aging treatments.

Figure 7.9 shows typical atom configurations on one atom layer of (001) plane in the Mg- and (Mg+Ag)-added Al-(Li)-Cu alloys simulated at 433K for 5×10^6MCs. Although Li atoms are not illustrated in these figures, it is sufficiently reasonable to consider that the extremely rapid clustering of Li atoms also takes place as observed in the low-temperature aging in Chapter 6. Unlike the previous cases of Al-Cu (Chapter 4), Al-Li (Chapter 5) and

Table 7.1 Ordering parameters utilized in the simulation of Al-(Li)-Cu-Mg-Ag alloys (in kJ/mol). It should be noted that an interaction of divacancy is also taken into account.

	Al	Mg	Ag	Cu	Vacancy
Al	—	1.18	1.29	2.20	—
Mg	—	—	-1.80	0.50	—
Ag	—	—	—	2.40	—
Cu	—	—	—	—	—
Vacancy	0	-8.50	2.16	0.860	-18.1

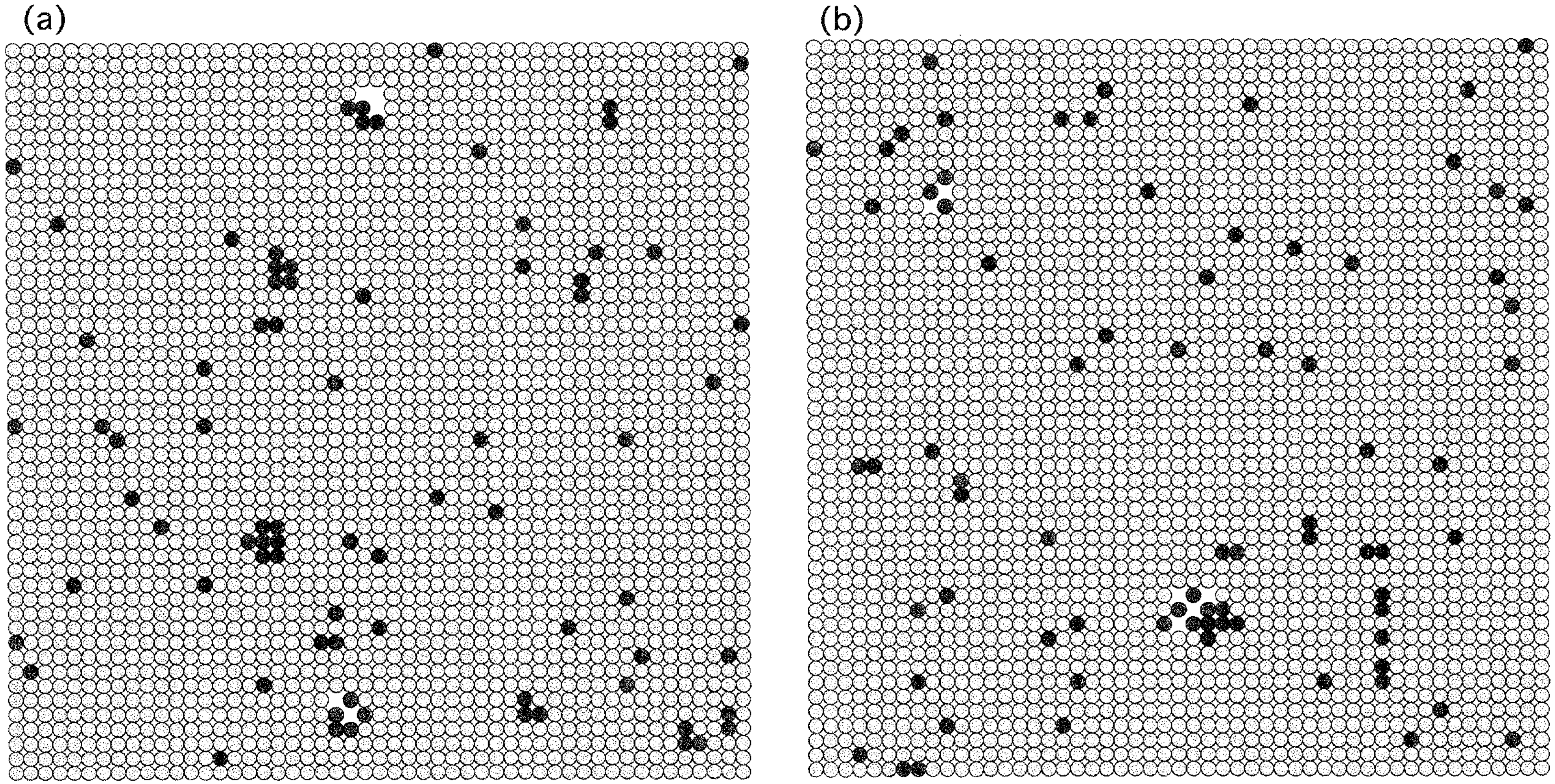

Fig.7.9 Typical atom configurations on one atom layer of (001) plane in Mg-added(a) and (Mg+Ag)-added(b) Al-(Li)-Cu alloys simulated at 433K for 5×10^6MCs. The yellow, black, red and blue circles represent Al, Cu, Mg and Ag atoms, respectively.

Al-Li-Cu (Chapter 6) alloys, however, it is obviously seen that a relatively high number density of vacancy clusters indicated by omitted circles are formed mostly next to Mg atoms indicated by red circles (Fig.7.9(a)). Cu atoms indicated by black circles are also detected around these Mg/Vacancy clusters because of the strong interaction between Cu and Mg in Table 7.1. Figure 7.10 shows the variations in number density, *N*, and average size, *n*, of vacancy clusters during dynamical evolution of the Mg- and (Mg+Ag)-added Al-(Li)-Cu alloys simulated at 433K. The small addition of Ag obviously affects the formation behavior of vacancy clusters resulting in a smaller and more densely distribution. The similar tendency is observed in the clustering behavior of Cu atoms as shown in Fig.7.11. These results strongly suggest that a small amount of Ag increases the number density of the T_1 phase by increasing the number of Mg/Cu/Vacancy complexes, which act as heterogeneous nucleation sites for the T_1 phase, because of a strong tendency of Ag to trap Mg atoms resulting in the suppressed diffusion of Mg. Such the effect is revealed in the atom configuration of (Mg+Ag)-added Al-(Li)-Cu alloy in Fig.7.9(b), in which the fourth additional Ag indicated by blue circles is most frequently detected around Mg/Cu/Vacancy clusters.

7.5.3 Proposed mechanism on T_1 phase nucleation

A new mechanism for the enhanced T_1 phase nucleation by additional Mg is proposed as follows. As strongly suggested by previously reported binding energies (Table 1.2) and utilized simulation parameters (Table 7.1), a relatively strong Mg-Vacancy interaction will contribute to the rapid formation of Mg/Vacancy pairs in the early stage of aging. Furthermore, because of a strong interaction between Mg and Cu (Table 7.1) Cu atoms also intend to combine with Mg atoms to form Mg/Cu/Vacancy complexes throughout the Al matrix. At elevated aging temperatures higher than ~400K, therefore, these complexes extremely stimulate the transgranular nucleation of the T_1 phase because a high number density of stacking faults are easily provided with the surrounding Cu- and presumably Li-rich regions. Figure 7.12(a) shows the high-resolution lattice images of the T_1 phase in the (Mg+Ag)-added alloy aged at 433K for 18ks, which almost corresponds to the time when the hardness starts to increase in Fig.7.2. From the stage of the precipitate nucleation, thin plates consisting of four layers, which yield a thickness equal to one T_1 unit cell[27], are observed showing the stacking of $(0001)_{T1}$ planes. This image contrast is entirely compatible with that of the grown T_1 phase as shown in Fig.7.12(b), which reveals that new four layers are added to increase the plate thickness at growth ledges on the plates. This experimental observation strongly supports that the stacking faults on the $\{111\}_\alpha$ planes are extremely

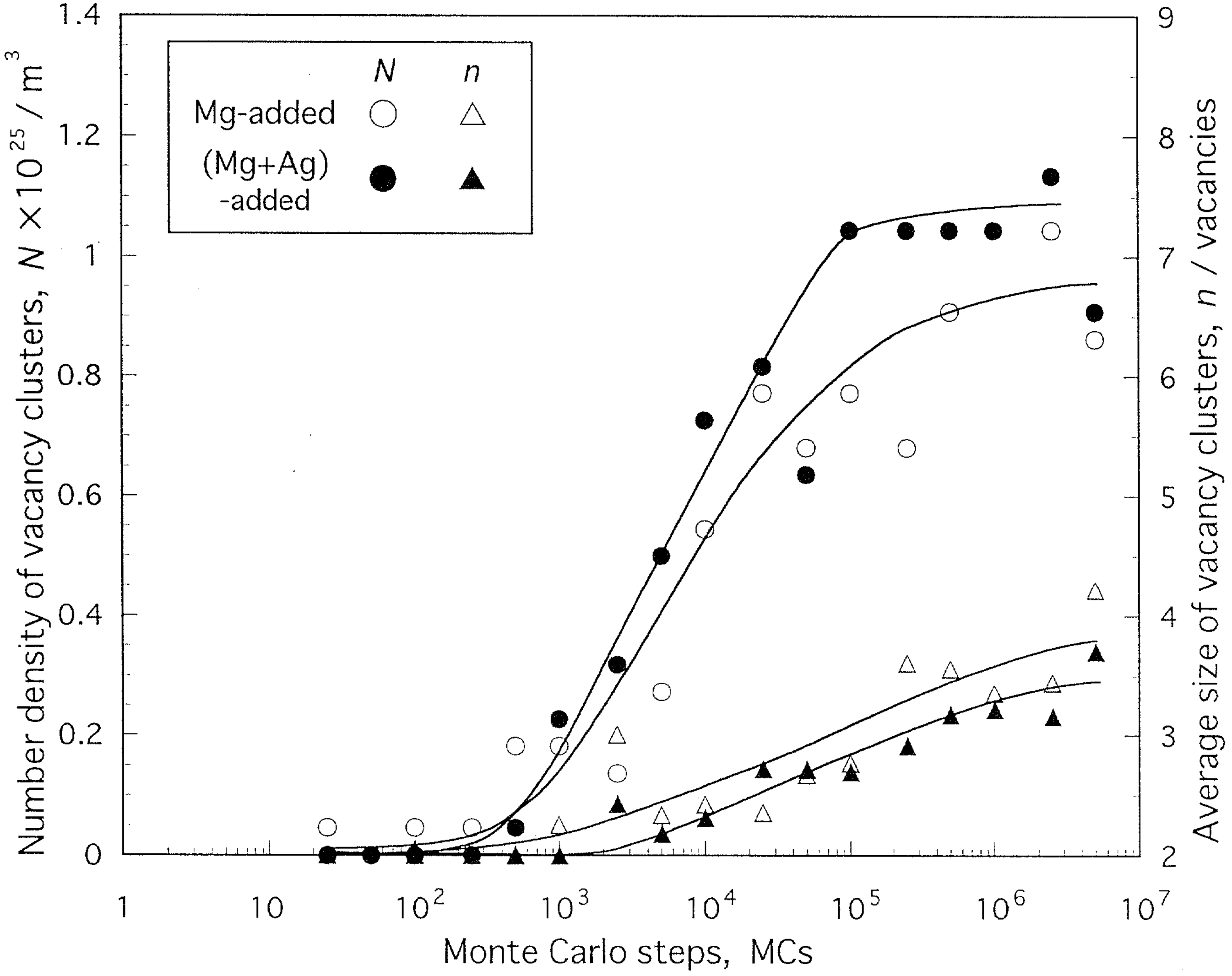

Fig.7.10 Variations in number density, *N*, and average size, *n*, of vacancy clusters with Monte Carlo steps(MCs) for Mg- and (Mg+Ag)-added alloys simulated at 433K.

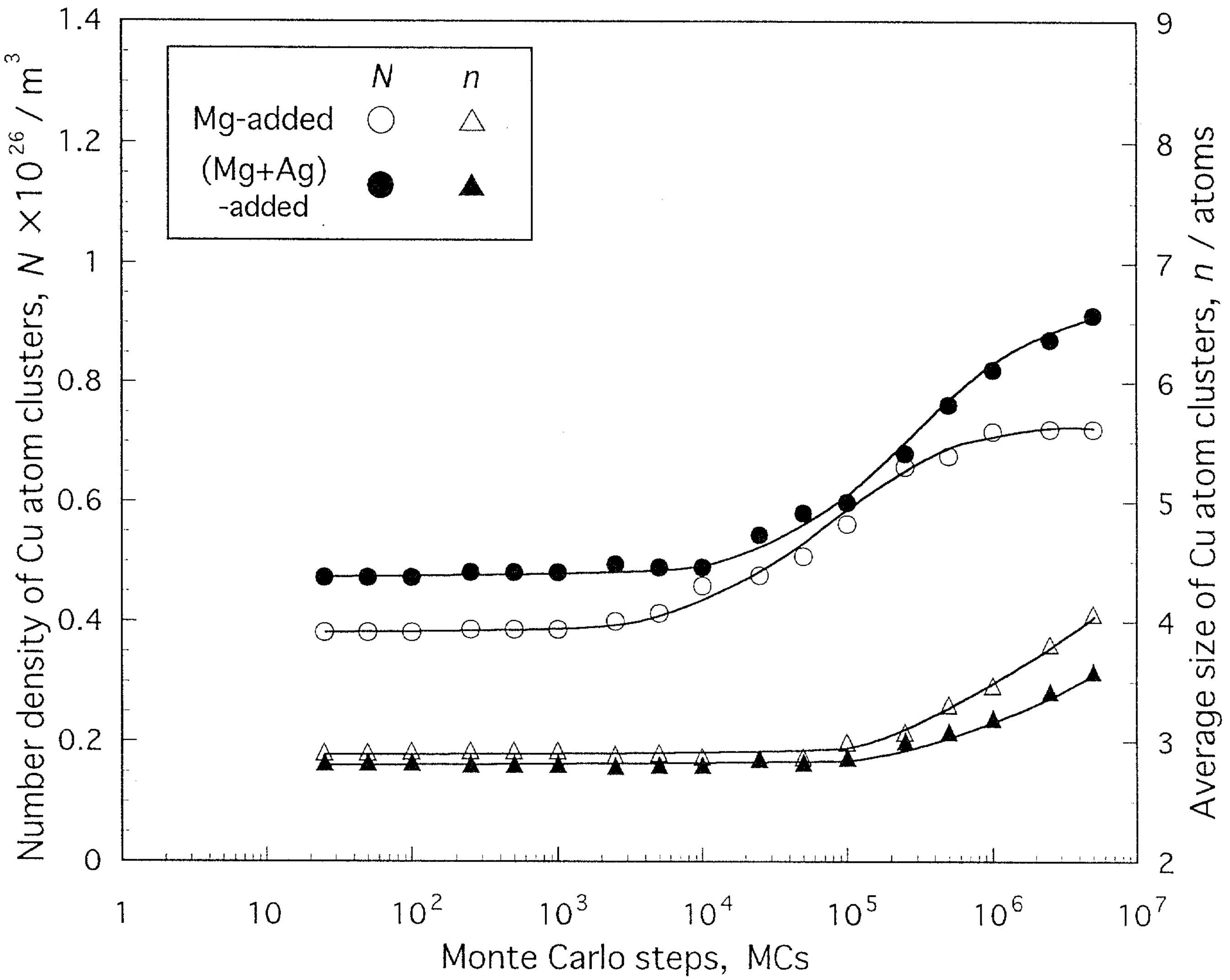

Fig.7.11 Variations in number density, *N*, and average size, *n*, of Cu atom clusters with Monte Carlo steps(MCs) for Mg- and (Mg+Ag)-added alloys simulated at 433K.

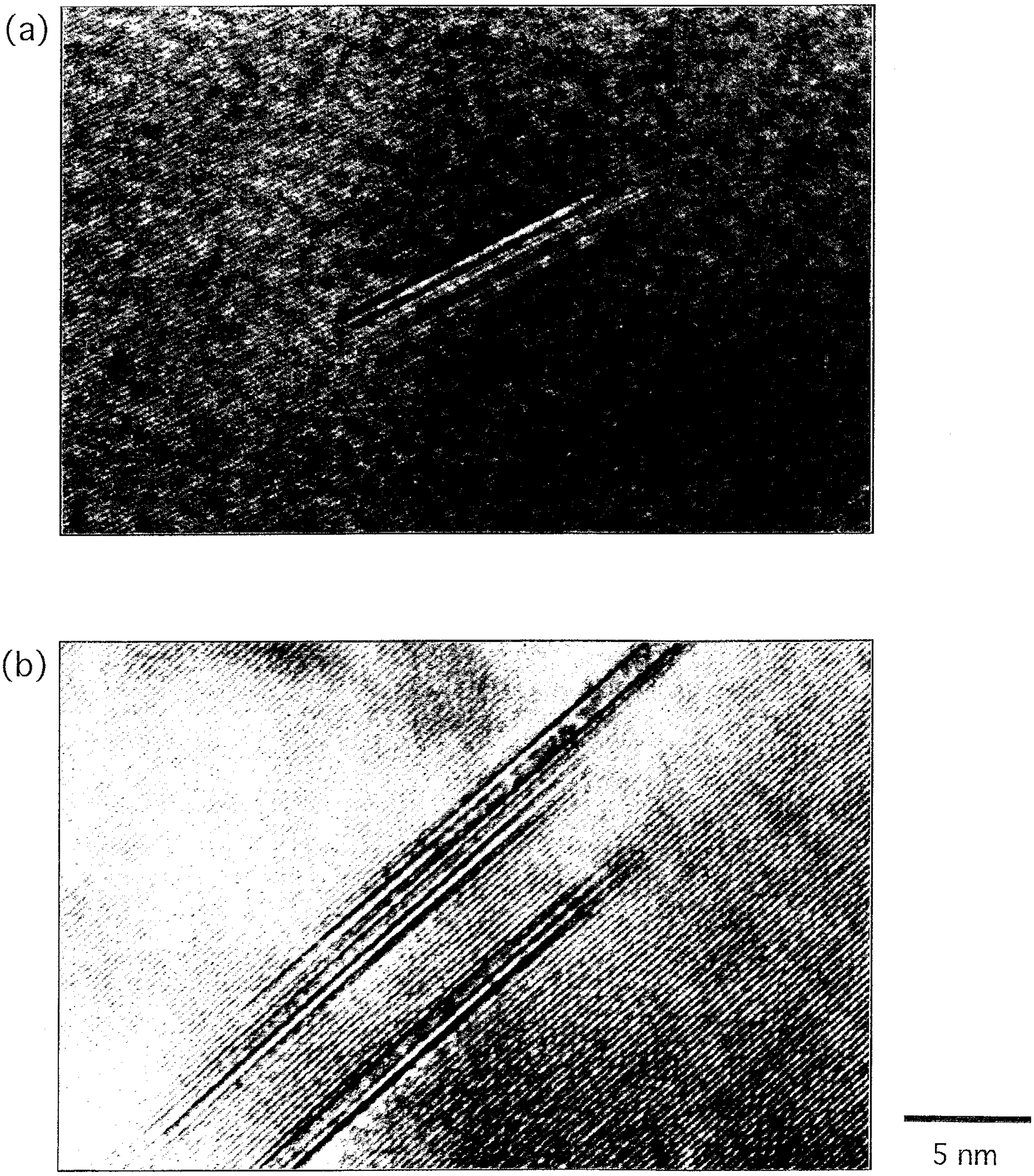

Fig.7.12 High-resolution lattice images of the T1 phase in (Mg+Ag)-added Al-Li-Cu alloys aged at 433K for 18ks(a) and 345.6ks(b)

essential and easily provided if a small amount of Mg is added to Al-Li-Cu alloys. The proposed mechanism of the effect of Mg/Cu/Vacancy complexes, therefore, is considered to be sufficiently probable. The simultaneous addition of Ag with Mg is also effective to increase further the number density of Mg/Cu/Vacancy complexes because of the strong interaction between them as suggested along the vertical axis in Fig.7.13. It should be noted that Zn is also expected to be the effective element to improve the mechanical properties of Al-Li-Cu alloys because of the strong interaction with Mg atoms.

The proposed mechanism; i.e. Mg/Cu/Vacancy complex mechanism, well explains the experimental results obtained in this work. Under this mechanism, since the size distributions of Mg/Cu/Vacancy complexes in Mg-added Al-Li-Cu alloys; e.g. (Mg+Ag)-added alloy, are considered to be determined by the concentrations of quenched-in excess vacancies, D.Q. and S.Q. treatments are expected to give the different size distributions of the complexes depending on *Tb* as illustrated in Fig.7.14(a). Therefore, the variation in peak hardness for the (Mg+Ag)-added alloy after D.Q. treatment (Fig.7.7(a)) is well interpreted by the continuous decrease in the number density of the complexes with larger sizes than an effective critical size, r*, for the T_1 phase nucleation. Under the mechanism ①, on the other hand, the number density of precursory structures formed at *Tb* is expected to be as illustrated in Fig.7.14(b). At an aging temperature *Ta*, therefore, the available number of nucleation sites increases with increasing *Tb*, which leads to contradictory results of D.Q. treatments in Fig.7.7. Therefore, the proposed mechanism in which Mg/Cu/Vacancy complexes play an important role in the T_1 phase nucleation in Al-Li-Cu alloys is sufficiently probable. Unfortunately, no other additional elements form such the complexes with Cu, even if they have strong interactions with vacancies as Ge and Si (Table 1.2), because these elemental atoms preferentially combine with Li atoms, not with Cu atoms, as predicted from characteristic interactions in Figs.4.8 and 5.10.

7.6 Conclusions

The effects of microalloying elements and quenching conditions on the age-hardening behavior and precipitation microstructures in an Al-5.0Li-2.3Cu-0.04Zr (in mol%) alloy were investigated at aging temperatures from 403 to 523K using hardness measurement and transmission electron microscopy. Six types of alloys; i.e. the Ag-, Ge-, Zn-, Si-, Mg- and (Mg+Ag)-added alloys, were prepared and three different quenching conditions; i.e. W.Q.(water-quench), D.Q.(direct-quench) and S.Q.(step-quench) treatments, were applied.

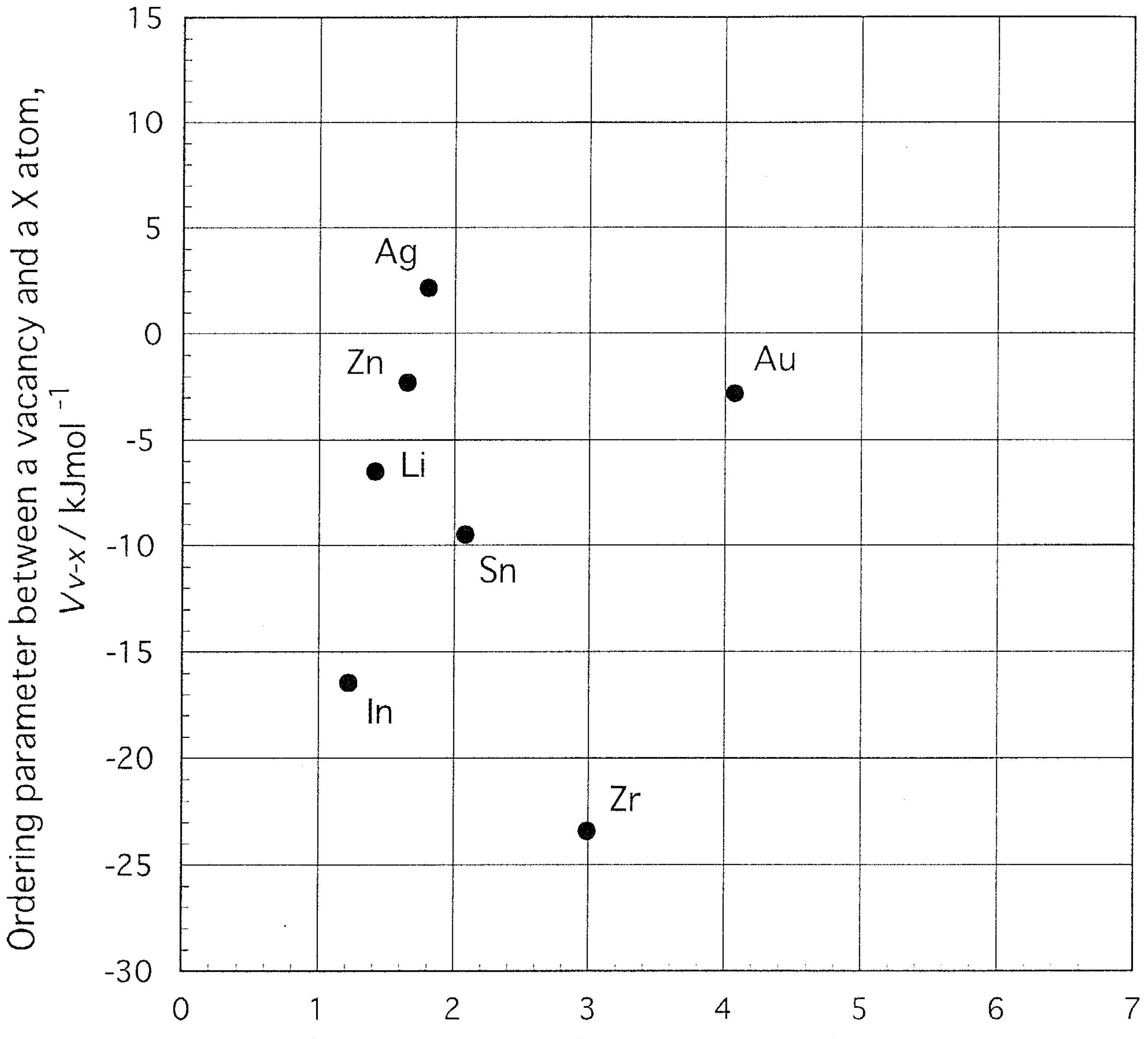

Fig.7.13 Relationships between $V_{v\text{-}x}$ and $V_{Mg\text{-}x}$ for various elemental atoms, x ($V_{v\text{-}x}$: ordering parameter between a vacancy and a x atom, $V_{Mg\text{-}x}$: ordering parameter between Mg and x atoms).

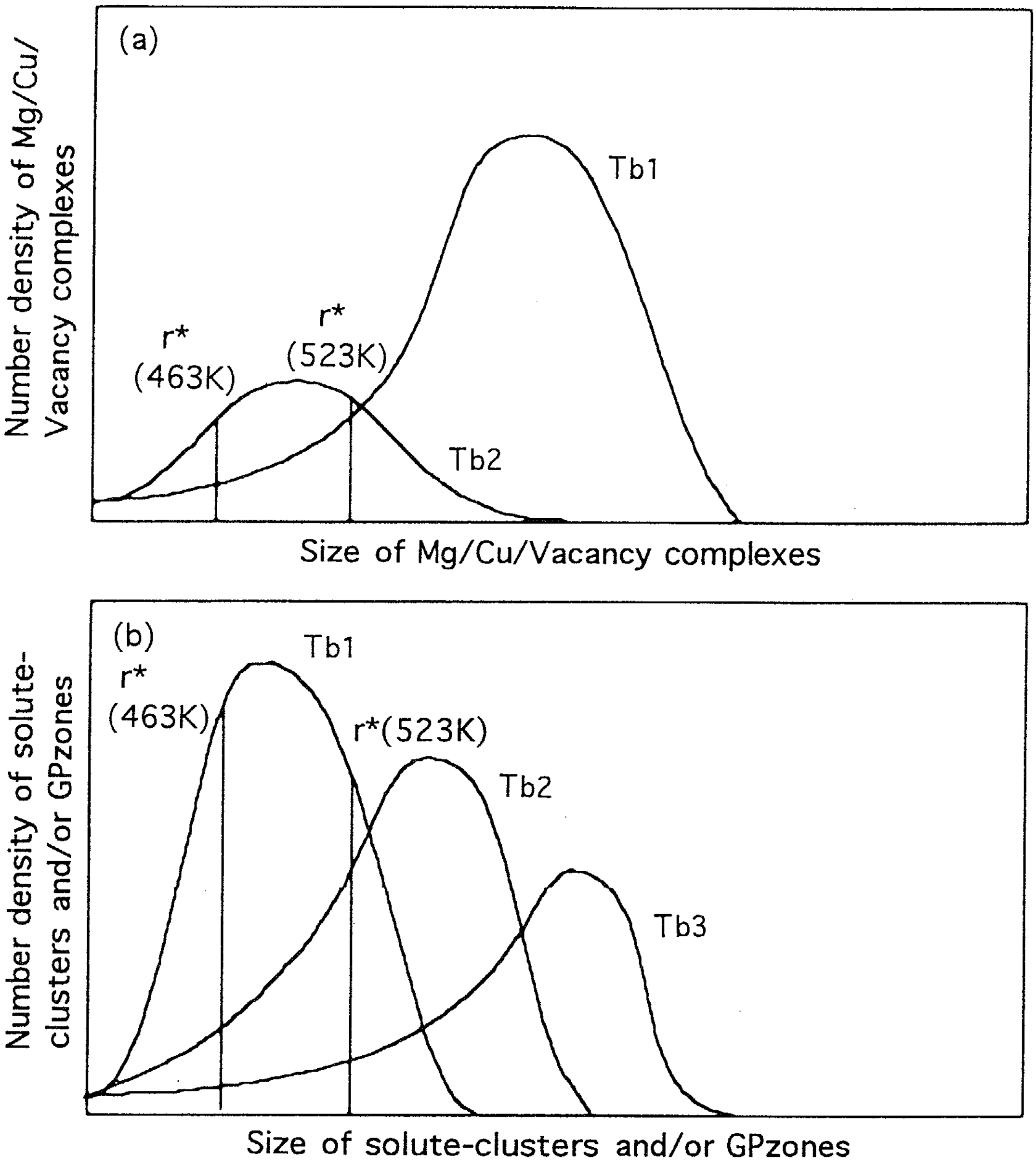

Fig.7.14 Schematic illustrations of nuclei size distributions for the T_1 phase in Al-Li-Cu alloys after D.Q. treatment at different quenching bath temperatures, Tb1, Tb2 and Tb3 (Tb1< Tb2<Tb3). (a) Mg/Cu/Vacancy complexes and (b)solute-clusters and/or GP zones. Note that the vacancy concentration increases with decreasing Tb. (r* : critical size).

The obtained results are summarized as follows.

(1) A small amount of additional Mg to the quaternary alloy markedly stimulates the T_1 phase precipitation resulting in an enhanced age-hardening at elevated aging temperatures higher than ~400K. This is because that Mg/Cu/Vacancy complexes act as heterogeneous nucleation sites for the T_1 phase. Such situations can be directly observed in atom configurations during the simulation.

(2) In contrast, Ag-, Ge-, Zn- or Si-added Al-Li-Cu-Zr alloy exhibits the similar microstructure to that in the quaternary alloy, which composes of GP zones and/or the θ' phase with the coarsened T_1 phase only at subgrain boundaries. This is because no complexes including Cu atoms and vacancies are formed in these alloys.

(3) The variations in the T_1 phase distribution with *Tb* (quenching bath temperature) in D.Q treatment can not be explained by the nucleation mechanism relating to solute atom clusters and/or metastable precipitates, but can reasonably explained by the size distributions of Mg/Cu/Vacancy complexes determined by the introduced concentrations of quenched-in excess vacancies.

References

[1] T.J.Langan and J.R.Pickens: Proc. 5th Int. Al-Li Conf., **Vol.2** (1987), 691.

[2] J.R.Pickens, F.H.Heubaum, T.J.Langan and L.S.Kramer: Proc. 5th Int. Al-Li Conf., **Vol.3** (1987), 1397.

[3] I.J.Polmear and R.J.Chester: Scripta Metall., **23** (1989), 1213.

[4] I.J.Polmear: Trans. Met. Soc. AIME, **Vol.230** (1964), 1331.

[5] J.A.Taylor, B.A.Parker and I.J.Polmear: Metal Sci., **12** (1978), 478.

[6] R.J.Chester and I.J.Polmear: *The Metallurgy of Light Alloys*, Inst. of Metals, London, (1983), p.75.

[7] S.Kerry and V.D.Scott: Metal Science, **18** (1984), 289.

[8] B.C.Muddle and I.J.Polmear: Acta metall., **37** (1989), 777.

[9] H.Suzuki, M.Kanno and N.Hayashi: J. Jpn. Inst. Light Metals, **32** (1982), 577.

[10] V.D.Scott, S.Kerry and R.L.Trumper: Mater. Sci. and Tech., **3** (1987), 827.

[11] G.Itoh, Q.Cui and M.Kanno: Mater. Sci. and Eng. A, **A221** (1996), 128.

[12] H.Suzuki, M.Kanno and N.Hayashi: J. Jpn. Inst. Light Metals, **32** (1982), 88.

[13] R.J.Rioja and E.A.Ludwiczak: Proc. 3th Int. Al-Li Conf., (1985), 471.

[14] H.K.Hardy and J.M.Silcock: J. Inst. Met., **84** (1955-56), 423.

[15] B.Noble and G.E.Thompson: Met. Sci. Jour., **6** (1972), 167.

[16] J.C.Huang and A.J.Ardell: Mater. Sci. Tech., **3** (1987), 176.

[17] W.A.Cassada, G.J.Shiflet and E.A.Starke, Jr.: Scripta Metall., **21** (1987), 387.

[18] V.Radmilovic and G.Thomas: J. de Physique, colloque, **C3** (1987), 385.

[19] J.M.Howe: J. Metals, **39** (1987), 13.

[20] K.S.Vecchio and D.B.Williams: Metall. Trans. A, **19A** (1988), 2885.

[21] J.C.Huang: Scripta Metall., **27** (1992), 755.

[22] H.Inoue, T.Sato, Y.Kojima and T.Takahashi: Metall. Trans. A, **12A** (1981), 1429.

[23] R.W.Siegel: J. Nuclear Materials, **69&70** (1978), 117.

[24] Landolt-Bornstein: *Numerical Data and Functional Relationship in Science and Technology*, **Vol.25**, *Atomic Defects in Metals*, ed. by H.Ullmaier, Springer-Verlag, Berlin, (1991).

[25] M.Doyama: Bulletin of Japan Inst. Metals, **34** (1995), 559.

[26] S.Ozbilen and H.M.Flower: Acta matall., **37** (1989), 2993.

[27] W.A.Cassada, G.J.Shiflet and E.A.Starke, Jr: Metall. Trans. A, **22A** (1991), 287.

Chapter 8
Prediction of Effects of Microalloying Elements and Application to Alloy Designing of New Al-Li-Cu Base Alloys

8.1 Effects of microalloying elements on mechanical properties of alloys

In general, small amounts of metallic elements inevitably get mixed in alloys not only as microalloying elements but also as impurities from ingots and/or crucible. Especially from a commercial application point of view, therefore, it has been extremely required to elucidate the detailed effects of these elements on mechanical properties of alloys. Although the considerable number of investigations on microalloying additions have been made for various alloy systems so far, most of them were conducted with a great deal of effort in a haphazard way, in a manner of speaking. Recently, some theoretical approaches[1-8] were also proposed to predict the effects of microalloying elements, but they mainly address the microstructure changes induced by the microalloying additions rather than the improved mechanical properties of the alloys. In this work, as an alternative and effective approach to the latter purpose, a computer simulation using a Monte Carlo method has been applied to each case of Al-Cu, Al-Li and Al-Li-Cu alloys containing various additional elements. The obtained simulation results are well classified in terms of the characteristic features of each microalloying element in these alloys.

8.1.1 Classification of effects of microalloying elements

In this work, some unsolved problems in the investigated alloys were taken up and those mechanisms were proposed based on a theoretical approach using a Monte Carlo simulation. In particular, the characteristic effects of Mg addition, which include both the accelerated nucleation of GP zones and the T_1 phase and the suppressed growth of GP zones and the δ' phase, were revealed for the first time by taking into account the roles of additional Mg and quenched-in excess vacancies. The classification of the predicted effects of each microalloying element in Al-Cu, Al-Li and Al-Li-Cu alloys is summarized in Table 8.1. Not only good agreement with previously reported results (Tables 4.3 and 5.5) but also first prediction for previously never reported elements is a most important result obtained in this work. These results are entirely ascribed to the utilized simulation parameters, which were derived from characteristic quantities of each element in Chapter 3. Although few reported values of maximum solubility of solute elements in pure Li unfortunately decrease the number of predictable elements, the pronounced effects of Mg are well

Table 8.1 Classification of the effects of various microalloying elements in Al-Cu, Al-Li and Al-Li-Cu alloys obtained from this simulation.

	Growth of GP(1) zones in Al-Cu alloys (Chapter 4)	Growth of δ' or its precursory structures in Al-Li alloys (Chapter 5)	Simultaneous formation of GP(1) zone and δ' in Al-Li-Cu alloys (Chapter 6)	Formation of T_1 phase in Al-Li-Cu alloys (Chapter 7)
Elements to accelerate	—	—	Mg (Nucleation of GP zone)	Mg, (Mg+Ag) (Nucleation of T_1)
Elements to exert no influence	Ti, V, Cr, Fe, Co, Ni, Zn, Nb, Ag, Ta, W, Au	Cu, Zn, Ag, Au	Zn, Ag	Zn?, Ag
Elements to suppress	Li, Mg, Zr, Cd, In, Sn, Pb	Mg, Cd, In	Mg, Cd, In (Growth of both precipitates)	—

explained by simultaneous strong interactions with both Li and Cu as shown in Fig.8.1. Zn is also expected to be the second effective element to improve the mechanical properties of Al-Li-Cu alloys as illustrated in Figs.7.13 and 8.1. As for the effect of Mg on the suppressed growth of GP zones and the δ' phase, in contrast, the preferential vacancy trapping mechanism[9] is applicable similarly to the well-known cases of Sn, In and Cd because the utilized interactions between a solute atom x and a vacancy; i.e. ordering parameter $V_{v\text{-}x}$, (Figs.4.8 and 5.10), are qualitatively well compatible with experimentally reported binding energies(Table 1.2). In order to inquire atomistic events never detected using any available experimental methods, therefore, the Monte Carlo simulation is proved to be sufficiently effective if reliable interactions can be utilized.

8.1.2 Extension of the simulation model to other alloy systems

The utilized simulation model appears to be applicable to other alloy systems. Even only in Al base alloys, clustering processes of solute atoms are observed in Al-Ag and Al-Zn systems, whereas ordering processes of $L1_2$-type structures take place in Al-Zr and Al-Sc systems. Under a regular solution approximation, the corresponding phase diagram provides reasonable interactions between the constituent two atom species. As for maximum solubilities of solute elements in pure Li, few values were unfortunately reported resulting in the decreased number of predictable elements in this simulation model(Table 3.6). However, the absence of experimentally reported phase diagrams may be substituted with the Computer Calculation of Phase Diagram (CALPHAD) method[10]. The interactions between non-metallic atom species is also another problem. Since the proposed parameter derivation method in Chapter 3 is valid only for crystal structures of fcc, hcp and bcc, microalloying elements having other crystal structures can not be estimated. In fact, under the same derivation method Si or Ge has an anomalous strong interaction between the same atom species, which forms clusters even at solution treatment temperatures during the simulation, as suggested in Fig.5.6. Therefore, the extension of the utilized simulation model to a wide range of alloy systems requires a further improved derivation method of accurate interatomic interactions.

8.2 Concept for alloy designing of new high strength Al-Li-Cu alloys

In this work, according to the obtained theoretical prediction on the role of microalloying elements, a concept for alloy designing of new high strength Al-Li-Cu alloys was proposed. As described in Chapter 1, to propose the concept is one of major objectives in the present

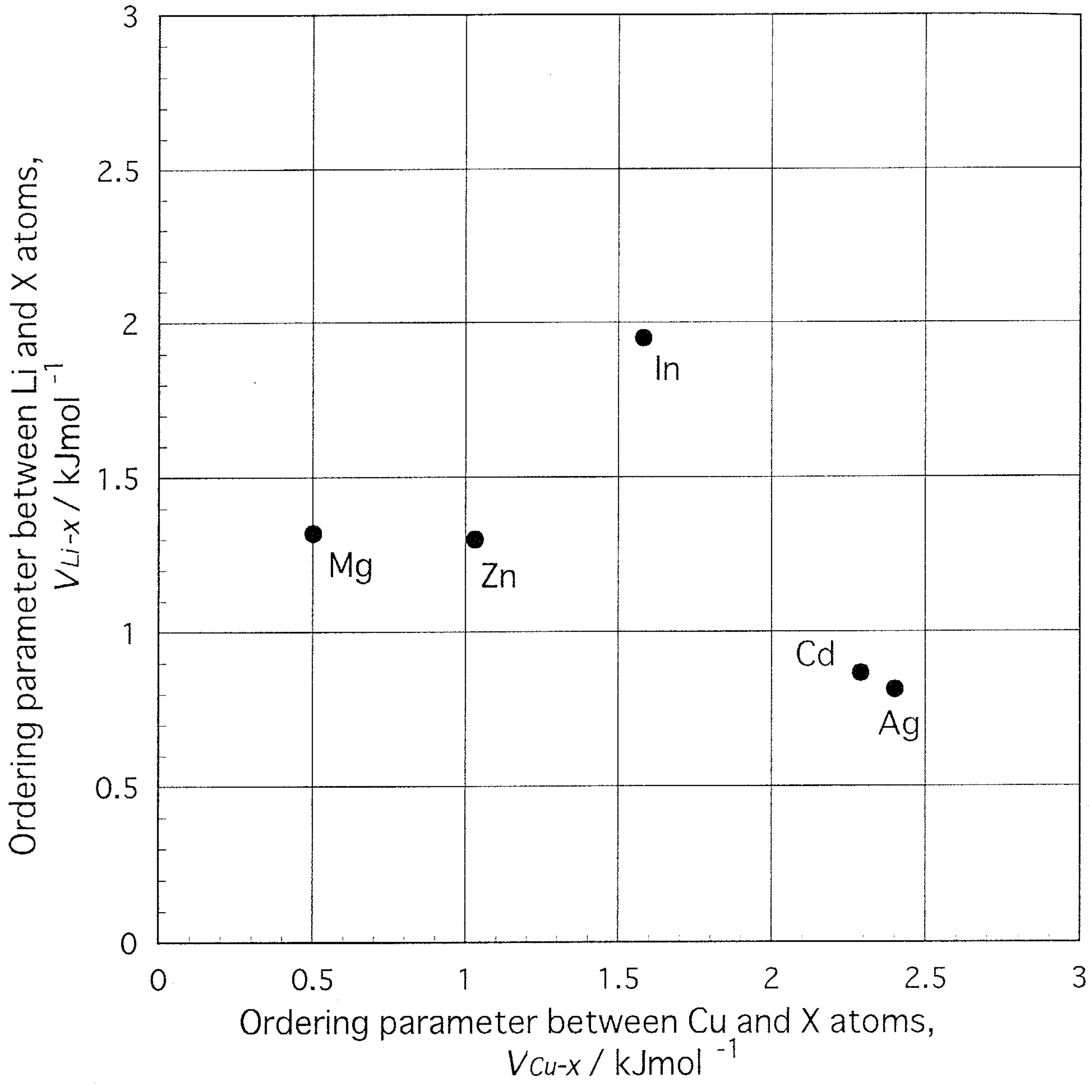

Fig.8.1 Relationships between $V_{Li\text{-}x}$ and $V_{Cu\text{-}x}$ for various elemental atoms, x ($V_{Li\text{-}x}$: ordering parameter between Li and x atoms, $V_{Cu\text{-}x}$: ordering parameter between Cu and x atoms).

thesis. The concept of alloy designing is composed of ①the control of Cu and Mg contents, ②the selection of microalloying elements and ③the optimization of applied solution treatment temperatures.

8.2.1 Optimization of alloy composition

From the results in the preceding chapters, the role of each element in Al-Li-Cu-Mg-Ag-Zr alloys and its desirable content are summarized as follows.

Li : Although higher concentrations are desirable for high specific strength and low density of the alloys, a reported optimum amount of 1.3mass% (4.8mol%) [11] was selected in order to avoid the δ ' phase formation, which results in a low ductility and low fracture toughness of the alloys due to the superlattice dislocation mechanism (i.e. planner sliding of dislocations).

Cu : For good age-hardenability and weldability, a relatively high content was selected despite less superiority of density because these properties are entirely attributed to Cu-bearing precipitates; i.e. GP zones and the T_1 phase.

Mg: The pronounced effects on the increased mechanical strength of Al-Li-Cu alloys are quite essential because any other microalloying elements can not achieve the same high strength as that of Mg-added alloys.

Ag : Under the artificial aging condition, the simultaneous addition with Mg is extremely effective to increase the number density of the T_1 phase, resulting in the higher mechanical strength of the alloys.

Zr : The dispersoid formation of β ' particles significantly decreases grain size resulting in the increased mechanical strength of the alloys.

Since the effectiveness of small amounts of Ag and Zr was already established in the preceding chapters, only optimum contents of constituent Cu and Mg have been controlled in this work.

8.2.2 Selection of microalloying elements

For the optimum alloy composition described in the preceding section, further improvement of mechanical properties of the alloy was intended by means of microalloying additions. In this work, from the theoretical prediction using a Monte Carlo simulation, Zn was selected as a most potent microalloying element to increase the mechanical strength of Al-Li-Cu-Mg-Ag-Zr alloys. As illustrated in Fig.7.2, the Zn-added Al-Li-Cu-Zr alloy reveals the most increased peak hardness in 433K aging except for two Mg-bearing alloys; i.e. (Mg+Ag)-added and Mg-added alloys. This is presumably attributed to the simultaneous strong interactions of Li-Zn and Cu-Zn pairs as shown in Fig.8.1. It should be noted that no other additional element simultaneously correlates with Li and Cu atoms within predictable elemental species in Fig.8.1. The Zn addition to Al-Li alloys is also reported to improve further both the SCC (stress corrosion cracking) resistance and exfoiliation corrosion resistance of the alloys[12].

In general, Al-Li alloys suffer from both the low fracture toughness in the short-transverse (S-L) direction and the anisotropy of mechanical properties[13, 14]. The significant difference in the yield strength between the longitudinal(L) and long transverse(L-T) orientations is reported to be as much as 240MPa for the 2090 alloy[15], which limits a wide range of commercial applications because minimum properties in all orientations must be considered in designing of structural components. These properties are mostly attributed to crystallographic textures, which are developed during rolling and the subsequent heat treatments. Although Zr is one of the most effective elements to retard recrystallization of Al alloys, this effect is generally so strong that the pronounced mechanical anisotropy remains even in the final products. Mn or Cr is a next candidate for the recrystallization inhibitor which reveals the medium effect on the microstructural refinement of Al alloys. In this work, Mn was selected as the second microalloying element to improve the mechanical anisotropy of Al-Li-Cu-Mg-Ag-Zr alloys. This selection is also on the basis of the theoretical prediction in Fig.4.8, which suggests the strong interaction between Mn and Cu atoms resulting in a somewhat modified Cu-bearing precipitate formation.

8.2.3 Optimization of applied solution treatment temperatures

As for the low fracture toughness of Al-Li alloys, the optimization of applied solution treatment temperatures is quite effective because the crack initiation to failure generally takes place at coarsened grain-boundary precipitates in alloys. In the investigated Al-Li-Cu base alloys, solution treatments at 778K can not completely achieve the α single-phase structure because of the high concentrations of alloying elements. Lynch[13] reported that the brittle intergranular fracture in the 8090 alloy is attributed to both the large area fraction of Li-segregated grain-boundary precipitates and the soft precipitation free zone (PFZ) adjacent to grain boundaries. Therefore, it is beneficial that applied solution treatment temperatures are raised as high as possible without partial melting of some compounds. In this work, the results of differential scanning calorimetry (DSC) determine an optimum solution treatment temperature for the investigated Al-Li-Cu-Mg-Ag-Zr alloys.

8.3 Development of new high strength Al-Li-Cu alloys

8.3.1 Experimental Procedures

The alloys utilized in this chapter were supplied by Alithium Limited. Six type Al-Li-Cu-(Mg)-Ag-Zr alloys and one developed Al-Li-Cu-Mg-Ag-Zn-Mn-Zr alloy were prepared from high-purity materials under Ar gas atmosphere followed by continuous casting. The chemical compositions of the alloys are listed in Table 8.2 together with the variations in Cu and Mg contents (Fig.8.2). For simplicity, an alloy containing x mol%Cu and y mol%Mg is designated as xCu -yMg alloy, whereas the equivalent alloy containing Zn and Mn is designated as xCu -yMg-Zn-Mn alloy, respectively.

All the ingots were homogenized by two steps; i.e. 723K for 86.4ks and 773K for 21.6ks, and fabricated to 1.6mm-thick sheets through hot- and cold-rolling. Solution treatments were carried out in a salt bath at 778K or 793K for 1.8ks followed by water quenching at ~298K. 793K is the optimum solution temperature determined by differential scanning calorimetry (DSC). The subsequent aging treatments were performed at 433K for various aging times. The specimens for DSC measurement were prepared from the fabricated sheets with dimensions of ϕ4.0mm × 1.6mm^t and weight of ~50mg. The DSC measurement was carried out at a heating rate of ~0.33K/s under Ar gas atmosphere. Scanning electron microscopy (SEM) was also performed at an accelerating voltage of 10kV for as-polished specimens etched for 2s with Tucker's regent; i.e. HCl 15, HNO_3 5, HF 5 and H_2O 75. The other experiments in this chapter; i.e. hardness measurement, tensile test and transmission electron microscopy, were performed in the same manner described in Chapter 2.

Table 8.2 Chemical compositions of the alloys utilized in this chapter (mol%).

Alloys	Li	Cu	Mg	Ag	Zr	Zn	Mn	Al
1.7Cu-0.6Mg	5.04	1.75	0.527	0.0866	0.0439	—	—	bal.
1.7Cu-1.2Mg	6.03	1.72	1.17	0.0957	0.0406	—	—	bal.
1.7Cu-1.8Mg	5.44	1.70	1.730	0.0961	0.0408	—	—	bal.
2.3Cu-0Mg	5.23	2.39	—	0.0948	0.0443	—	—	bal.
2.3Cu-0.6Mg	5.27	2.33	0.553	0.0972	0.0471	—	—	bal.
2.3Cu-1.2Mg	5.67	2.30	1.20	0.0968	0.0411	—	—	bal.
2.3Cu-0.6Mg-Zn-Mn	5.29	2.34	0.667	0.0951	0.0444	0.0207	0.221	bal.

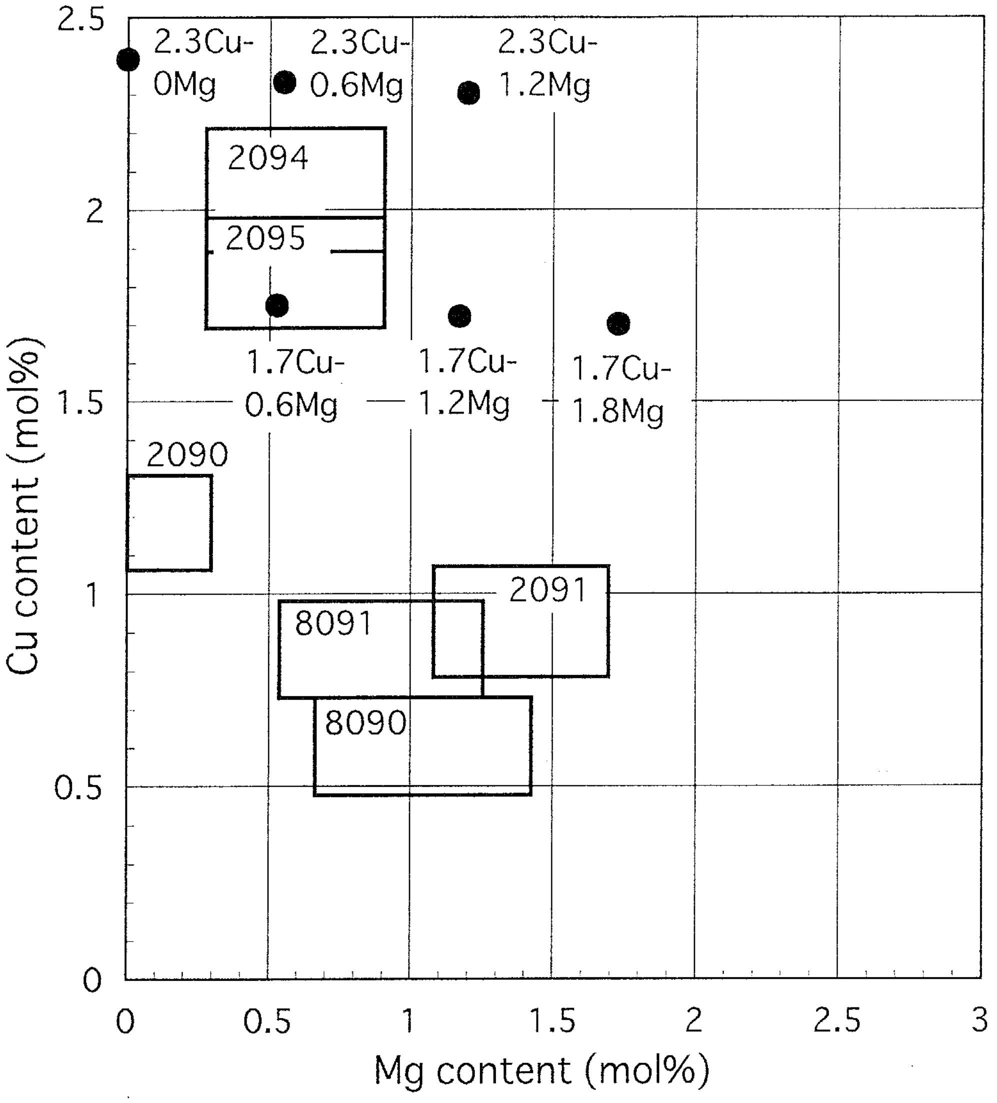

Fig.8.2 Variations in Cu and Mg contents of Al-5.3Li-Cu-Mg-0.1Ag-0.04Zr (in mol%) alloys utilized in this chapter. The squares indicated by four-digit numbers represent the compositional limits of registered alloys.

8.3.2 Optimization of Cu and Mg contents

Figure 8.3 shows isothermal aging curves of hardness for the 1.7Cu-0.6Mg, 1.7Cu-1.2Mg and 1.7Cu-1.8Mg alloys aged at 433K. In the case of the constant Cu content of 1.7mol%, the increased Mg content decreases the values of peak hardness. This pronounced difference in the age-hardenability is well explained by the precipitate microstructures in Fig.8.4, which reveals the remarkable change of strengthening phases from GPB zone and T_1 (1.7Cu-0.6Mg and 1.7Cu-1.2Mg alloys) to S' (1.7Cu-1.8Mg alloy). These results confirm that much content of Mg against 1.7mol%Cu produces the lath-shape S' phase, which is heterogeneously formed with a low number density, resulting in the decreased hardness of the 1.7Cu-1.8Mg alloy. If Mg is not added at all, however, the age-hardenability becomes decreased as suggested in the case of the 2.3mol%Cu content. Figure 8.5 shows isothermal aging curves of hardness for the 2.3Cu-0Mg, 2.3Cu-0.6Mg and 2.3Cu-1.2Mg alloys aged at 433K. The absence of Mg significantly brings about the lower peak hardness because of the heterogeneous precipitation of the T_1 phase at subgrain boundaries as shown in Fig.8.6(c). The mechanism of the T_1 phase nucleation in Mg-bearing Al-Cu-Mg alloys is proposed in Chapter 7. From the comparison between the values of peak hardness, therefore, the 2.3Cu-0.6Mg alloy was selected as an optimum combination of Cu and Mg contents to the investigated Al-Li-Cu-Mg-Ag-Zr alloys.

8.3.3 Effects of microalloying elements of Zn and Mn

The additions of Zn and Mn are quite effective to improve the mechanical properties of Al-Li alloys such as the fracture toughness and mechanical anisotropy. As shown in Fig.8.5, the peak hardness of the 2.3Cu-0.6Mg-Zn-Mn alloy is significantly higher than that of the 2.3Cu-0.6Mg alloy, which was selected as the highest strength Al-Li-Cu alloy with optimum Cu and Mg contents in the preceding section. The increment in the peak hardness by additions of Zn and Mn; i.e. ~HV20, directly reflects the higher tensile strength of the 2.3Cu-0.6Mg-Zn-Mn alloy. Figure 8.7 shows tensile properties in three orientations of the 2.3Cu-0.6Mg and 2.3Cu-0.6Mg-Zn-Mn alloys aged at 433K for 346ks. Here, L, 45° and L-T refer to the longitudinal, 45° from the rolling direction and long-transverse orientations, respectively. Not only the increased tensile strength in all orientations but also the improved properties of both the ductility in the L-T direction and the mechanical anisotropy obviously prove the success of Zn and Mn additions. The latter improvement is presumably attributed to the dispersoid formation as shown in the bright field TEM image for the 2.3Cu-0.6Mg-Zn-Mn alloy aged at 433K (Fig.8.8(a)). The block-shaped or rod-shaped precipitates are homogeneously distributed with the average size of ~200nm, and these

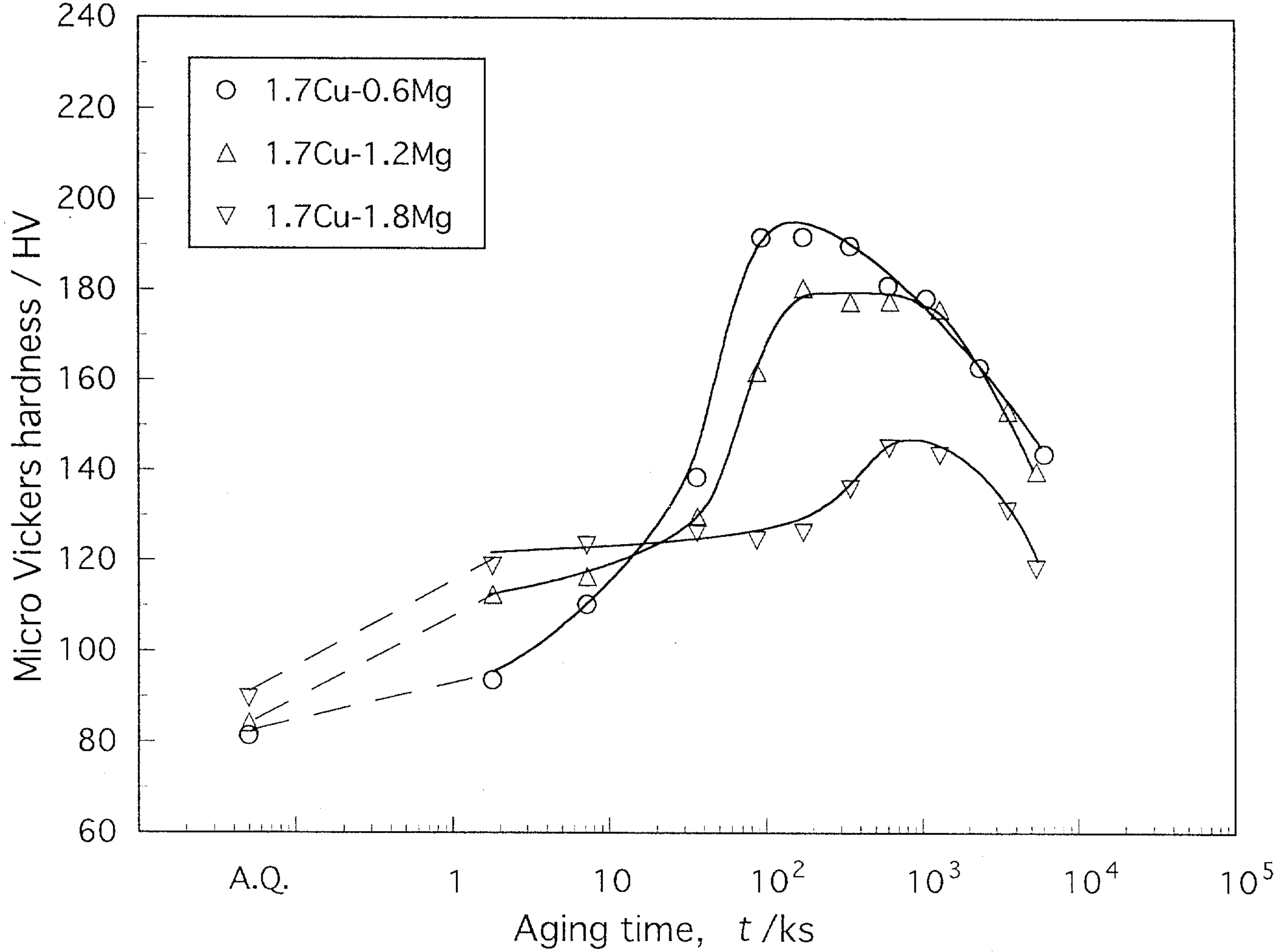

Fig.8.3 Isothermal aging curves of hardness for 1.7Cu-0.6Mg, 1.7Cu-1.2Mg and 1.7Cu-1.8Mg alloys aged at 433K.

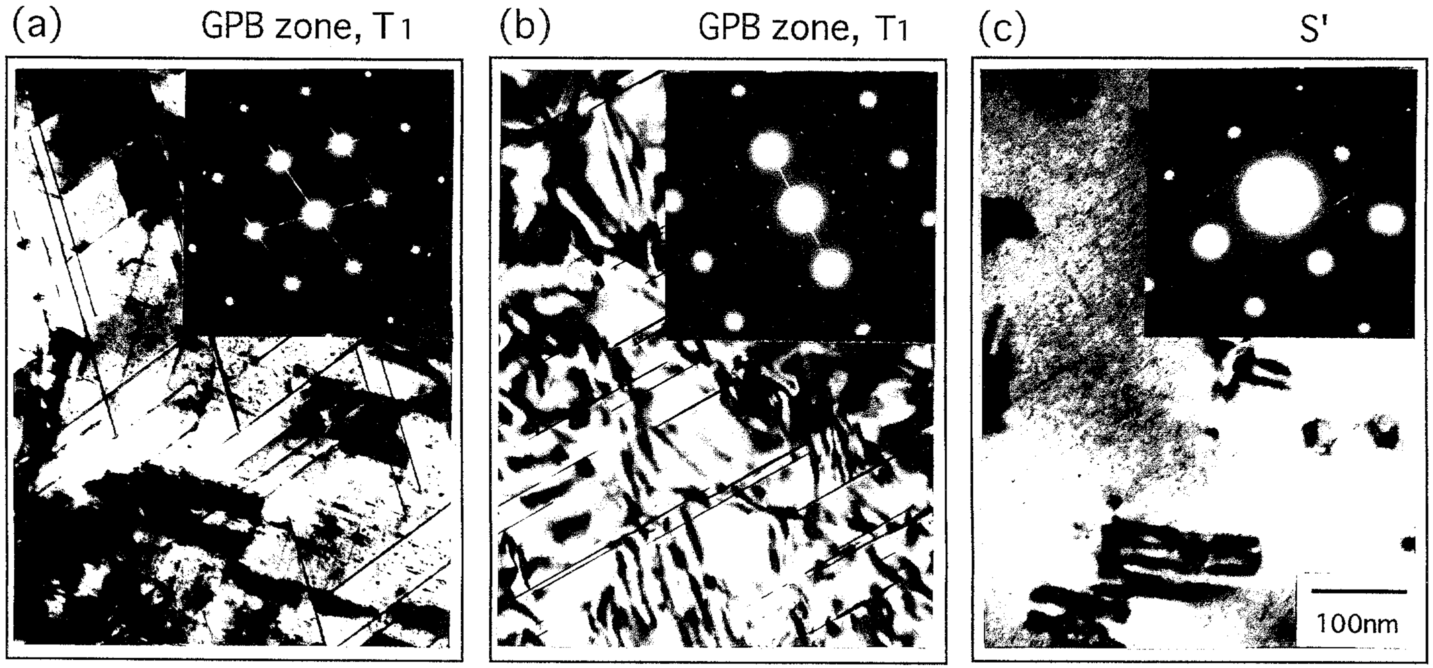

Fig.8.4 Electron micrographs with diffraction patterns for 1.7Cu-0.6Mg(a), 1.7Cu-1.2Mg(b) and 1.7Cu-1.8Mg(c) alloys aged at 433K for 346ks.

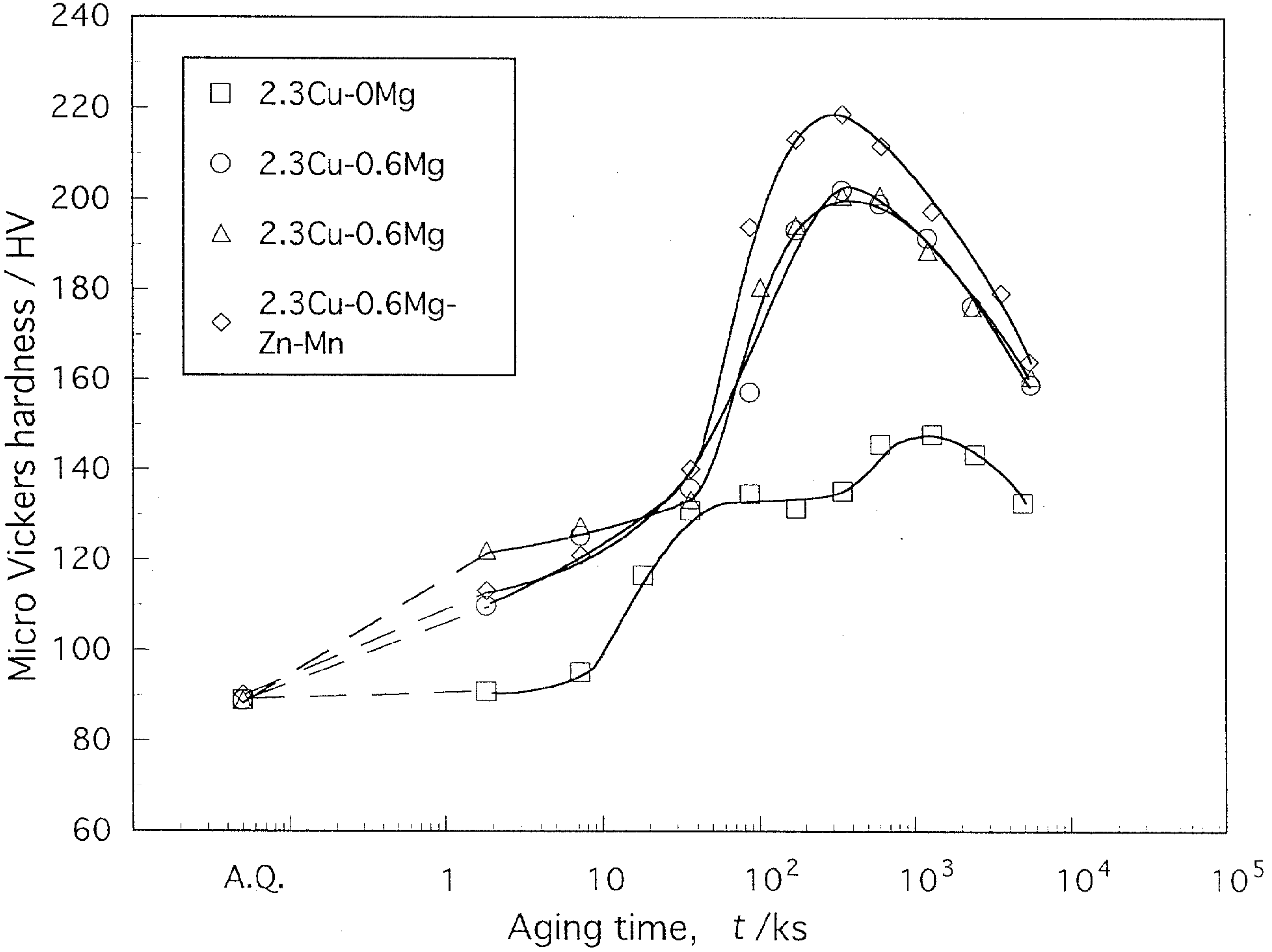

Fig.8.5 Isothermal aging curves of hardness for 2.3Cu-0Mg, 2.3Cu-0.6Mg, 2.3Cu-1.2Mg and 2.3Cu-0.6Mg-Zn-Mn alloys aged at 433K.

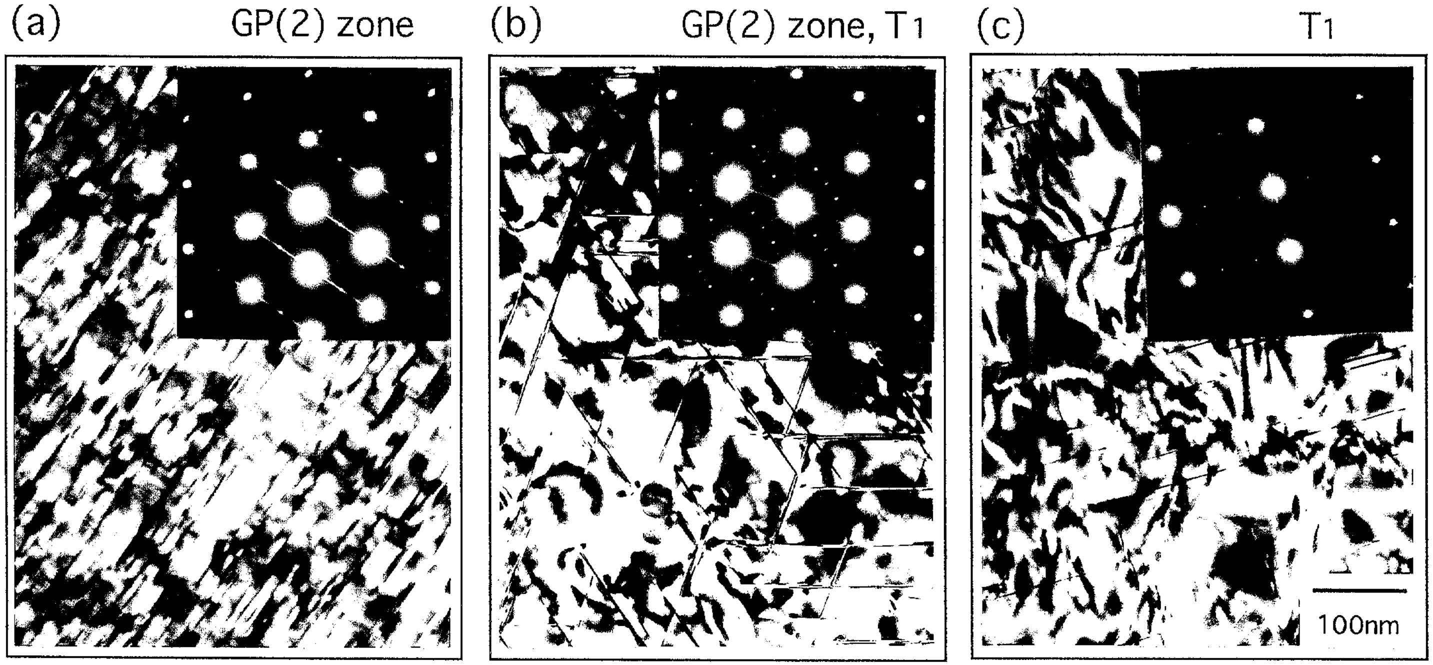

Fig.8.6 Electron micrographs with diffraction patterns for 2.3Cu-0Mg(a), 2.3Cu-0.6Mg(b) and 2.3 Cu-1.2Mg(c) alloys aged at 433K for 346ks.

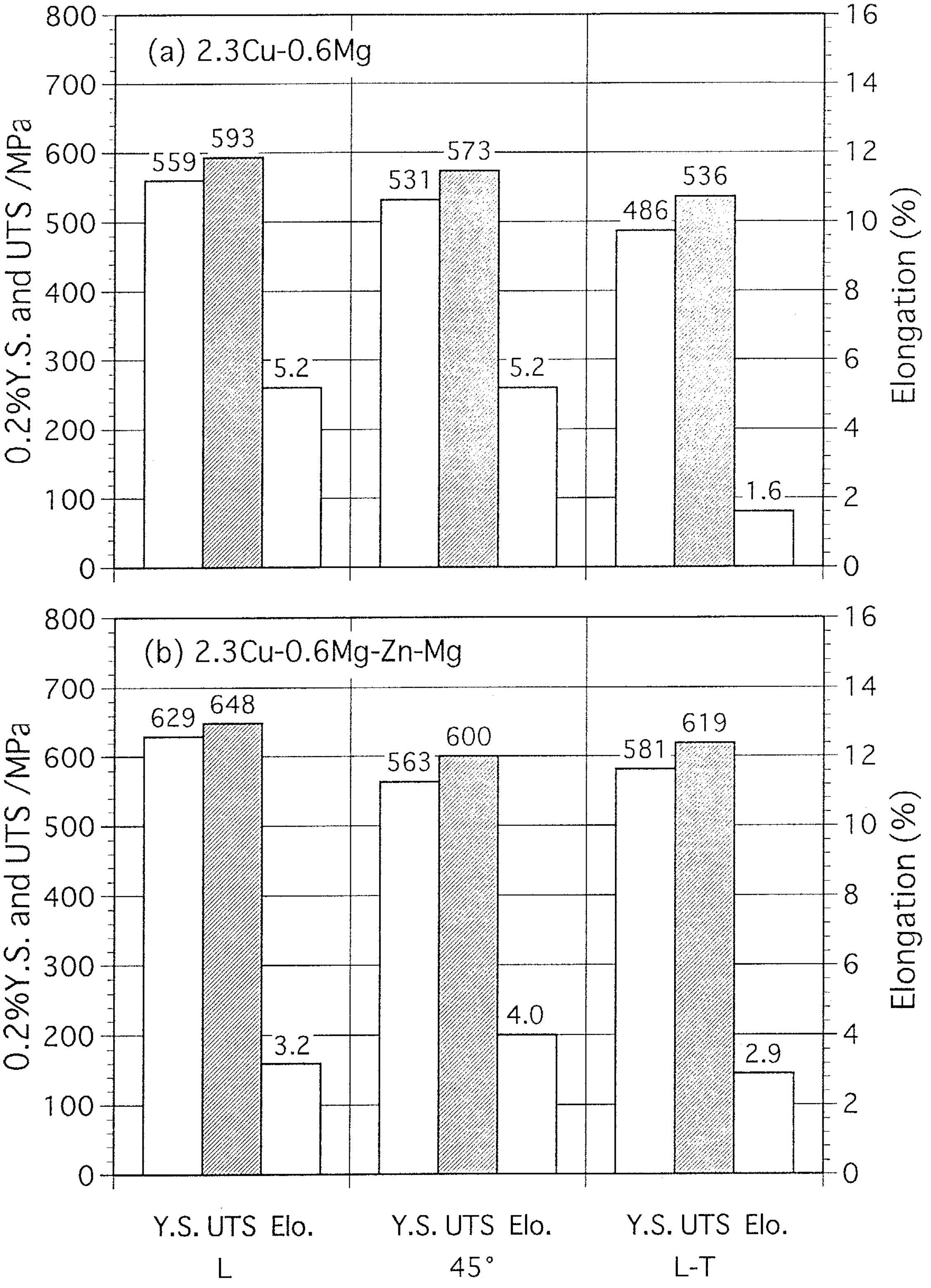

Fig. 8.7 Tensile properties in three orientations for 2.3Cu-0.6Mg(a) and 2.3Cu-0.6Mg-Zn-Mn (b) alloys aged at 433K for 346ks after solution treatment at 773K.

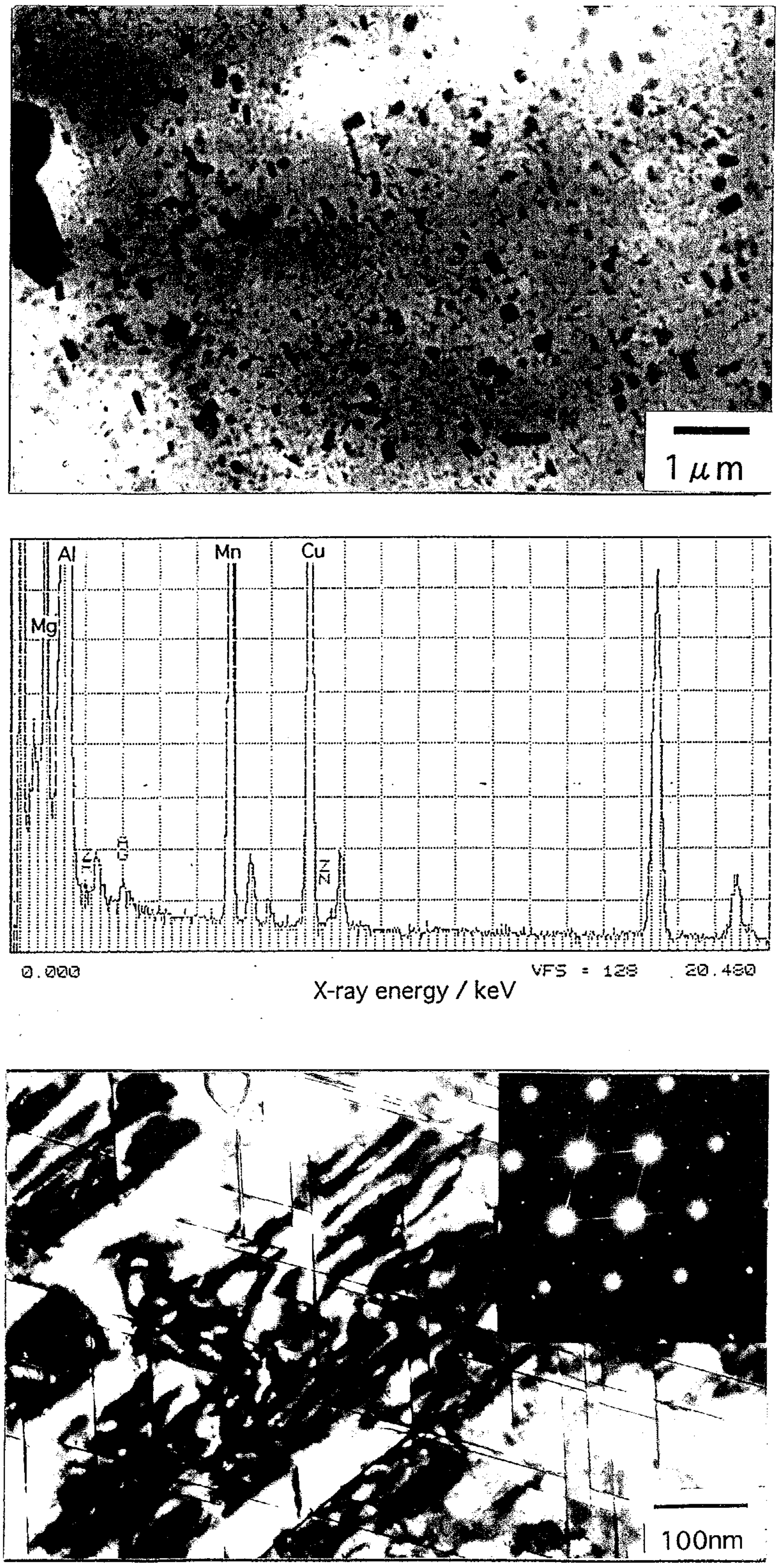

Fig.8.8 Electron micrographs(a)(c) for 2.3Cu-0.6Mg-Zn-Mn alloy aged at 433K for 346ks and EDS analysis profile(b) of the block-shaped or rod-shaped precipitates in micrograph(a).

profile of energy dispersive X-ray spectroscopy (EDS) (Fig.8.8(b)) clearly indicates that these phases contain Al, Cu and Mn although the identification was not done. This dispersoid formation also affects the composition of the matrix resulting in the pronounced change of precipitate microstructures; i.e. from a mixture of GP(2) zone and the T_1 phase (2.3Cu-0.6Mg alloy (Fig.8.6(b)) to only the T_1 phase (2.3Cu-0.6Mg-Zn-Mn alloy (Fig.8.8(c)). As for the effect of Zn, on the other hand, the EDS analysis unfortunately failed to detect any Zn-rich regions. However, the increased mechanical properties of the 2.3Cu-0.6Mg-Zn-Mn alloy appear to be responsible for the more densely formation of the T_1 phase by the microalloying addition of Zn as theoretically predicted in Chapter 7.

8.3.4 Optimization of applied solution treatment temperatures

In general, most of Al-Li-Cu-Mg-Zr alloys are applied to solution heat-treatments at around 778K because the eutectic temperature of Al-Al_2Cu(θ)-Al_2CuMg(S) is located at 781K. Depending on the Cu/Mg ratio (in mass%), however, coexisting stable phases in the Al-Cu-Mg system are reported to be transformed as follows[16].

$$\xleftarrow[Al2Cu(\theta)]{} 8:1 \xleftrightarrow[Al2Cu(\theta),\, Al2CuMg(S)]{} 4:1 \xleftrightarrow[Al2CuMg(S)]{} 1.5:1 \xrightarrow[Al6CuMg4(\sigma)]{}$$

In the case of the investigated Al-Li-Cu-Mg-Ag-Zr alloys, the Cu/Mg ratio of 11:1 (in mass%) is too high to form the S phase. In fact, the bright field TEM images for the 2.3Cu-0.6Mg alloy after solution treatment at 778K(Fig.8.9) reveal no existence of the S phase resulting in any other equilibrium phase region; e.g. Al_2LiCu(T_1)-Al_6Li_3Cu(T_2) or Al_5Li_3Cu(R)-unknown phase. This is also confirmed by the result of DSC measurement in Fig.8.10, which indicates that no partial melting of some stable phases occurs up to ~ 793K. Therefore, 793K can be sufficiently selected as an optimum solution treatment temperature for the investigated Al-Li-Cu-Mg-Ag-Zr alloys. Figure 8.11 shows isothermal aging curves of hardness for the 2.3Cu-0.6Mg alloys aged at 433K after solution treatments at 778 and 793K. The increased solution temperature obviously contributes to the higher peak hardness because of the decreased volume fraction of insoluble phases after solution treatments(Fig. 8.12). The results of tensile test clearly confirm the effectiveness of the increased solution treatment temperature on the improvements of both the ductility in the L-T direction and the mechanical anisotropy (Fig.8.7(a) and 8.13(a)). As a consequence of the proposed concepts of alloy designing, the highest tensile strength of 656MPa in the L direction is achieved in the Al-5.3Li-2.3Cu-0.6Mg-0.1Ag-0.04Zr-Zn-Mn (in mol%) alloy solution-treated at 793K as shown in Fig.8.13(b).

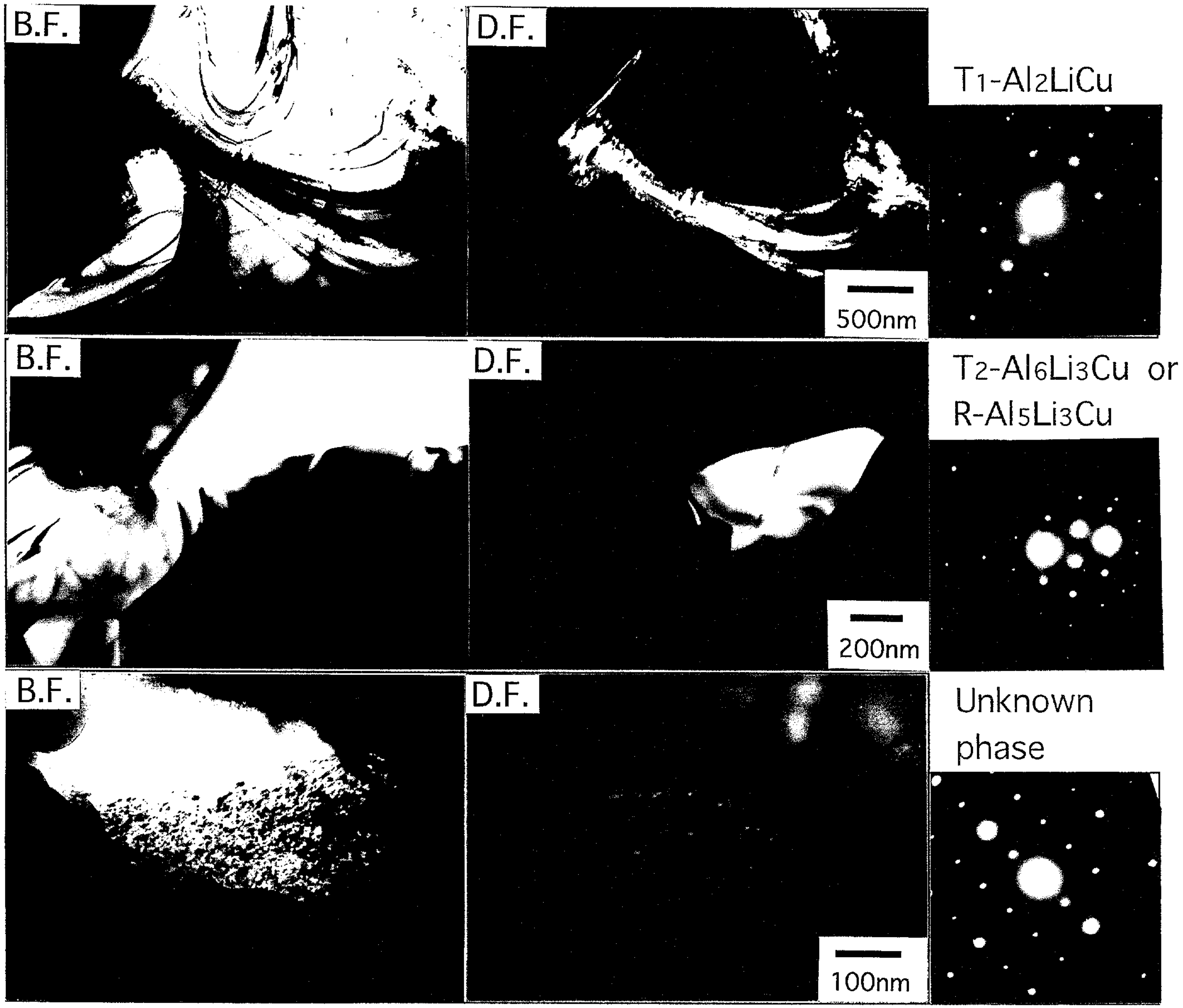

Fig.8.9 Electron micrographs of stable phases observed in 2.3Cu-0.6 Mg alloy after solution treatment at 778K for 1.8ks.

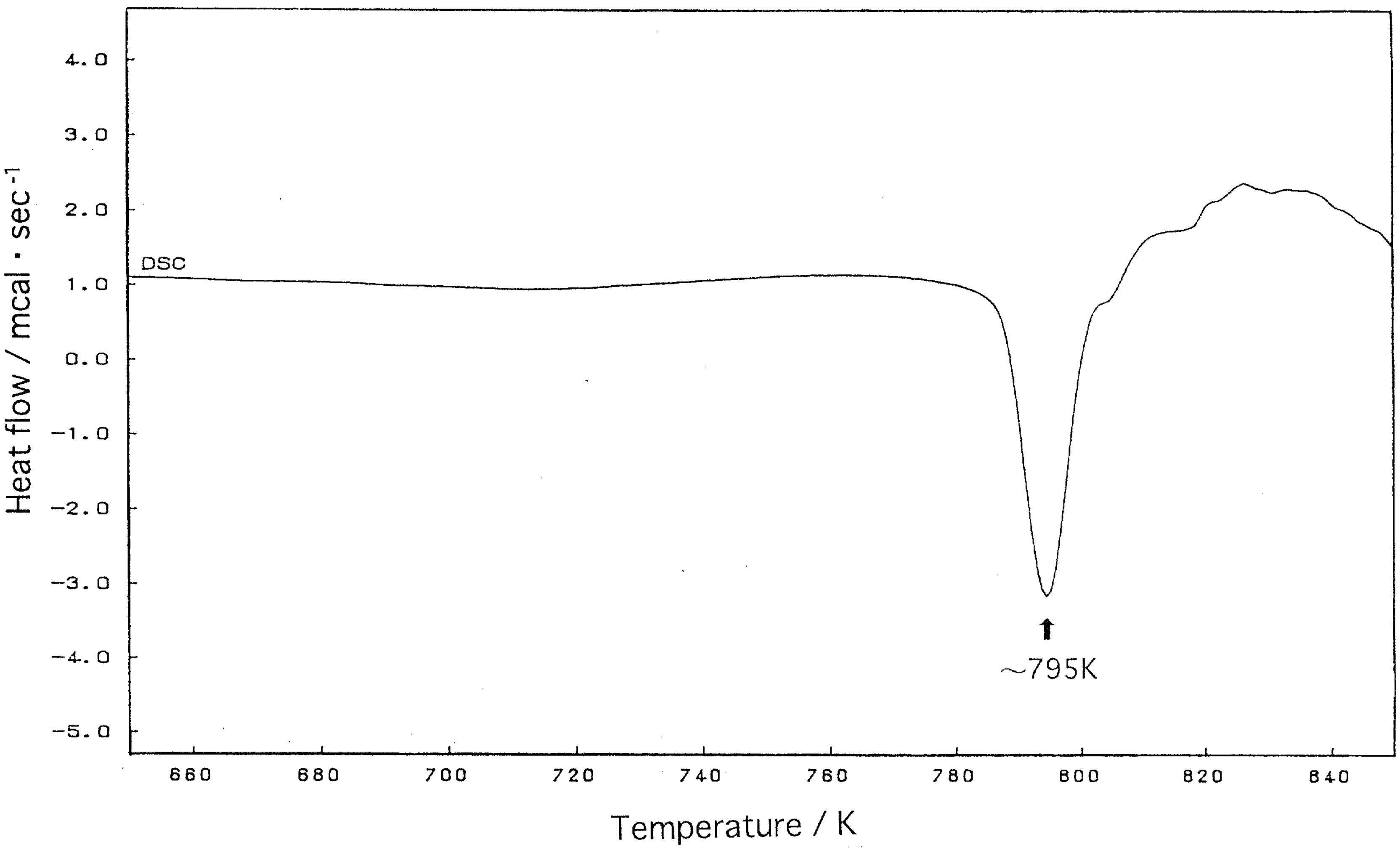

Fig.8.10 Schematic DSC curve for as-rolled 2.3Cu-0.6Mg alloy (Heating rate : 0.33K/s).

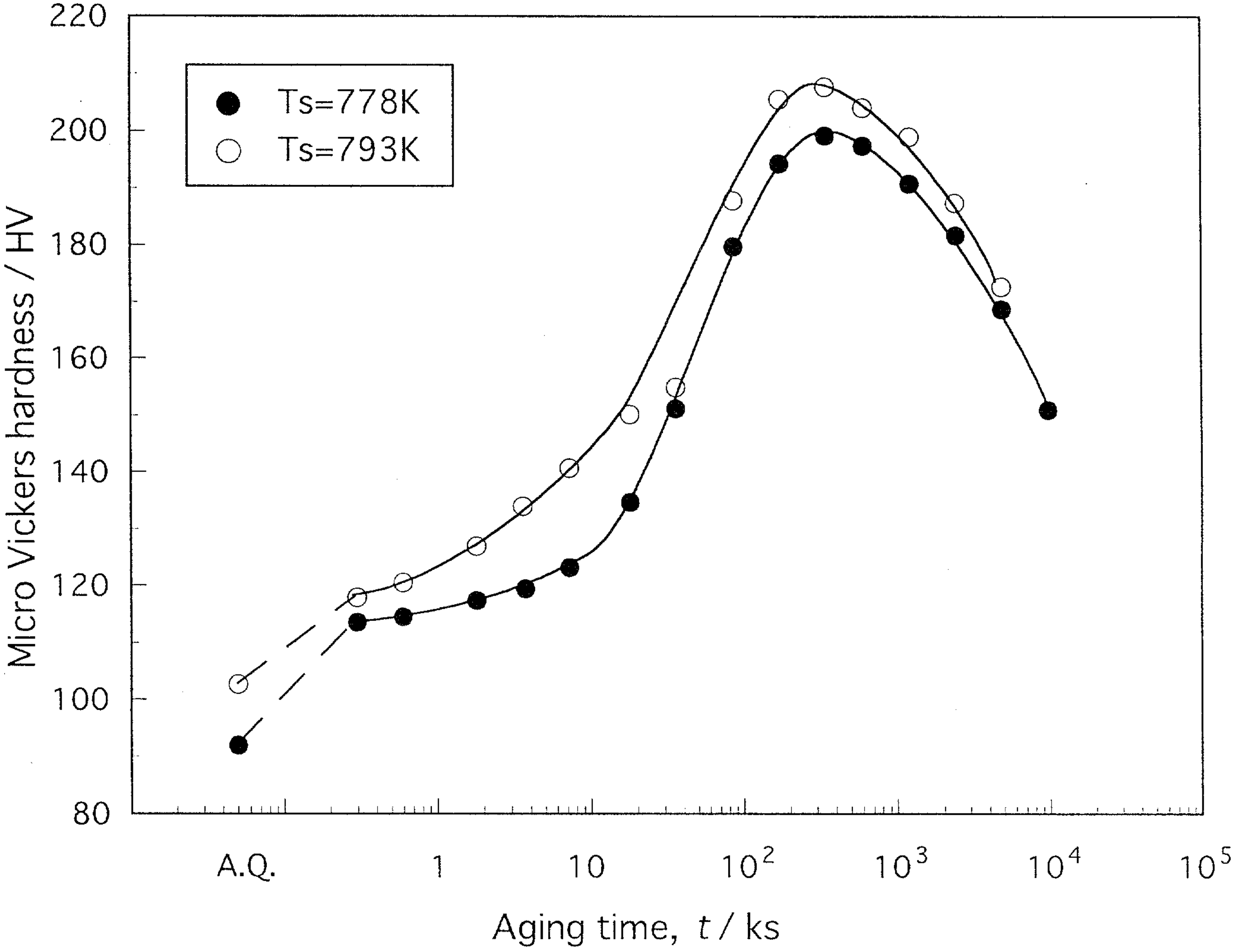

Fig.8.11 Isothermal aging curves of hardness for 2.3Cu-0.6Mg alloys aged at 433K after solution treatments at 778K and 793K.

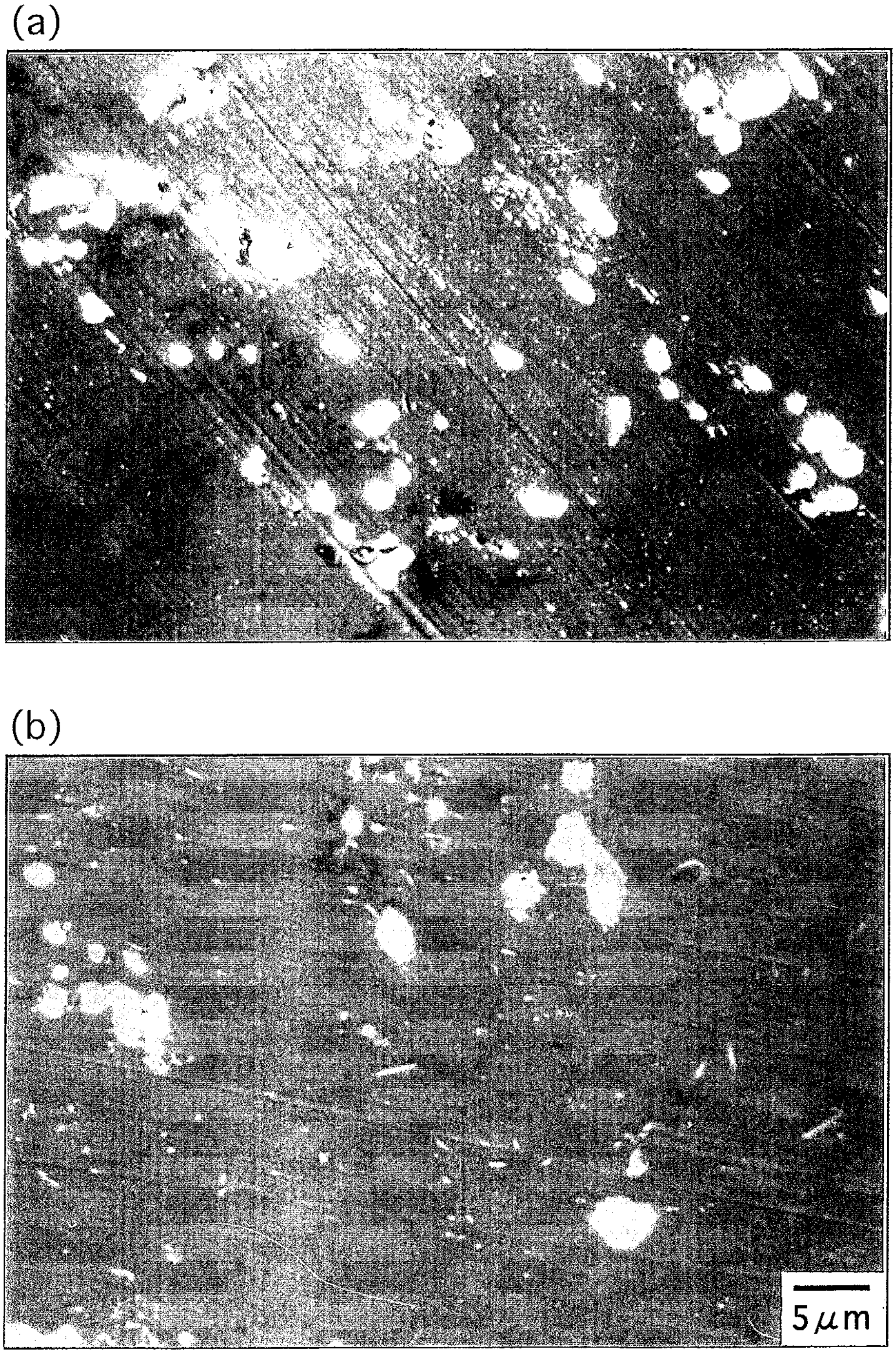

Fig.8.12 SEM micrographs for 2.3Cu-0.6Mg alloys after solution treatments at 778K for 1.8ks(a) and 793K for 1.8ks(b).

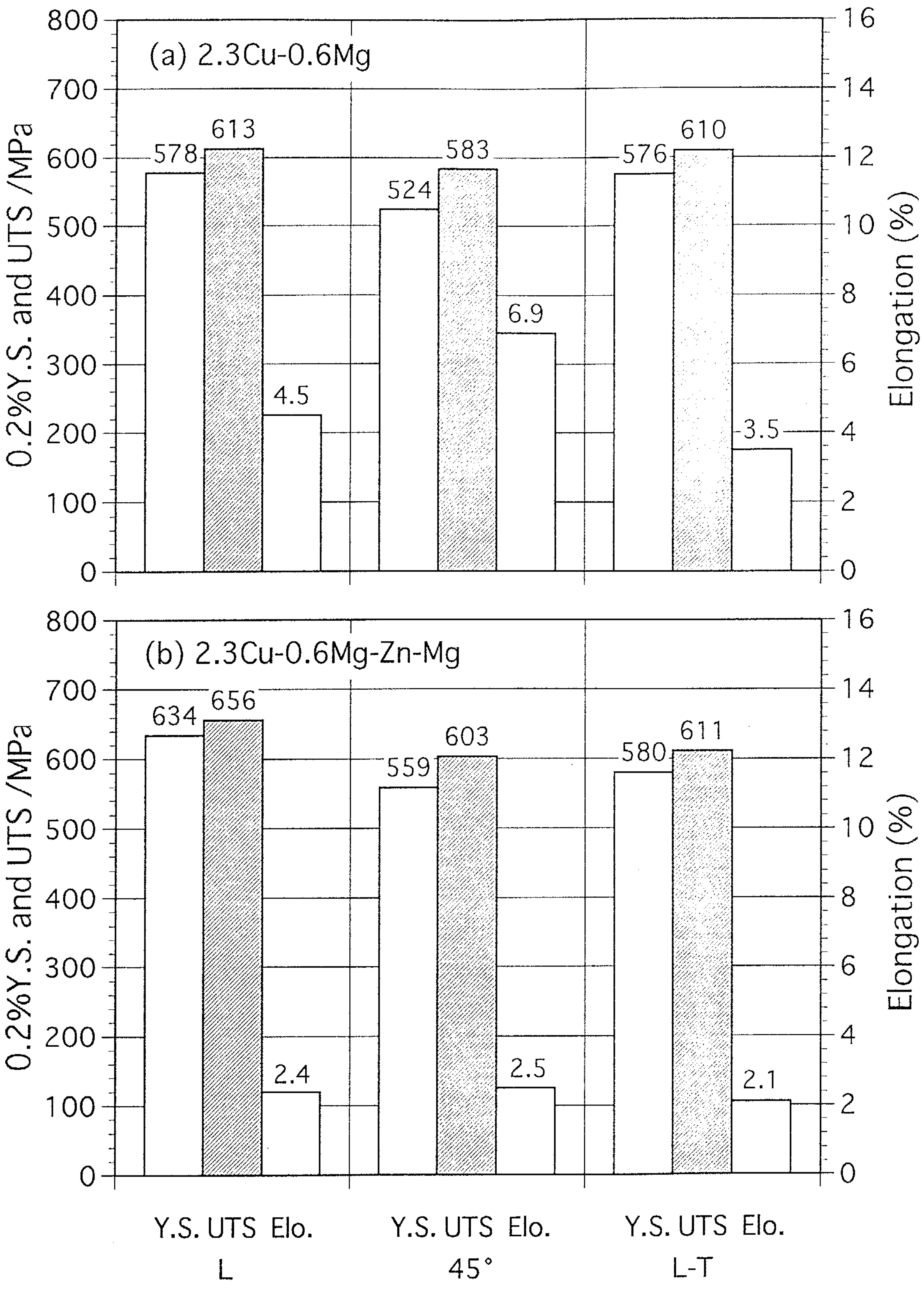

Fig. 8.13 Tensile properties in three orientations for 2.3Cu-0.6Mg(a) and 2.3Cu-0.6Mg-Zn-Mn (b) alloys aged at 433K for 346ks after solution treatment at 793K.

8.4 Conclusions

In this chapter, the simulation results obtained in this work were classified in terms of the characteristic features of each microalloying element. From the theoretical prediction on the role of microalloying elements, a concept for alloy designing of new high strength Al-Li-Cu alloys is proposed. The concept is composed of the control of Cu and Mg contents, the selection of microalloying elements and the optimization of applied solution treatment temperatures. The obtained results are summarized as follows.

(1) In order to inquire such atomistic events as the nucleation and growth of precipitates, which have been never detected using any available experimental methods, a Monte Carlo simulation is proved to be sufficiently effective if reasonable interactions can be estimated. The proposed simulation models with parameters derived from characteristic quantities of each element appear to be applicable to other alloy systems.

(2) In the case of the combination of 2.3mol%Cu and 0.6mol%Mg, an Al-5.3Li-Cu-Mg-0.1Ag-0.04Zr (in mol%) alloy exhibits the highest value of peak hardness in 433K aging. The results of tensile test, however, still indicate both the low ductility in the long-transverse(L-T) direction and the mechanical strength anisotropy of the alloy.

(3) The microalloying additions of Zn and Mn are extremely effective to improve the mechanical properties of the Al-Li-2.3Cu-0.6Mg-Ag-Zr alloy. Not only the increased tensile strength in all orientations but also the improved properties of both the ductility in the L-T direction and mechanical anisotropy are successfully achieved by microalloying elements of Mg and Ag. The latter improvement is mainly due to the dispersoid formation of Al-Cu-Mn compounds, which are homogeneously distributed with the average size of ~ 200nm. The increased tensile strength, on the other hand, appears to be almost responsible for the more densely formation of the T_1 phase by the microalloying addition of Zn.

(4) The increased solution treatment temperature; i.e. from 778K to 793K, contributes to increase the peak hardness of Al-Li-Cu base alloys because of the decreased volume fraction of insoluble phases after solution treatments. The results of tensile test clearly confirm the effectiveness of the increased solution temperature on the improvements of both the ductility in the L-T direction and the mechanical anisotropy with the highest tensile strength of 656MPa(L direction) in the newly developed Al-5.3Li-2.3Cu-0.6Mg-0.1Ag-0.04Zr-Zn-Mn (in mol%) alloy.

References

[1] H.Adachi and S.Imoto: Bulletin of Japan Inst. Metals, **17** (1978), 490.

[2] M.Morinaga, N.Yukawa and H.Adachi: Bulletin of Japan Inst. Metals, **23** (1984), 911.

[3] M.Morinaga, N.Yukawa and H.Adachi: Bulletin of Japan Inst. Metals, **27** (1988), 165.

[4] R.Ninomiya, H.Yukawa and M.Morinaga: J. Japan Inst. Light Metals, **44** (1994), 171.

[5] S.Yamamoto, M.Mizuno and H.Kobayashi: J. Japan Inst. Metals, **57** (1993), 402.

[6] S.Yamamoto, T.Wakabayashi and H.Kobayashi: J. Japan Inst. Metals, **57** (1993), 1367.

[7] S.Yamamoto: J. Japan Inst. Light Metals, **44** (1994), 733.

[8] M.Takeda and H.Oka and I.Onaka: Phys. stat. sol. (a), **132** (1992), 305.

[9] H.Kimura and R.R.Hasiguti: Acta metall., **9** (1961), 1076.

[10] For example, T.Mohri: Bulletin of Japan Inst. Metals, **28** (1989), 268.

[11] T.J.Langan and J.R.Pickens: Proc. 5th Int. Al-Li Conf., (1989), 691.

[12] K.Kobayashi, S.Ohsaki, A.Kamio, T.Sato and Y.Tsuji: J. Jpn. Inst. Light Metals, **42** (1992), 211.

[13] S.P.Lynch: Mater. Sci. Eng. A, **A136** (1991), 25.

[14] F.W.Gayle, W.T.Tack, G.Swanson, F.H.Heubaum and J.R.Pickens: Scripta Metall. Mater., **30** (1994), 761.

[15] K.P.Armanie, G.Kuhlman, R.Rioja and A.Chakrabarti: *Aluminum-Lithium Alloys Suitable for Forgings*, US Patent 5, (1992).

[16] L.F.Mondolfo: *Aluminum Alloys: Structure and Properties*, BUTTER WORTHS, London, (1976).

Chapter 9
Conclusions

The objectives of the present thesis described in Chapter 1; i.e.

① to elucidate the role of microalloying elements on the mechanical strength and precipitate microstructures of Al-Li-Cu alloys

and

② to propose a new high strength Al-Li-Cu alloy based on a theoretical prediction from the results of a Monte Carlo simulation

are successfully achieved throughout the previous chapters. In this chapter, conclusion remarks of the present thesis are summarized based on both the obtained results and discussion described in each chapter.

In Chapter 2, the pronounced effects of a simultaneous addition of Mg and Ag on the mechanical properties and precipitate microstructures of an Al-Li-Cu-Zr alloy are revealed under various aging conditions. Transmission electron microscopy (TEM) analysis attributes the increased mechanical strength to the accelerated nucleation of GP(1) zone and the T_1 phase by the microalloying additions of Mg and Ag. The two-stage increase in electrical resistivity at below ~373K suggests that the simultaneous formation of GP(1) zone and the δ' phase (and/or its precursory precipitates) takes place during phase decomposition in the multicomponent Al-Li-Cu alloys. These experimental results lead to the reason why simple Al-Cu and Al-Li binary alloys were investigated first in Chapters 3 and 4.

In Chapter 3, after the descriptions of both fundamentals and conditions of the utilized simulation models, simulation parameters are derived from the knowledge of experimental thermodynamic or kinetic quantities. A Monte Carlo simulation is proved to be sufficiently effective to inquire atomistic events occurring in alloys, which have been never detected using any available experimental methods. The calculated electrical resistivity from the obtained simulation results establish the reliability of the utilized simulation models by comparing with experimentally measured electrical resistivity.

In Chapter 4, the effects of third additional elements on the formation behavior of GP zones in an Al-Cu alloy have been investigated in the temperature range from 278 to 373K. In particular, slightly complicated effects of small additional Mg are revealed for the first time in the present thesis. The Monte Carlo simulation reveals that additional Mg preferentially traps free-vacancies available for Cu diffusion and also affects the nucleation behavior of GP zones with the aid of Mg/Cu/Vacancy complexes. Such the effects can be frequently observed in atom configurations during the simulation. In contrast, additions of Ag and Zn exert no marked influence on the kinetics of the GP zone formation in Al-Cu alloys. This pronounced difference in phase decomposition behavior is well explained in terms of the characteristic features of each microalloying element.

In Chapter 5, the effects of third additional elements on the kinetics of low-temperature precipitation in an Al-Li alloy have been investigated at temperatures from 278 to 373K. The obtained resistivity changes well demonstrate phase decomposition stages previously observed in Al-Li alloys. The extended simulation model, in which pair interactions between up to second nearest neighbor atoms are taken into account, reveals the similar effect of Mg to that in Al-Cu alloys; i.e. the so-called vacancy-trapping effect. This is because that Mg atoms preferentially trap free-vacancies available for Li diffusion to form ordered structures due to the relatively strong interaction with vacancies. Such situations can be frequently observed in atom configurations during the simulation. As for the substitution behavior of third additional atoms within a $L1_2$-type ordered structure, Ag and Cu exhibit a strong tendency toward substituting Al-sites of the ordered structure, whereas Mg and Zn have a feasibility of both site substitutions.

In Chapter 6, the effects of various additional elements on the age-hardening behavior and precipitate microstructures of an Al-Li-Cu-Zr alloy have been investigated in the temperature range from 278 to 373K. From the atomistic analysis using a Monte Carlo simulation, the characteristic decomposition mechanism in Al-Li-Cu-Zr alloys is revealed in the comparison with the simple Al-Cu (Chapter 4) and Al-Li (Chapter 5) binary alloys. A small addition of Mg to Al-Li-Cu-Zr alloys markedly accelerates the GP(1) zone nucleation resulting in both an enhanced age-hardening and more rapid increase in resistivity. This is well explained by taking into account an important role played by Mg/Cu/Vacancy complexes, which significantly increase the nucleation rate of GP zones with decreased activation energies.

In Chapter 7, the effects of various additional elements on the age-hardening behavior and precipitate microstructures of an Al-Li-Cu-Zr alloy have been investigated in the temperature range from 403 to 523K. In particular, a small addition of Mg, which is most effective to improve the mechanical properties of the quaternary alloy, is closely related to the nucleation mechanism of the T_1 phase. From the difference in the T_1 phase distributions between three quenching conditions; i.e. W.Q.(water-quench), D.Q.(direct-quench) and S.Q.(step-quench), the substantial amount of vacancies are found to be required for the T_1 phase nucleation. This strongly supports that Mg/Cu/Vacancy complexes act as heterogeneous nucleation sites for the T_1 phase. In fact, such situations can be directly observed in atom configurations during the simulation. In contrast, Ag, Ge, Zn and Si additions exhibit the similar microstructures consisting of GP zones and/or the θ' phase with the coarsened T_1 phase only at subgrain boundaries to that of the quaternary alloy. This is because no complexes including both Cu atoms and vacancies are formed in these alloys as predicted based on a theoretical prediction from the obtained results of a Monte Carlo simulation.

In Chapter 8, the obtained simulation results in the present thesis were classified in terms of the characteristic features of each microalloying element. The proposed simulation models appear to be applicable to other alloy systems. From the theoretical prediction on the roles of microalloying elements, furthermore, a concept for alloy designing of new high strength Al-Li-Cu alloys is proposed. The concept is composed of the control of Cu and Mg contents, selection of microalloying elements and optimization of applied solution treatment temperatures. As a consequence of these alloy designing methods, the highest tensile strength of 656MPa in the L (longitudinal) direction is achieved in a newly developed Al-Li-Cu-Mg-Ag-Zr-Zn-Mn alloy.

Appendix
Simulation Program for Microstructure Evolution in Phase Decomposition of Al-Cu-X alloys by Microsoft Visual Basic.

General declaration

```
    Private x(7000) As Integer       'x coordinate of a solute atom on analyzing clusters
    Private y(7000) As Integer       'y coordinate of a solute atom on analyzing clusters
    Private z(7000) As Integer       'z coordinate of a solute atom on analyzing clusters
    Private xv(200) As Integer       'x coordinate of a vacancy
    Private yv(200) As Integer       'y coordinate of a vacancy
    Private zv(200) As Integer       'z coordinate of a vacancy
    Private toki(30) As Long         'Monte Carlo steps on analyzing clusters
    Private totaltoki As Integer     'total times for analyzing clusters
    Private pnt(-1 To 100, -1 To 100, -1 To 100) As Integer     'pointer indicating atom species; i.e.
                                                                  Al(0), Cu(1), X(2) and vacancy(3)
    Private sou As Integer           'visualized layer normal to the z direction
    Private zjiku As Integer         'the number of stacking layers normal to the z direction
    Private ta As Integer            'total number of solute atoms within the simulation system
    Private la As Integer            'the number of Cu atoms within the simulation system
    Private ma As Integer            'the number of X atoms within the simulation system
    Private kaisuu As Long           'total attempt Monte Carlo steps in the simulation
    Private Temp As Integer          'absolute temperature
    Private ct2 As Integer           'the number of isolated X atoms surrounded by Al atoms
```

Sub start_Click()

```
    Open namae1.Text For Output As #1
    Caption = "1"
    la = 2388
    ma = 398
    monte                            'link with the simulation program for exchanging two atom
                                     positions; i.e. Private Sub monte().
    Close #1

End Sub
```

Private Sub monte()

```
    Dim kaisuu2 As Integer
    keisan = 0
1   Cls                              'clearance of CRT
    Randomize                        'initialization of randomly generated numbers
    kaisuu = 0
    kaisuu2 = 0                      'pointer for displaying a bar counter
    siten = 0                        'width of the bar counter

    ta = la + ma
    va = 20                          'the number of vacancies within the simulation system
    Vla = 2200                       'ordering parameter between Al and Cu atoms
```

```
Vam = 1180                       'ordering parameter between Al and Mg atoms
Vlm = 500                        'ordering parameter between Cu and Mg atoms
Vlv = 860                        'ordering parameter between a Cu atom and a vacancy
Vav = 0                          'ordering parameter between an Al atom and a vacancy
Vmv = -8500                      'ordering parameter between a Mg atom and a vacancy
r = 8.31441                      'gas constant
Temp = 273                       'simulation temperature

kuukou.FillStyle = 0
sou = 26
zjiku = 51

'scales of the bar counter
kuukou.Line (5300, 500)-Step(400, 1), , BF
kuukou.Line (5300, 1000)-Step(400, 1), , BF
kuukou.Line (5300, 1500)-Step(400, 1), , BF
kuukou.Line (5300, 2000)-Step(400, 1), , BF
kuukou.Line (5300, 2500)-Step(500, 1), , BF
kuukou.Line (5300, 3000)-Step(400, 1), , BF
kuukou.Line (5300, 3500)-Step(400, 1), , BF
kuukou.Line (5300, 4000)-Step(400, 1), , BF
kuukou.Line (5300, 4500)-Step(400, 1), , BF
kuukou.Line (5300, 5000)-Step(500, 1), , BF
kuukou.Line (5300, 5500)-Step(400, 1), , BF
kuukou.Line (5300, 6000)-Step(400, 1), , BF

'Monte Carlo steps on analyzing clusters
toki(1) = 5
toki(2) = 500
toki(3) = 1000
toki(4) = 2000
toki(5) = 5000
toki(6) = 10000
toki(7) = 20000
toki(8) = 50000
toki(9) = 100000
toki(10) = 200000
toki(11) = 500000
toki(12) = 1000000
toki(13) = 2000000
toki(14) = 5000000
toki(15) = 10000000
toki(16) = 20000000
toki(17) = 50000000
toki(18) = 100000000
totaltoki = 18

'arrangement of Al atoms at all lattice sites within the simulation system
For l = 1 To zjiku
For m = 1 To 51
For n = 1 To 51
```

```
pnt(n, m, l) = 0

          If l = 1 Then
          p = n * 100 - 50
          q = m * 100 - 50
          kuukou.FillColor = RGB(0, 255, 255)
          Circle (p, q), 50, RGB(0, 0, 0)
          End If

Next n
Next m
Next l

'arrangement of Cu atoms at randomly chosen lattice sites within the simulation system
For n = 1 To la
h = Int(51 * Rnd + 1)
k = Int(51 * Rnd + 1)
zl = Int(zjiku * Rnd + 1)
pnt(h, k, zl) = 1
xl = h * 100 - 50
yl = k * 100 - 50
          If zl = sou Then
          kuukou.FillColor = RGB(0, 0, 0)
          Circle (xl, yl), 50, RGB(0, 0, 0)
          End If
Next n

'arrangement of X atoms at randomly chosen lattice sites within the simulation system
For n = 1 To ma
h = Int(51 * Rnd + 1)
k = Int(51 * Rnd + 1)
zm = Int(zjiku * Rnd + 1)
pnt(h, k, zm) = 2
xm = h * 100 - 50
ym = k * 100 - 50
          If zm = sou Then
          kuukou.FillColor = RGB(255, 0, 0)
          Circle (xm, ym), 50, RGB(0, 0, 0)
          End If
Next n

'arrangement of vacancies at randomly chosen lattice sites within the simulation system
For n = 1 To va
h = Int(51 * Rnd + 1)
k = Int(51 * Rnd + 1)
zv(n) = Int(zjiku * Rnd + 1)
pnt(h, k, zv(n)) = 3
xv(n) = h * 100 - 50
yv(n) = k * 100 - 50
          If zv(n) = sou Then
          kuukou.FillColor = RGB(150, 150, 150)
          Circle (xv(n), yv(n)), 50, RGB(150, 150, 150)
          End If
Next n

For i = 1 To 100000000               'total attempt Monte Carlo steps in this simulation

kaisuu2 = kaisuu2 + 1
'getting the bar counter into operation
If kaisuu2 >= 10000 Then
      Line (5300, siten)-Step(300, 5), , BF
      siten = siten + 0.5
      kaisuu2 = 0
End If

'link with the simulation program for analyzing clusters; i.e. Private Sub kazoeru().
kaisuu = kaisuu + 1
      For j = 1 To totaltoki
      If kaisuu = toki(j) Then
      kazoeru
      End If
      Next j

'random selection of a vacancy to migrate
a = Int(va * Rnd + 1)
      p = xv(a)
      q = yv(a)
      l = zv(a)

'random selection of one direction for the vacancy migration
w = Int(120 * Rnd) Mod 12
If zv(a) Mod 2 = 1 Then              'in case that the vacancy is located on odd layers normal to the
                                      z direction

      If w = 1 Then p = p + 100
            If p > 5050 Then p = 50
      ElseIf w = 2 Then p = p - 100
            If p < 50 Then p = 5050
      ElseIf w = 3 Then q = q + 100
            If q > 5050 Then q = 50
      ElseIf w = 4 Then q = q - 100
            If q < 50 Then q = 5050
      ElseIf w = 5 Then q = q - 100
            If q < 50 Then q = 5050
            l = l + 1    If l > zjiku Then l = 1
      ElseIf w = 6 Then p = p - 100
            If p < 50 Then p = 5050
            l = l + 1    If l > zjiku Then l = 1
      ElseIf w = 7 Then p = p - 100
            If p < 50 Then p = 5050
            q = q - 100
            If q < 50 Then q = 5050
```

```
          l = l + 1    If l > zjiku Then l = 1
     ElseIf w = 8 Then l = l + 1
          If l > zjiku Then l = 1
     ElseIf w = 9 Then q = q - 100
          If q < 50 Then q = 5050
          l = l - 1    If l < 1 Then l = zjiku
     ElseIf w = 10 Then p = p - 100
          If p < 50 Then p = 5050
          l = l - 1    If l < 1 Then l = zjiku
     ElseIf w = 11 Then p = p - 100
          If p < 50 Then p = 5050
          q = q - 100    If q < 50 Then q = 5050
          l = l - 1    If l < 1 Then l = zjiku
     Else
          l = l - 1    If l < 1 Then l = zjiku
     End If

Else                    'in case that the vacancy is located on even layers normal to the z direction

     If w = 1 Then p = p + 100
          If p > 5050 Then p = 50
     ElseIf w = 2 Then p = p - 100
          If p < 50 Then p = 5050
     ElseIf w = 3 Then q = q + 100
          If q > 5050 Then q = 50
     ElseIf w = 4 Then q = q - 100
          If q < 50 Then q = 5050
     ElseIf w = 5 Then q = q + 100
          If q > 5050 Then q = 50
          l = l + 1    If l > zjiku Then l = 1
     ElseIf w = 6 Then p = p + 100
          If p > 5050 Then p = 50
          l = l + 1    If l > zjiku Then l = 1
     ElseIf w = 7 Then p = p + 100
          If p > 5050 Then p = 50
          q = q + 100    If q > 5050 Then q = 50
          l = l + 1    If l > zjiku Then l = 1
     ElseIf w = 8 Then l = l + 1
          If l > zjiku Then l = 1
     ElseIf w = 9 Then q = q + 100
          If q > 5050 Then q = 50
          l = l - 1    If l < 1 Then l = zjiku
     ElseIf w = 10 Then l = l - 1
          If l < 1 Then l = zjiku
     ElseIf w = 11 Then p = p + 100
          If p > 5050 Then p = 50
          q = q + 100    If q > 5050 Then q = 50
          l = l - 1    If l < 1 Then l = zjiku
     Else
          l = l - 1    If l < 1 Then l = zjiku
     End If
```

```
End If

p1 = (p + 50) / 100          'x coordinate of the selected atom position for the vacancy
                              migration
q1 = (q + 50) / 100          'y coordinate of the selected atom position for the vacancy
                              migration
X1 = (xv(a) + 50) / 100      'original x coordinate of the vacancy
Y1 = (yv(a) + 50) / 100      'original y coordinate of the vacancy
                             '(X1,Y1,zv(a)) → (p1,q1,l)

'in case that the selected atom position for the vacancy migration is occupied by a vacancy
If pnt(p1, q1, l) = 3 Then GoTo 100

d1 = 0          'the number of nearest neighbor Cu atoms around the original vacancy position
d2 = 0          'the number of nearest neighbor Cu atoms around the selected atom position
                 for the vacancy migration
d3 = 0          'the number of nearest neighbor X atoms around the original vacancy position
d4 = 0          'the number of nearest neighbor X atoms around the selected atom position
                 for the vacancy migration

ue1 = zv(a) + 1     'upper layer of the original vacancy position
sita1 = zv(a) - 1   'lower layer of the original vacancy position
ue2 = l + 1         'upper layer of the selected atom position for the vacancy migration
sita2 = l - 1       'lower layer of the selected atom position for the vacancy migration

'periodic boundary conditions for calculating the energy difference
If ue1 > zjiku Then ue1 = 1
If sita1 < 1 Then sita1 = zjiku
If ue2 > zjiku Then ue2 = 1
If sita2 < 1 Then sita2 = zjiku

'checking the number of nearest neighbor Cu atoms around the original vacancy position
If pnt(X1 - 1, Y1, zv(a)) = 1 Then d1 = d1 + 1
If pnt(X1, Y1 - 1, zv(a)) = 1 Then d1 = d1 + 1
If pnt(X1, Y1 + 1, zv(a)) = 1 Then d1 = d1 + 1
If pnt(X1 + 1, Y1, zv(a)) = 1 Then d1 = d1 + 1

If zv(a) Mod 2 = 1 Then
     If pnt(X1 - 1, Y1, ue1) = 1 Then d1 = d1 + 1
     If pnt(X1, Y1 - 1, ue1) = 1 Then d1 = d1 + 1
     If pnt(X1 - 1, Y1 - 1, ue1) = 1 Then d1 = d1 + 1
     If pnt(X1, Y1, ue1) = 1 Then d1 = d1 + 1

     If pnt(X1 - 1, Y1, sita1) = 1 Then d1 = d1 + 1
     If pnt(X1, Y1 - 1, sita1) = 1 Then d1 = d1 + 1
     If pnt(X1 - 1, Y1 - 1, sita1) = 1 Then d1 = d1 + 1
     If pnt(X1, Y1, sita1) = 1 Then d1 = d1 + 1

Else
     If pnt(X1 + 1, Y1, ue1) = 1 Then d1 = d1 + 1
     If pnt(X1, Y1 + 1, ue1) = 1 Then d1 = d1 + 1
```

```
    If pnt(X1 + 1, Y1 + 1, ue1) = 1 Then d1 = d1 + 1
    If pnt(X1, Y1, ue1) = 1 Then d1 = d1 + 1

    If pnt(X1 + 1, Y1, sita1) = 1 Then d1 = d1 + 1
    If pnt(X1, Y1 + 1, sita1) = 1 Then d1 = d1 + 1
    If pnt(X1 + 1, Y1 + 1, sita1) = 1 Then d1 = d1 + 1
    If pnt(X1, Y1, sita1) = 1 Then d1 = d1 + 1
End If

'checking the number of nearest neighbor Cu atoms around the selected atom position for the vacancy migration
If pnt(p1 - 1, q1, l) = 1 Then d2 = d2 + 1
If pnt(p1, q1 - 1, l) = 1 Then d2 = d2 + 1
If pnt(p1, q1 + 1, l) = 1 Then d2 = d2 + 1
If pnt(p1 + 1, q1, l) = 1 Then d2 = d2 + 1

If l Mod 2 = 1 Then
    If pnt(p1 - 1, q1, ue2) = 1 Then d2 = d2 + 1
    If pnt(p1, q1 - 1, ue2) = 1 Then d2 = d2 + 1
    If pnt(p1 - 1, q1 - 1, ue2) = 1 Then d2 = d2 + 1
    If pnt(p1, q1, ue2) = 1 Then d2 = d2 + 1

    If pnt(p1 - 1, q1, sita2) = 1 Then d2 = d2 + 1
    If pnt(p1, q1 - 1, sita2) = 1 Then d2 = d2 + 1
    If pnt(p1 - 1, q1 - 1, sita2) = 1 Then d2 = d2 + 1
    If pnt(p1, q1, sita2) = 1 Then d2 = d2 + 1

Else
    If pnt(p1 + 1, q1, ue2) = 1 Then d2 = d2 + 1
    If pnt(p1, q1 + 1, ue2) = 1 Then d2 = d2 + 1
    If pnt(p1 + 1, q1 + 1, ue2) = 1 Then d2 = d2 + 1
    If pnt(p1, q1, ue2) = 1 Then d2 = d2 + 1

    If pnt(p1 + 1, q1, sita2) = 1 Then d2 = d2 + 1
    If pnt(p1, q1 + 1, sita2) = 1 Then d2 = d2 + 1
    If pnt(p1 + 1, q1 + 1, sita2) = 1 Then d2 = d2 + 1
    If pnt(p1, q1, sita2) = 1 Then d2 = d2 + 1
End If

'checking the number of nearest neighbor X atoms around the original vacancy position
If pnt(X1 - 1, Y1, zv(a)) = 2 Then d3 = d3 + 1
If pnt(X1, Y1 - 1, zv(a)) = 2 Then d3 = d3 + 1
If pnt(X1, Y1 + 1, zv(a)) = 2 Then d3 = d3 + 1
If pnt(X1 + 1, Y1, zv(a)) = 2 Then d3 = d3 + 1

If zv(a) Mod 2 = 1 Then
    If pnt(X1 - 1, Y1, ue1) = 2 Then d3 = d3 + 1
    If pnt(X1, Y1 - 1, ue1) = 2 Then d3 = d3 + 1
    If pnt(X1 - 1, Y1 - 1, ue1) = 2 Then d3 = d3 + 1
    If pnt(X1, Y1, ue1) = 2 Then d3 = d3 + 1

    If pnt(X1 - 1, Y1, sita1) = 2 Then d3 = d3 + 1
    If pnt(X1, Y1 - 1, sita1) = 2 Then d3 = d3 + 1
    If pnt(X1 - 1, Y1 - 1, sita1) = 2 Then d3 = d3 + 1
    If pnt(X1, Y1, sita1) = 2 Then d3 = d3 + 1

Else
    If pnt(X1 + 1, Y1, ue1) = 2 Then d3 = d3 + 1
    If pnt(X1, Y1 + 1, ue1) = 2 Then d3 = d3 + 1
    If pnt(X1 + 1, Y1 + 1, ue1) = 2 Then d3 = d3 + 1
    If pnt(X1, Y1, ue1) = 2 Then d3 = d3 + 1

    If pnt(X1 + 1, Y1, sita1) = 2 Then d3 = d3 + 1
    If pnt(X1, Y1 + 1, sita1) = 2 Then d3 = d3 + 1
    If pnt(X1 + 1, Y1 + 1, sita1) = 2 Then d3 = d3 + 1
    If pnt(X1, Y1, sita1) = 2 Then d3 = d3 + 1
End If

'checking the number of nearest neighbor X atoms around the selected atom position for the vacancy migration
If pnt(p1 - 1, q1, l) = 2 Then d4 = d4 + 1
If pnt(p1, q1 - 1, l) = 2 Then d4 = d4 + 1
If pnt(p1, q1 + 1, l) = 2 Then d4 = d4 + 1
If pnt(p1 + 1, q1, l) = 2 Then d4 = d4 + 1

If l Mod 2 = 1 Then
    If pnt(p1 - 1, q1, ue2) = 2 Then d4 = d4 + 1
    If pnt(p1, q1 - 1, ue2) = 2 Then d4 = d4 + 1
    If pnt(p1 - 1, q1 - 1, ue2) = 2 Then d4 = d4 + 1
    If pnt(p1, q1, ue2) = 2 Then d4 = d4 + 1

    If pnt(p1 - 1, q1, sita2) = 2 Then d4 = d4 + 1
    If pnt(p1, q1 - 1, sita2) = 2 Then d4 = d4 + 1
    If pnt(p1 - 1, q1 - 1, sita2) = 2 Then d4 = d4 + 1
    If pnt(p1, q1, sita2) = 2 Then d4 = d4 + 1

Else
    If pnt(p1 + 1, q1, ue2) = 2 Then d4 = d4 + 1
    If pnt(p1, q1 + 1, ue2) = 2 Then d4 = d4 + 1
    If pnt(p1 + 1, q1 + 1, ue2) = 2 Then d4 = d4 + 1
    If pnt(p1, q1, ue2) = 2 Then d4 = d4 + 1

    If pnt(p1 + 1, q1, sita2) = 2 Then d4 = d4 + 1
    If pnt(p1, q1 + 1, sita2) = 2 Then d4 = d4 + 1
    If pnt(p1 + 1, q1 + 1, sita2) = 2 Then d4 = d4 + 1
    If pnt(p1, q1, sita2) = 2 Then d4 = d4 + 1
End If

'in case that the selected atom position for the vacancy migration is occupied by a Cu atom
If pnt(p1, q1, l) = 1 Then GoTo 20

'in case that the selected atom position for the vacancy migration is occupied by a Li atom
```

```
    If pnt(p1, q1, l) = 2 Then GoTo 30

    'in case that the selected atom position for the vacancy migration is occupied by an Al atom
    before = (d1 * Vlv + d3 * Vmv + (12 - d1 - d3) * Vav) + (d2 * Vla + Vav + d4 * Vam)
    after = (d1 * Vla + Vav + d3 * Vam) + (d2 * Vlv + (12 - d2 - d4) * Vav + d4 * Vmv)
    vc = after - before
    W1 = Exp((-1) * vc / (r * Temp)) / (1 + Exp((-1) * vc / (r * Temp)))
    W2 = Rnd(1)
    If W2 > W1 Then GoTo 100
    pnt(X1, Y1, zv(a)) = 0          'locating the original vacancy position with an Al atom
    pnt(p1, q1, l) = 3              'locating the selected atom position for the vacancy migration
                                     with a vacancy
    If zv(a) = sou Then
    kuukou.FillColor = RGB(0, 255, 255)
    Circle (xv(a), yv(a)), 50, RGB(0, 0, 0)
    End If
    If l = sou Then
    kuukou.FillColor = RGB(150, 150, 150)
    Circle (p, q), 50, RGB(150, 150, 150)
    End If
    GoTo 90

20  before = (d1 * Vlv + (12 - d1 - d3) * Vav + d3 * Vmv) + ((11 - d2 - d4) * Vla+ Vlv + d4 * Vlm)
    d1 = d1 - 1
    d2 = d2 + 1
    after = ((11 - d1 - d3) * Vla + Vlv + d3 * Vlm) + (d2 * Vlv + (12 - d2 - d4) * Vav + d4 * Vmv)
    vc = after - before
    W1 = Exp((-1) * vc / (r * Temp)) / (1 + Exp((-1) * vc / (r * Temp)))
    W2 = Rnd(1)
    If W2 > W1 Then GoTo 100
    pnt(X1, Y1, zv(a)) = 1          'locating the original vacancy position with a Cu atom
       pnt(p1, q1, l) = 3           'locating the selected atom position for the vacancy migration
                                     with a vacancy
    If zv(a) = sou Then
    kuukou.FillColor = RGB(0, 0, 0)
    Circle (xv(a), yv(a)), 50, RGB(0, 0, 0)
    End If
    If l = sou Then
    kuukou.FillColor = RGB(150, 150, 150)
    Circle (p, q), 50, RGB(150, 150, 150)
    End If
    GoTo 90

30  before = (d1 * Vlv + (12 - d1 - d3) * Vav + d3 * Vmv) + ((11 - d2 - d4) * Vam+ d2 * Vlm + Vmv)
    d3 = d3 - 1
    d4 = d4 + 1
    after = ((11 - d1 - d3) * Vam + d1 * Vlm + Vmv) + (d2 * Vlv + (12 - d2 - d4) * Vav+ d4 * Vmv)
    vc = after - before
    W1 = Exp((-1) * vc / (r * Temp)) / (1 + Exp((-1) * vc / (r * Temp)))
    W2 = Rnd(1)
    If W2 > W1 Then GoTo 100
```

```
    pnt(X1, Y1, zv(a)) = 2          'locating the original vacancy position with a X atom
    pnt(p1, q1, l) = 3              'locating the selected atom position for the vacancy migration
                                     with a vacancy
    If zv(a) = sou Then
    kuukou.FillColor = RGB(255, 0, 0)
    Circle (xv(a), yv(a)), 50, RGB(0, 0, 0)
    End If
    If l = sou Then
    kuukou.FillColor = RGB(150, 150, 150)
    Circle (p, q), 50, RGB(150, 150, 150)
    End If

'making the selected atom position for the vacancy migration to be a new vacancy position
90  xv(a) = p
    yv(a) = q
    zv(a) = l

100 Next i

End Sub
```

Private Sub kazoeru()

```
    Dim kaiseki(100, 100, 100) As Integer        'three-dimensional variable indicating a cluster
                                                  number
    Dim kaiseki2(100, 100, 100) As Integer
    Dim m(12) As Integer                         'variable for accommodating cluster numbers
                                                  of nearest neighbor atoms
    Dim m2(12) As Integer
    Dim ct(1000) As Integer                      'the number of clusters consisting of (number)
                                                  atoms
    Dim tt(1000) As Integer
    Dim ookisa(5000) As Integer                  'the number of constituent atoms within a cluster
    Dim ookisa2(5000) As Integer
    Dim clstr(7000) As Integer                   'pointer for cluster numbers
    Dim clstr2(7000) As Integer

    'simulation program for analyzing clusters
1   n = 1
    For p = 1 To 51
    For q = 1 To 51
    For s = 1 To zjiku
    If pnt(p, q, s) = 1 Or pnt(p, q, s) = 2 Then kaiseki(p, q, s) = n
    x(n) = p
    y(n) = q
    z(n) = s
    clstr(n) = n
    n = n + 1
    End If
    Next s
    Next q
```

```
Next p

For n = 1 To ta

        For i = 1 To 12
        m(i) = 0
        Next i

        If x(n) < 1 Then
        GoTo 20
        End If

'accommodating cluster numbers of nearest neighbor solute atoms with m(i)
If pnt(x(n) - 1, y(n), z(n)) = 1 Or pnt(x(n) - 1, y(n), z(n)) = 2
                                Then m(1) = kaiseki(x(n) - 1, y(n), z(n))
If pnt(x(n), y(n) - 1, z(n)) = 1 Or pnt(x(n), y(n) - 1, z(n)) = 2
                                Then m(2) = kaiseki(x(n), y(n) - 1, z(n))
If pnt(x(n), y(n) + 1, z(n)) = 1 Or pnt(x(n), y(n) + 1, z(n)) = 2
                                Then m(3) = kaiseki(x(n), y(n) + 1, z(n))
If pnt(x(n) + 1, y(n), z(n)) = 1 Or pnt(x(n) + 1, y(n), z(n)) = 2
                                Then m(4) = kaiseki(x(n) + 1, y(n), z(n))

If z(n) Mod 2 = 1 Then
If pnt(x(n) - 1, y(n), z(n) + 1) = 1 Or pnt(x(n) - 1, y(n), z(n) + 1) = 2
                                Then m(5) = kaiseki(x(n) - 1, y(n), z(n) + 1)
If pnt(x(n), y(n) - 1, z(n) + 1) = 1 Or pnt(x(n), y(n) - 1, z(n) + 1) = 2
                                Then m(6) = kaiseki(x(n), y(n) - 1, z(n) + 1)
If pnt(x(n) - 1, y(n) - 1, z(n) + 1) = 1 Or pnt(x(n) - 1, y(n) - 1, z(n) + 1) = 2
                                Then m(7) = kaiseki(x(n) - 1, y(n) - 1, z(n) + 1)
If pnt(x(n), y(n), z(n) + 1) = 1 Or pnt(x(n), y(n), z(n) + 1) = 2
                                Then m(8) = kaiseki(x(n), y(n), z(n) + 1)
If pnt(x(n) - 1, y(n), z(n) - 1) = 1 Or pnt(x(n) - 1, y(n), z(n) - 1) = 2
                                Then m(9) = kaiseki(x(n) - 1, y(n), z(n) - 1)
If pnt(x(n), y(n) - 1, z(n) - 1) = 1 Or pnt(x(n), y(n) - 1, z(n) - 1) = 2
                                Then m(10) = kaiseki(x(n), y(n) - 1, z(n) - 1)
If pnt(x(n) - 1, y(n) - 1, z(n) - 1) = 1 Or pnt(x(n) - 1, y(n) - 1, z(n) - 1) = 2
                                Then m(11) = kaiseki(x(n) - 1, y(n) - 1, z(n) - 1)
If pnt(x(n), y(n), z(n) - 1) = 1 Or pnt(x(n), y(n), z(n) - 1) = 2
                                Then m(12) = kaiseki(x(n), y(n), z(n) - 1)

Else
If pnt(x(n) + 1, y(n), z(n) + 1) = 1 Or pnt(x(n) + 1, y(n), z(n) + 1) = 2
                                Then m(5) = kaiseki(x(n) + 1, y(n), z(n) + 1)
If pnt(x(n), y(n) + 1, z(n) + 1) = 1 Or pnt(x(n), y(n) + 1, z(n) + 1) = 2
                                Then m(6) = kaiseki(x(n), y(n) + 1, z(n) + 1)
If pnt(x(n) + 1, y(n) + 1, z(n) + 1) = 1 Or pnt(x(n) + 1, y(n) + 1, z(n) + 1) = 2
                                Then m(7) = kaiseki(x(n) + 1, y(n) + 1, z(n) + 1)
If pnt(x(n), y(n), z(n) + 1) = 1 Or pnt(x(n), y(n), z(n) + 1) = 2
                                Then m(8) = kaiseki(x(n), y(n), z(n) + 1)
If pnt(x(n) + 1, y(n), z(n) - 1) = 1 Or pnt(x(n) + 1, y(n), z(n) - 1) = 2
                                Then m(9) = kaiseki(x(n) + 1, y(n), z(n) - 1)
```

```
If pnt(x(n), y(n) + 1, z(n) - 1) = 1 Or pnt(x(n), y(n) + 1, z(n) - 1) = 2
                                Then m(10) = kaiseki(x(n), y(n) + 1, z(n) - 1)
If pnt(x(n) + 1, y(n) + 1, z(n) - 1) = 1 Or pnt(x(n) + 1, y(n) + 1, z(n) - 1) = 2
                                Then m(11) = kaiseki(x(n) + 1, y(n) + 1, z(n) - 1)
If pnt(x(n), y(n), z(n) - 1) = 1 Or pnt(x(n), y(n), z(n) - 1) = 2
                                Then m(12) = kaiseki(x(n), y(n), z(n) - 1)
End If


    For i = 1 To 12
        If m(i) = 0 Then GoTo 10

        'changing cluster numbers with smaller ones
        If clstr(n) < clstr(m(i)) Then
                For l = 1 To ta
                If clstr(l) = clstr(m(i)) Then clstr(l) = clstr(n)
                Next l

        ElseIf clstr(n) > clstr(m(i)) Then
                For l = 1 To ta
                If clstr(l) = clstr(n) Then clstr(l) = clstr(m(i))
                Next l
        End If

10      Next i

    Next n

20      ct2 = 0                    'simulation program for counting the number of isolated X atoms
                                   surrounded by Al atoms

        For p = 1 To 51
        For q = 1 To 51
        For s = 1 To zjiku

        w1 = 0
        If pnt(p, q, s) = 2 Then
        x(n) = p
        y(n) = q
        z(n) = s

        'accommodating cluster numbers of nearest neighbor solute atoms with w1
        If pnt(x(n) - 1, y(n), z(n)) = 1 Or pnt(x(n) - 1, y(n), z(n)) = 2 Then w1 = w1 + 1
        If pnt(x(n), y(n) - 1, z(n)) = 1 Or pnt(x(n), y(n) - 1, z(n)) = 2 Then w1 = w1 + 1
        If pnt(x(n), y(n) + 1, z(n)) = 1 Or pnt(x(n), y(n) + 1, z(n)) = 2 Then w1 = w1 + 1
        If pnt(x(n) + 1, y(n), z(n)) = 1 Or pnt(x(n) + 1, y(n), z(n)) = 2 Then w1 = w1 + 1

        If z(n) Mod 2 = 1 Then
        If pnt(x(n) - 1, y(n), z(n) + 1) = 1 Or pnt(x(n) - 1, y(n), z(n) + 1) = 2 Then w1 = w1 + 1
        If pnt(x(n), y(n) - 1, z(n) + 1) = 1 Or pnt(x(n), y(n) - 1, z(n) + 1) = 2 Then w1 = w1 + 1
        If pnt(x(n) - 1, y(n) - 1, z(n) + 1) = 1 Or pnt(x(n) - 1, y(n) - 1, z(n) + 1) = 2 Then w1 = w1 + 1
```

```
If pnt(x(n), y(n), z(n) + 1) = 1 Or pnt(x(n), y(n), z(n) + 1) = 2 Then w1 = w1 + 1
If pnt(x(n) - 1, y(n), z(n) - 1) = 1 Or pnt(x(n) - 1, y(n), z(n) - 1) = 2 Then w1 = w1 + 1
If pnt(x(n), y(n) - 1, z(n) - 1) = 1 Or pnt(x(n), y(n) - 1, z(n) - 1) = 2 Then w1 = w1 + 1
If pnt(x(n) - 1, y(n) - 1, z(n) - 1) = 1 Or pnt(x(n) - 1, y(n) - 1, z(n) - 1) = 2 Then w1 = w1 + 1
If pnt(x(n), y(n), z(n) - 1) = 1 Or pnt(x(n), y(n), z(n) - 1) = 2 Then w1 = w1 + 1

Else
If pnt(x(n) + 1, y(n), z(n) + 1) = 1 Or pnt(x(n) + 1, y(n), z(n) + 1) = 2 Then w1 = w1 + 1
If pnt(x(n), y(n) + 1, z(n) + 1) = 1 Or pnt(x(n), y(n) + 1, z(n) + 1) = 2 Then w1 = w1 + 1
If pnt(x(n) + 1, y(n) + 1, z(n) + 1) = 1 Or pnt(x(n) + 1, y(n) + 1, z(n) + 1) = 2
                                        Then w1 = w1 + 1
If pnt(x(n), y(n), z(n) + 1) = 1 Or pnt(x(n), y(n), z(n) + 1) = 2 Then w1 = w1 + 1
If pnt(x(n) + 1, y(n), z(n) - 1) = 1 Or pnt(x(n) + 1, y(n), z(n) - 1) = 2 Then w1 = w1 + 1
If pnt(x(n), y(n) + 1, z(n) - 1) = 1 Or pnt(x(n), y(n) + 1, z(n) - 1) = 2 Then w1 = w1 + 1
If pnt(x(n) + 1, y(n) + 1, z(n) - 1) = 1 Or pnt(x(n) + 1, y(n) + 1, z(n) - 1) = 2
                                        Then w1 = w1 + 1
If pnt(x(n), y(n), z(n) - 1) = 1 Or pnt(x(n), y(n), z(n) - 1) = 2 Then w1 = w1 + 1
End If

If w1 = 0 Then ct2 = ct2 + 1
End If

Next s
Next q
Next p

30    For n = 1 To ta                  'simulation program for estimating structural parameters
      saizu = 0

         For k = n To ta
         If n = clstr(k) Then saizu = saizu + 1
         Next k

      ookisa(n) = saizu
      Next n

      For k = 1 To 500
      ct(k) = 0
      Next k

      For n = 1 To ta
         aa = ookisa(n)
         ct(aa) = ct(aa) + 1
      Next n

      elm = 0
      avr = ta - ct(1)

         For n = 2 To 500
         elm = ct(n) + elm
         Next n
```

```
    avr = avr / elm

    q = ct(1) - ct2

    Write #1, kaisuu, q, ct2, elm, avr          'storage of estimated structural parameters

End Sub
```

LIST OF PUBLICATIONS FOR THE PRESENT THESIS

1. *"Effects of additional elements and quenching conditions on the T1 phase precipitation in Al-1.3%Li-5.5%Cu-0.13%Zr alloys"*
S. Hirosawa, T. Sato, A. Kamio, K. Kobayashi and T. Sakamoto
J. Jpn. Inst. Light Metals, 46 (1996), 119-125.

2. *English translate version*
S. Hirosawa, T. Sato, A. Kamio, K. Kobayashi and T. Sakamoto
Light Metals Review, 4(1997), 14-20.

3. *"Effects of Mg addition on the kinetics of low-temperature precipitation in Al-Li-Cu-Ag-Zr alloys"*
S. Hirosawa, T. Sato and A. Kamio
Mat. Sci. and Eng. A, 242 (1998), 196-202.

4. *"Comparison between Resistivity Changes and Monte Carlo Simulation for GP Zone Formation in Al-Cu Alloys Containing Additional Elements"*
S. Hirosawa, T. Sato, J. Yokota and A. Kamio
Mater. Trans., JIM, 39 (1998), 139-146.

5. *"Effects of Additional Elements on phase decomposition of Al-Li alloys and Computer Simulation"*
J. Yokota, S. Hirosawa, T. Sato and A. Kamio
J. Jpn. Inst. Light Metals, to be published.

ABSTRACT OF THE PRESENT THESIS

As a new light material for the 21st century, Al-Li-Cu alloys have been received considerable attention because of their excellent combination of high specific strength and low density. The small additions of alloying elements; e.g. Mg and Ag, are extremely effective in achieving the ultra-high strength of the alloys due to the enhanced nucleation of strengthening phases. The present thesis aims to elucidate the roles of microalloying elements on the mechanical strength and precipitate microstructures of Al-Li-Cu alloys. The microstructures observed with transmission electron microscopy (TEM) and hardness changes indicate that a small amount of Mg markedly accelerates the nucleations of both GP zone and the $T_1(Al_2LiCu)$ phase, resulting in the enhanced age-hardening. Quantitative analysis of the precipitation kinetics by the electrical resistivity changes also reveals the detailed effects of Mg; i.e. an accelerated nucleation and suppressed growth of the above precipitates. This is well explained in terms of both the extremely increased number density of Mg/Cu/Vacancy complexes and the pronounced decrease in free-vacancies available for Cu diffusion due to the preferential vacancy trapping by Mg atoms. Such situations are directly observed in atom configurations during the computer simulation based on a Monte Carlo method. The proposed simulation models with parameters derived from characteristic quantities of each element can successfully predict the role of an arbitrary microalloying element in Al-Li-Cu alloys. The theoretical prediction led to a concept for alloy designing of new Al-Li-Cu alloys having higher tensile strength of 656MPa.

概要
(Abstract)

次世代の軽量・高性能構造用材料として期待されるAl-Li-Cu系合金には，合金の機械的強度の増大を図るため，種々の微量元素が添加されている．これらの微量添加元素の役割を原子レベルで解明することは，合金設計の観点からも重要である．本論文では，従来の実験手法では観測が困難な溶質原子クラスタの動的な形成挙動を，モンテカルロ・シミュレーションを用いて原子レベルで解析した．さらに，実験的に得られる相分解速度とクラスタのサイズ分布や析出密度などのミクロ的な組織因子との関係を定量的に明らかにした．また，マイクロアロイングの手法による合金の特性改善に有効な添加元素を系統的に分類・予測し，実際に新合金の開発を行った．本論文は9章から構成されており，各章の概要は以下の通りである．

Chapter 1 では，実用合金としてのAl-Li-Cu系合金の優位点および問題点を述べ，マイクロアロイング元素による合金特性の向上および計算機シミュレーションを用いた相分解挙動解析のこれまでの研究例を概説した．さらに，本研究の目的および構成についても述べた．

Chapter 2 では，実用Al-Li-Cu系合金に添加されているMgおよびAgによる合金の特性改善の一例を示し，微量のMg添加による①低温時効温度(278～373K)でのGPゾーンの形成の促進，および②高温時効温度(403～523K)でのT_1相の粒内析出の促進，の機構解明の必要性を指摘した．

Chapter 3 では，モンテカルロ法を用いた計算機シミュレーションの利点および本論文で構築したシミュレーションモデルについて概説した後，各元素に固有の各種物性値から相互作用パラメータを導出する手法を新たに提案した．さらに，実験的に得られる電気比抵抗変化$\Delta\rho$と，シミュレーションの進行に伴う計算比抵抗ρ_{Cal}との比較により，得られたシュミレーション結果の妥当性を評価した．

Chapter 4 では，比抵抗変化測定から得られるAl-Cu系合金のGPゾーンの形成速度とシミュレーションの解析結果を比較することで，Cu原子クラスタの形成挙動に及ぼす第三添加元素の影響を系統的に分類した．特にMgは，空孔との強い相互作用のために，優先的に空孔をトラップしてGPゾーンの成長速度を遅滞させるが，同時にCu原子とも強い相互作用をもつために，Mg/Cu/Vacancy複合体を形成する．これはMgに特有の性質によって説明され，これと類似の複合体を形成する元素は他

には予測されなかった.

Chapter 5 では, Al-Li系合金の低温時効析出挙動に対する第三添加元素の影響をモンテカルロ・シミュレーションを用いて系統的に分類した. 第二近接原子間までの相互作用を考慮することにより, $L1_2$型規則構造をもつδ'相(Al_3Li)の析出現象をシミュレーションすることができるようになり, さらに規則相内での第三添加元素の優先置換サイトも予測可能となった.

Chapter 6 では, Chapter 4および5で得られたAl-Cu, Al-Li両二元合金に対する第三添加元素の影響をもとに, GPゾーンとδ'相が同時に析出するAl-Li-Cu系合金の相分解挙動について検討を行った. Al-Li-Cu-X四元系合金(X:微量添加元素)へのシミュレーションモデルの拡張により, Cu原子およびLi原子両クラスタの同時析出をシミュレーションすることができ, 微量のMg添加はLiによる空孔トラップ作用で遅滞したCu原子クラスタの形成速度を再び促進することを明らかにした. これは, Mg/Cu/Vacancy複合体がGPゾーンの異質核生成サイトとして働くためであり, ρ_{Cal}が$\Delta\rho$と良く一致することからも, Mg/Cu/Vacancy複合体機構の妥当性が検証された.

Chapter 7 では, 実用Al-Li-Cu系合金の高強度を担っているT_1相の核生成の機構について, 溶質原子と空孔の働きに注目して検討を行った. 空孔間の相互作用を考慮したシミュレーションにより, Mg/Cu/Vacancy複合体による積層欠陥の形成が, hcp構造をもつT_1相の有効な異質核として働くことを明らかにした. Mgとの強い相互作用をもつAgの複合添加は, Mg/Cu/Vacancy複合体の分布状態をより高密・微細にするために, 本系合金の機械的強度の一層の増大を引き起こす.

Chapter 8 では, 本研究で確立したAl-Li-Cu系合金における各微量添加元素の効果の予測をもとに, 本系合金のさらなる特性改善のための合金設計の概念を提案し, 実際に新合金の開発を行った. 本モデルでMgとの複合添加の有効性が予測されたZnは, 実際に合金の大幅な高強度化を達成することができ, 合金特性の向上に有効なマイクロアロイング元素の選定に, 本モデルが適用できることを実証した. さらに, 微量のMnを添加することで, 従来合金を超える引張強さをもつ高強度Al-Li-Cu系合金を開発した.

Chapter 9 では, 本論文を総括し結論を記した.

謝辞
(Acknowledgments)

初めに，研究室所属以来6年半に渡って本研究を遂行する場を与えて下さった，金属工学科神尾彰彦教授に深く感謝致します．先生には，三度の国際会議を含む計十回の地方での学術会議に参加する機会を賜ったばかりでなく，常に優しい笑顔と広い心で私の研究成果に対する的確なご指導を頂きました．神尾研究室の一卒業生として，先生の学生に対する教育姿勢に敬意を表したいと思います．これからも末永く叱咤激励の程を宜しくお願い申し上げます．

金属工学科里達雄助教授には，直接の指導教官として非常に多くのご指導・ご助言を賜りました．深夜，終電時間ぎりぎりまでディスカッションして一緒に駅まで走っていただいたことや，土曜日や日曜日にまでお宅に押しかけてご迷惑をお掛けしたことをお詫びするとともに，常に真理を探究しようとする姿勢に心から敬服致します．先生は，研究に臨むに当たっての心構えや研究者としてのあり方を教えて下さった最良のお見本であり，私がこれから研究者として進んでいく際の大きな目標でもあります．先生のこれからの益々のご活躍を心よりお祈り致しております．

金属工学科手塚裕康助手には，実験における直接の手助けを賜ったばかりでなく，私の考察の巧拙への的確なご指摘を穏和な口調で幾度となく授かりました．また，公私に渡って非常に多くのことを教えて頂き，私との年齢差を感じさせない若さは，私の長期に及ぶ研究室生活の大きな精神的な支えでもありました．今後とも変わらぬご指導を下さいますよう宜しくお願い致します．

金属工学科入戸野修教授，松尾孝教授，中村吉男助教授には，非常に有益かつ示唆に富んだご指摘・ご助言を賜り，博士論文としてよりふさわしい内容に仕上げるための大きな指針を与えて下さいました．更に松尾孝教授には，卒業後英国ロンドン大学インペリアルカレッジで研究する機会もご紹介頂きました．この場をお借りして各先生方に厚く御礼を申し上げます．

また，研究室在籍中に助手として多くのお世話を頂きました，小林郁夫，細田秀樹，洪性吉，片山英樹，張時栄，佐伯雅之各博士には，私が論文をまとめる際の貴重なアドバイスを賜り，心から感謝致しております．私も先輩方に負けぬよう精一杯努力するつもりでおりますので，これからも引き続き宜しくお願い致します．

早稲田大学理工学部齊藤良行教授および京都大学工学研究科奥田浩司助手には，

モンテカルロ法を用いた計算機シミュレーションを行うに当たっての有益なご助言を多く賜りました．お忙しい中直接お会いしてお話を伺う機会を設けて下さり，本当に心より感謝致しております．

株式会社アリシウムの坂本敏正氏(現株式会社神戸製鋼所)および小林一徳氏(現株式会社神戸製鋼所)には，本論文で用いた試料を提供して下さいました．多くのディスカッションを行ったなかで，企業としてのものの考え方に触れることができたことは，私にとっても非常に有意義なことでありました．ここに深く御礼申し上げます．

私の後輩でもある修士課程の横田純一君には，本シュミレーションのプログラム開発を一からお願いしたばかりでなく，論文の本質に関する多くの的確な指摘を受けて，非常に有意義な議論を数多く行うことができました．彼の研究に取り組む姿勢は見習うべき箇所が多くあり，共同研究者として一緒に切磋琢磨できたことは，私にとって大きな財産であります．新たな分野での益々のご活躍を期待しています．
また，多くのご迷惑をお掛けした諸先輩方，常に良きライバルであった同期の仲間，そして個性豊かなかわいい後輩諸君，本当にいろいろとご協力ありがとうございました．

最後に，これまで温かく見守ってくれた両親および婚約者の内田歩さんに心から感謝致します．これからも変わらずに宜しくお願い致します．

1998年3月

廣澤渉一